Riboflavin-based amphiphiles for tumour-targeted nanosystems

Nataliia Subbotina Beztsinna

THÈSE PRÉSENTÉE

POUR OBTENIR LE GRADE DE

DOCTEUR DE

L'UNIVERSITÉ DE BORDEAUX

ÉCOLE DOCTORALE Sciences de la Vie et de la Santé

SPÉCIALITÉ Interface Chimie Biologie

Par Nataliia SUBBOTINA BEZTSINNA

RIBOFLAVIN-BASED AMPHIPHILES FOR TUMOUR-TARGETED NANOSYSTEMS

Dérivés amphiphiles de la riboflavine pour le développement de nano-systèmes à ciblage tumoral

Sous la direction de : Isabelle BERQUE-BESTEL

Soutenue le 26/11/2015

Membres du jury:

M. DUFOURC, Erick J, Directeur de recherche, UMR 5248, Université de Bordeaux	**Président**
Mme MIGNET, Nathalie, Directrice de recherche, UMR 8258-Inserm 1022, Université Paris Descartes	**Rapporteur**
M. VANDAMME, Thierry, Pr, Directeur-adjoint chargé de recherche, UMR 7199, Université de Strasbourg	**Rapporteur**
M. KIESSLING, Fabian, Pr., Directeur du département ExMI, Université RWTH Aachen	**Examinateur**
M. GROSSET, Christophe, Chargé de recherche 1, Inserm U1073 GREF, Université de Bordeaux	**Examinateur**
Mme. BERQUE-BESTEL Isabelle, Pr., Directrice des études, Université de Bordeaux	**Directrice de thèse**

Acknowledgements

Firstly, I would like to express my sincere gratitude to my supervisor Prof. Isabelle Berque-Bestel for the continuous support during this Ph.D study, her patience, understanding, motivation, and vast knowledge. Despite a very busy schedule, she was always there for me. Her guidance inspired me and helped a lot during my research and writing of this thesis. I could not have imagined having a better supervisor and mentor for my Ph.D study.

Besides my supervisor, I would like to thank the rest of my thesis committee: Dr. Nathalie Mignet, Prof. Thierry Vandamme, Dr. Erick J Dufourc, Prof. Fabian Kiessling and Dr. Christophe Grosset, for taking time out from their busy schedule to help as thesis reporters and examiners.

This work was realised in three research institutes at different time-points of my PhD – ARNA, U869 Inserm and CBMN, UMR 5248 in Bordeaux, France and ExMI in Uniklinik RWTH Aachen in Germany. Therefore, my sincere thanks goes to all the members of these laboratories and especially to Dr. Jean-Louis Mergny, Prof. Phillipe Barthélemy, Dr. Erick J Dufourc, Dr. Sophie Lecompte and Prof. Fabian Kiessling, who hosted my research activity and gave me access to the laboratories and research facilities. Without their precious support it would not be possible to conduct this research.

I recognise that this research would not have been possible without the financial assistance of "Initiative d'Exellence" of the University of Bordeaux, that gave me a exceptional chance to perform the part of this project in Germany, and Ligue National contre le Cancer for financial support, and express my gratitude to those agencies.

I highly appreciate the help of all the people who participated in the realisation of this project in France –Rémy Bailly, Arnaud Pol and Dr. Boutayna Frih, Prof. Alain Brisson, Sisareuth Tan and in Germany – Dr. Twan Lammers, Yoanna Tsvetkova, Marek Weiler and Diana Moeckel.

The particular acknowledgement I address to Axelle Grelard and Dr. Erick J Dufourc for the solid state NMR experiments, the help in data interpretation and motivating discussions.

I would like again to express my gratefulness to Prof. Fabian Kiessling, who organised the animal experiments and gave me the unique opportunity to work with such fascinating imaging facilities like photoacoustic imaging and combined μCT/FMT imaging system.

A very special thanks goes out to Sybille Kennel, who as an excellent friend was always willing to help and give her best suggestions. She was there for me even during the hardest times, especially on the last days before submitting this thesis... And of course, my experience in the chemistry lab would have never been the same without her.

I would also like to acknowledge all members of our MMBE team in Bordeaux - Marion Solé, Rémy Bailly, Dr. Nada Taib, Annie Lagardere for their support and fruitful discussions, and especially Dr. Jean Dessolin for careful reading of this manuscript and critical remarks. I also wish all the best to my friend, Marion Solé, who is going to pursuate this project in her thesis.

I acknowledge my colleagues, who helped me with encouraging advises and expressed their critical opinions about this work – Dr. Cathy Staedel, Dr. Laurent Azéma, Dr. Amit Patwa, Dr. Khalid Ouzmil, Brune Vialet, Ananda Appavoo, Dr. Christophe Grosset, Claude Manigand, Dr. Jithin Jose, Dr. Wa'El Al Rawashdeh and Anne Rix.

Last but not the least, my deepest appreciation goes to my husband, Artem. His love, support, patience, and understanding have made it possible for me to finish this Ph.D. I also appreciate the sacrifices of my family in order that I might devote time and energies to my studies. I would also like to thank my dear parents and my brother for supporting me emotionally throughout these three years and especially during the writing of this thesis.

Abreviations

Ab - antibody

ACN – acetonitrile

ACUPA - S,S-2-[3-[5-amino-1-carboxypentyl]-ureido]-pentanedioic acid

CAC – critical aggregation concentration

CAN - cerium ammonium nitrate

CMC - critical micelle concentration

CPP - critical packing parameter

Cryo-TEM - cryo transmission electron microscopy

DAPI - 4',6-diamidino-2-phenylindole

DBU - 1,8-diazebicycloundec-7-ene

DCC - N,N'-Dicyclohexylcarbodiimide

DCM – dichloromethane

DEAD - diethylazodicarboxylate

DiR - 1,1'-dioctadecyl-3,3,3',3'-tetramethylindotricarbocyanine iodide

DLS - dynamic light scattering

DMAP - 4-dimethylaminopirydine

DMF – dimethylformamide

DMPC - 1,2-dimyristoyl-sn-glycero-3-phosphocholine

DMPG - 1,2-dimyristoyl-sn-glycero-3-phosphoglycerol

DMSO – dimethylsufoxide

DMT – dimethoxytrityl

DSC - differential scanning calorimetry

EPR - enhanced permeability and retention

ESI - electrospray ionisation

FACS – fluorescence activated cell sorting

FAD - flavin adenine dinucleotide

FBS - foetal bovine serum

FDA - US food and drug administration

FID – free induction decay

FMN - flavin mononucleotide

FMT – fluorescence molecular tomography

FRI – fluorescence reflectance imaging

GRAS – generally recognised as safe

HDL - high-density lipoprotein

HEPES - 4-(2-hydroxyethyl)-1-piperazineethanesulfonic acid

HER2 - human epidermal growth factor receptor 2

HPLC - high pressure liquid chromatography

HUVEC - human umbilical vein endothelial cells

i.v. – intravenous

ICG - indocyanine green

IPA – intensity of PA signal

ITC – isothermal titration calorimetry

LDL - low-density lipoprotein

LRhPE - 1,2-dimyristoyl-sn-glycero-3-phosphoethanolamine-N-(lissamine rhodamine B sulfonyl)

LUV – large unilamellar vesicles

MALDI-MS - matrix-assisted laser desorption ionisation mass spectrometry

MeOH – methanol

MLV – multilamellar large vesicles

MPS - mononuclear phagocytic system

MRI - magnetic resonance imaging

MTT - 3-(4,5-dimethylthiazol-2-yl)-2,5-diphenyltetrazolium bromide

MW - molecular weight

NGR - asparaginylglycylargininic acid

NIR – near infrared

NMR – nuclear magnetic resonance

OxyHemo and deOxyHemo – oxygenated and deoxygenated haemoglobin

PA – photoacoustic

PAI - photoacoustic imaging

PBS – phosphate buffered saline

PC - phosphatidylcholine

pcCPP - photolabile-caged cell-penetrating peptide

PCS - photon correlation spectroscopy

PDI - polydispersity index

PE - phosphatidylethanolamine

PEG - polyethylene glycol

PFA – performic acid

PG - phosphatidylglycerol

PI - phosphatidylinositol

PMP – paramethoxyphenol

PS - phosphatidylserine

PS - photoacoustic signal

PSA - prostate specific antigen

RCP - RF carrier protein

RES - reticuloendothelial system

RF - riboflavin

RFA - RF amphiphile

RfdiC14 - 5'O -dimyristoyl-phosphoriboflavin

RGD - arginylglycylaspartic acid

RhB - Rhodamine B

ROI - region of interest

RRM2 - M2 subunit of rinonucleotide reductase

RT – room temperature

SASA – solvent accessible surface area

SAXS - small-angle X-ray scattering

siRNA - small interfering ribonucleic acid

ss NMR – solid state NMR

TEA - triethylamine

TFA – trifluoroacetic acid

THF - tetrahydrofuran

TLC - thin layer chromatography

Tm –transition temperature

TOF – time of flight (in mass spectrometry)

US - ultrasound

UV-Vis - ultraviolet–visible spectroscopy

VEGF - vascular endothelial growth factor

VPF - vascular permeability factor

μCT – micro-computer tomography

Table of contents

1 Chapter I. Introduction: state of the art in modern drug delivery systems

1.1 Amphiphile self-assemblies in drug delivery

1.1.1 Generalities

Amphiphile is a term commonly used to describe a molecule containing both hydrophilic and hydrophobic moieties linked by covalent bonds.[1] The non-polar hydrophobic part is generally represented as a tail (composed from one or more hydrocarbon, fluorocarbon or dimethylsiloxane chains) and the polar hydrophilic part is represented as a charged or uncharged headgroup (Figure 1.1).[2] The unique property of amphiphiles is their capacity to self-assembly in aqueous solution and form well-defined structures, such as micelles, liposomes, cubic and hexagonal phases, emulsions and nanoparticles. These auto-assemblies found their application in diverse fields from nanodevices, drug delivery to template synthesis, and cell imaging.[1] The properties of the formed nanosystems arise from amphiphile architectures (innate hydrophilic–hydrophobic balance and geometric packing constraints) and experimental conditions, such as concentration, temperature, pH, salt content and presence of co-solutes.[1,2]

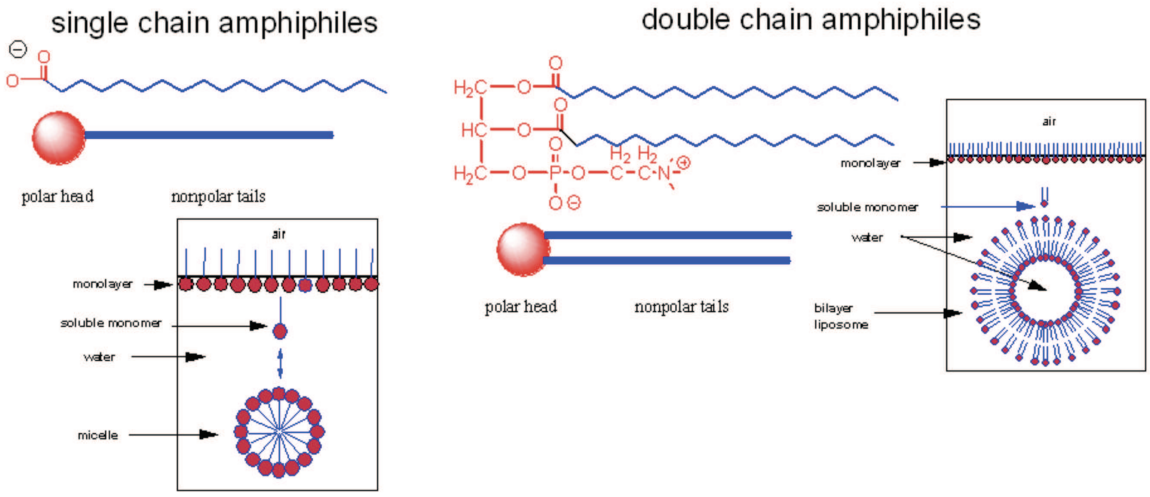

Figure 1.1 Schematic representation of single or double chain amphiphiles structures, water-air distribution and self-assembly.[3]

Low molecular weight amphiphiles are generally referred as surfactants (Figure 1.2). Charged surfactants could be anionic or cationic regarding the overall net charge of their headgroup. Uncharged surfactants are non-ionic, while zwitterionic surfactants contain in their structure both a negative and a positive charge. For instance, phospholipids are natural zwitterionic amphiphiles and play a significant role in living organisms as their auto-assemblies form cell membranes. Moreover, natural and synthetic phospholipids are extensively used in drug delivery since they can form a variety of interesting self-assemblies (liposomes, in particular) with low toxicity and biocompatibility. In addition, variety of new synthetic surfactants of low toxicity and high biodegradability exist. Among them, surfactants with carbohydrate or amino acid polar headgroups displayed promising results.[2,4]

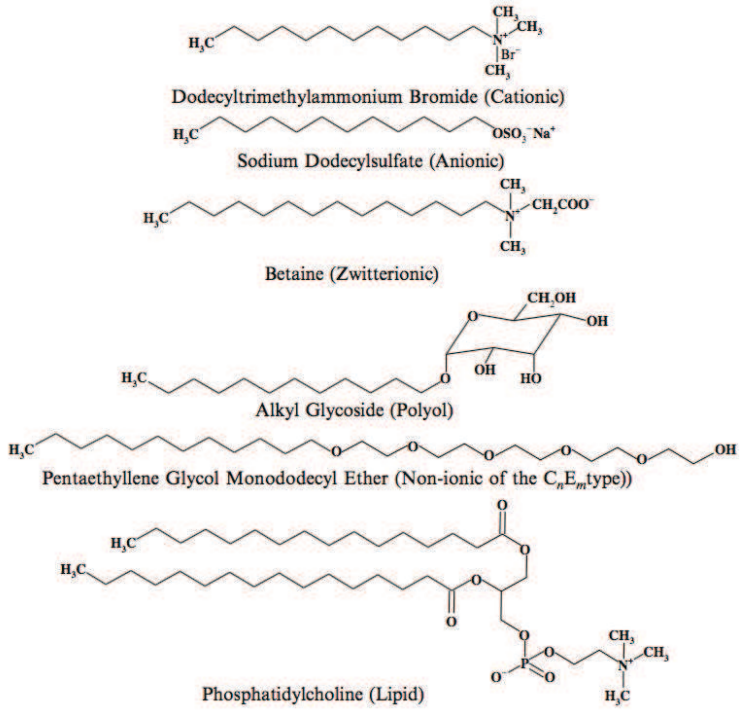

Figure 1.2 Chemical structures of some common surfactants.[2]

1.1.1.1 Unusual amphiphiles

Nowadays, plenty of unconventional small molecule amphiphiles exists. Here we will briefly cite a couple of interesting examples. For instance, amphiphiles with unusual headgroup such as lipopolythioureas,[5] nucleolipids[6] or amino acid-nucleolipids[7] were reported as efficient carriers for the nucleic acid delivery (Figure 1.3). The advantage of lipopolythioureas over conventional cationic lipids, used for nucleic acid complexation, is the absence of positive charge, which is often related to *in vivo* toxicity. The efficient interactions with DNA are ensured by the thiourea headgroups creating strong hydrogen bonds with phosphate moieties.[5] Nucleolipids were initially designed to facilitate the transport of nucleotides or nucleosides to the cells and later on were shown to form interesting self-assemblies by themselves. Moreover, nucleotides being the constituting monomers of nucleic acids, could entrap DNA, RNA or oligonucleotides in these systems trough base–base interactions between nucleic acids and nucleolipids.[6] Interestingly, the addition of an amino acid group to the nucleolipid structure changed the architecture of formed auto-assemblies offering greater potential for the encapsulation of both water-soluble and insoluble drugs.[7]

The headgroup replacement with natural and/or bioactive oligomer such as peptide or oligonucleotide could create amphiphiles with interesting self-assembly topologies and even pro-drug properties. For instance, siRNA (small interfering RNA) conjugated to a natural lipid squalene (Figure 1.3), forms an amphiphile able to auto-assembly in nanoparticles and even suppress tumour growth *in vivo* by the action of siRNA.[8] Thus, the headgroup modification allows the formation of additional interactions (i.e. hydrogen bonds, π-stacking, electrostatic attraction) between amphiphiles and/or their cargo.

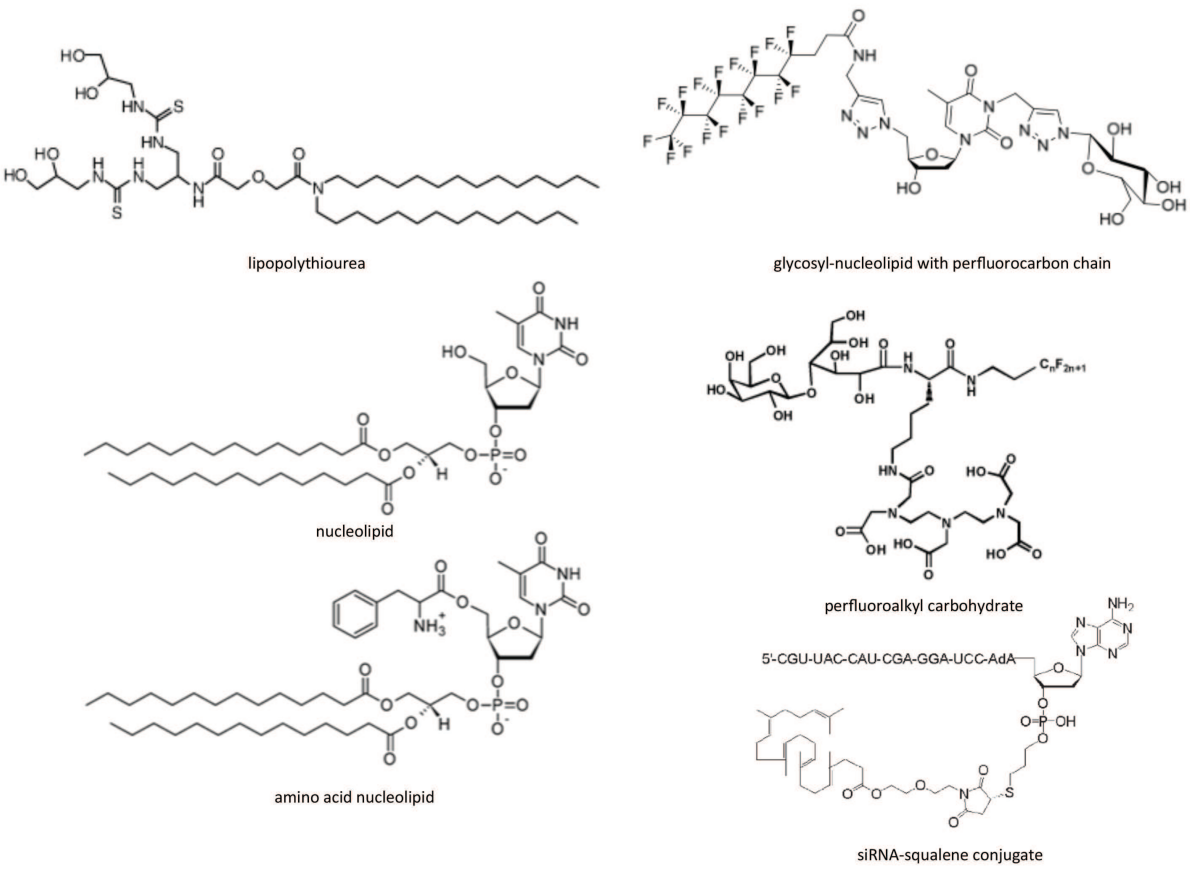

Figure 1.3 Examples of unconventional amphiphiles: lipopolythiourea,[5] nucleolipid,[7] amino acid-nucleolipid,[7] glycosyl-nucleolipid,[9] perfluoroalkyl carbohydrate[10] and siRNA-squalene conjugate.[8]

On the other hand, the non-polar tail could be also customised. For example, the classical alkyl chain was replaced by perfluorocabon analogue in some glycosyl-nucleolipids[9] and perfluoroalkyl carbohydrates[10] (Figure 1.3). Perfluorocarbons tend to be hydro- and lipophobic at the same time. This makes them less toxic towards living cells because they do not mix with cell membranes and thus avoid the detergency effect, typically observed for single alkyl chain amphiphiles.[10]

Some other unconventional amphiphiles exhibit more rigid molecular structures and form less dynamic self-assemblies. Thus, bile salts and derivatives own the steroid nucleus and non-trivial distribution of hydrophobic and hydrophilic regions. This leads to complex and ordered arrangements in supramolecular frameworks such as fibers, gels or tubules. Such structures allow efficient cell membrane penetration and have large drug encapsulation capacities.[11] Tripod amphiphiles represent another interesting example. They have bifurcations on the hydrophilic or hydrophobic portions allowing them to possess multiple polar headgroups and also generating more rigid self-assemblies. Such surfactants were shown extremely useful for membrane protein solubilisation, where the rigid arrangement of formed self-assembly allows the preservation of native protein structure.[12]

These few examples illustrate the multiplicity of amphiphile chemistry and the huge potential that non-conventional amphiphiles could offer in the field of drug delivery.

1.1.1.2 Self-assembly formation

Due to the unique structure of amphiphiles, they tend to accumulate at the boundary of two phases. In aqueous solutions, hydrophobic moieties of the molecule are removed from the aqueous environment in order to achieve a state of minimum free energy (Figure 1.1). When the concentration of surfactant in solution increases, the free energy of the system begins to rise due to unfavourable interactions between water and the hydrophobic moiety of the molecule causing the structuring of the surrounding water molecules and a subsequent decrease in entropy. There is a specific and narrow concentration range of amphiphile in solution, referred as critical micelle concentration (CMC). At this concentration range, surfactants are able to self-assemble into micelles – spherical small-sized particles that form a homogeneous solution with low viscosity. Thus, CMC is an extremely important parameter to characterise self-association. It relies mainly on the chemical structure of an amphiphile and a solvent. The number and size of the hydrophobic tails is also very important. The micelle formation minimises unfavourable interactions between the surrounding water and the hydrophobic groups of the surfactant. At CMC, the fraction of free amphiphiles in solution is the same as the fraction of molecules building up the micelle. Accordingly, micelles are thermodynamically stabilised against disassembly when the amphiphile concentration is above the CMC. In contrast, dilution below the CMC leads to micelles disassembly which is dependent on the amphiphile structure and the interactions between the hydrophobic chains.[2,13]

The micellisation process is also temperature-dependent. The temperature point where solubility of surfactant reaches CMC is known as Krafft temperature (*Figure 1.4*). Below this point no aggregation occurs. But at Krafft point the amphiphile solubility dramatically increases and the solution consists of a mixture between micelles and single molecules. However, above a certain temperature the micellisation also does not take place.[2,13]

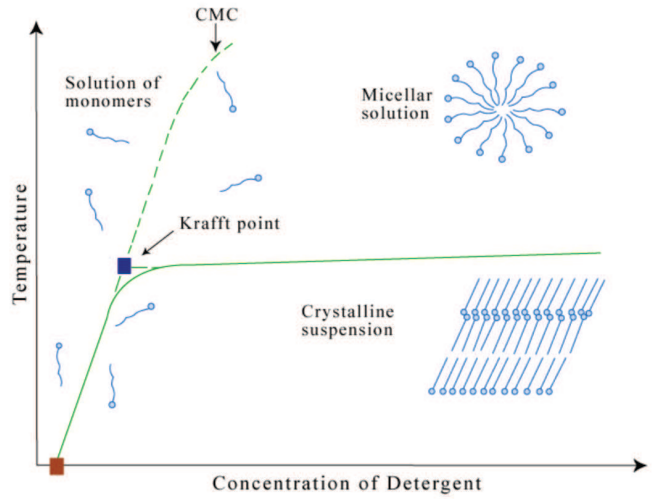

Figure 1.4 Schematic representation of CMC and Krafft point (adapted from https://www.flickr.com/photos/mitopencourseware/4799104711, image licence ocw.mit.edu/terms).

When small-molecule surfactants are combined with polymers or biological molecules, they are able to form well-defined assemblies at the concentration of surfactants lower than CMC. This concentration is referred as critical aggregation concentration (CAC).[14]

CAC is useful in the interaction studies between biopolymers, and surfactants such as self-assembly of membrane-protein complexes.[15]

Interestingly, a simple sphere-shaped micelle is able to evolve into anisotropic cylindrical structures. However, the resulting solution still represents a single phase. If the surfactant concentration is further increased, the linear micelle growth could give rise to branched structures that may lead to interconnected structures (bicontinuous). In this case the solutions are not only continuous in the aqueous solution but also in the surfactant. Additional concentration increase could lead to a rich variety of self-assemblies (Figure 1.5). Hence, the interplay between amphiphile chemical structure, concentration, solvent properties and temperature may allow the transition of one structure into another, and thus opens a field of opportunities for drug encapsulation and delivery.[2]

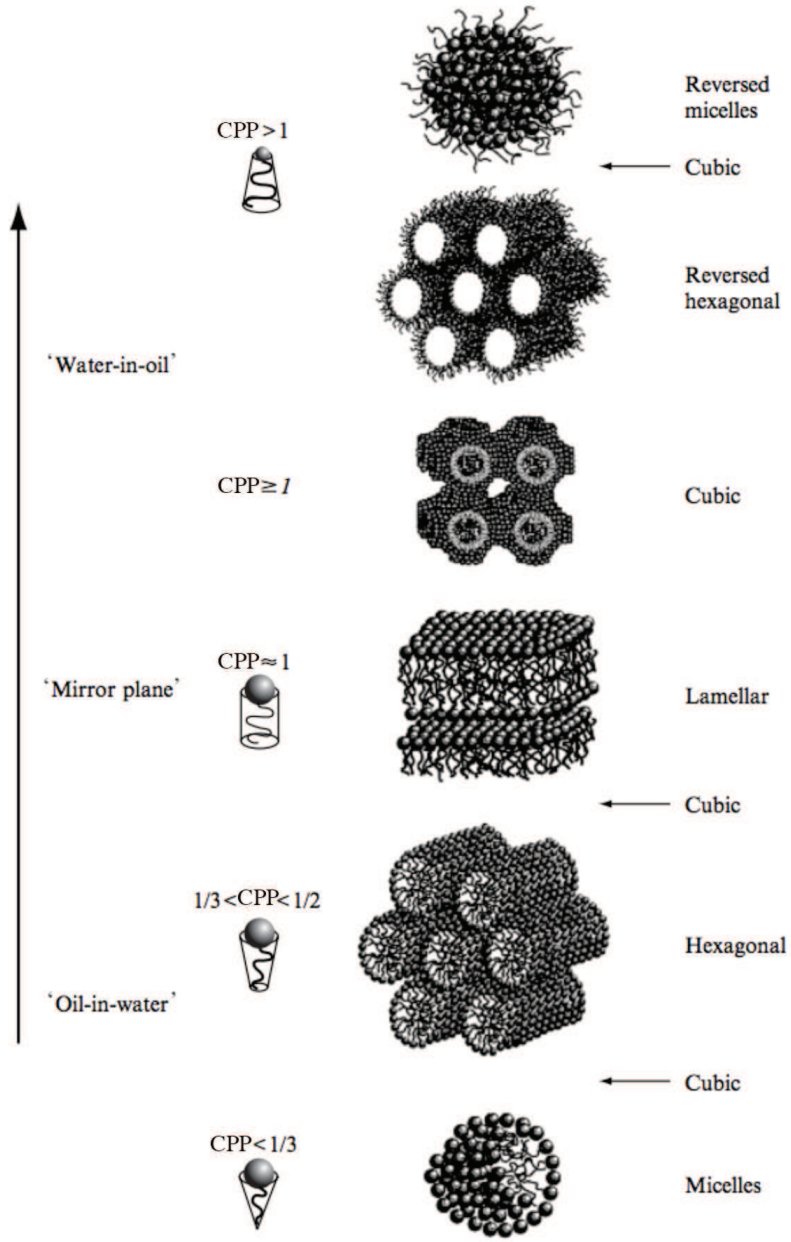

Figure 1.5 Examples of surfactant auto-assemblies in accordance with their CPP value.[16]

Supramolecular amphiphile self-assemblies are fluid-like, flexible and easily affected by weak external forces as they held together by weak van der Waals, hydrogen interactions or hydrophobic effect and thus are considered as soft colloidal systems. Such systems could be divided into two main groups: limited or discrete aggregates represented by spherical, prolate or cylindrical shapes; and unlimited or infinite structures that are interconnected over large distances in two or three dimensions. For instance, hexagonal phase (Figure 1.5), constructed from infinitely long cylindrical micelles assembled in hexagonal pattern represents an example of one-dimensional continuity. Bicontinuous cubic and the sponge structures are examples of three-dimensional continuity.[2]

The capacity of an amphiphile to form one or another type of self-assembly relies not only on external environmental conditions (pH, temperature, ionic force *etc*.) but also on its chemical structure. In particular, putative auto-assembly could be predicted by so-called critical packing parameter (CPP), which represents amphiphile geometry (Equation 1).[2]

$$CPP = \frac{v}{a_s l_c} \quad (1)$$

Equation 1, where a_S is the effective area per headgroup, v the volume of the hydrocarbon chain and l_C is the maximum effective length that the hydrocarbon chain can undertake.[2]

The direct correlation between CPP and the type of self-assembly exists.[2,16] For instance, when CPP is lower than 1/3, spherical micelles with extremely small radius are formed. A CPP is between 1/3 and 1/2 could predict the formation of cylindrical micelles, which is very a frequent case for single chain surfactants with small polar headgroup. For double chain phospholipids with large headgroup CPP is generally between 1/2 and 1. These amphiphiles are not able to pack themselves in micelles and thus form lamellar bilayers or vesicles. When hydrophobic tail is very large compare to polar head, the CPP is greater than 1, inversed structures are formed in non-polar solvents. CPP could be tuned by addition of other surfactant and by changes in temperature, pH or ionic force.[2,17]

In the next section we will present several amphiphile self-assemblies and their potential utility in drug delivery and controlled release.

1.1.2 Micelles

Lipid derived micelles are small spherical aggregates (diameter 5-50 nm) characterised by a core-shell architecture in which the inner core is composed of the hydrophobic chains creating a cargo space for the lipophilic drugs.[2] Micelle-forming amphiphiles are widely employed in personal hygiene and skin care products. They also serve as tools for RNA and DNA extraction from biological specimens, cell lysis and membrane protein solubilisation.[18]

Compared to other amphiphile self-assemblies, micelles are less employed in the drug delivery field. This is mostly due to their quick disassembly upon dilution in the blood flow which limits clinical utilisation.[19]

However, some micellar formulations are used as solubilisers for water-insoluble drugs leading to injectable preparations more suitable for human administration and less toxic.[20] A couple of micelle-derived nanoparticles exist on the market. Among them, a stable mixed micellar nanodisks (bicelles) from cholesterol sulphate with Amphotericin B (commercialised as Amphotec®) are used for fungal infections treatment.[20,21]

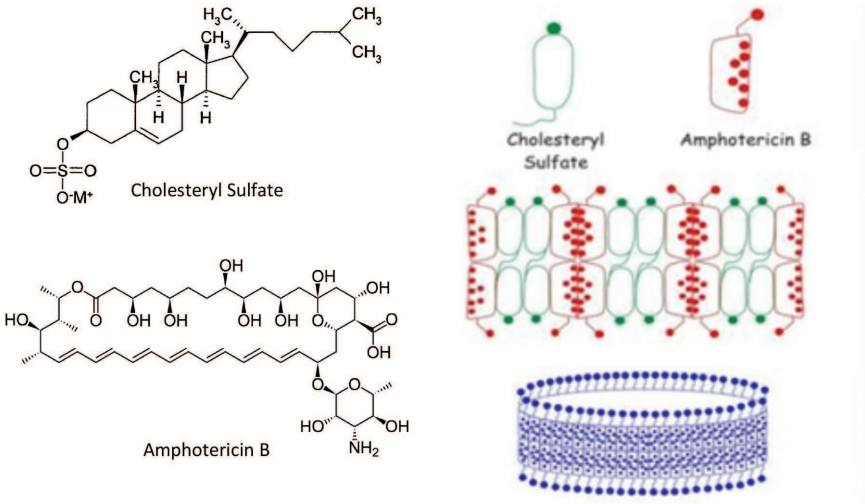

Figure 1.6 Chemical composition of Amphotec® and schematic presentation of self-assembly (http://www.veomed.com/va041141872010).

Estrasorb® is another example of FDA (US Food and Drug Administration) approved micellar formulation. It is used for the estradiol delivery into the bloodstream after topical application to treat menopausal symptoms. This formulation is also micelle-derived nanoparticle and includes soyabean oil, water, polysorbate 80 and ethanol in order to encapsulate estradiol in hemihydrate form.[22]

Reverse micelles are also used for the topical delivery and sustained release of water-soluble drugs. After the contact of a reverse micellar formulation with aqueous body fluids (i.e. mucosa) the reverse micelles convert into a liquid crystalline phase. This reduces the release rate of the solubilised drug molecules. Such formulations could be beneficial for ophthalmological administration as well as for nasal, buccal, rectal, vaginal or even parenteral subcutaneous application.[23]

1.1.3 Cubosomes and hexasomes

When cubic or hexagonal phases are dispersed in excess of water and stabilised, they are able to form nanoparticles termed cubosomes and hexasomes respectively. These structures are highly ordered and thermodynamically stable and thus could represent a major interest in the field of controlled drug release and diffusion.[24,25] The changes in pH and ionic strength were reported to induce reversible transitions from cubic to hexagonal phase and sustained drug release which makes them promising carriers for oral administration route.[26]

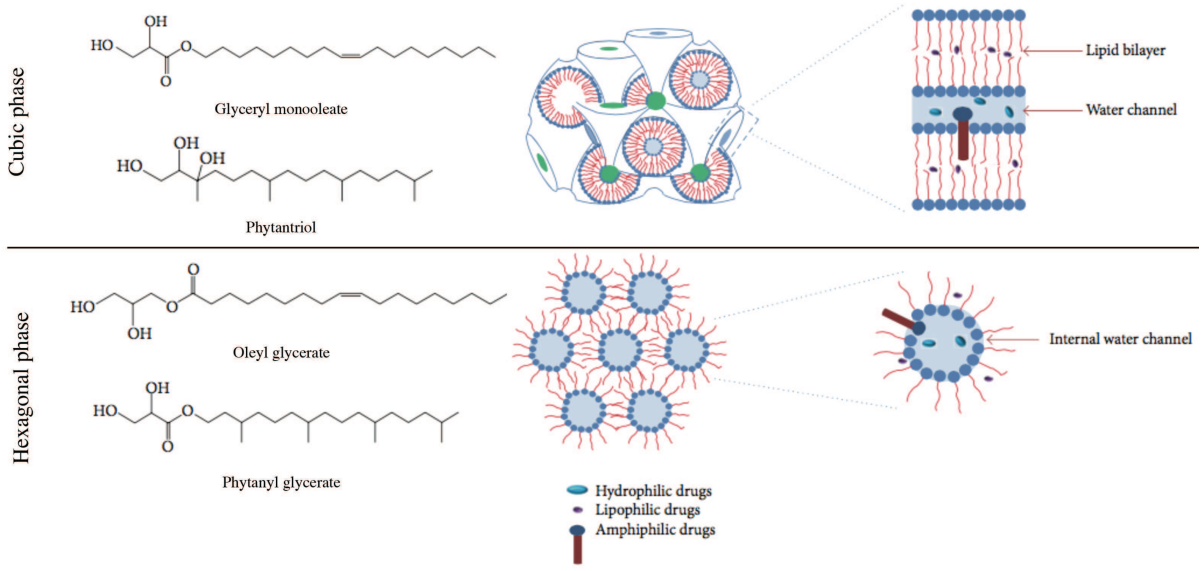

Figure 1.7 Chemical structures of lipids utilised for the preparation of cubic and hexagonal phases, their schematic representations and drug loading capacities.[24]

Cubic phase, generally prepared from glyceryl monooleate, is represented by two continuous nonintersecting water channels separated by a lipid bilayer. It is able to encapsulate hydrophilic drugs in water channels, hydrophobic in the bilayer and amphiphilic on the interface (Figure 1.7). For instance, cubosomes were reported as efficient carriers for Cinnarizine or Amphotericine B oral administration. Cubic gel phase was used for Sulforhodamine or Paeonol transdermal delivery.[24]

Hexagonal phase and hexosomes were reported to induce membrane fusion and thus enhance penetration of drugs. Lopes *et al*. showed enhanced transdermal delivery of Vitamine K encapsulated in liquid crystalline hexagonal phase from glyceryl monooleate.[27] Moreover, hexagonal nanoparticles from soy phosphatidylcholine and monooleate encapsulating Paclitaxel displayed improved concentration- and time-dependent uptake with involvement of both clathrin and caveolae/lipid raft-mediated endocytosis *in vitro*. The *in vivo* study showed that the oral bioavailability of these nanosystems was 2.1 times higher than for the commercial formulation of Paclitaxel (Taxol®).[28]

However, cubic and hexagonal phase nanosystems often suffer from short release duration and the extremely high viscosity which may limit their use in certain clinical applications.[2]

1.1.4 Liposomes

The spherical vesicles formed from one or more lipid bilayers surrounding equal number of water compartment are termed as **liposomes**.[17,29] The number of lipid bilayers and liposome size determine their classification. Thus, liposomes with one lipid bilayer are known as Unilamellar and those with two or more – Multilamellar. Regarding their size, both of these groups could be classified into three categories – Small (diameter 20-100 nm), Large (diameter > 100 nm) and Giant (diameter > 1000) (Figure 1.8). For instance, 110 nm in size liposomes with single bilayer will be classified as LUV – large unilamellar vesicles.[29,30]

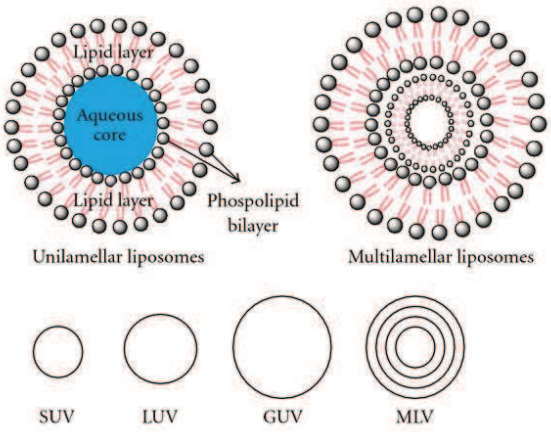

Figure 1.8 Schematic representation of liposomes and their classification.[31]

There are various liposome preparation technics, which yield different vesicle types and size. Accordingly to the specific requirements or the administration route, a certain preparation method may be necessary or preferred. Once liposomes are prepared, a particular attention should be pointed at the stability of vesicles towards aggregation or fusion and the leakage rate of solubilised or encapsulated drugs.[2]

Generally, liposomes are composed from natural and/or synthetic phospholipids (phosphatidylethanolamine - PE, phosphatidylglycerol - PG, phosphatidylcholine - PC, phosphatidylserine - PS, phosphatidylinositol - PI) (Figure 1.9). The alkyl chains of the phospholipid are also abbreviated, for instance DM states for dimyristoyl, DP for dipalmitoyl, DS for distearoyl *etc*. PC or lecithin and PE are the two major components of cell membranes. This similarity represents one of the important advantages of liposomes - the biocompatibility and low toxicity towards living cells. The physicochemical properties of a liposome membrane such as surface charge, fluidity and permeability can be tuned by simply modifying the composition and molar ratio of constituent lipids.[32]

Other components like cholesterol or modified lipids could be added to formulation to increase liposome stability or give it some specific behaviour. Cholesterol is known to improve membrane fluidity, bilayer stability and to reduce membrane permeability of liposomes.[30] Hydrophilic polymer-lipid conjugates such as PEG2000-DSPE (Figure 1.9) were shown to greatly improve liposome circulation time in the bloodstream and prevent their aggregation in solution.[33]

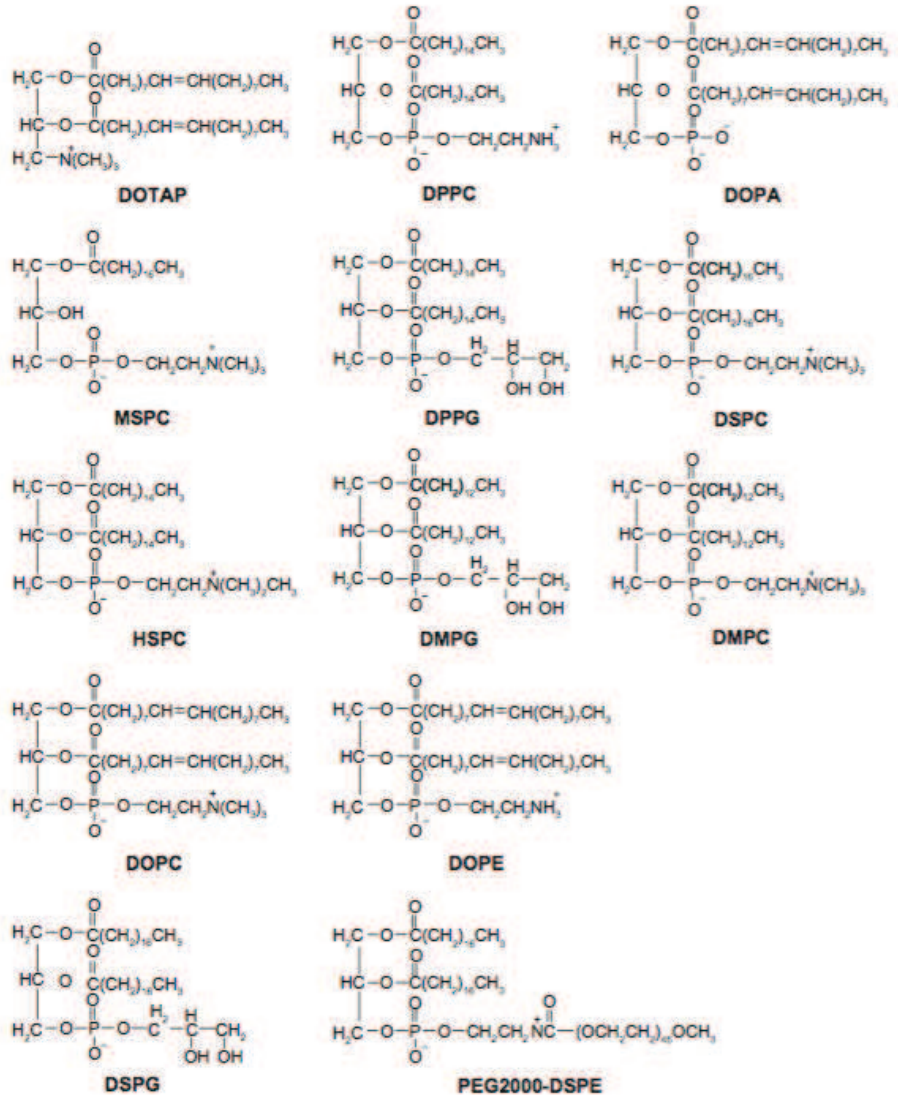

Figure 1.9 Chemical structures of lipids commonly used in liposome preparation.[32]

Due to their low toxicity, high biocompatibility and the capacity to encapsulate both hydrophilic (within the water compartment) and hydrophobic (within the lipid bilayer) drugs, liposomes represent a tremendous sector in modern drug delivery field.[29,32] The lipid bilayer could protect drugs from fast hydrolysis or oxidative degradation and as a consequence, minimise toxicity (by improving the therapeutic index). Moreover, prolonged circulation time in the bloodstream may increase drug bioavailability (reduce clearance) and provide enough time for it to reach target organs and tissues.

The first liposomal formulation approved for human use by FDA in 1995 was Doxil® – doxorubicin encapsulated in PEG-coated liposomes. Nowadays, Doxil® is extensively used to treat ovarian cancer and Kaposi's sarcoma. It allows not only an increase in doxorubicin levels in sarcoma tissues but also a patient protection against cardiotoxicity associated with free doxorubicin.[20] More than 8 liposomal formulations of various drugs are already on the market (Table 1.1) and many are currently in clinical trials. Among the studied and approved drugs, one could mainly find anticancer and antibacterial agents, imaging and probing agents, peptide hormones, proteins, enzymes, vaccines, and genetic material.[20,29,32]

Table 1.1 Examples of liposomal drug formulations available on the market[32,34]

Product name	Drug	Composition (molar ratios)	Indication
Doxil/Caelyx	Doxorubicin	HSPC, cholesterol, and DSPE-PEG2000 (56:39:5)	AIDS-related Kaposi's sarcoma, recurrent ovarian cancer, metastatic breast cancer and multiple myeloma
DaunoXome	Daunorubicin	DSPC and cholesterol (2:1)	Kaposi's sarcoma
Marqibo	Vincristine	Sphingomielin and cholesterol (58:42)	Acute lymphoblastic leukaemia
AmBisome	Amphotericin B	HSPC, DSPG, cholesterol, and amphotericin B (2:0.8:1:0.4)	Sever fungal infections
Nyotran	Nystatin	DMPC, DMPG and nystatin (7:3:1)	Topical antifungal agent
Myocet	Doxorubicin	EPC and cholesterol (55:45)	Combination therapy with cyclophosphamide in metastatic breast cancer
DepoDur	Morphine sulfate	Cholesterol, Triolein, DOPC and DPPG (11:1:7:1)	Pain management
Depocyt	Cytarabine	Cholesterol, Triolein, DOPC and DPPG (11:1:7:1)	Neoplasic meningitis and lymphomatous meningitis

Hydrophobic drugs like amphotericin B, taxol or annamycin, can be directly incorporated into lipid bilayer during vesicle formation, and the amount of uptake and retention depend on the drug-lipid interactions. Trapping effectiveness of such drugs varies with their solubility in the liposome membrane. Passive entrapment of water-soluble drugs relies on the ability of liposomes to encapsulate aqueous buffer with a dissolved drug during vesicle formation. Encapsulation efficiency in this case is generally limited by the volume entrapped in the liposomes and drug solubility in buffer.[29,30]

Although liposomes are generally constituted from natural or biocompatible phospholipids, after contact with plasma proteins they could be recognised by the mononuclear phagocytic system (MPS). This induces fast cleavage from the blood stream. To minimise the interactions with plasma proteins, synthetic hydrophilic polymer - lipid conjugates could be incorporated in the formulation (e.g., PEG2000-DSPE, Figure 1.9). Coating with PEG makes 'stealth' liposomes with reduced macrophage uptake and extended blood circulation time. On the other hand, decrease in liposome size, negative charge density and bilayer fluidity could also lead to prolonged circulation.[32–34]

To give liposomes new features various lipid conjugates with fluorescent dyes,

antibodies or drugs are used. For instance, pro-drug lipid conjugates incorporated in liposomes could enable controlled drug release due to pH, redox changes or enzymatic cleavage.[34] Moreover, various surface modifying ligands could be employed to increase liposome accumulation in target organ or tissue. Among them one can find antibodies or their fragments, cell-penetrating peptides, specific proteins, sugars and small molecules.[34,35] This approach, referred as active targeting, will be discussed in the corresponding section (see 2. Targeted drug delivery systems).

Thus, liposomes represent a highly versatile drug carrier system that could be adapted and functionalised for numerous pathologies. The multifunctional potential of liposomes is summarised on Figure 1.10.

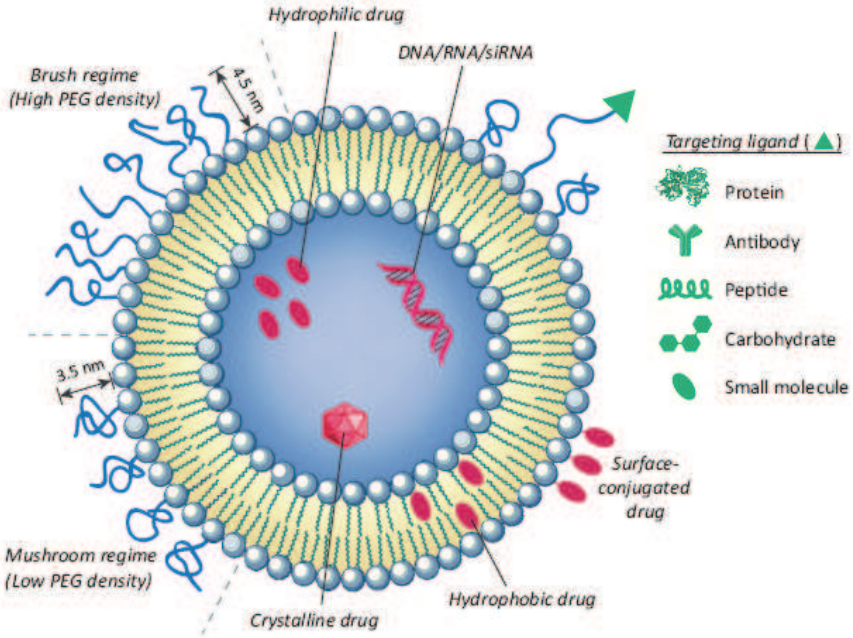

Figure 1.10 Scheme of possible ways of liposome utilisation as drug carriers.[35]

1.1.5 New-generation liposomes

The subsequent couple of examples illustrate the multiplicity of hybrid liposomal-based drug delivery systems.

Liposomes which surface was modified with fusogenic viral proteins are named *virosomes* (Figure 1.11). These innovative systems benefit from the advantages of both viral and non-viral pharmaceutical carriers. They are utilised not only for the intracellular delivery of peptides, proteins, nucleic acids and small molecules, but also in vaccine development. Virosomes were shown to be highly efficient in the delivery of protein antigens to the immune system. As a consequence, a whole set of virosome-based vaccines was developed. However, their utilisation in clinics may be sometimes problematic because of stability/leakiness problems and potential immunogenicity.[34,37]

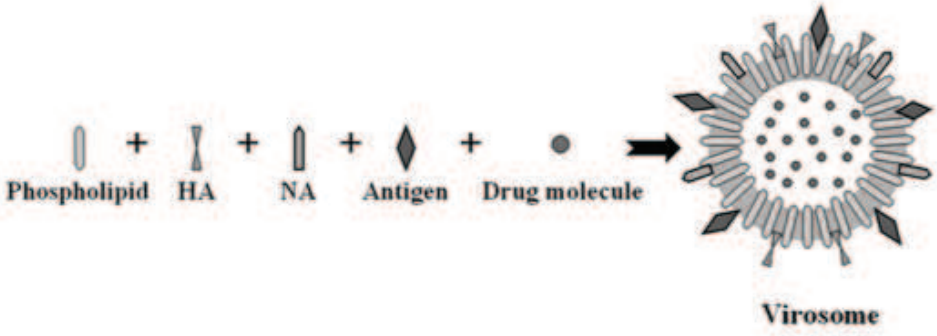

Figure 1.11 Scheme of virosome derived from influenza virus. The composition mimics envelope of influenza virus - phospholipid bilayer associated with viral glycoproteins hemagglutinin (HA) and neuraminidase (NA), antigens presented on the surface of the virosome and encapsulated drug molecules.[37]

The intimate combination between liposomes and ferrofluids generates *magnetoliposomes*. This approach allows targeted drug delivery under the action of magnetic field and at the same time an imaging modality (as iron oxides are established contrast agents in MRI – magnetic resonance imaging). Moreover, magnetoliposomes could be used in tumour treatment with hyperthermia.[34,38] In these structures, the inner layer of phospholipids is strongly bound to the iron oxide surface by chemisorption forces, while outer layer could be easily functionalised with fluorophores or targeting agents.[39,40] For instance, galactose functionalised magnetoliposomes showed their efficiency in hepatocyte magnetic labelling *in vitro*[40] and *in vivo*.[41] Another group[42] reported controlled release of doxorubicin encapsulated in carboxymethyl dextran-coated magnetoliposomes under low-frequency alternating magnetic field (Figure 1.12.A). Though iron oxide toxicity is attenuated by liposome encapsulation, it remains a major drawback, which could be overcome by the active targeting approach.

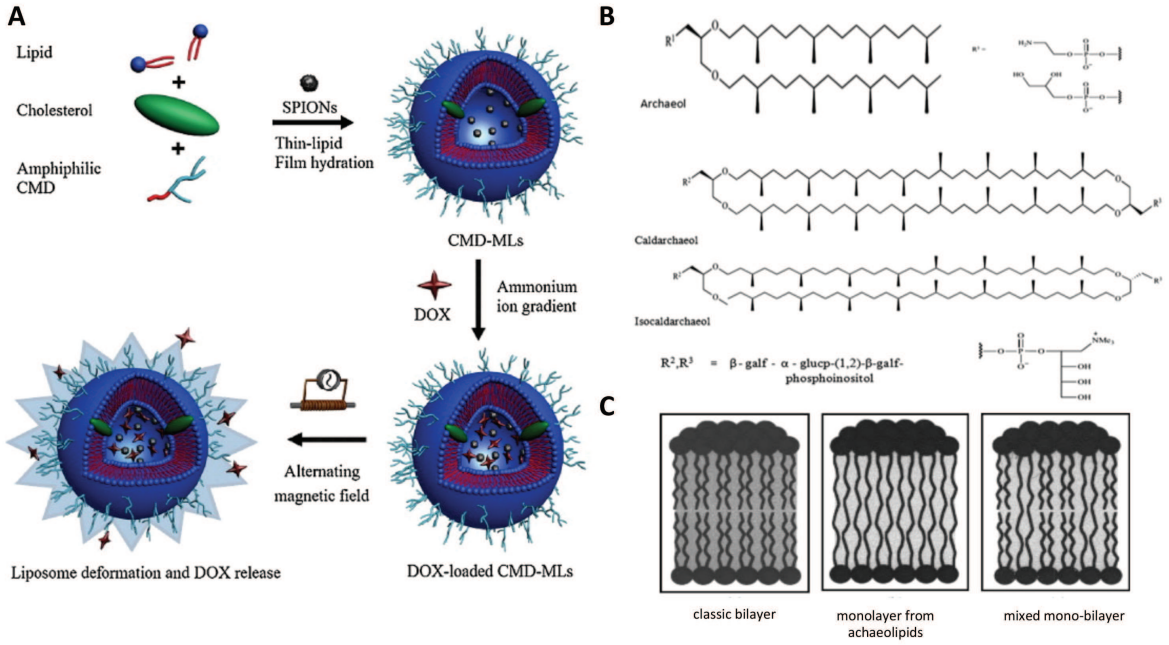

Figure 1.12.A. Scheme for the preparation of stimuli-responsive magnetoliposomes;[42] *B. Chemical structures of archaeolipids;*[43] *C. Differences between classical bilayer and monolayer or mixed mono-bilayer from archeolipids.*[44]

Even more exotic drug carriers, *archaeosomes*, were recently developed.[44] They are constituted from natural archaeal membrane bipolar lipids (tetraethers, Figure 1.12.B) such as archaeol and caldarchaeol and/or synthetic lipid analogues. Interestingly, such membranes don't display conventional bilayer structure, but a monolayer or mixed bilayer-monolayer, when combined with regular phospholipids (Figure 1.12.C).[44] As a consequence, archaeosomes exhibit high stabilities at low or high temperatures, acidic or alkaline pH, oxidative conditions, high pressure, action of phospholipases, bile salts and serum proteins.[45] These unique properties make them promising carrier systems for proteins and peptides, genes, antigens and natural antioxidant compounds.[43] Archaeosomes were also shown to be safe and helpful adjuvants in vaccines, especially against Chagas disease.[46]

1.1.6 Lipid nanoparticles and micro/nanoemulsions

Lipid nanoparticles, introduced in 1991, represent an alternative carrier system to conventional colloidal carriers. They combine advantages of the traditional systems and at the same time avoid some of their major drawbacks. In contrast to liposomes, they could be produced in a large scale without significant batch-to-batch differences.[47] Nanoparticles are generally constituted from phospholipids, cationic lipids, cholesterol and polymer lipid conjugates for prolonged circulation time.[48] Lipid nanoparticles were extensively studied in the field of nucleic acid delivery and showed their efficiency in siRNA transport to the liver.[49] Figure 1.13.A illustrates typical lipid nanoparticle composition and architecture suitable for this purpose. However, they still suffer from a lack of cell specificity, which could represent a major drawback in gene delivery. Small molecule ligands could be utilised to solve this issue.

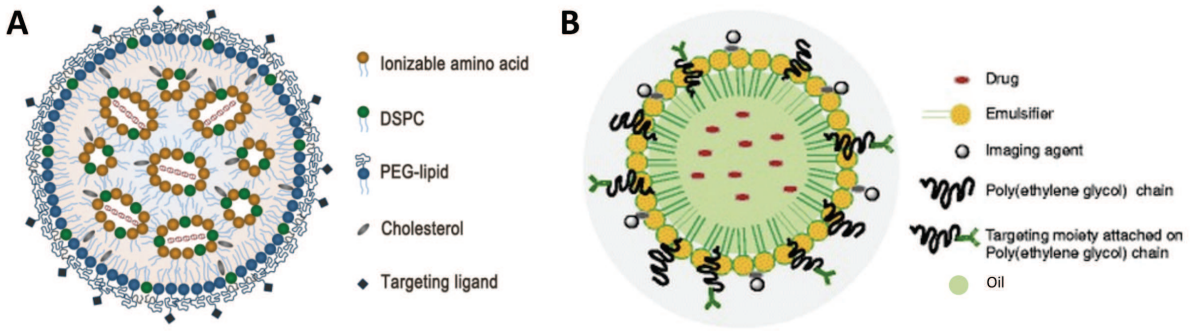

Figure 1.13.A. Example of lipid nanoparticle composition for nucleic acid delivery;[47] B. Example of nanoemulsion suitable for targeted drug delivery.[50]

In contrast to lipid nanoparticles, micro- and nanoemulsions are colloidal systems constituted from water, oil and surfactant. Regarding the ratios between dispersed oil and water phases, micro- and nanoemulsions could be divided into oil in water (O/W) or water in oil (W/O) formulations. Both types are stabilised with surfactants such as fatty alcohols, glycerol esters, soaps, sulfonates *etc*.[51]

The microemulsion solution is optically isotropic, low viscous, thermodynamically stable and capable to solubilise both water- and oil-soluble drugs. The manufacturing process is simple, reproducible and could be adapted for the large scale.[2] Due to their large interfacial area and thus high loading capacity, microemulsions are mainly used in parenteral nutrition. Formulations with drugs are mainly known for diazepam and etomidate. Generally, they reduce drug side effects, for instance pain and inflammation on the site of injection (for diazepam). Despite its biocompatibility, microemulsion utilisation in drug delivery field stays limited due to physical instability caused by the encapsulated drug and upon dilution in the bloodstream. However this could be advantageous in some specific cases.[47]

In contrast to microemulsions, nanoemulsions display greater kinetic stability mostly due to their submicron size (<300 nm), which prevents oil droplets from flocculation and coalescence. As a consequence, nanoemulsions remain stable under various 'stress' conditions such as temperature, pH and osmolarity changes.[52] The capacity to dissolve large amounts of hydrophobic drugs and protect them from degradation makes nanoemulsions ideal vehicles for parenteral nutrition. Moreover, the above-mentioned kinetic stability allows slow

and controlled drug release. Other nanoemulsions applications include intranasal, transdermal and ophthalmic drug delivery.[53] The nanoemulsions formulations utilised in clinics are summarised in Table 1.2.

Table 1.2 Commercial nanoemulsion formulations.[50,53]

Product name	Drug	Indication
Liple	Palmitate alprostadil	Vasodilator, platelet inhibitor
Limethasone	Dexamethasone	Steroid
Diprivan	Propofol	Anaesthetic
Cleviprex	Clevipide	Calcium channel blocker
Diazemuls	Diazepam	Sedative
Lipfen	Fluriprofentaxil	NSAID
Ropion	Fluriprofentaxil	NSAID
Vitalipid	Vitamins A, D, E, K	Parenteral nutrition

Additional advantage of nanoemulsions compared to microemulsions is utilisation of smaller amount of surfactant and thus lower potential toxicity. Moreover, nanoemulsions are commonly prepared from FDA approved Generally Recognized as Safe (GRAS) grade excipients. On the other hand, the preparation of nanoemulsions often requires high-energy methods such as ultrasonication, high-pressure homogenisation or microfluidics, which could be expensive on the industrial scale. Whereas microemulsions are prepared with low-energy methods that do not require expensive equipment.[53]

Due to their submicron size, nanoemulsions could penetrate the skin and even act as targeted drug carriers (see section 2.1 Passive targeting). Recent studies suggest the utilisation of nanoemulsions in targeted cancer therapy[50,54–56] and preclinical imaging.[54,57] They employ polymer coating for prolonged circulation in blood (i.e. DSPE-PEG), conjugation of specific ligands to the surfactants, encapsulation of cytostatic drugs and/or imaging agents (Figure 1.13.B). For instance, Ganta S. and co-workers[54] developed an EGFR-targeted theranostic nanoemulsion and showed its efficiency *in vivo* for ovarian tumour targeting and MRI contrast enhancement. Another group[55] prepared albumin anchored docetaxel lipid nanoemulsion, which also demonstrated improved tumour growth suppression *in vivo*.

Taken together, lipid nanoparticles and nanoemulsions represent a great promise for the encapsulation of various drugs and contrast agents for the specific delivery to target tissues or organs. However, more preclinical studies are needed in the field of targeted delivery to facilitate the translation of these multifunctional systems to the clinics.

1.1.7 Amphiphile polymer-based auto-assemblies

Nowadays, the concept of amphiphiles includes not only small molecules, but also polymers and macrocycles.[2,4,19] A polymer amphiphile is generally represented by a hydrophilic and hydrophobic segments linked together with a covalent bound. The advantage of such molecules is their structural density, enhanced stability and larger capacity for drug loading compare to low molecular weight surfactant self-assemblies.[2]

Amphiphile block copolymers are able to form various self-assemblies such as micelles, nanospheres and nanocapsules. As for low molecular weight amphiphiles, the type of formed self-assembly depends on polymer chemistry (Figure 1.14) and environmental conditions (T, pH, solvent, co-solutes). Here we will briefly introduce polymer auto-assembly systems and their utility in drug delivery field.

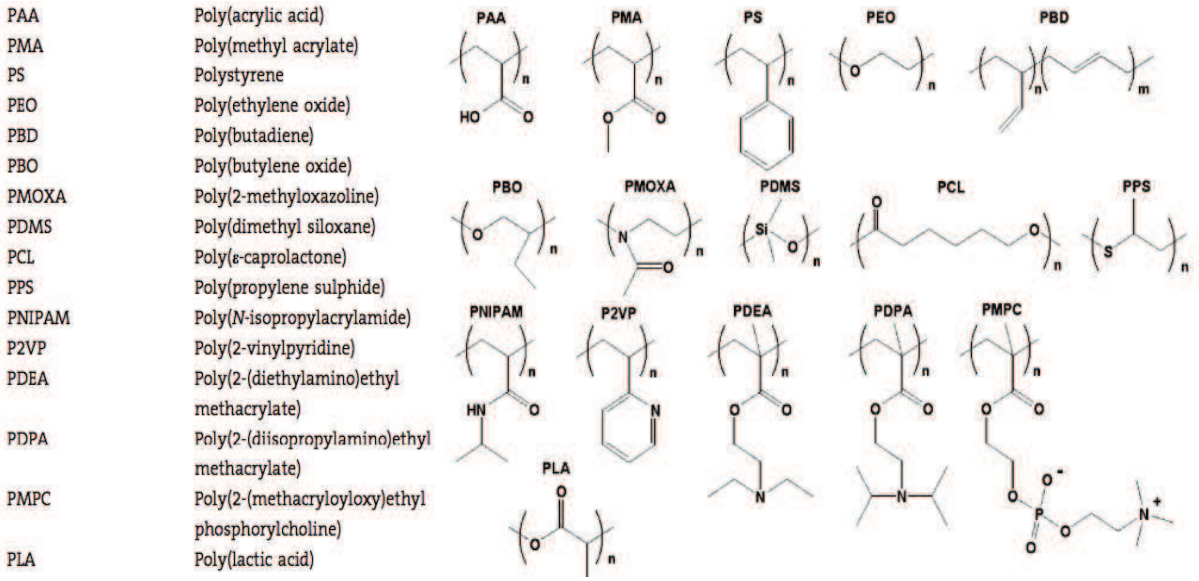

Figure 1.14 Abbreviations and chemical structures of some polymers.[58]

Amphiphilic copolymer micelles are spherical colloid nanoparticles, 5-100 nm in size, which form spontaneously in aqueous buffer.[2,59] They display a core-shell structure where more hydrophobic drugs are located inside the core and less hydrophobic closer to hydrophilic corona (Figure 1.15). The hydrophilic shell provides prolonged circulation half-life and allows surface modification.[19,59] The main advantage of such systems compare to conventional micelles is low CMC, which prevents disassembly upon dilution in the blood flow. Generally, polymer micelles are utilised to solubilise poorly water-soluble drugs and increase their oral availability. For instance a poly (D, L-lactide)-MePEG diblock copolymer micelles increased Paclixatel solubilisation rates up to 5000-fold.[60] This nanosystem is approved for human use in South Korea for breast cancer treatment and thus represents one of the most successful examples of polymeric micelle formulations.[59] Specific polymer building blocks could be incorporated to produce pH-sensitive or mucoadhesive micelles enhancing their absorption trough gastro-intestinal tract.[59]

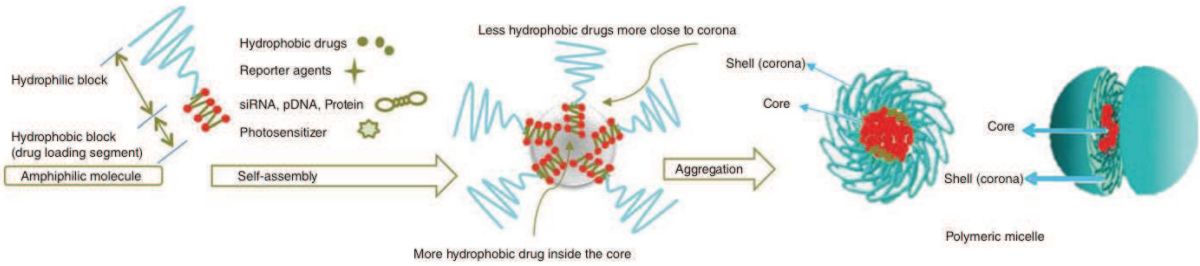

Figure 1.15 Structure and formation of an amphiphilic polymer micelle.[59]

Another type of self-assembly – *polymeric nanosphere* is represented by a matrix-type, solid colloidal particle where drugs could be dissolved, encapsulated, conjugated or adsorbed. The particles are generally 100-200 nm in size and when made from amphiphilic block copolymers (i.e. MePEG-b-PLA) display 'stealth' behaviour towards plasma proteins and extended blood circulation.[19] The utility of polymeric nanospheres in drug delivery is mostly the same than for polymer micelles – solubilisation and increase in bioavailability of poorly water soluble drugs for potential intravenous[61] or oral[62] administration routes.

Vesicular nanosystems with a cavity surrounded by a polymer coating stand for polymeric *nanocapsules* and *polymersomes*. The difference between them is in the core structure and surrounding polymer layer. Nanocapsules generally have oily core and single polymer layer. They display efficient encapsulation of hydrophobic drugs like Ru 58668, methotrexate, xanthone and 3-methylxanthone.[19] Polymersomes have aqueous core surrounded by an amphiphilic polymer bilayer. Similar to liposomes, polymersomes are able to encapsulate hydrophilic drugs in their aqueous reservoir. Thus, their ability to deliver nucleic acids is widely studied.[63] Although some constructs showed good efficacy in nucleic acid and drug delivery,[62,64,65] like other nanosystems such as non-targeted liposomes or lipid nanoparticles, they often experience the lack of tissue specificity and preferentially accumulate in the liver.[66] Moreover, a lot of polymers utilised for polymersomes (i.e. PEG-b-PBD and PEG-b-PEE, Figure 1.14) suffer from toxicity and poor biodegradability.[19]

1.1.8 Macrocyclic amphiphile self-assemblies

Novel class of synthetic amphiphiles appeared recently. They are synthesised on the basis of macrocycles such as cyclodextrins and thus termed macrocyclic amphiphiles (Figure 1.16).[4] Compared to conventional amphiphiles, macrocyclic amphiphiles could be designed to promote multi-dimensional and hierarchical self-assemblies with new interesting topological structures. Cyclodextrins possess a cavity formed by polymeric sugar backbone. The cavity has two sides that differ in their diameter. Drug encapsulation in this cavity could be achieved trough hydrophobic and/or host-guest interactions.[1,4,67] As sugar moieties are hydrophilic, the amphiphilic character of cyclodextrins is ensured by attachment of lipid moieties to the smaller side of cyclodexrin cavity (Figure 1.16).

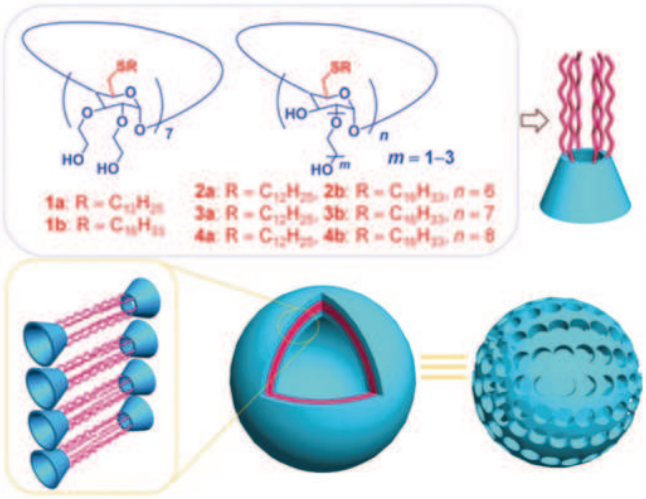

Figure 1.16 Example of macrocyclic amphiphile: chemical structures of amphiphilic cyclodextrins and their corresponding auto-assembly into bilayer vesicles.[4]

Recent advances in macrocycle amphiphile chemistry allow engineering of diverse nanosystems such as nanoparticles, micelles, vesicles, nanogels, nanopolyplexes and supramolecular hydrogels. For instance, cyclodextrin-derived amphiphiles were utilised to formulate various lipophilic drugs for dermal, buccal, oral, sublingual, rectal, ophthalmic, intramuscular, and intravenous administration. However, most of these studies are proof of concept and successful translation of these innovations to the clinics remains challenging.[68]

Nevertheless, alpha-, beta- and gammacyclodextrins are GRAS and approved by the FDA for utilisation in food industry. Therefore, macrocycles and in particular cyclodextrins, are a very promising field for the development of drug delivery systems.

1.1.9 Conclusions

All presented amphiphile self-assemblies are generally in submicron size range (except microemulsions) and thus are considered as nanosystems (nanocarriers or nanomedicines). The advantages and limitations of these nanosystems as drug carriers are presented in Table 1.3.

Table 1.3 Advantages and limitations of various amphiphile-based drug delivery nanosystems

Nanosystems	Advantages	Limitations
Micelles	Easy and non-costly production	Disassembly upon dilution; too fast drug release; only suitable for lipophilic drugs
Cubosomes & Hexasomes	Very ordered; high encapsulation efficiency; suitable for oral administration	Extremely high viscosity; short release duration
Liposomes	Biocompatible, biodegradable; extremely versatile; high-throughput synthesis, lyophilization; surface modifications; new generation hybrid systems	Limited shelflife (in solution); too slow drug release; hydrophilic drug leakage
Lipid nanoparticles	Biocompatible; high drug loading; batch-to-batch reproducibility; easy to scale-up and sterilise; long shelflife	Drug loading is limited by its solubility in lipid melt; risk of drug expulsion after polymeric transition
Nanoemulsions	Kinetically stable; high drug loading capacity; biocompatible; slow and controlled drug release	High cost of industrial production
Polymer-based self-assemblies	Possible "smart" drug release (pH, temperature, redox sensitive); adaptable chemistry	Costly synthesis; safety and biodegradability concerns
Macrocycle self-assemblies	Multi-dimensional hierarchical self-assemblies; novel topological structures	High cost of production; poor water solubility; low biocompatibility

Although, there are a great variety of amphiphile self-assemblies with interesting chemistry, and topology mostly due to numerous innovations in polymer chemistry, liposomes still stay a golden standard for drug delivery in clinics due to their simplicity, biocompatibility and high versatility. Polymeric micelles, nanoemulsions and lipid nanoparticles also represent promising ways for controlled drug delivery and release.

In the next section we are going to discuss the state of the art in targeted delivery to tumours by amphiphile self-assembled nanosystems.

1.2 Tumour-targeted drug delivery systems

Biodistribution of a drug delivery system in the body depends on its size, surface features and nature of the cargo. Nanosystems with mean diameter smaller than 6 nm will be subject to renal filtration and thus rapidly excreted from systemic circulation.[69] On the other hand, a mean diameter over 500 nm and excessive surface charge or hydrophobicity induce rapid recognition by reticuloendothelial system (RES) and liver clearance.[69,70] Thus, the "ideal" nanocarrier is supposed to be around 100-200 nm in size owning neutral, hydrophilic surface.

Most of the discussed earlier amphiphile-based nanosystems are utilised as drug carriers in anticancer therapy. This is related not only to the emergency in finding new therapeutic strategies for cancer treatment, but also to the specific tumour biology, allowing preferential accumulation of nanosized materials. This phenomenon termed *enhanced permeability and retention (EPR) effect*[71,72] will be discussed in following section.

1.2.1 Passive targeting

It is now a well-established fact that under certain conditions (inflammation/hypoxia, which is typical for tumours), the endothelium of blood vessels becomes more permeable than in the healthy state.[70] Upon hypoxia, rapidly growing tumours recruit new vessels or engulf existing blood vessels. These newly formed leaky vessels allow selective *enhanced permeation* of macromolecules larger than 40kDa and nanosystems to the tumour stroma. Furthermore, the absence of normal lymphatic drainage in the tumour contributes to their *retention*.[71] However, this unique feature is not applicable to small molecule drugs, which have generally short circulation time and fast wash-out from the tumour. Thus, the encapsulation of small-molecule drugs in nanosized drug carriers enhances their pharmacokinetics (prolonged systemic circulation), provides some tumour selectivity and, as a consequence, decreases side effects. This type of tumour targeting was termed 'passive', as it relies on carrier characteristics (size, circulation time) and tumour biology (vascularity, leakiness etc), but does not possess a ligand for specific tissue or organ binding.[71,73]

Since the discovery of EPR effect in 1980s by Maeda and co-workers[72] a lot of efforts were put to understand the significance of this phenomenon in tumour targeting and develop appropriate drug delivery systems. Some of these nanocarriers, such as discussed previously Doxil© and Caelyx©, are now successfully used in the clinics and EPR effect became a golden standard in the design of passive tumour-targeted systems.[70]

However, EPR effect provides rather modest tumour specificity with about 20-30% in delivery increase compared to normal organs. The EPR effect is highly dependent from the intrinsic tumour biology (Figure 1.17) and in particular: 1. The degree of angiogenesis and lymphangiogenesis. 2. The degree of perivascular tumour growth and the density of the stromal response. 3. Intratumoural pressure.[69] All these factors, together with nanocarrier physicochemical characteristics, will determine its drug delivery efficiency.

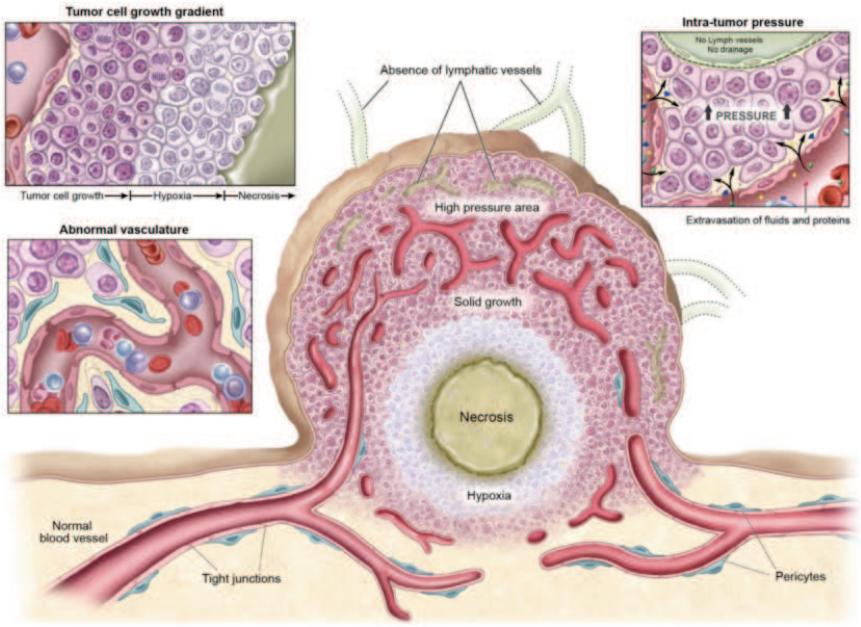

Figure 1.17 Tumour physiology that could facilitate/restrain nanoparticle accumulation.[69]

Although the leakiness of newly formed tumour vessels influences the nanomedicine permeation, it also contributes to the high interstitial pressure, which in contrast, is able to inhibit the accumulation of drug carriers in tumour.[69] Moreover, due to the disproportion of pro- and anti-angiogenic signalling inside different parts of the tumour, vessels are abnormal with dilated, tortuous, and saccular channels, disorganised patterns of interconnection and branching.

Due to such heterogeneous blood supply, tumour cells also grow irregularly - those that are near blood vessels proliferate faster than those that are in the tumour core and receive less nutrients and oxygen. This explains hypoxic/necrotic areas in the cores of large tumours (i.e. 1-2 cm in diameter in mice) and often impossibility for nanomedicines to reach these areas. Moreover, blood vessels in the central area of the tumour do not leak as much as one could expect due to the high interstitial pressure. Such phenomenon was observed in various kinds of murine and human tumours. High interstitial pressure not only inhibits drug delivery by convection but also compresses newly formed blood vessels. In this way, blood is conducted away from the centre of the tumour towards the periphery.[69,73]

However, it is possible to modulate EPR effect chemically or mechanically to achieve vascular normalisation and, as a result, higher accumulation of nanocarriers. Among chemical EPR enhancers one could find bradykinin (kinin), nitric oxide, peroxynitrite, prostaglandins, vascular permeability factor (VPF) / vascular endothelial growth factor (VEGF) and other cytokines.[71,73] These molecules induce hypertension or vascular normalisation, which could temporary enhance tumour perfusion. Other approaches utilise ultrasound, radiation, hyperthermia or photoimmunotherapy to modulate tumour vasculature and increase nanosystems permeation. Nevertheless, all described methods have their limitations and contraindications and thus require careful consideration.[69,73,74]

Other crucial factors influencing EPR-based tumour targeting are nanomedicine size and circulation time. On the one hand, size is important for the permeation and retention in the tumour and thus is limited by the fenestrations in tumour vessels (200-800 nm).[70] On the other hand, as we already discussed, nanomedicine diameter influences on its excretion – renal (less than 6 nm) or through RES (more than 500 nm). Thus, as already mentioned, the optimal size range is around 20-200 nm.[69]

Surface chemistry and charge also play important role in the circulation time – too hydrophobic or charged systems are rapidly opsonised by MPS. Hence, it is preferred to make nanoparticle surface 'look like water' – hydrophilic and neutral or slightly anionic. For this purpose water-soluble polymers (generally PEGs) are grafted on the nanocarrier surface.[33,70] Moreover, PEGylation prevents nanoparticle aggregation and non-specific interactions by changing surface charge and hydration.[75] This strategy is successfully utilised in discussed previously liposomal formulations Doxil® and Caelyx® (see Table 1.1). The optimal loading of PEG-modified lipids in the liposome has been shown to be around 5 - 9 mol% of classically utilised DSPE-PEG2000. At this concentration each polymer chain adopts a mushroom-like globular structure with slight overlay between distinct polymers and ensures a complete 'stealth' nanoparticle surface coverage.[75]

However, the first injection of PEGylated liposomes was shown to induce PEG-specific IgM and as a consequence, rapid elimination and enhanced hepatic uptake of a second dose of PEGylated liposomes. This is known as an accelerated blood clearance phenomenon and represents an important obstacle to the pharmacokinetics and pharmacodynamics of PEGylated liposomes and particles. In addition PEG corona could also be a steric hindrance preventing efficient internalisation of nanosystems into tumour cells. This issue is termed in literature as 'PEG dilemma'.[70,73] Thus, in a design of a drug delivery carrier one should find an appropriate compromise between prolonged circulation time and better intracellular trafficking. The possible solutions could be shorter PEG chains (i.e., Mw<1000), PEG attachment by enzyme-cleavable bound or utilisation of specific tumour-targeting ligands.[73]

Nevertheless, PEGylation is a clinically accepted tool to control nanoparticle surface properties and produce 'stealth' drug delivery carriers. Moreover, it offers a possibility to chemically bound a targeting ligand on its surface and, as a result, enhance intracellular uptake.[75] This so-called 'active targeting' approach will be discussed in the following section.

1.2.2 Active targeting

The term 'active targeting' implies the utilisation of targeting ligands, which are recognised by receptors overexpressed in malignant cells compared to normal tissues (or not at all expressed in normal tissues). In the field of cancer research, various types of targeting ligands were studied, including macromolecules such as monoclonal antibodies (or their fragments), aptamers, proteins and peptides; and small molecules such as vitamins and sugars.[75,76]

Active targeting is able to significantly increase the quantity of drug delivered to the target cell compared to free drug or passively targeted nanosystems. It offers selective cellular binding and receptor-mediated endocytosis (Figure 1.18) that could improve therapeutic efficiency of the drug and reduce systemic toxicity.

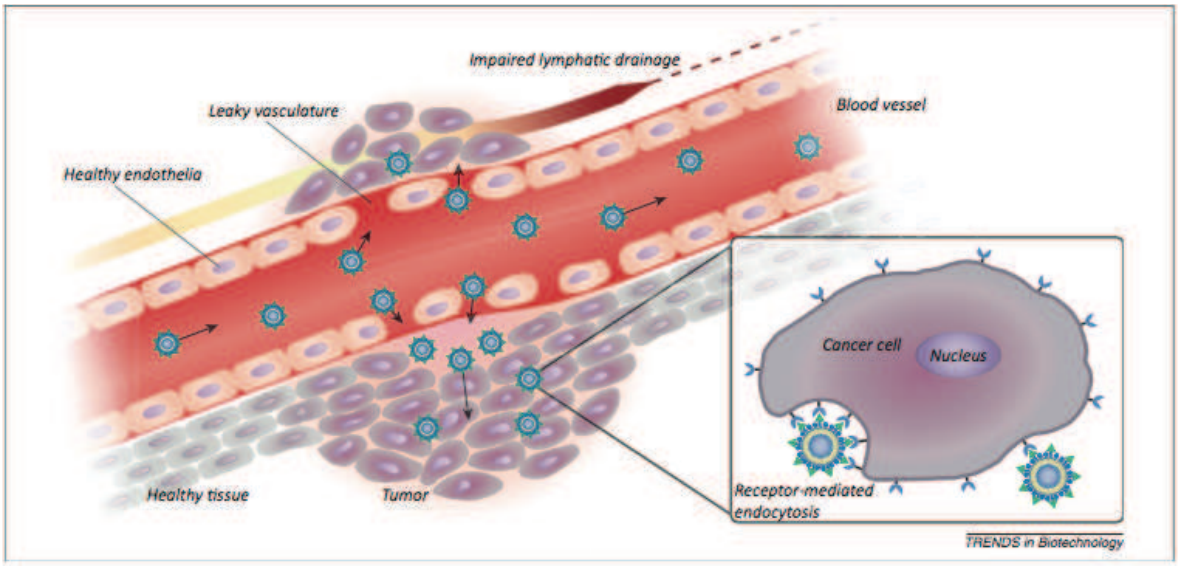

Figure 1.18 Schematic illustration of active targeting.[75]

The 'ideal' targets are overexpressed homogenously by all cells in the tumour and have negligible or low expression in non-tumour tissues. For example, HER2 (human epidermal growth factor receptor 2) displays 1000-fold stronger expression in breast cancer than in normal tissue (in 25% of breast cancer cases). Moreover, they should be expressed at cell surface to facilitate their recognition and binding.[75] So far, the most explored targets in cancer are folate receptor, transferrin receptor, EGFR (epidermal growth factor receptor), specific antigens (i.e. prostate specific antigen – PSA, HER2 etc).[75,77] However, one should be aware of cell heterogeneity in primary tumours signifying that potential targets are not always overexpressed by the totality of cancer cells.[78]

Another interesting strategy is to target angiogenic endothelial cells. This will reduce blood supply to the tumour and deprive cancer cells from oxygen and nutrients with subsequent hypoxia and necrosis.[77] The integrins ($\alpha_{2b}\beta_3$, $\alpha_v\beta_3$ and $\alpha_5\beta_1$) and aminopeptidase-N (CD13) are the most common targets for tumour neovasculature. They are recognised by cyclic and linear derivatives of the peptide RGD (arginylglycylaspartic acid) and NGR (asparaginylglycylargininic acid) respectively.[76]

There is also a possibility to target a specific organ or tissue where tumour is formed.

For instance, asialoglycoprotein receptors expressed on the surface of hepatocytes recognise and bind β-D-galactose residues[79,80] or hydroxyapatite in bone metastases could be targeted with alendronate.[81]

The most common targeting ligands are presented in Table 1.4.

Table 1.4 Examples of commonly used targeting agents.[75]

Class	Ligand	Targets	Advantages	Limitations
Antibodies	Herceptin Rituxan CD19	HER2 CD20 CD19 antigen	High affinity and strong binding; already in clinical trials; therapeutic potential	High production cost; pharmacokinetics; 'binding site barrier effect'; potential immunogenicity
Peptides	RGD NGR	$\alpha_v\beta_3$ integrins, Aminopeptisase N	High affinity	Reduced circulation half life
Proteins	Transferrin LHRH	Transferrin receptor LHRH receptor	Already in clinical trials	High production cost
Aptamers	Pegaptanib	VEGF receptor	Possible to develop for any target	High production cost
Small molecules	Folate Galactose	Folate receptor Asialoglycoprotein receptor	Low production cost, low molecular weight; simple chemistry	Could reduce circulation time

When designing targeted drug delivery system, the essential parameters of the ligand itself should be also taken into consideration, including molecular weight (MW), targeting affinity, valence and biocompatibility.[82]

The amount of targeting agent or *valence* plays an important role in uptake efficiency and biodistribution. For instance, in targeted liposomes concentration of ligand below 1% molar is sufficient.[83]

The important *MW* could influence on the nanosystem recognition with RES. For example, monoclonal antibodies (Ab) due to their high MW are recognised by plasma proteins and eliminated faster than their fragments or new original Ab analogues - nanobodies.[76,84] In this regard small molecules such as galactose or folic acid are interesting candidates for targeted systems due to their small size, simple chemistry, extremely low cost and easy handling compared to complex expensive systems such as Ab, proteins, peptides and aptamers.

The *targeting affinity* of a ligand plays a crucial role in nanomedicine penetration within the tumour. Thus, the very high affinity binding of Ab could lead to 'binding site barrier effect', which limits nanosystems penetration into the tumour tissue. It is a consequence of the tight binding of an Ab to the first encountered antigen in the periphery of the tumour. In contrast, ligands with moderate affinity are not retained by their first encountered receptor and penetrate deeper into the tumour, resulting in more uniform tissue distribution and higher tumour uptake.[85]

As we already mentioned in previous section (see 1.2.1 Passive targeting), the

nanomedicine circulation time plays a major role in its drug delivery capacities. The conjugation of a targeting ligand to the long-circulating nanosystem changes its surface properties and, as a result, exposes it to the higher risk of immune system recognition. Therefore, ligand *biocompatibility* is a critical parameter to consider. Hence, a lot of active targeting drug delivery systems are often very efficient *in vitro*,[79,86] while they do not always enhance tumour localisation *in vivo*[87–89] most likely due to decrease of the circulation time compared to completely 'stealth' non-targeted systems. Nevertheless, active targeting could be beneficial in the case of delivery to the liver[79,80] as nanoparticles, even recognised by the MPS, are eliminated trough this organ and accumulate there in large amounts.

An elegant method to overcome pharmacokinetics issues of targeted systems was shown by McNeeley et al.[90] They developed a liposome formulation where classical Folate-PEG2000 lipid conjugate (0.15 mol%) was first 'masked' by another PEG-lipid (8 mol%) owing longer polymer chain (MW=5000) and cleavable disulfide bond. Once the majority of liposomes were gone from the bloodstream and passively accumulated in the tumour site, active targeting was promoted in a controlled manner. The exogenous administration of a safe cleaving agent (cysteine) induced a detachment of PEG5000 from the liposomes. Targeted liposomes with cleavable PEG5000-lipid exhibited the same circulation time *in vivo* and enhanced cell uptake compared to non-targeted formulation.

1.2.2.1 Examples of targeted nanosystems

For the delivery of nucleic acids active targeting could be an extremely useful approach.[89] As they are large, polyanionic molecules, are not able to penetrate cells on their own because of electrostatic repulsions from negatively charged cellular membrane. In addition, DNA and siRNA site of action is inside the cells and their unselective uptake might provoke additional side effects. In contrast, the active targeting is able to enhance nucleic acid cellular internalisation and at the same time limit off-target side effects.[91] Moreover, as already mentioned, cationic lipids classically used for nucleic acid delivery could induce *in vivo* toxicity.[5]

Recent study using double-targeted pcCPP (photolabile-caged cell-penetrating peptide)/NGR liposomes encapsulating siRNA showed efficacy in c-myc gene silencing *in vitro* and *in vivo*.[91] pcCPP/NGR liposomes demonstrated enhanced uptake and endosomal escape in HT1080 cell line. After systemic administration in mice pcCPP/NGR liposomes were preferentially accumulated in the tumour and delayed tumour growth via RNA interference.

The first evidence of RNA interference in *humans* was shown with targeted nanoparticles.[92] The latters consisted of cyclodextrin-based polymer functionalised with free PEG and PEG-transferrin conjugates. siRNA was designed to silence the expression of the M2 subunit of ribonucleotide reductase (RRM2). Systemic administration of nanoparticles revealed their dose-dependent accumulation in tumours and the decrease in RRM2 protein and corresponding mRNA. This study demonstrates that RNA interference could occur in humans after systemic administration of siRNA in targeted nanoparticulate carrier and thus could be utilised as a gene-specific therapeutics (Table 1.5).

Preclinical trials and subsequent clinical translation were shown for targeted polymeric micelles encapsulated docetaxel (BIND-014).[93] The micelles combine passive targeting via the EPR with active targeting provided by peptide derivative S,S-2-[3-[5-amino-1-carboxypentyl]-ureido]-pentanedioic acid (ACUPA), a PSMA (prostate specific membrane antigen) substrate analogue inhibitor. Administration in mice, rats and non-human primates showed prolonged circulation time (compared to free drug), minimal accumulation in the liver and controlled drug release. The same pharmacokinetics was observed in first Phase I human trials.

Table 1.5 Examples of targeted nanomedicine formulations in clinical trials.[76,94]

Nanoplatform	Drug	Ligand	Target	Cancer type	Phase
Liposomes	Oxaliplatin (MBP-426)	transferrin (tr)	tr receptor	Advanced/metastatic solid tumours	I/II
	Doxorubicin (MCC-465)	F(ab')2 from GAH		Metastatic stomach cancer	I
	p53 gene (SGT53-01)	scFv	tr receptor	Solid tumours	Ib
	RB94 plasmid DNA (SGT-94)	scFv	tr receptor	Solid tumours	I
	Doxorubicin (MM-302)	scFv	ErbB2 (HER2)	Advanced breast cancer	I
	Melanoma Ag and IFNγ (Lipovaxin-MM)	Single domain Ab fragment	DC-SIGN	Melanoma vaccine	I
Polymers	Docetaxel (BIND-014)	ACUPA peptide	PSMA	Solid tumours	I
	RRM2 siRNA (CALAA-01)	tr	tr receptor	Solid tumours	I

Ab and their fragments are so far one of the most studied targeting agents in pre-clinical and clinical trials. For instance, HER2-targeted PEGylated liposomal doxorubicin formulation was developed to reduce unspecific cardiotoxicity of anthracyclines and enhance the drug therapeutic potential.[95] The successful results obtained in pre-clinical studies in mice and embryonic stem cells derived cardiomyocytes brought the formulation to Phase I clinical trials (MM-302) in patients with advanced breast cancer. Another immunoliposome doxorubicin formulation (MCC-465) undergoing Phase I clinical trials showed no specific cardiac toxicity and pharmacokinetics comparable to Doxil©.[96] Here a F(ab')2 fragment of the human monoclonal antibody GAH (recognises >90% of stomach cancer tissues) was conjugated to standard PEGylated doxorubicin formulation. Other targeted nanosystems undergoing clinical trials are presented in Table 1.5.

As mentioned earlier, small natural molecules such as sugars and vitamins could represent interesting alternatives to antibodies and peptides. Moreover, they are easily metabolised and should not induce toxicity or side effects. One of the successful examples in

small molecule targeting are galactosylated solid lipid nanoparticles with encapsulated doxorubicin that showed enhanced cellular uptake and similar bio-distribution *in vivo* compared to non-targeted.[79]

Despite the advantages that active targeting could provide and a lot of efforts that were put by the scientific community over the last 20 years for its development, clinical outcomes stay quite modest. This is often due to discrepancies between animal models and human primary tumours, tumour heterogeneity in target expression and rapid blood clearance. When designing targeted systems a careful attention should be pointed at ligand properties, target expression profile and nanoparticle surface chemistry. It is however important to point out that active targeting strategies are still highly needed for the delivery of fragile bioactive molecules such as peptides, proteins and especially nucleic acids. Thus novel targets and ligands could represent a major interest in this field.

1.2.3 Conclusions and perspectives in tumour targeting

The choice between active or passive tumour targeting should first of all rely on characteristics of the drug to deliver. For the drugs, that do not have issues with cell penetration, such as doxorubicin, the simple encapsulation in 'stealth' nanosystem is sufficient. This will extent the drug blood half-life, increase its chances of tumour accumulation and decrease the toxicity towards highly perfused organs like heart, kidneys and liver. But for the therapeutic molecules that have difficulties to cross cell membrane and could induce severe damage to normal cells, active targeting should be a preferential strategy.

Described earlier, nucleic acids are an excellent example of drugs that require the development of ligand-targeted systems. While cationic non-targeted nanosystems could induce the interactions with cell membrane, they are non selective and toxic. Whereas, targeted carriers will stimulate receptor-mediated endocytosis and the delivery of nucleic acids to their site of action – cytoplasm or even nucleus. This will also minimise off-target side effects and general toxicity. The general principles of active and passive tumour targeting are summarised in Figure 1.19.

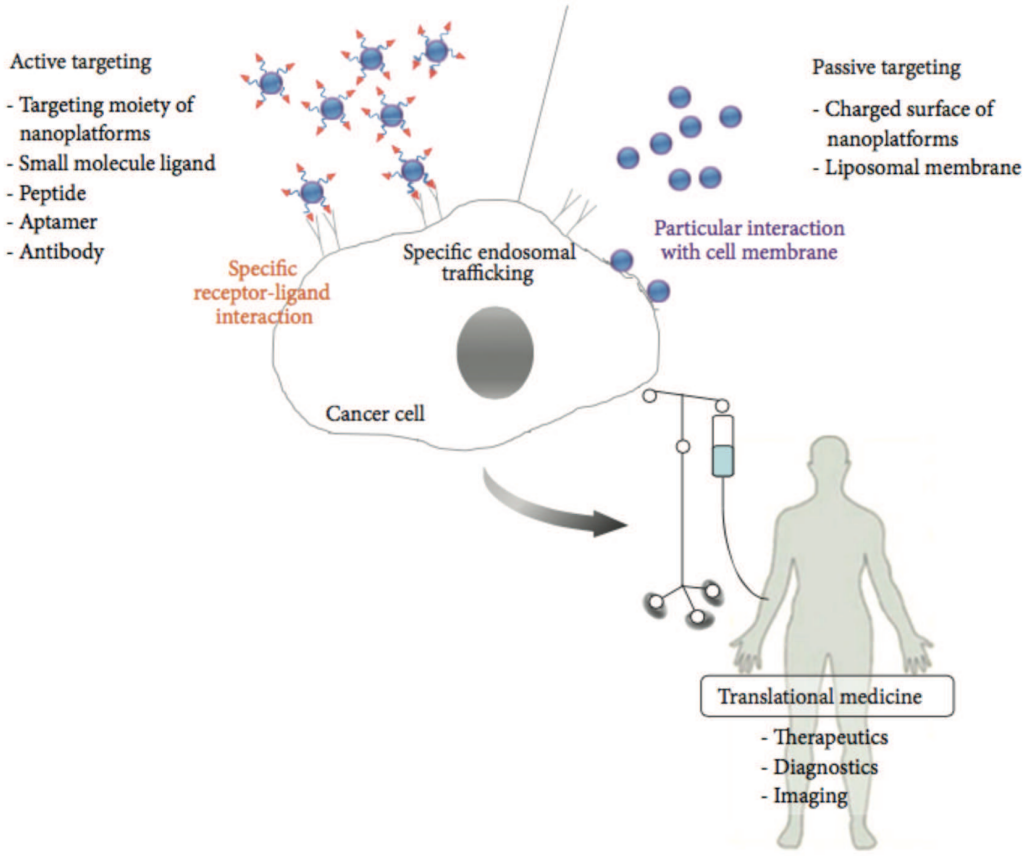

Figure 1.19 General principles of active and passive cancer targeting.[76]

A combination of active or passive drug carrier with an imaging or a diagnostic agent will generate 'intelligent' theranostic system able to monitor disease progression and evaluate therapeutic efficacy of the drug in real time. The development of such systems relies on the careful consideration of tumour biology and at the same time on the exploration of new targets potential and original drug carriers.

1.3 Riboflavin and its potential in health technologies

The physicochemical and biological properties of riboflavin (RF) as well as its potential in modern nanotechnologies are described in the following review, written by Beztsinna N. *et al* (submitted to Biomaterials journal).

Bioengineered riboflavin in nanotechnology

N. Beztsinna, M. Solé, N. Taib, I. Bestel

MMBE team, UMR 5248 CBMN, Bordeaux University, Pessac, France
Corresponding author: isabelle.berque-bestel@u-bordeaux.fr

1. Introduction

Riboflavin (RF) or vitamin B2 is a water-soluble vitamin widely presents in both animal and plant derived foods. Its history starts in 1879, when it was isolated from milk. For this reason, RF was initially named lactochrome. Thanks to the identification of its chemical structure, it was further renamed as RF – *flavin* because of the isoalloxazine ring (*flavus* from latin –yellow) and *ribo*- from ribitol chain. Vitamin properties of this yellow pigment were established only in the early 1930[1-3] revealing the role of its biologically active forms, flavin adenine dinucleotide (FAD) and flavin mononucleotide (FMN). Their activities as coenzymes for flavoenzymes and their participation in a range of redox reactions, highly important for energetic metabolism in aerobic cells, emphasize the extraordinary properties of RF and its derivatives.[1]

RF attracted a lot of attention from researchers in the 1960-70s (Figure 1). Then the number of publications related to RF was more or less stable and they deal mostly with flavoenzymes and biochemical functions of RF. In the early 2000s the outbreak of nanotechnologies brought an important increase of RF-related publications in particular in the

field of health technologies and bioengineering. The interest of academic and industrial investigators for this unique pleiotropic molecule still continues to grow.

In this review we will briefly introduce RF chemical and biological properties and summarize recent applications in the field of sensing, active targeting, tissue and bio-electronic engineering.

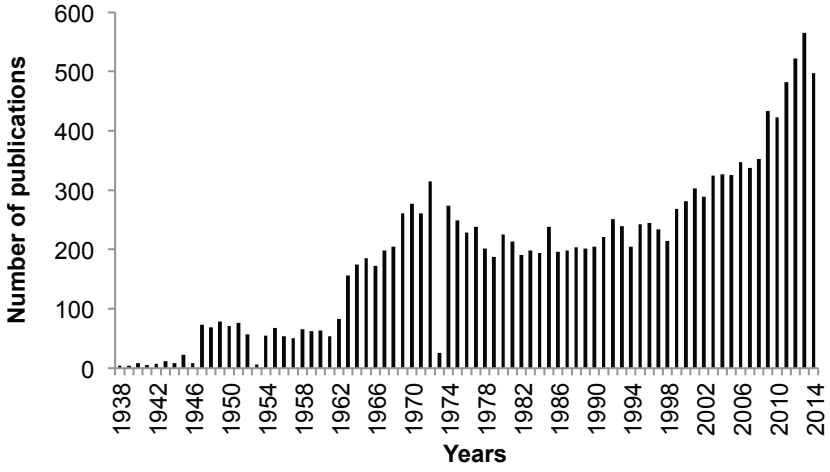

Figure 1. PubMed database statistics 2014: number of publications per year mentioning "Riboflavin".

2. Chemical and biological properties

2.1. Chemical properties

From a chemical point of view, RF consists of an isoalloxazine ring (flavin) substituted at the N10 position by the five-carbon carbohydrate ribitol (Figure 2.A). This is an orange-yellow powder, heat stable, light sensitive and weakly soluble in water and acid (1 g in 3-15 L of water). In contrast, its derivatives FMN and FAD are highly water soluble thanks to their ionic phosphate groups.[1]

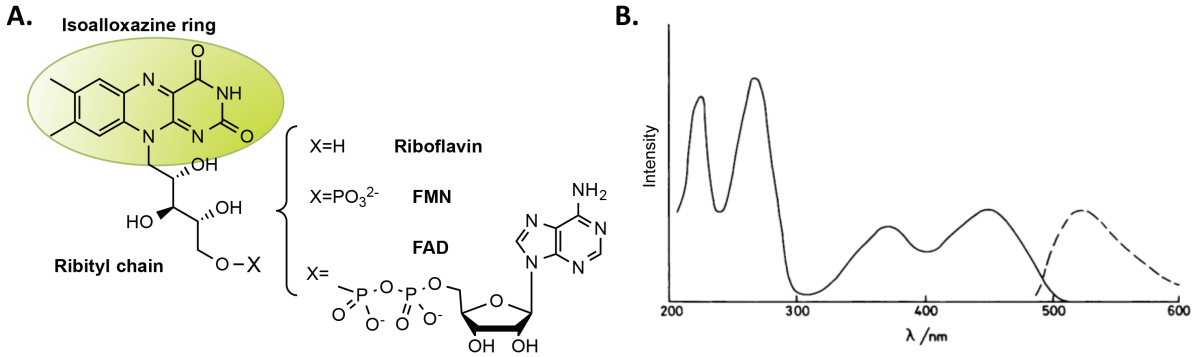

Figure 2.A. Structures of RF, FMN and FAD.[4] **B.** Normalized absorption (−−) and fluorescence emission (---) spectra of RF.[5]

The isoalloxazine ring of RF and its derivatives is responsible for the UV absorption, fluorescence, redox properties and photosensitivity.

In aqueous media, flavins exhibit four absorption maxima: 446 (n- π* transition), 375, 265, and 220 nm (π-π* transition) (Figure 2.B) with high molar extinction coefficients (> 10^4

$M^{-1}cm^{-1}$)[5] and a bright yellow fluorescence (excitation λ = 446 nm, emission λ = 525 nm). The fluorescence quantum yield is low compared to other fluorophores and is dependent from solvent polarity (0.45 in acetonitrile and 0.26 in water).[5-6]

The aqueous solution of flavins consists of equilibrium between three redox forms: the oxidized, the one-electron-reduced (semiquinone) and the fully (two-electron) reduced (hydroquinone) form (Figure 3.A). [4,7] Each state exists under ionized and neutral forms.

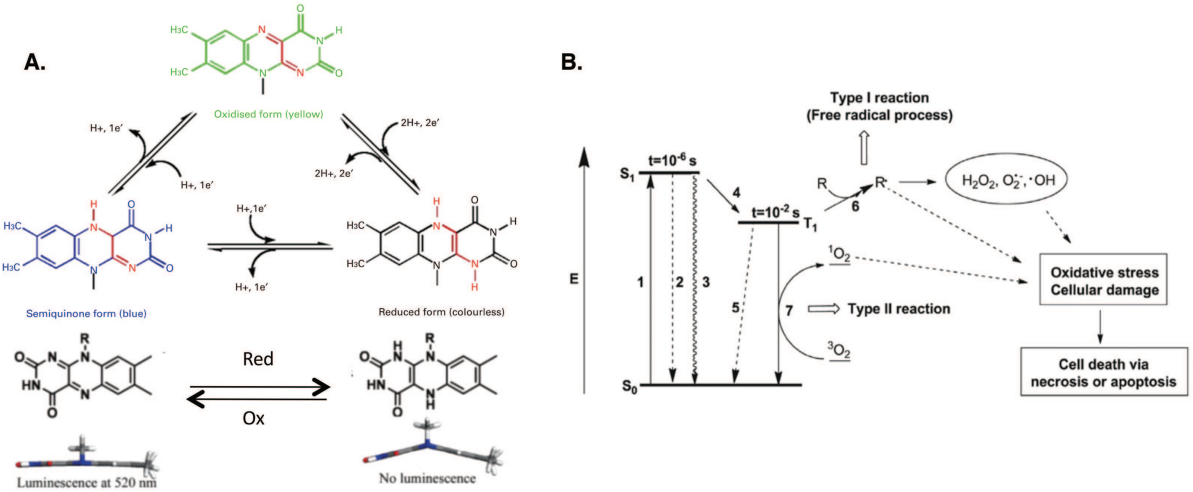

Figure 3.A Conversion between oxidized and reduced forms of RF. [2], [8] **B.** Modified Jablonski diagram. Photophysical process: 1) absorption; 2) fluorescence; 3) internal conversion; 4) intersystem crossing; 5) phosphorescence; 6) formation of free radicals by energy transfer from T1 photosensitizer to biological substrates; and 7) formation of singlet oxygen ($^1O_2$) by energy transfer from T1 photosensitizer to triplet oxygen ($^3O_2$).[9]

The redox state of flavins dramatically influences on their physicochemical properties.[5] Oxidized flavins are yellow-colored with a specific absorption peak near 450 nm and yellowish green fluorescence. In the reduced semiquinone form flavins turn to blue or red color, depending on the protonation state of the isoalloxazine ring.[4,7] Moreover, in the fully reduced state, flavins almost lose their color and become pale yellow.[7] Another consequence of flavin reduction is a pronounced conformational change of the isoalloxazine ring from planar to roof-shaped geometry (Figure 3.A).[8]

Flavins are also known to participate in type I and type II photosensitized oxidation reactions upon exposure to visible or UV-A light (Figure 3.B). Isoalloxazine ring can form a singlet state with bright fluorescence, but short lifetime (τ = 5 ns in water). This singlet state decays by intersystem crossing to the extremely reactive and long-lived triplet-excited state (τ = 15 μs).[5,10-11] The latter is a powerful biradical oxidant able to oxidize a broad spectrum of biomolecules in type I photooxidation processes[10,11] and to generate the reactive electrophilic singlet-excited state oxygen in type II photooxidation mechanisms.[5,9-10]

Thus, thanks to its unique properties like fluorescence, redox induced conformational changes and photosensitizing, RF appears as a promising building block for the development of redox-based sensors, optical catalysts, bio-electronic and tissue-engineered materials.

2.2. Biological properties

2.2.1. Role and transporters

RF belongs to the family of B vitamins and strongly participates in numerous processes in aerobic cells, such as growth, enzyme function and energy production.[3,12] It is also involved in the maintenance of the immune and nervous systems, red blood cells development, cell reproduction, and activation of folate and pyridoxine.[3]

The RF derivatives, FMN and FAD, are enzyme cofactors, whose redox properties play a key role in two-electron dehydrogenation and one-electron transfer reactions. Therefore, they often form parts of enzymes with multiredox centers, for instance, the succinate and NADH dehydrogenases, xanthine oxidase and dehydrogenase, cytochrome P450 systems and nitric oxide synthase.[4] Flavoproteins are also involved in apoptosis signal transduction, biological clocks regulation and biosynthesis of essential cofactors, hormones, such as coenzyme A, coenzyme Q, heme, pyridoxal 5′-phosphate, steroids and thyroxine. In plants, they also participate in several light-dependent processes, like photosynthesis, DNA damage repair and phototropism.[4,13]

Mammals are not able to synthesize RF *in situ* and should obtain it from diet (normal uptake for human adult is 2-3 mg/day).[14] In humans, RF internalization is mediated by three RF transporters RFT-1,[15] RFT-2[16] and RFT-3[17] recently renamed as RFVT-1 (RFT-1), RFVT-2 (RFT-3) and RFVT-3 (RFT-2).[18] These proteins were described and assigned into a new family of transporters - SLC52. RFVT-1 and -2 share 86% identity whereas RFVT-3 shares only 44% identity with RFVT-1 and -2.[18] They are predicted to possess 10 or 11 transmembrane domains and demonstrate similar specificity for all flavins with weaker affinity for FMN and FAD (Figure 4).[17]–[19] The apparent Michaelis-Menten constants for RF are 1.38, 0.33 and 0.98 μM (for RFVT1, -2 and -3 respectively), which are moderately higher than the normal RF concentration in human plasma (0.004-0.049 mM).[18], [19] RFVT-1 and 2 are pH-independent receptors, regulated by substrate level (upregulated in case of RF deficiency) and mainly present in placenta, small intestine (RFVT-1) and brain (RFVT-2).[15-16,18] In contrast, RFVT-3 is pH-sensitive and is mainly expressed in testis, small intestine and prostate.[18]

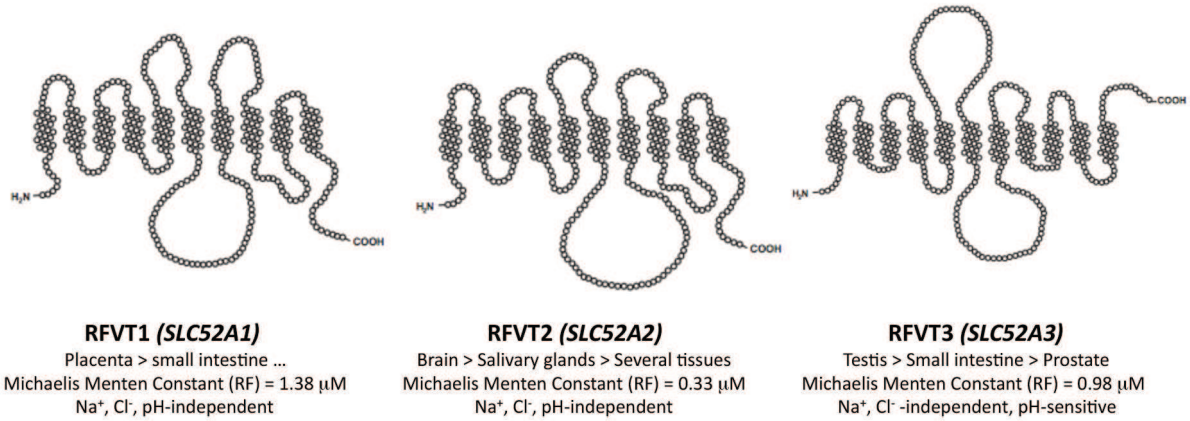

Figure 4. RF transporters RFVT1, RFVT2, RFVT3. Adapted from [18].

The increased need of RF during foetal development requires the expression of a RF carrier protein (RCP).[20-21] The high degree of RCP similarity between species (birds and mammals) in terms of physicochemical and immunological characteristics demonstrates its

importance in normal foetal development and survival.[20,22-23] In human, RCP is mainly found in amniotic fluid and plasma during pregnancy and its expression is hormonally regulated.[24-25] Chicken RCP (cRCP) crystallization allowed a better understanding of the protein structure and of the RF binding site (Figure 5).[23] RCP is a globular protein characterized by an unusually elevated degree of cross-linking (nine disulfide bridges) related to the conformation of ligand binding domain.[22-23] The RF binds into a folded pocket and its isoalloxazine ring is stacked between the rings of Tyr75 and Trp156 (Figure 5.C). These π-stacking interactions are associated with a loss of RF fluorescence upon binding to the RCP.[23]

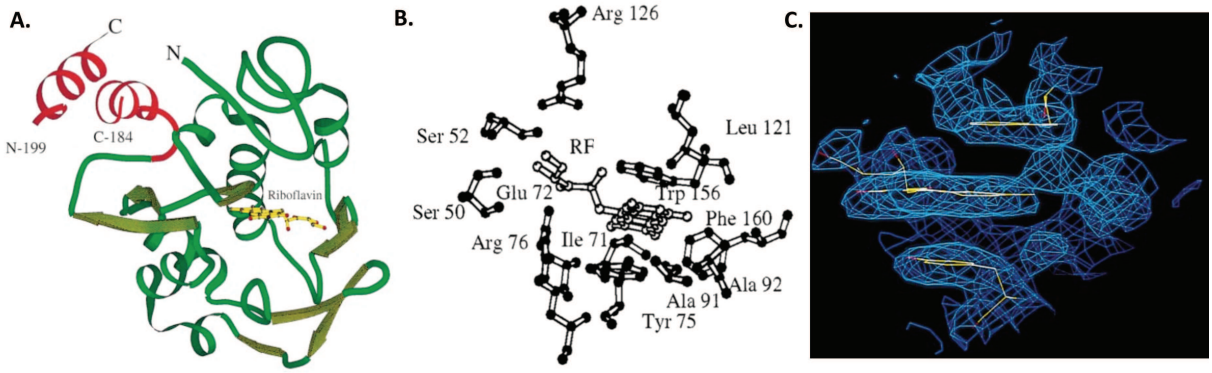

Figure 5. Chicken RCP structure **A.** Ribbon diagram of the RCP: ligand binding domain is presented in green and phosphorylated motif in red; yellow stick drawing represents RF; letters 'N' and 'C' indicates the N- and C-termini of RCP; gap between the two helices in the red motif is the disordered part of the molecule (phosphorylated region between Leu184 and Glu199). **B**. Amino-acids in the ligand binding site that are in closest contact with RF. **C.** Electron density of RF and the rings of Tyr75 and Trp156 in the solvent-flattened map (contoured at a level of 1.0 s). Adapted from [23].

Despite several recent findings, RFVT transporters are still not completely characterized, their crystal structures are not resolved and the exact transport mechanisms of RF with involvement of RFVT and RCP remain unclear.

2.2.2. Related pathologies

Taking into account its involvement in a lot of metabolic reactions, RF deficiency causes a variety of pathological states, such as angular stomatitis, seborrhoea, glossitis, neuropathy, growth retardation, acidosis, indigestion, night blindness and anemia.[1,12] Other studies revealed that lack of RF could be associated with cell stress, apoptosis, impaired protein folding, genomic instability and even cancer.[26] Moreover, a slight deficiency was shown to increase levels of plasma homocysteine favoring the risk of cardiovascular disease.[1] The involvement of RF in foetal development also explains the multiple abnormalities in offspring triggered by RF deficiency during pregnancy.[1,4]

Finally, mutations in RFVT genes (SLC52A1-3) generate dysfunctional RF transporters leading to multiple acyl-CoA dehydrogenase deficiency (MADD), Brown-Vialetto-Van Laere syndrome (neurological disorder), and affecting amino-acid and fatty acid metabolism.[1,12] Therefore, RF supplementation is beneficial in prophylaxis of anemia, cataracts, hyperhomocystemia, migraine, MADD, Brown-Vialetto-Van Laere syndrome and dermatoses. [13]

Some studies also suggest that it could be useful in combined photo- and

chemotherapy of cancer[14,27-28]. Due to its photosensitizing potential it could increase cell apoptosis and autophagy and on the other hand, prevent side effects like DNA damage, mutations, intestinal mucosa damage and inflammation during radio/chemotherapy. Furthermore, it has been shown to increase antiangiogenic factors during breast cancer treatment contributing to tumor burden reduction and subsequent good prognosis.[29]

Currently, RF supplementation is based on natural RF and its hydrophobic analogues like 2',3',4',5'-RF-tetrabutyrate (RTB) or RF laurate in oily formulation (Figure 6) known to improve tissue absorption.[28,30-31]

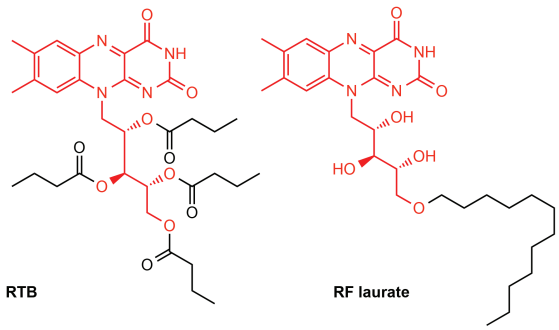

Figure 6. Chemical structures of RF derivatives – RF tetrabutyrate (left) and RF laurate (right). [28,30]

3. Applications in health nanotechnologies

3.1. Active targeting

The relationships between RF and cancer are quite complex and regulative mechanisms are still not well understood.[26-27,29,32] Surprisingly, RCP mainly detected during foetal development, was shown to be overexpressed in breast[33-34], prostate cancers[35] and hepatocellular carcinoma.[36] Although RCP is known to be an estrogen-induced protein, its overexpression was significant in both estrogens/androgen-dependent and -independent breast and prostate cancers and thus seemed to be dissociated from hormonal regulation.[33,35]

The level of RCP in the serum of healthy women varies during menstrual cycle (mean 3.8 ng/ml) and drops down with the onset of menopause (1.7 ng/ml). In contrast, patients with diagnosed breast carcinoma, showed from 3- to 4-fold RCP level increase for cycling women (14,7 ng/ml) and even higher, 9-11 times, for post-menopausal women (17,0 ng/ml). Moreover, the levels of serum RCP revealed a noteworthy correlation with the stage of disease and metastasis formation (higher with advanced stage).[33-34,36] In hepatocellular carcinoma (HCC), high RCP levels were also found in serum and tumor tissue samples of patients (mean serum RCP concentration on 22 patients: 21.75 ± 14.66 ng/ml) compared to normal controls (0.73 ± 0.25 ng/ml), alcoholic hepatitis (1.92 ± 0.82 ng/ml) or cirrhosis (5.02 ± 1.52 ng/ml). However, there was no reported elevation of RCP in serum of prostate cancer patients.[35] Nevertheless, immunostaining of tumor samples revealed a variation of RCP localization between early and late stage of disease: clustered into the tubular epithelium for the former and widely dispersed for the latter.[35]

Altogether these findings emphasize the growing interest of detecting RCP as a serum marker for early breast and HCC detector and a prognosis indicator in breast, prostate cancer and HCC biopsies.[33-36] On the other hand, RF could be a promising ligand for the specific

delivery of anticancer therapeutics to the breast, prostate or liver tumors.

3.1.1. RF-biomolecule conjugates

Holladay *et al.* first shown that a biomolecule (protein BSA – bovine serum albumin) could be internalized in different cancerous cell lines (SKOV, SKLU, A549 and KB) when conjugated to RF.[37] The cellular uptake was monitored by fluorescence microscopy and quantified with fluorescein isothiocyanate (FITC) probe conjugated to BSA. As depicted on Figure 7.A., the internalization of FITC-BSA conjugate was significantly dependent on RF conjugation demonstrating the role of RF as a targeting agent. Surprisingly, competition experiments revealed a conjugate internalization process different from natural RF or FMN cell uptake.

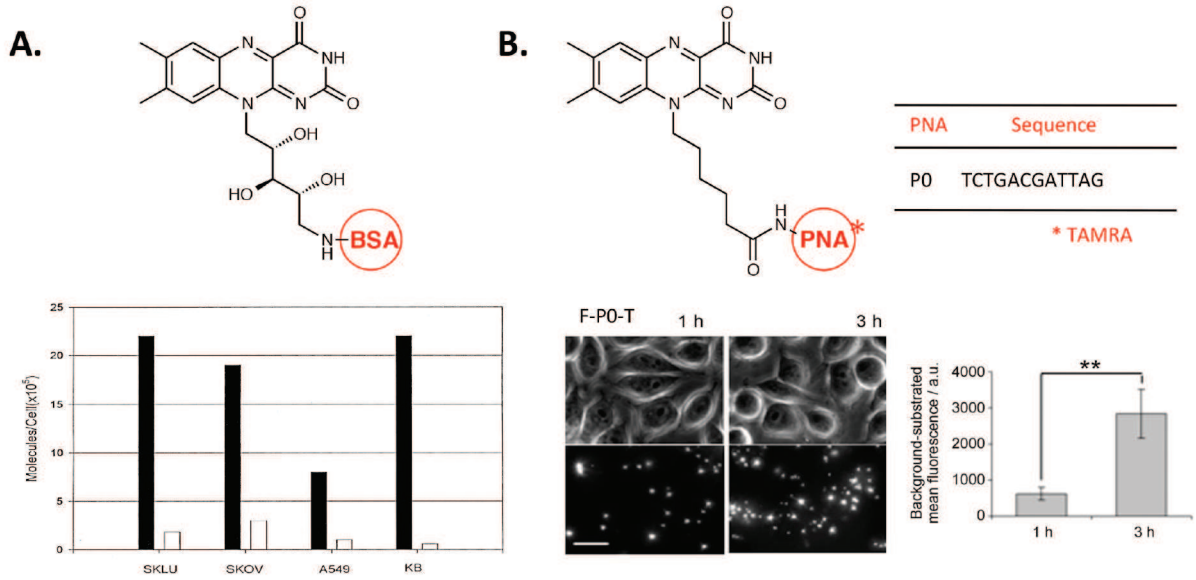

Figure 7.A. BSA-RF conjugate (up); internalization of FITC-BSA-RF conjugate (black bars) and FITC-BSA (white bars) in different cell lines. Adapted from [37] **B.** Structure of Flavin-PNA-TAMRA conjugate (up, left), PNA sequence (up, right) and cellular internalization – fluorescence images (down, left) and quantification (down right). Adapted from [38].

Another group demonstrated the interest of the flavin moiety as targeting agent for nucleic acid delivery. They conjugated a RF derivative to an antisense Peptide Nucleic Acid (PNA), known for its difficulties to enter cells by its own.[38] In this study, the ribitol chain of RF was replaced by hexanoic acid and conjugated to PNA *via* an amide bound (Figure 7.B). A fluorescent marker – tetramethylrhodamine (TAMRA) was also attached to PNA to quantify internalization by fluorescence microscopy and flow cytometry. Flavin-PNA-TAMRA conjugate (F-PNA-T) was shown to enter HeLa cells rapidly and in an energy-dependent manner in contrast to PNA-T. After treatment with chloroquine (an endosomolytic agent), a diffusive fluorescence in the cytoplasm was observed and the antisense activity checked, demonstrating PNA cell delivery triggered by RF.

3.1.2. RF-decorated nanosystems

Up to date, RF or its derivatives were utilized as a targeting moiety towards cancerous cells in dendrimers[39-41] and iron oxide nanoparticles.[42-43]

Thomas *et al.* conjugated RF to the fifth generation (G5) polyamidoamine (PAMAM)

dendrimer.[39] This dendrimer was about 5.4 nm in diameter and had many free chemical functional groups on its surface allowing easy and efficient conjugation. Two types of dendrimers were prepared – one with RF and FITC dye and another bearing RF and the cytotoxic drug methotrexate (Figure 8.A). The uptake of RF-FITC dendrimer in KB cells was monitored by flow cytometry and was shown to be time- and dose-dependent. On the other hand, cytotoxicity tests revealed the inhibition of cellular growth induced by RF-methotrexate dendrimer. The same team in their later studies aimed to optimize RF-dendrimer conjugates by varying RF orientation and RF number per dendrimer.[40] Hence, RF was attached to the dendrimer via N3 nitrogen of the isoalloxazine ring (N(3)-conjugates) or primary alcohol of ribitol chain (N(10)-conjugates) (Figure 8.A). Isothermal titration calorimetry (ITC) experiments were used to determine K_D values of each RF-dendrimer towards RCP and showed that N(3)-conjugates had a greater affinity for RCP compared to N(10)-conjugates.

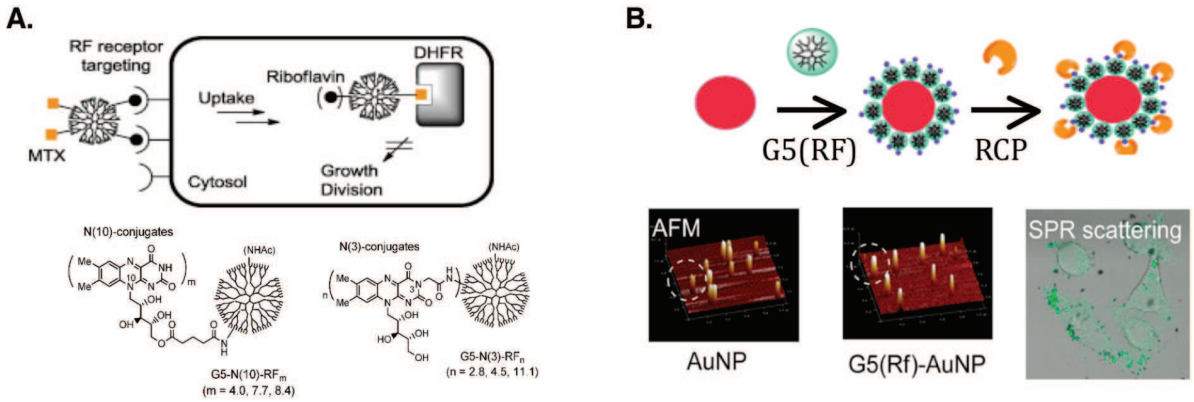

Figure 8.A. PAMAM dendrimers conjugated with RF and methotrexate – (MTX)-RF-PAMAM dendrimer conjugates: *via* isoalloxazine ring (left), *via* ribitol chain (right).[40] **B.** Schematic representation of AuNP−dendrimer preparation (down) and AFM images of its morphology (up left).[41]

In a follow-up study, Witte *et al*. prepared golden nanoparticles with chemisorbed PAMAM-conjugated RF (AuNP-dendrimer, Figure 8.B).[41] They evaluated their binding to RCP by atomic force microscopy (AFM) that detected the increase in size (from 22.8 to 26.7 nm) induced by complex formation. The co-incubation with free RF as a competitive ligand inhibited RCP binding and thus supports the selectivity of the interactions at the AuNP-dendrimer surface. Taking into account surface plasmon properties of gold, this nanocomposite opens a new avenue for cancer-targeted imaging.

Recently, the same team extended their obtained PAMAM dendrimer platform towards the transport of therapeutic nucleic acid.[44] The device consisted of a PAMAM core decorated with RF units and DAPP (3,8-diamino-6-phenylphenanthidinium) – a well known dsDNA intercalator (Figure 9). The DNA loading on RF-PAMAM dendrimer and its complex formation with the RCP was demonstrated by SPR (surface plasmon resonance), DLS and surface potential measurements. Moreover, to confirm DNA cell delivery, the authors investigated whether the polyplexes containing a luciferase-encoding plasmid induced luciferase expression in KB tumor cells *in vitro*. It was shown, that compared to controls, RF allows a specific nucleic acid cell delivery. This study serves as a proof of concept for the design of multivalent dendrimer vectors for targeted gene delivery based on a DNA-ligand intercalation strategy.

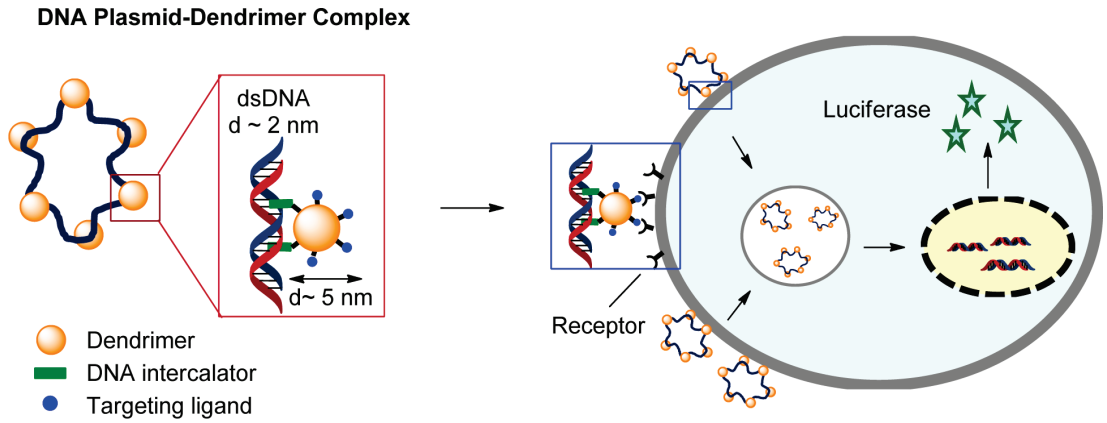

Figure 9. Concept for multivalent dendrimer vectors with DNA intercalation motifs for targeted delivery of DNA payloads to a cancer cell. The dendrimer conjugate presents a multivalent array of two functionally orthogonal ligands, one for anchoring DNA payloads and the other for targeting cancer cell associated receptors.[44]

Jayapaul *et al*. constructed a nanosystem for targeted magnetic resonance imaging (MRI) based on ultrasmall iron oxide nanoparticles (USPIO) and RF derivative. Charged RF derivatives, FMN[43] or FAD[42], were directly adsorbed on nanoparticles *via* electrostatic interactions leading to a bimodal imaging nanodevice (fluorescent and superparamagnetic) named FLUSPIO (fluorescent USPIO) (Figure 10. A, B). Characterization by transmission electron microscopy (TEM), scanning electron microscopy (SEM), DLS, MRI and fluorescence spectroscopy revealed a spherical particles 28 nm in diameter, negative zeta potential, intensive fluorescence emission at 530 nm and paramagnetic properties close to Resovist (a contrast agent used in clinics). *In vitro* evaluations of these systems revealed their biocompatibility and specificity towards RF transporters (by the pre-incubation with free FMN) in metabolically active cells (prostate cancer cell lines PC3, LnCap and human umbilical vein endothelial cells (HUVEC)).[43] *In vivo* studies on prostate cancer xenografts in mice showed efficient accumulation of FLUSPIOs in tumor and surrounding blood vessels.[42] In conclusion, these innovative RCP-targeted bimodal imaging could serve for the assessment of vascular metabolism in tumors.

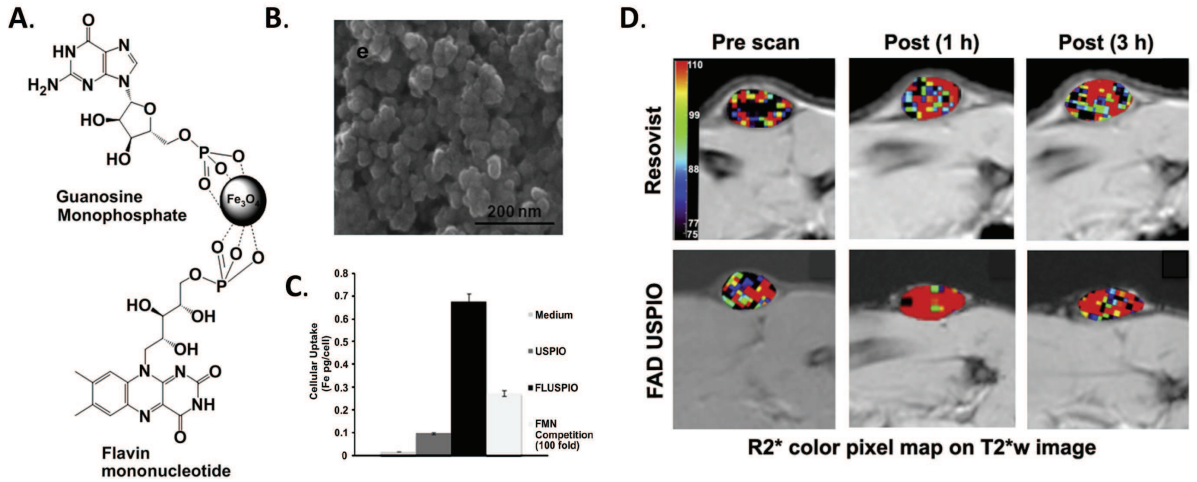

Figure 10.A. Schematic presentation of FLUSPIOs. **B.** Its morphology by SEM. **C.** Cellular uptake of FLUSPIOs.[43] **D.** *In vivo* accumulation of FLUSPIOs compare to Resovist. Adapted from [42].

The discussed bioconjugates and nanoparticles are the only systems to date that exploit RF as targeting agent. However, it could represent a promising alternative for tumor-targeted nanomedecines due to RF biocompatibility, low cost, versatile chemistry and specific transporter systems overexpressed in metabolically active cells.

3.2. Catalysis and sensing

The unique physicochemical properties of RF open a lot of possibilities in the field of organocatalysts and biosensor design.

3.2.1. Chiral organocatalyst

Iida's team investigated the influence of RF redox behavior on the conformation and chirality of a polymeric helix.[45] For that purpose, RF was covalently bound *via* its ribitol chain to an acetylene monomer that was subsequently polymerized using a rhodium catalyst. Thus, the obtained polymer consists in a polystyrene backbone with pendant RF residues (optically active). Circular dichroism studies revealed an ordered one-handed helical conformation, induced by the π-π stacking interactions between flavins. In contrast, the reduction with dithionite induces a loss of planarity of the isoalloxazine moities and the disruption of π-π interactions resulting in conformational changes in helix chirality to almost racemic disordered array. The initial one-handed helical conformation was completely restored upon air oxidation (Figure 11.A). Hence, this new RF-bearing polymer could constitute a starting point for the development of a chiral organocatalyst for enantioselective oxidation.

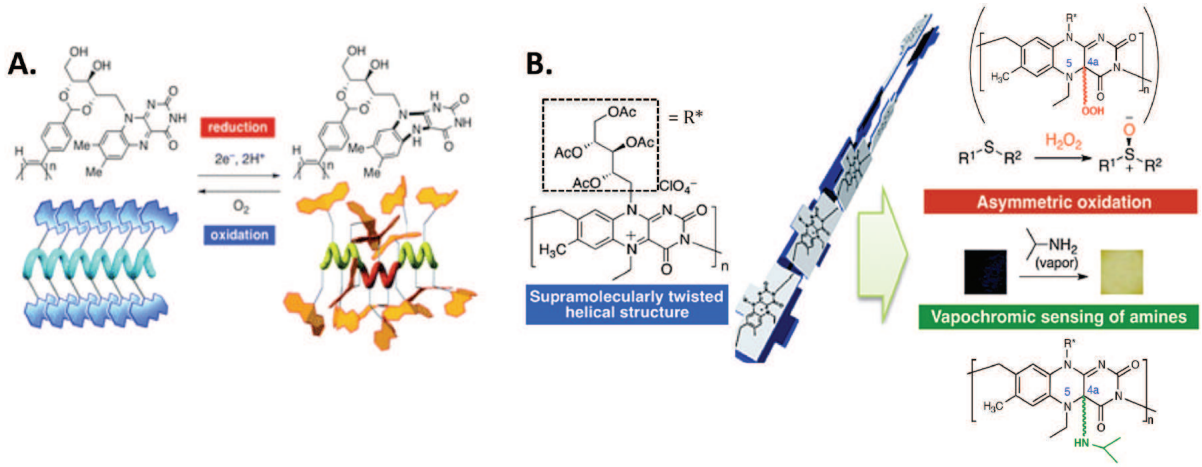

Figure 11.A. Schematic illustration of the redox-triggered switching of the helical structure with riboflavin pendants.[45] **B.** Schematic representation of polymer-based RF structure and applications. Adapted from [46].

Later on, the same team developed a novel optically active polymeric helix consisting in RF units as the main chain.[46] The basic polymer was prepared from commercially available RF in three steps by linking the isoalloxazine phenyl part of one unit to the isoalloxazine ureido part of a second unit. RF units in this polymer were then converted in 5-ethylriboflavinium (ethyl-RF) perchlorate salts that loosed RF initial fluorescence but displayed a purple color. The face-to-face π-stacking interactions of riboflavinium residues stimulated supramolecular self-organization of the polymer into twisted, duplex-like, one-handed helical structure (Figure 11.B). This polymer was able to catalyze the H_2O_2-mediated asymmetric organocatalytic oxidation of sulfides with enantioselectivities up to 60%. The

stereoselective oxidation involved the formation of an oxidatively active 4a-hydroperoxyflavin intermediate with high stereoselectivity thanks to the twisted helical π-stacked structure of polymer. Consequently, this polymer might constitute a novel class of green asymmetric organocatalysts.

3.2.2. Amine sensing

The discussed previously 5-ethylriboflavinium perchlorate-based polymer was utilized for primary and secondary amines sensing.[46] The polymer, once processed into homogeneous films, showed a vapochromic behavior upon exposure to amine vapors (Figure 11.B). The detection triggered a color change of the film from initial purple to yellow. This colorimetric response is selective and reversible and can be explained by the nucleophile and basic behavior of amines that stimulate the formation of the corresponding 4a-aminoflavin adducts and ammonium perchlorate. Nevertheless, the detection was only based on a reversible colorimetric response since ethylriboflavinium cations and corresponding 4a adducts are non-fluorescent.

Lately, the sensor was improved by adding a fluorogenic feature.[47] The sensing polymer (Figure 12) was made from the 4a-hydroxy adduct of an ethyl-RF-based polymer that give a purple-colored non-fluorescent film and a free RF that brought a fluorescence dimension to the material (Film A). Then, the sensing film (Film B) was generated by addition of aqueous perchloric acid, which protonated both free RF (RFH) and ethyl-RF-based polymer inducing a fluorescence quenching and thus a polymer color change to purple. Once in contact with primary or secondary amine vapors, the fluorescence of the film was immediately restored (Film C) accompanied by a color change from purple to yellow. It could be explained by: i. neutralization of perchloric acid with basic amines that restores the fluorescence of free RF; ii. nucleophile addition of the amines to ethyl-RF-based polymer in 4a position with the formation of ammonium perchlorate. This new fluorogenic sensor presents an advantage compare to previous colorimetric one, in terms of detection response, sensitivity and detection limit.[46] Moreover, it is able to distinguish quite accurately chiral amines that opens a way to a new chemo- and enantioselective fluorogenic sensory materials.

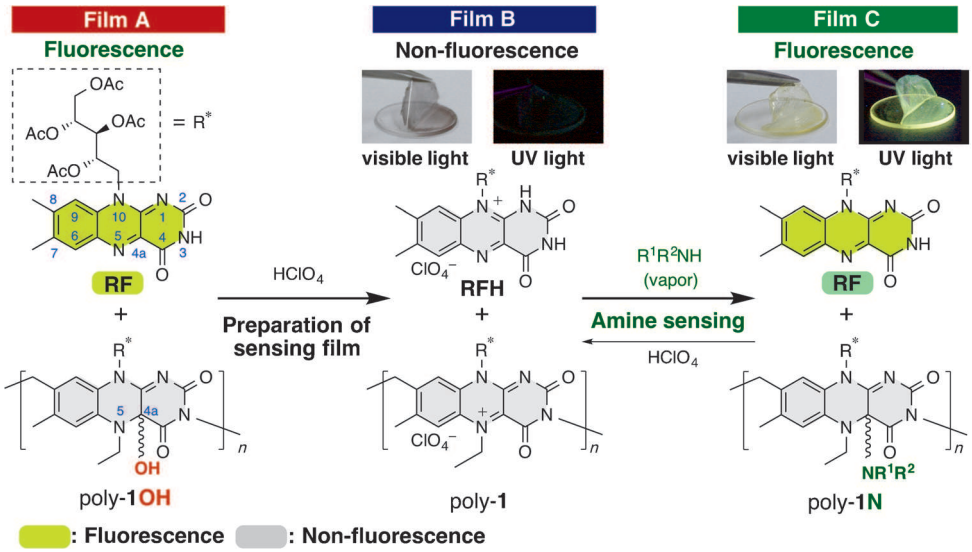

Figure 12. Schematic representation of sensor principles.[47]

3.2.3 Theophylline and adenosine sensing

Another sensor, based on fluorescent properties of RF, was prepared by Sato and co-workers.[48] The sensor was made of a DNA duplex aptamer containing an abasic site, capable of specifically recognizing theophylline. Initially, RF was positioned in the abasic site of the aptamer and its fluorescence was quenched by the stacking interactions between izoalloxazine ring and neighbouring guanine residues. The corresponding aptamer sequence was previously optimized to allow effective recognition and positioning of RF.[49] Theophylline has higher affinity for the abasic site than RF and consequently, upon the aptamer interaction with theophylline, RF was released and its fluorescence was restored (Figure 13.A). The fluorescence response was linear in the concentration range from 1.0–32.5 μM of theophylline in horse serum samples, while the response for caffeine and theobromine was negligible. In summary, the developed RF-based sensor was selective enough for the detection of serum theophylline in a therapeutic concentration range. In addition, a similar RF-aptamer sensing system was developed for the detection of adenosine.[50]

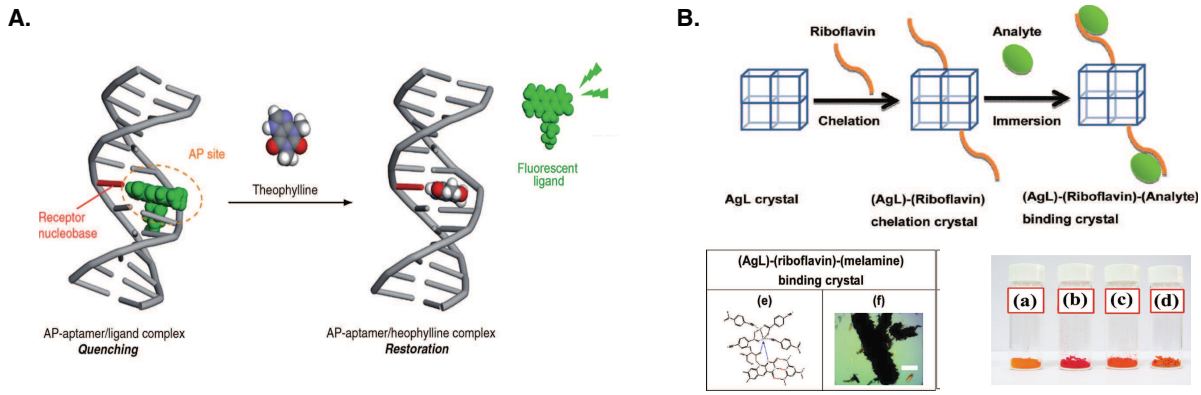

Figure 13.A. The principle of work of fluorescent abasic site containing aptamer sensor for recognition of theophylline. Fluorescent ligand stands for RF.[48] **B.** Scheme of work of AgL-RF system - crystal morphogy - color changes in different crystals: a) RF, b) AgL-RF, c) AgL-RF-melamine, d) AgL-RF-acetoglutamine.[51]

3.2.4. Melamine sensing

The capacity of RF to form hydrogen bonds and π-π interactions was exploited in the construction of metallic-organic framework (MOF) sensor for detection of melamine or acetoglutamine.[51] MOF represented a porous material made of silver and L-4-cyanobenzoate (AgL), which was further chelated with RF (Figure 13.B). This light-emitting system was able to detect melamine and acetoglutamine *via* the interactions with RF, which induced a photoluminescent signal. The study of these interactions by FTIR (Fourier transform infrared spectroscopy) revealed the hydrogen bonds between the carbonyl (C=O) of RF and the amine (NH_2) of melamine or acetoglutamine. In addition, the fixation of the ligand could be detected with a naked eye due to the color change of RF-AgL crystals.

RF was also demonstrated to form photoluminescent fibrillar hydrogels with melamine (Figure 14.A).[6,52] Interestingly, due to the hydrogen bond formation, conformational ordering and π-stacking interactions between these molecules, the photoluminescence of the formed hydrogel was much stronger than the one of free RF.

The presented RF-hydrogel or MOF could be promising sensor systems for rapid and easy melamine detection.

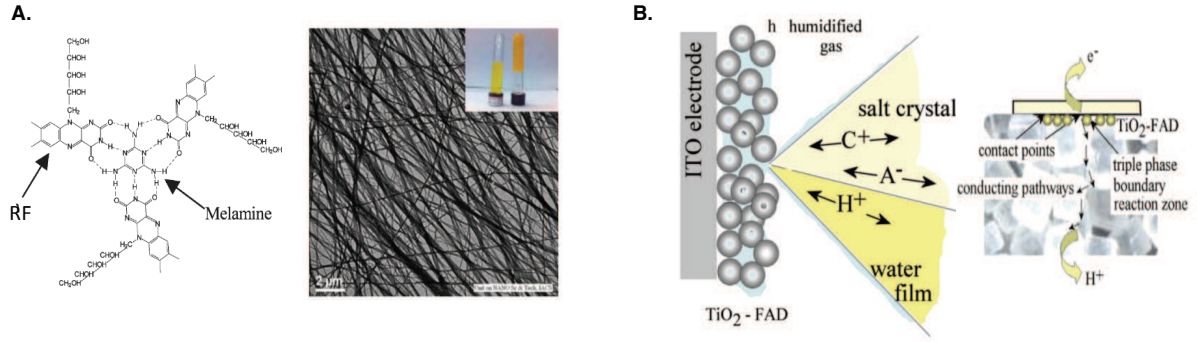

Figure14.A. Schematic model of RF-melanine supramolecular complex – TEM picture of RF-melanine hydrogel (0.02% w/v).[6,52] **B.** Schematic representation of the salt-electrode point with a mesosporous TiO_2-FAD film deposit (TiO_2 nanoparticles are indicated as balls) and a microphase of saturated salt solution – schematic drawing of the working electrode-TiO_2-FAD-salt interface. [53]

3.2.5. Carbon dioxide sensing

The nano-TiO_2-FAD films on tin-doped indium oxide (ITO) electrodes were developed to study redox processes and enable carbon dioxide sensing (Figure 14.B).[53] The films were produced using layer-by-layer deposition on ITO electrodes to yield mesoporous films with four 30 nm layers. The redox reactions conducted by FAD in contact to aqueous electrolyte media (for diluted and saturated electrolyte) and in contact to solid humidified salt electrolyte (for extreme salt levels and different types of salts) were investigated. This conditions created an aqueous microphase at the gas/salt/electrode interface, which was studied by cyclic voltammetry. In summary, it was shown that 2-electron-2-proton reduction of FAD is able to indicate local pH (15, 12 or 7) at the gas/salt/electrode interface in contact with K_3PO_4, K_2HPO_4, and KH_2PO_4, respectively. Moreover, the exposure to carbon dioxide vapors induced the changes in surface pH and this feature could be utilized in the future for new types of air-quality and gas-sensing devices.

Hence, RF has been explored in a variety of innovative sensing systems to detect individual molecules in vapors, gazes or liquid samples.

3.3. Tissue engineering

Previously discussed FLUSPIOs were recently shown to be useful for cell labeling and monitoring in tissue-engineered implants (Figure 15.A).[54] First, Mertens *and al.* investigated the uptake and cytotoxicity of FMN-coated iron oxide nanoparticles on HUVECs, smooth muscle cells (SMC) and fibroblasts (FB). Consequently, FLUSPIOs were well tolerated by studied cell types, rapidly internalized and still detectable after 16 days in culture (by MRI and fluorescence). Moreover, it was possible to follow the colonization of collagen scaffolds by FLUSPIO labeled HUVECs *via* fluorescence imaging. Finally, the visualization of endothelial cell growth on tissue-engineered vascular grafts was studied. A significant increase in MRI signal (R2* relaxation times) was observed for grafts colonized with FLUSPIO-labeled HUVECs. In conclusion, FLUSPIO-labeling could be suitable for monitoring endothelial cells growth and colonization of collagen scaffolds and tissue-engineered vascular grafts.

In another study, RF was used as a polymerization photoinitatior in polyethylene glycol diacrylate scaffolds.[55] Due to their biocompatibility and biodegradability, these

scaffolds are designed for tissue engineering and especially for controlled 3D-cultivation of cells (Figure 15.B). However, commercially available photoinitiators like Michler's ketone, Irgacure® 369 and Irgacure® 2959 (BASF Schweiz AG, Switzerland) were shown to exhibit some toxicity towards fibroblasts, chondrocytes, corneal epithelial cells, mesenchymal stem cells, osteoblasts and embryonic germ cells. In this context, authors suggested to utilize RF-triethanolamine (TEOHA) mixture as two-photon polymerization initiator. Although, the photosensitivity of RF-TEOHA was lower compare to commercial Irgacure 369 and Irgacure 2959, the biocompatibility tests revealed a much lower cyto- and genotoxicity of RF-TEOHA generated polymer scaffold. Thus, after enhancement of its photoinitiator properties, the RF–TEOHA photoinitiator could be a potent tool for realizing the two-photon or UV polymerization of fully biocompatible scaffolds for tissue engineering.

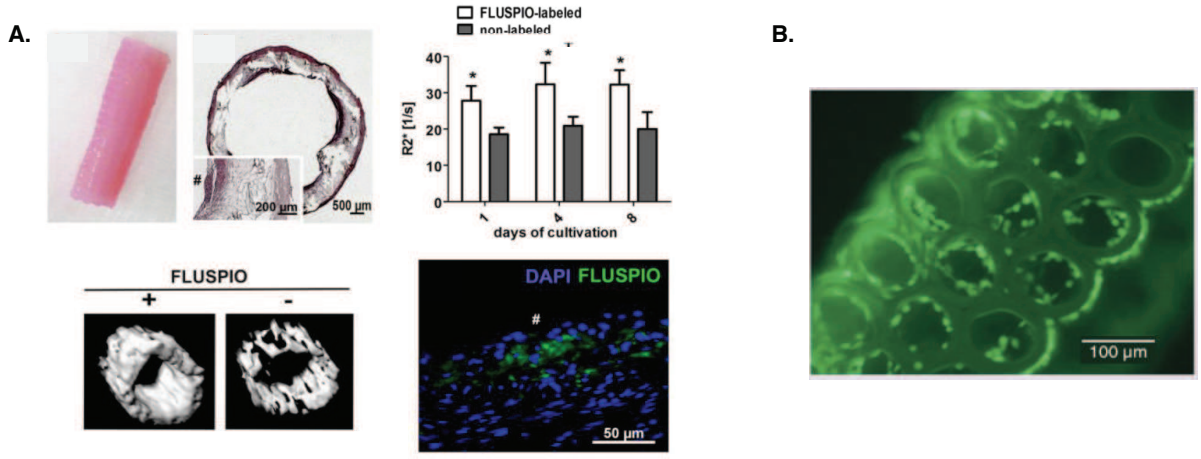

Figure 15.A. FLUSPIO-labeled HUVECs for monitoring growth and colonization on collagen scaffolds: Prussian blue staining, MRI results (R2* relaxation times), fluorescence microscopy image. Adapted from [54] **B.** RF–TEOHA photoinitiated scaffold.[55]

Currently, RF is used as a polymerization photoinitiator for corneal collagen cross-linking in the treatment of keratoconus (rare corneal decease, which causes its deformation, swelling and loss of elasticity).[56] The corneal collagen cross-linking (CXL), developed in the early 2000s, is a golden standard in keratokonus treatment. CXL increases corneal strength and stops the disease progression. Special RF formulation utilized for CXL, is installed on the eye and irradiated with UVA. The produced free radicals enable the polymerization of collagen fibrils *in vivo* and reinforces the corneal tissue with preserving its transparency (Figure 16.A).[57]

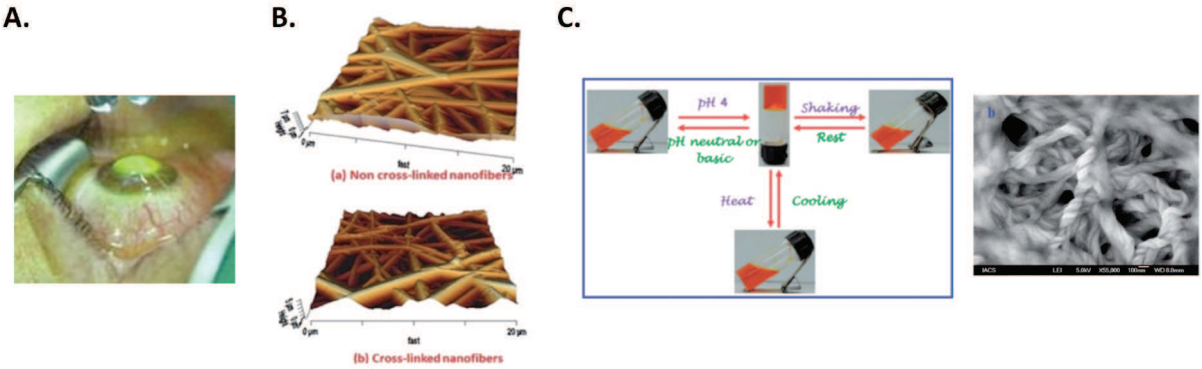

Figure 16.A. Photograph of CXL technique (image adapted from the internet). **B.** RF-loaded PCL nanofibers for free radical generation and tissue engineering.[58] **C.** Photographs of FMN-adenine

hydrogel in different conditions – field emission SEM images of gel.[59]

Sridhar et *al.* developed a protocol for stabilizing protein nanofibers by cross-linking with the help of RF in very similar way to the CXL utilized for keratoconus treatment.[58] RF-gelatin fibers in film or solution were irradiated with UV and generated reactive oxygen species that induced subsequent cross-linking of gelatin and enhancement of its mechanical strength. Similarly, gelatine and fibrinogen were cross-linked by RF released from RF-loaded polycaprolactone (PCL) nanofibers upon UV irradiation (Figure 15.B). The RF encapsulation in the PCL nanofiber allowed the continuous drug release, and the free radical generating nanofibers could serve for cross-linking of any protein fiber or fibrous tissue, such as ocular, skin or cardiac, suitable for tissue engineering.

Recently, FMN was shown to form a hydrogel when mixed with adenine.[59] An equimolar mixture of both molecules in a phosphate buffer (pH 4.0, 1.0% w/v) produced a red fluorescent hydrogel after heating to 100 °C and subsequent cooling to 30 °C. The gel showed a fibrillar structure and pH-, heat-dependent and thixotropic behavior (Figure 15.C). At pH=7 or higher, the phosphoric acid group and ribitol alcohols were protonated and might exert a steric hindrance for intermolecular π-π interactions. Moreover, the deprotonation of FMN and adenine at basic pH caused the loss of hydrogen bonds between molecules. Thus the gelation was limited in the pH range 2-5. Similarly to melamine-RF, FMN-adenine hydrogel showed a significant enhancement in fluorescence intensity compared to free FMN. Taking into account its thixotropic, pH- and heat-dependent behavior and biocompatibility of FMN and adenine, this new hydrogel could be used in cellular culture, cell imaging and tissue engineering.

Thus, thanks to its fluorescence, photosensitizing behavior and low cytotoxicity, RF could become a promising adjuvant in various tissue-engineering scaffolds – from vascular grafts to fibrous and corneal tissues.

3.4. Optoelectronic devices

The previously discussed redox properties of RF were extensively utilized in the construction of responsive systems based on carbon nanotubes.[8] In this study, Ju *et al.* covalently attached a FMN derivative to single-walled carbon nanotubes (SWNT) *via* EDC (1-Ethyl-3-(3-dimethylaminopropyl)carbodiimide)-assisted coupling. They eventually added a six-carbon spacer to get some flexibility between SWNT and the FMN derivative (Figure 17.A). The authors observed a significant decrease in fluorescence of the conjugated FMN compared to its free form. The *π-π* stacking between the isoalloxazine ring and the side-walls of SWNTs seems to be responsible for such quenching. It was possible to detach the flavin moiety from SWNT side-walls by either sonication or chemical reduction of FMN to $FMNH_2$. The reduction induces a flavin luminescence quenching and a deep conformational change in the isoalloxazine ring away from planarity, which disturbed the *π-π* stacking with SWNT. The reoxidation with air restored RF fluorescence, the aromatic ring became planar and was again collapsed to SWNT. The addition of a surfactant - sodium dodecyl sulfate (SDS) induced SWNT micellization and could prevent the collapse of FMN onto the SWNTs. This fundamental study helped to understand of the redox-assisted conformational behavior of covalently bound SWNT-FMN derivatives and could be used for design of new functional bioelectronic devices.

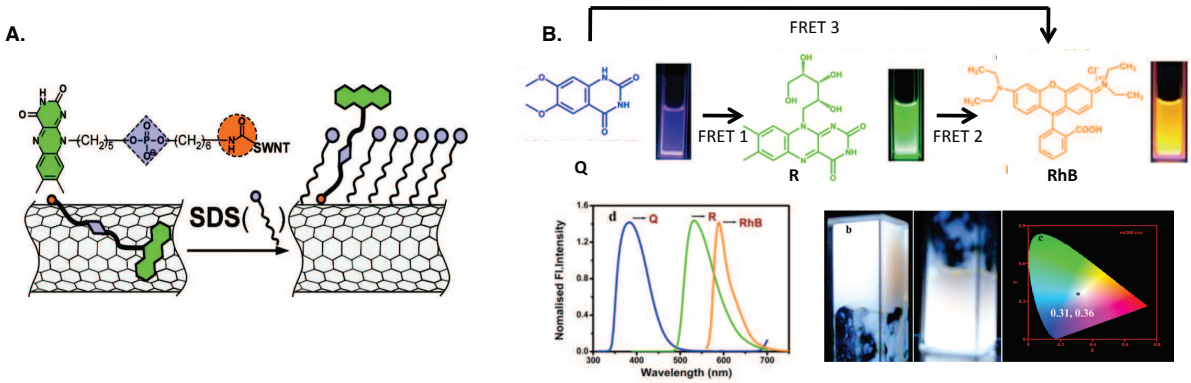

Figure 17.A. Flavin-tethered SWNTs and its conformation in the absence and presence of SDS.[8] **B.** Chemical structure of Q, RF, RhB and FRET phenomena in gel (up); spectral overlaps between Q, R and RhB (down, left); photograph and CIE coordinate diagram for white-light-emitting gel with molar ratio Q:M:R:RhB 100:100:0.5:0.02 (down, right). Adapted from [60].

Another study reported the utilization of hydrogels as optoelectronic systems. Bairi *et al*. prepared light harvesting hydrogels from melamine, fluorescent 6,7-dimethoxy-2,4[1*H*,3*H*]- quinazolinedione (Q) and RF.[61] Upon irradiation the system exhibited a fluorescence energy transfer (FRET) from Q (λexc ~ 297 nm, λem ~ 384 nm in solution) to RF (Figure 17.B) supported by a gradual decrease of Q fluorescence in accordance with RF concentration increase. This FRET phenomenon, specifically observed in a gel state, is explained by a 50 nm red shift of emission maximum of Q (434 nm) compared to emission wavelength in solution. This system allowed the implementation of more complex white-light-emitting hydrogel with the help of a fourth component – rhodamine B (RhB).[60] The fluorescence spectrum of RhB overlaps the one of RF, and thus decreases its fluorescence emission and creates a second FRET phenomenon in the system from RF to RhB. Moreover a third FRET phenomenon was observed from Q to RhB thanks to the red shift of Q emission in gel. As a result, a combination of energy transfer processes in appropriate proportion in the gel state as able to emit the white light composed of the three primary colors blue (Q), green (RF) and red (RhB). The CIE's (Commission Internationale de L'eclairage) coordinate diagram for the white light emission of the hydrogel gave values that were very close to pure light coordinates. These new hydrogels were able to emit light upon excitation in the range of 300-600 nm and they may offer an opportunity to conceive future optoelectronic devices.

5. Conclusions

Thus, RF and its derivatives FMN and FAD may serve as highly versatile building blocks for the construction of various nanosystems. Their particular chemistry allows the attachment by covalent bonds to polymers,[39,45] proteins,[37] nucleic acids[38] etc. On the other hand, they are able to form non-covalent bonds such as π-π stacking,[8,45] hydrogen,[6,51] or electrostatic interactions.[43]

Since RF is an essential vitamin, mammals posses a specific transporter system for its transportation to the cells.[18,22] These systems are upregulated in metabolically active cells like prostate,[35] breast[33] and liver cancer.[36] As a consequence, RF was utilized in several tumor-targeted delivery systems that showed good specificity, low toxicity and efficient delivery *in vitro*[37-39,43-44] and *in vivo*.[42] However, the knowledge about exact RF transporter mechanisms is so far limited and thus further investigations on RF transporter proteins structure and function are needed.

The redox, photosensitizing and fluorescence properties of RF were exploited for the construction of chiral organocatalysts for asymmetric reactions[45-46] and biosensors for the

detection of melamine,[6,51] adenine,[49] theophylline,[48] primary and secondary amines[46-47] and carbon dioxide.[53] The sensors were prepared in various forms like films, hydrogels, metallic-organic crystals or electrodes and were able to detect molecules in solution, solid or gaz.

On the other hand, RF was utilized for the generation of tissue-engineered scaffolds, [55] the visualization of vascular grafts colonization by endothelial cells[54] and protein fiber cross-linking.[57-58] The obtained implants were biocompatible, biodegradable and non-toxic for the living cells, even at high concentrations. Moreover, due to the innate RF fluorescence such tissue-engineered platforms could be monitored in real time without additional imaging facilities.

Finally, RF-functionalized carbon nanotubes[8] and light-emitting hydrogels[60-61] employed optical and redox properties of RF and could be applied for the construction of future optoelectronic nanodevices.

Thus, RF and its derivatives open numerous opportunities in the field of nanotechnology and bioengineering (Figure 18). We hope that this review will inspire readers for future research in bioengineered RF constructs.

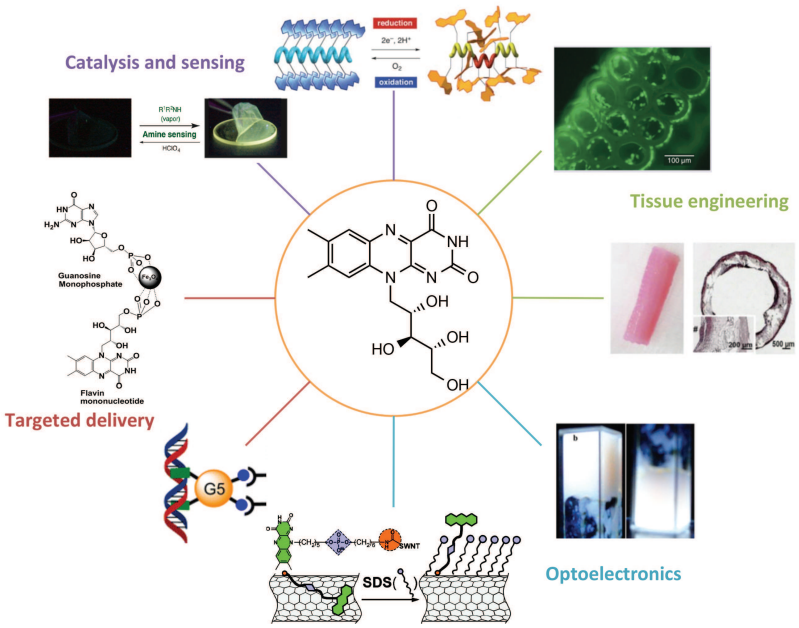

Figure 18. Examples of RF-functionalized biomaterials in various fields of nanotechnology.

Acknowledgments

This work was supported by the Ligue Nationale contre le cancer, the Initiative d'Excellence grant from University of Bordeaux, and by the Centre national de la recherche scientifique (CNRS). The authors gratefully acknowledge Dr. Jean Dessolin and Dr. Claude-Eric Roy for the manuscript reading and providing critical comments.

References

[1] H. J. Powers, 'Riboflavin (vitamin B-2) and health', *Am. J. Clin. Nutr.*, vol. 77, no. 6, pp. 1352–1360, Jun. 2003.

[2] M. Ashoori and A. Saedisomeolia, ‘Riboflavin (vitamin B2) and oxidative stress: a review’, *Br. J. Nutr.*, pp. 1–7, Mar. 2014.
[3] C. A. Northrop-Clewes and D. I. Thurnham, ‘The discovery and characterization of riboflavin’, *Ann. Nutr. Metab.*, vol. 61, no. 3, pp. 224–230, 2012.
[4] V. Massey, ‘The chemical and biological versatility of riboflavin’, *Biochem. Soc. Trans.*, vol. 28, no. 4, pp. 283–296, 2000.
[5] P. F. Heelis, ‘The photophysical and photochemical properties of flavins (isoalloxazines)’, *Chem. Soc. Rev.*, vol. 11, no. 1, pp. 15–39, Jan. 1982.
[6] S. Manna, A. Saha, and A. K. Nandi, ‘A two component thermoreversible hydrogel of riboflavin and melamine: Enhancement of photoluminescence in the gel form’, *Chem. Commun. Camb. Engl.*, no. 41, pp. 4285–4287, Nov. 2006.
[7] T. Senda, M. Senda, S. Kimura, and T. Ishida, ‘Redox control of protein conformation in flavoproteins’, *Antioxid. Redox Signal.*, vol. 11, no. 7, pp. 1741–1766, Jul. 2009.
[8] S.-Y. Ju and F. Papadimitrakopoulos, ‘Synthesis and redox behavior of flavin mononucleotide-functionalized single-walled carbon nanotubes’, *J. Am. Chem. Soc.*, vol. 130, no. 2, pp. 655–664, Jan. 2008.
[9] I. Yoon, J. Z. Li, and Y. K. Shim, ‘Advance in Photosensitizers and Light Delivery for Photodynamic Therapy’, *Clin. Endosc.*, vol. 46, no. 1, p. 7, 2013.
[10] D. R. Cardoso, S. H. Libardi, and L. H. Skibsted, ‘Riboflavin as a photosensitizer. Effects on human health and food quality’, *Food Funct.*, vol. 3, no. 5, pp. 487–502, May 2012.
[11] J. M. Grippa, A. de Zawadzki, A. B. Grossi, L. H. Skibsted, and D. R. Cardoso, ‘Riboflavin Photosensitized Oxidation of Myoglobin’, *J. Agric. Food Chem.*, vol. 62, no. 5, pp. 1153–1158, Feb. 2014.
[12] ‘Riboflavin. Monograph’, *Altern. Med. Rev. J. Clin. Ther.*, vol. 13, no. 4, pp. 334–340, Dec. 2008.
[13] W.-D. Lienhart, V. Gudipati, and P. Macheroux, ‘The human flavoproteome’, *Arch. Biochem. Biophys.*, vol. 535, no. 2, pp. 150–162, Jul. 2013.
[14] H. M. Said, ‘Intestinal absorption of water-soluble vitamins in health and disease’, *Biochem. J.*, vol. 437, no. 3, pp. 357–372, Aug. 2011.
[15] A. Yonezawa, S. Masuda, T. Katsura, and K. Inui, ‘Identification and functional characterization of a novel human and rat riboflavin transporter, RFT1’, *Am. J. Physiol. Cell Physiol.*, vol. 295, no. 3, pp. C632–641, Sep. 2008.
[16] S. Yamamoto, K. Inoue, K. Ohta, R. Fukatsu, J. Maeda, Y. Yoshida, and H. Yuasa, ‘Identification and functional characterization of rat riboflavin transporter 2’, *J. Biochem. (Tokyo)*, vol. 145, no. 4, pp. 437–443, Apr. 2009.
[17] Y. Yao, A. Yonezawa, H. Yoshimatsu, S. Masuda, T. Katsura, and K.-I. Inui, ‘Identification and comparative functional characterization of a new human riboflavin transporter hRFT3 expressed in the brain’, *J. Nutr.*, vol. 140, no. 7, pp. 1220–1226, Jul. 2010.
[18] A. Yonezawa and K. Inui, ‘Novel riboflavin transporter family RFVT/SLC52: identification, nomenclature, functional characterization and genetic diseases of RFVT/SLC52’, *Mol. Aspects Med.*, vol. 34, no. 2–3, pp. 693–701, Jun. 2013.
[19] M. Fujimura, S. Yamamoto, T. Murata, T. Yasujima, K. Inoue, K. Ohta, and H. Yuasa, ‘Functional characteristics of the human ortholog of riboflavin transporter 2 and riboflavin-responsive expression of its rat ortholog in the small intestine indicate its involvement in riboflavin absorption’, *J. Nutr.*, vol. 140, no. 10, pp. 1722–1727, Oct. 2010.
[20] A. B. Foraker, C. M. Khantwal, and P. W. Swaan, ‘Current perspectives on the cellular uptake and trafficking of riboflavin’, *Adv. Drug Deliv. Rev.*, vol. 55, no. 11, pp. 1467–1483, Nov. 2003.
[21] N. Vasudevan, U. Bahadur, and P. Kondaiah, ‘Characterization of chicken riboflavin carrier protein gene structure and promoter regulation by estrogen’, *J. Biosci.*, vol. 26, no. 1, pp. 39–46, Mar. 2001.
[22] M. L. Y. Bangaru and A. A. Karande, ‘Biochemical characterization of recombinant chicken Riboflavin carrier protein’, *Mol. Cell. Biochem.*, vol. 308, no. 1–2, pp. 1–7, Jan. 2008.
[23] H. L. Monaco, ‘Crystal structure of chicken riboflavin-binding protein.’, *EMBO J.*, vol. 16, no. 7, pp. 1475–1483, Apr. 1997.
[24] C. W. Mason, V. M. D’Souza, L. M. Bareford, M. A. Phelps, A. Ray, and P. W. Swaan, ‘Recognition, co-internalization, and recycling of an avian riboflavin carrier protein in human placental trophoblasts’, *J. Pharmacol. Exp. Ther.*, vol. 317, no. 2, pp. 465–472, May 2006.
[25] P. M. P D Prasad, ‘Isolation and characterization of riboflavin carrier protein from human amniotic fluid.’, *Biochem. Int.*, vol. 27, no. 3, pp. 385–95, 1992.
[26] I. Hassan, S. Chibber, and I. Naseem, ‘Vitamin B_2: a promising adjuvant in cisplatin based chemoradiotherapy by cellular redox management’, *Food Chem. Toxicol. Int. J. Publ. Br. Ind. Biol. Res. Assoc.*, vol. 59, pp. 715–723, Sep. 2013.
[27] A. H. Chaves Neto, K. J. Pelizzaro-Rocha, M. N. Fernandes, and C. V. Ferreira-Halder, ‘Antitumor activity of irradiated riboflavin on human renal carcinoma cell line 786-O’, *Tumour Biol. J. Int. Soc.*

Oncodevelopmental Biol. Med., Oct. 2014.
[28] M. A. Muñoz, A. Pacheco, M. I. Becker, E. Silva, R. Ebensperger, A. M. Garcia, A. E. D. Ioannes, and A. M. Edwards, 'Different cell death mechanisms are induced by a hydrophobic flavin in human tumor cells after visible light irradiation', *J. Photochem. Photobiol. B*, vol. 103, no. 1, pp. 57–67, Apr. 2011.
[29] V. G. Premkumar, S. Yuvaraj, S. Sathish, P. Shanthi, and P. Sachdanandam, 'Anti-angiogenic potential of CoenzymeQ10, riboflavin and niacin in breast cancer patients undergoing tamoxifen therapy', *Vascul. Pharmacol.*, vol. 48, no. 4–6, pp. 191–201, Jun. 2008.
[30] Z. Xuan, Y. An, D. Yang, S. Wang, Q. Xu, and S. Yuan, 'Exploration of the protection of riboflavin laurate on oral mucositis induced by chemotherapy or radiotherapy at the cellular level: what is the leading contributor?', *Int. J. Mol. Sci.*, vol. 14, no. 3, pp. 4722–4733, 2013.
[31] C. J. Key, C. J. Koh, and B. K. Cho, 'Oral Riboflavine Tetrabutyrate Therapy for Psoriasis', *Korean J. Dermatol.*, vol. 17, no. 2, pp. 117–121, Apr. 1979.
[32] R. S. Rivlin, 'Riboflavin and cancer: a review', *Cancer Res.*, vol. 33, no. 9, pp. 1977–1986, 1973.
[33] A. A. Karande, L. Sridhar, K. S. Gopinath, and P. R. Adiga, 'Riboflavin carrier protein: a serum and tissue marker for breast carcinoma', *Int. J. Cancer J. Int. Cancer*, vol. 95, no. 5, pp. 277–281, Sep. 2001.
[34] P. N. Rao, E. Levine, M. O. Myers, V. Prakash, J. Watson, A. Stolier, J. J. Kopicko, P. Kissinger, S. G. Raj, and M. H. Raj, 'Elevation of serum riboflavin carrier protein in breast cancer', *Cancer Epidemiol. Biomark. Prev. Publ. Am. Assoc. Cancer Res. Cosponsored Am. Soc. Prev. Oncol.*, vol. 8, no. 11, pp. 985–990, Nov. 1999.
[35] T. Johnson, A. Ouhtit, R. Gaur, A. Fernando, P. Schwarzenberger, J. Su, M. F. Ismail, H. I. El-Sayyad, A. Karande, Z. A. Elmageed, P. Rao, and M. Raj, 'Biochemical characterization of riboflavin carrier protein (RCP) in prostate cancer', *Front. Biosci. Landmark Ed.*, vol. 14, pp. 3634–3640, 2009.
[36] P. N. Rao, J. Crippin, E. Levine, J. Hunt, S. Baliga, L. Balart, L. Anthony, M. Mulekar, and M. H. G. Raj, 'Elevation of serum riboflavin carrier protein in hepatocellular carcinoma', *Hepatol. Res. Off. J. Jpn. Soc. Hepatol.*, vol. 35, no. 2, pp. 83–87, Jun. 2006.
[37] S. R. Holladay, Z. Yang, M. D. Kennedy, C. P. Leamon, R. J. Lee, M. Jayamani, T. Mason, and P. S. Low, 'Riboflavin-mediated delivery of a macromolecule into cultured human cells', *Biochim. Biophys. Acta*, vol. 1426, no. 1, pp. 195–204, Jan. 1999.
[38] F. Marlin, P. Simon, S. Bonneau, P. Alberti, C. Cordier, C. Boix, L. Perrouault, A. Fossey, T. Saison-Behmoaras, M. Fontecave, and C. Giovannangeli, 'Flavin Conjugates for Delivery of Peptide Nucleic Acids', *ChemBioChem*, vol. 13, no. 17, pp. 2593–2598, Nov. 2012.
[39] T. P. Thomas, S. K. Choi, M.-H. Li, A. Kotlyar, and J. R. Baker, 'Design of riboflavin-presenting PAMAM dendrimers as a new nanoplatform for cancer-targeted delivery', *Bioorg. Med. Chem. Lett.*, vol. 20, no. 17, pp. 5191–5194, Sep. 2010.
[40] A. B. Witte, C. M. Timmer, J. J. Gam, S. K. Choi, M. M. Banaszak Holl, B. G. Orr, J. R. Baker, and K. Sinniah, 'Biophysical characterization of a riboflavin-conjugated dendrimer platform for targeted drug delivery', *Biomacromolecules*, vol. 13, no. 2, pp. 507–516, Feb. 2012.
[41] A. B. Witte, A. N. Leistra, P. T. Wong, S. Bharathi, K. Refior, P. Smith, O. Kaso, K. Sinniah, and S. K. Choi, 'Atomic Force Microscopy Probing of Receptor–Nanoparticle Interactions for Riboflavin Receptor Targeted Gold–Dendrimer Nanocomposites', *J. Phys. Chem. B*, vol. 118, no. 11, pp. 2872–2882, Mar. 2014.
[42] J. Jayapaul, S. Arns, W. Lederle, T. Lammers, P. Comba, J. Gätjens, and F. Kiessling, 'Riboflavin carrier protein-targeted fluorescent USPIO for the assessment of vascular metabolism in tumors', *Biomaterials*, vol. 33, no. 34, pp. 8822–8829, Dec. 2012.
[43] J. Jayapaul, M. Hodenius, S. Arns, W. Lederle, T. Lammers, P. Comba, F. Kiessling, and J. Gaetjens, 'FMN-coated fluorescent iron oxide nanoparticles for RCP-mediated targeting and labeling of metabolically active cancer and endothelial cells', *Biomaterials*, vol. 32, no. 25, pp. 5863–5871, Sep. 2011.
[44] P. T. Wong, K. Tang, A. Coulter, S. Tang, J. R. Baker, and S. K. Choi, 'Multivalent Dendrimer Vectors with DNA Intercalation Motifs for Gene Delivery', *Biomacromolecules*, vol. 15, no. 11, pp. 4134–4145, Nov. 2014.
[45] H. Iida, T. Mizoguchi, S.-D. Oh, and E. Yashima, 'Redox-triggered switching of helical chirality of poly(phenylacetylene)s bearing riboflavin pendants', *Polym. Chem.*, vol. 1, no. 6, pp. 841–848, Jul. 2010.
[46] H. Iida, S. Iwahana, T. Mizoguchi, and E. Yashima, 'Main-Chain Optically Active Riboflavin Polymer for Asymmetric Catalysis and Its Vapochromic Behavior', *J. Am. Chem. Soc.*, vol. 134, no. 36, pp. 15103–15113, Sep. 2012.
[47] H. Iida, M. Miki, S. Iwahana, and E. Yashima, 'Riboflavin-based fluorogenic sensor for chemo- and enantioselective detection of amine vapors', *Chem. Weinh. Bergstr. Ger.*, vol. 20, no. 15, pp. 4257–4262, Apr. 2014.
[48] Y. Sato, Y. Zhang, S. Nishizawa, T. Seino, K. Nakamura, M. Li, and N. Teramae, 'Competitive assay for theophylline based on an abasic site-containing DNA duplex aptamer and a fluorescent ligand', *Chem. Weinh. Bergstr. Ger.*, vol. 18, no. 40, pp. 12719–12724, Oct. 2012.
[49] N. B. Sankaran, S. Nishizawa, T. Seino, K. Yoshimoto, and N. Teramae, 'Abasic-Site-Containing

Oligodeoxynucleotides as Aptamers for Riboflavin', *Angew. Chem. Int. Ed.*, vol. 45, no. 10, pp. 1563–1568, Feb. 2006.
[50] Y. Pang, Z. Xu, Y. Sato, S. Nishizawa, and N. Teramae, 'Base pairing at the abasic site in DNA duplexes and its application in adenosine aptasensors', *Chembiochem Eur. J. Chem. Biol.*, vol. 13, no. 3, pp. 436–442, Feb. 2012.
[51] T. Lee, M. H. Tsai, and H. L. Lee, 'Riboflavin Chelated Luminescent Metal–Organic Framework: Identified by Liquid-Assisted Grinding for Large-Molecule Sensing via Chromaticity Coordinates', *Cryst. Growth Des.*, vol. 12, no. 6, pp. 3181–3190, Jun. 2012.
[52] A. Saha, S. Manna, and A. K. Nandi, 'A mechanistic approach on the self-organization of the two-component thermoreversible hydrogel of riboflavin and melamine', *Langmuir ACS J. Surf. Colloids*, vol. 23, no. 26, pp. 13126–13135, Dec. 2007.
[53] J. E. Halls, S. E. C. Dale, and F. Marken, 'Nano-TiO(2)-flavin adenine dinucleotide film redox processes in contact to humidified gas | salt electrolyte', *Bioelectrochemistry Amst. Neth.*, vol. 86, pp. 54–59, Aug. 2012.
[54] M. E. Mertens, J. Frese, D. A. Bölükbas, L. Hrdlicka, S. Golombek, S. Koch, P. Mela, S. Jockenhövel, F. Kiessling, and T. Lammers, 'FMN-coated fluorescent USPIO for cell labeling and non-invasive MR imaging in tissue engineering', *Theranostics*, vol. 4, no. 10, pp. 1002–1013, 2014.
[55] A. K. Nguyen, S. D. Gittard, A. Koroleva, S. Schlie, A. Gaidukeviciute, B. N. Chichkov, and R. J. Narayan, 'Two-photon polymerization of polyethylene glycol diacrylate scaffolds with riboflavin and triethanolamine used as a water-soluble photoinitiator', *Regen. Med.*, vol. 8, no. 6, pp. 725–738, Nov. 2013.
[56] E. Chan, G. R. Snibson, and L. Sullivan, 'Treatment of infectious keratitis with riboflavin and ultraviolet-A irradiation', *J. Cataract Refract. Surg.*, vol. 40, no. 11, pp. 1919–1925, Nov. 2014.
[57] F. Raiskup and E. Spoerl, 'Corneal crosslinking with riboflavin and ultraviolet A. I. Principles', *Ocul. Surf.*, vol. 11, no. 2, pp. 65–74, Apr. 2013.
[58] R. Sridhar, K. Madhaiyan, S. Sundarrajan, A. Góra, J. R. Venugopal, and S. Ramakrishna, 'Cross-linking of protein scaffolds for therapeutic applications: PCL nanofibers delivering riboflavin for protein cross-linking', *J. Mater. Chem. B*, vol. 2, no. 12, pp. 1626–1633, Feb. 2014.
[59] P. Bairi, P. Chakraborty, S. Mondal, B. Roy, and A. K. Nandi, 'A thixotropic supramolecular hydrogel of adenine and riboflavin-5'-phosphate sodium salt showing enhanced fluorescence properties', *Soft Matter*, vol. 10, no. 28, pp. 5114–5120, Jul. 2014.
[60] P. Bairi, B. Roy, P. Chakraborty, and A. K. Nandi, 'Co-assembled white-light-emitting hydrogel of melamine', *ACS Appl. Mater. Interfaces*, vol. 5, no. 12, pp. 5478–5485, Jun. 2013.
[61] P. Bairi, B. Roy, and A. K. Nandi, 'A light harvesting Bi-component hydrogel with a riboflavin acceptor', *Chem. Commun.*, vol. 48, no. 88, pp. 10850–10852, Oct. 2012.

1.4 Aims of the present study

RF is an essential vitamin for humans and its derivatives (FMN and FAD) participate in fundamental physiological events including energetic process, lipid metabolism, vitamin synthesis.[97] From a chemical point of view, RF is composed of a D-ribitol chain and an isoalloxazine moiety responsible for electronic and optoelectronic properties.[98] As discussed in the review, due to these unique features RF represents a particular interest in the field of nanotechnologies. So far, RF was utilised in the construction or functionalisation of various nanosystems such as dendrimers,[99] polymeric helices,[100] hydrogels,[101,102] iron oxide nanoparticles,[103–105] carbon nanotubes[106] and metal-organic frameworks.[107]

On the other hand, several preclinical studies utilise RF in the development of various targeted drug delivery systems because of the presence of specific RF transporters. Such transporters were shown upregulated in certain types of cancer (prostate,[108] breast cancer[109] and hepatocellular carcinoma[110]) and angiogenic endothelium.[103] The ability to target both cancerous cells and tumour-supplying blood vessels makes RF a very promising delivery agent for cancer treatment.[103]

To date, little is known about the RF amphiphile derivatives and their potential auto-assemblies. For instance, RF laurate, also described in the review, is utilised in suspensions, but there is no evidence of its auto-organisation in aqueous solvents alone. RF laurate is mostly employed together with oils[111] and surfactants[112] allowing sustained RF release after injection. Very recently, a patent describing gel-forming RF-polysaccharide conjugate appeared.[113] The corresponding amphiphilic polymer forms a nanogel in water and due to the presence of several hydrophobic RF units (RF tetrabutyrate) is able to physically capture various drugs such as antibiotics or cytostatics (hydrophobic interactions).

Even though these applications of RF appear promising, we believe small molecule RF amphiphiles (RFA) and their auto-assemblies could bring new insights to the drug delivery field. Due to potential hydrophobic, electrostatic and π-stacking interactions RFA could build auto-organised nanosystems with various architectures such as micelles, vesicles or liquid crystalline phases. The formed nanosystems could benefit from the RF physicochemical properties like fluorescence, redox potential and photosensitizing. Otherwise, RFA could also provide tumour targeting potential if inserted into existing nanosystems.

Thus, the first aim of this project is to design, synthesise and study new RFA and their auto-assemblies. The second aim will be to utilise the selected RFA as a tool for functionalisation of conventional drug delivery systems to render them tumour-specific. The general strategy of the study is presented on Figure 1.20.

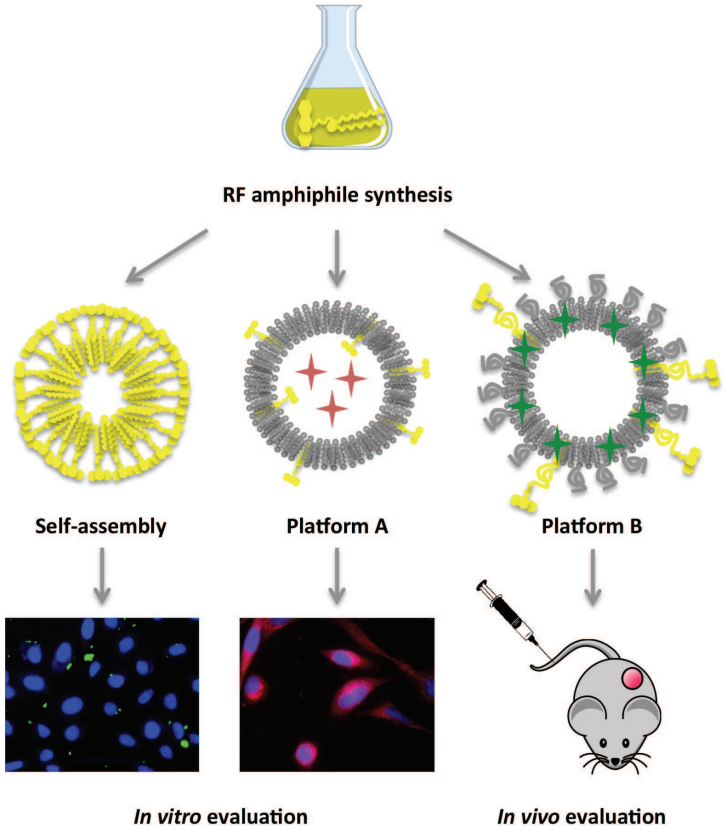

Figure 1.20 General strategy

The corresponding RF-functionalised nanosystems will be divided into three groups: RFA self-assemblies, Platform A – designated mainly for the proof of concept and *in vitro* studies of and Platform B – aimed to study RF targeted delivery *in vivo*. Consequently, the results section will be divided into four chapters, including RFA synthesis, study of its self-assemblies, implementation and optimisation of two RFA-functionalised platforms and their biological evaluation.

RFA auto-assemblies will be studied by theoretical and several experimental approaches (NMR, DLS, Cryo-EM). Their ability to enter cells will be also investigated *in vitro*. In contrast, for the preparation of Platform A only small amount of RFA will be utilised. As discussed earlier, only 1% molar of targeting ligand is sufficient to ensure proper recognition of nanosystem by a corresponding receptor. Thus, 1% of RFA will be inserted into simple liposome formulation to test its targeting potential towards various cell lines of metabolically active cells. A fluorescent dye will be encapsulated in the Platform A as a model drug and for cell uptake monitoring.

The composition of Platform B will be more adapted to *in vivo* conditions – it should be long-circulating (covered with hydrophilic polymer shield), stable and labelled for the detection in the therapeutic near-infrared window. For this reason the platform composition will be optimised and RFA owing a polymeric spacer will be synthesised. The targeting efficiency and pharmacokinetics of Platform B will be studied *in vitro* and *in vivo*.

2 Chapter II. Synthesis of RF amphiphiles

2.1 Strategy and design

The particular physicochemical properties of RF such as photosensitising, fluorescence and redox potential make it promising molecule for developing responsive drug delivery systems. Moreover, RF is transported into cells with specific proteins overexpressed in certain types of cancer.[109,110,114,115]

Few research groups have already attempted the utilisation of RF in drug delivery[116–119] and imaging[103,104] nanosystems. These systems were based on covalent bonds[116–119] or electrostatic interactions.[103,104] However, except RF-laurate oral emulsions,[111] little is known about RFA and their auto-organisation. Due to the simplicity and high versatility of auto-assembled systems the preparation of RFA and study of their supramolecular structures are of great interest.

Thus, in this section we will look for a simple and efficient synthetic strategy for the RFA preparation. Due to its many functional groups and solubility in water, RF is a challenging molecule for chemical reactions. Hence, various synthetic routes were tested and the optimisation of reaction conditions was required.

As we have already seen in the introduction section, the amphiphile chemistry has a direct impact on its potential self-assemblies. Thus, for the preparation of an amphiphile it is important to consider certain hydrophilic/hydrophobic balance in the molecule. Due to its chemical structure, RF already has inherent amphiphile properties – the isoalloxazine ring responsible for hydrophobicity and the ribitol chain responsible for hydrophilicity. However, the molecule is not known to form any auto-assemblies.

Taking into account that RF is a water-soluble vitamin that displays four free alcohol groups in the ribitol chain, we decided in a first strategy to enhance its hydrophobicity. For this purpose we planned to add alkyl chains of different length and in various positions of the molecule. The choice of lipid chains was based on their transition temperature. Thus, we selected simple alkyl chains with 12, 16 and 18 carbons and double chains with 14 carbons. The derivative with perfluorocarbon chain (10 carbons) was also prepared. On the other hand, the hydrophilicity enhancement by adding a charged phosphate group in the terminal position of the ribitol chain was also envisaged. The general strategies for RFA design are depicted on Figure 2.1.

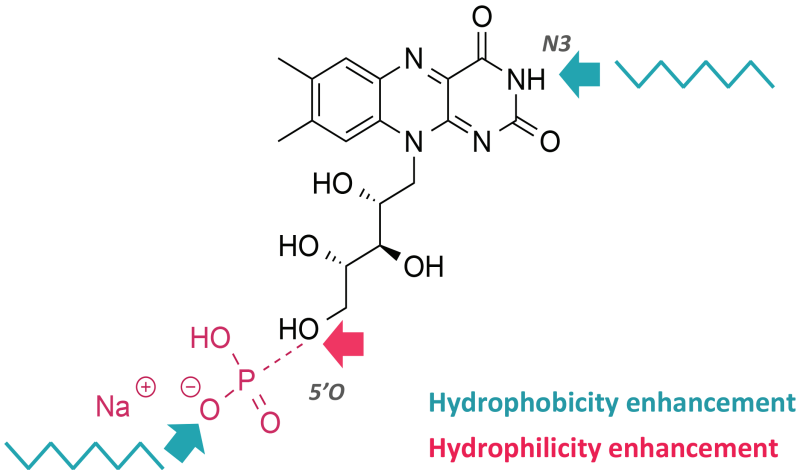

Figure 2.1 General strategies for RFA preparation.

Thanks to its chemistry, RF possesses several chemical groups accessible for functionalisation like the amine group of the ureido moiety of the isoalloxazine ring (N3 position) or the primary alcohol of the ribitol chain (5'O position). However, the modification of one or another position could have consequences on the RF interactions with its transporter proteins. As we already mentioned in the introduction section (1.3 Riboflavin and its potential in health technologies), mammals have specific transporter system for RF and derivatives. This system includes plasma RF carrier protein (RCP)[115] and a family of membrane proteins (SLC52).[120] The latter consists of three transmembrane proteins, which were recently discovered and their crystal structure is not yet resolved.

In contrast, the co-crystallisation of RCP with RF revealed π-stacking interactions between isoalloxazine ring and aromatic amino acid residues (Tyr75 and Trp156) of the protein.[121] Moreover, there are several possible hydrogen bonds between oxygen and nitrogen of the ureido group and ribitol chain hydroxyls with nearby amino acid residues. Even though, the chemical modification of RF could lead to the loss of some of these interactions, it will be still recognised by the RCP. In 2011 Witte A. *et al.*[99] performed an analytical screening of the affinity between RCP and various RF-dendrimer conjugates. Here RF was conjugated to a dendrimer platform in N3 or 5'O positions. The binding affinity to RCP was determined in a cell free solution with the help of isothermal titration calorimetry (ITC) and differential scanning calorimetry (DSC). Both techniques revealed a significant decrease in the RCP affinity towards RF-dendrimer conjugates compared to free RF. The N3 conjugates displayed greater binding affinity in comparison to 5'O series. Although, 5'O position seems to be less advantageous, the efficient cell internalisation was reported for several 5'O conjugates.[117,119] Taking into account all these data, we decided to explore both positions for the preparation of our RFA derivatives (Figure 2.1).

Additionally, we synthesised an RFA with a polymeric spacer between RF and lipid, which will be suitable for the *in vivo* investigations. This derivative was planned to serve for the preparation of long-circulating RF-functionalised platform. As polyethylene glycol (PEG) is a classically used approach for the surface coating in long-circulating liposome design, we decided to use it as a spacer between RF and lipid.

PEG (CAS number 25322-68-3) is a linear polyether diol widely employed in

biomedical applications due to its biocompatibility, solubility in aqueous and organic media, lack of toxicity, very low immunogenicity and antigenicity, and good excretion kinetics.[33] Moreover, the molecular weight and structure of PEG can be varied for specific purposes. To date, several polymer-lipid conjugates are commercially available. In addition, these conjugates may possess various active groups for easy chemical coupling. Therefore, we conjugated RF with a commercially available PEGylated lipid derivative (Figure 2.2).

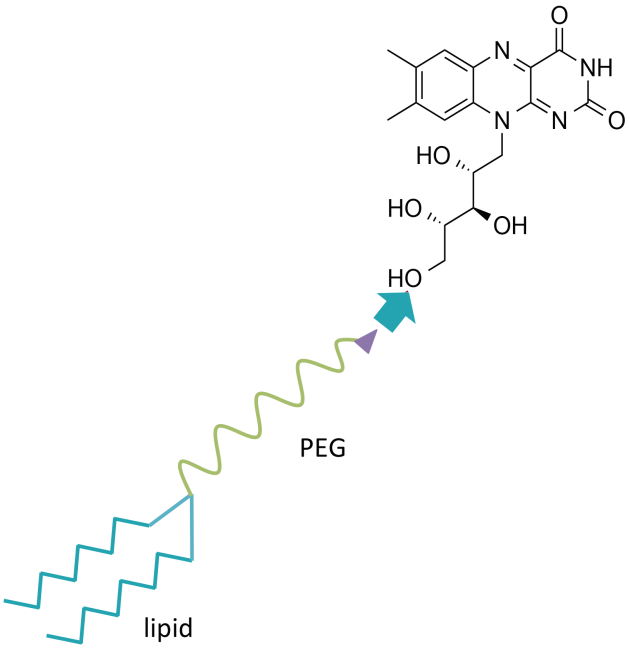

Figure 2.2 Strategy for PEGylated RFA preparation.

2.2 N3-RFA derivatives

For the preparation of N3-RFAs we chose click chemistry reaction and in particular Huisgen reaction catalysed with copper. This reaction belongs to the 1,3-dipolar cycloaddition group. It induces the formation of a triazole ring, which could potentially add supplementary stacking interactions beneficial for self-assembly formation.

The concept of click chemistry, introduced by B. Sharpless in 2001,[122] is very convenient for biomolecules preparation due to its generally high yields, simple reaction conditions, little amount of side products, possibility to work without protective groups and final purification. Huisgen reaction is one of on the most widely used among the variety of click chemistry reactions. It consisted in coupling between alkyne and azide moieties catalysed by copper (I) and subsequent generation of 1,3-triazole. The scheme of Huisgen cycloaddition is presented on Scheme 2.1.

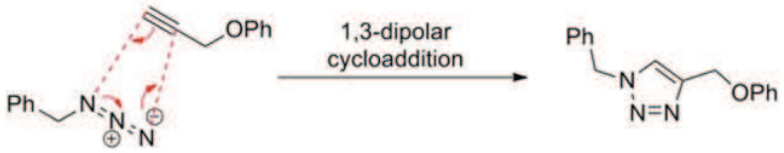

Scheme 2.1 Scheme of Huisgen reaction.

There are several methods to ensure Cu (I) ions in the reaction solution. One of them consists of *in situ* reduction of Cu (II) salts in the presence of a reducing agent (i.e. sodium ascorbate). Although, RF itself was shown[123] to act as reducing agent to Cu (II) upon irradiation at 420 nm, we decided to use Cu (I) in our strategy.

Thus we decided to functionalise RF in N3 position with an alkyne moiety and various single lipid chains with an azide moiety (Scheme 2.2). RF-alkyne was prepared by nucleophilic substitution of N3 nitrogen by a propargyl group. Normally, for this step OH-groups of the ribitol chain do not need to be protected. However, it was decided to protect them by acetate esters in order to increase the RF solubility in organic solvents.

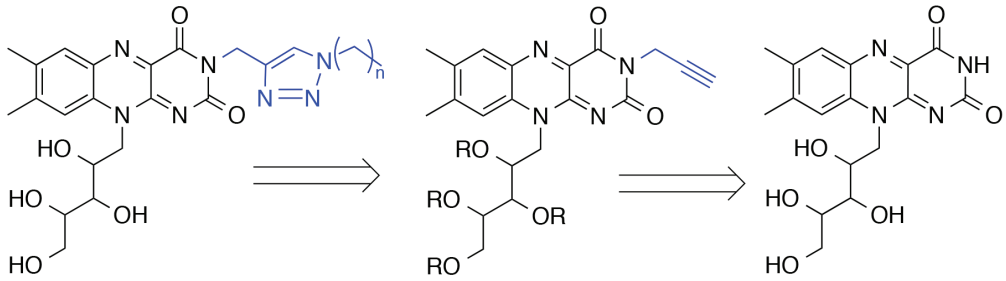

Scheme 2.2 Retrosynthetic scheme of N3-RFA preparation.

For hydroxyl protection, RF was solubilised in a solution of acetic acid and acetic anhydride in presence of a catalytic amount of perchloric acid[124] and product **1** was obtained with 95% yield (Scheme 2.3). Next, the peracetylated RF (**1**) was submitted to a nucleophillic substitution reaction with propargyl bromide in presence of 1,8-diazabicycloundec-7-ene (DBU), which was used for amine deprotonation.[100] The RF-alkyne (**2**) was obtained with an excellent yield of 94 % (Scheme 2.3).

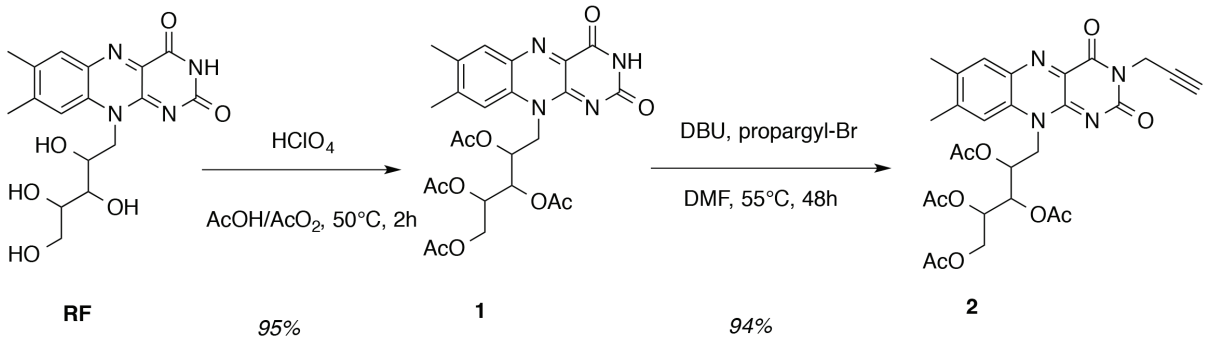

Scheme 2.3 Synthesis of RF-alkyne.

As hydrophobic part, it was decided to utilise lipids with various chain length in order to find appropriate hydrophobic/hydrophilic balance. Therefore, linear, saturated carbohydrates with C18, C16 and C12 carbons were selected as well as perfluorocarbon chain with C10 carbons (CF). The azide derivatives, required for the click chemistry reaction, were prepared from the corresponding halogenated (Br or I) lipid chains after nucleophilic substitution with sodium azide. The expected compounds C18-N_3 (3a), C16-N_3 (3b), C12-N_3 (3c) and CF-N_3 (3d) were obtained with good yields (Scheme 2.4).

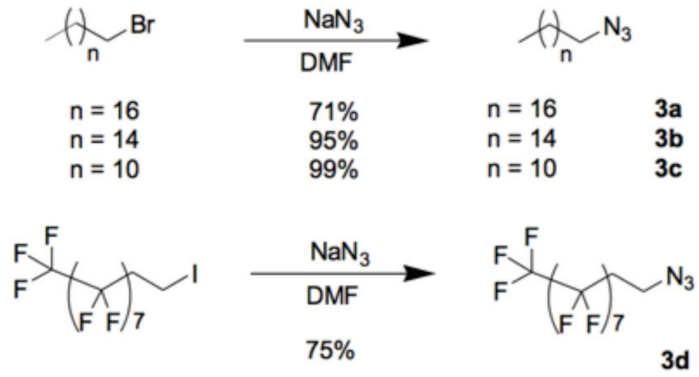

Scheme 2.4 Preparation of various lipid azides.

The prepared derivatives were used in the click chemistry reaction. For this purpose, the different lipid azides **3a-d** were reacted with RF-alkyne **2** in presence of copper iodide (CuI)[125] (Scheme 2.5). The reaction was quite fast (3h), but needed the heating up to 80°C. The fully protected RFAs – **4a**, **4b**, **4c** and **4d** were obtained with rather good yields (50, 66, 47 and 47 % respectively).

The final cleavage of the acetate protective groups from ribitol (**4a-4d)** induced by sodium methoxide in methanol yielded the desired compounds 5a, 5b, 5c and 5d with the following yields – 82 %, 100 %, 70 % and 39 %.

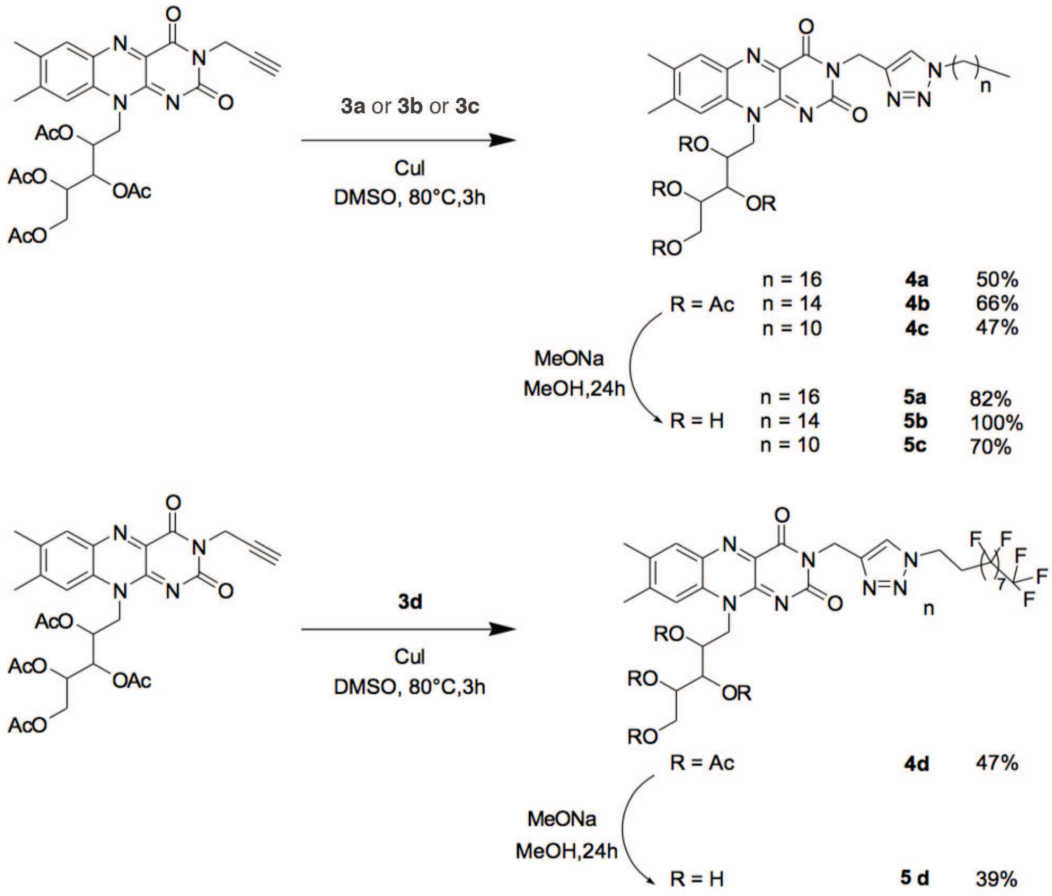

Scheme 2.5 N3-RFA synthesis.

In summary, four novel RFAs with various lipid chains at N3 position of isoalloxazine ring were synthesised in 4 steps with good yields. However, all prepared molecules were almost insoluble in water and poorly soluble in alcohols like methanol and ethanol. These results suggest that the hydrophobic part was predominant in all molecules and that free hydroxyls of the ribitol chain do not provide enough hydrophilicity. In order to improve the hydrophilicity, the addition of an ionised chemical function such as a carboxylate or phosphate is necessary.

2.3 5'O-RFA derivatives

The natural phosphorylated derivative of RF – FMN is 300 times more water-soluble than RF (30 g/L for FMN and 0,1 g/L for RF). Thus, the attachment of a lipid to the RF through the phosphodiester bond would enhance both hydrophilic and hydrophobic behaviours of the molecule. Moreover, this modification leads to RF-phospholipid derivative, which displays similarities with conventional phospholipids able to form auto-assemblies such as micelles, liposomes and liquid crystalline phases.

Concerning the phosphodiester coupling, we decided to use phosphoramidite chemistry, which is generally employed in nucleic acid synthesis. This reaction occurs between a phosphoramidite and hydroxyl moieties. The mechanism of the phosphodiester bond formation is depicted in Scheme 2.6. First, phophoramidite is mixed with an activator (tetrazole or derivative) leading to the protonation of its diisopropylamidite. This leaving group is rapidly displaced by attack of the hydroxyl group and a new phosphorus-oxygen bond is formed, creating a phosphite triester. Next, the formed unstable phosphite triester (P (III)) is converted into a stable phosphate group (P (V)) by iodine oxidation in presence of water and pyridine.[126]

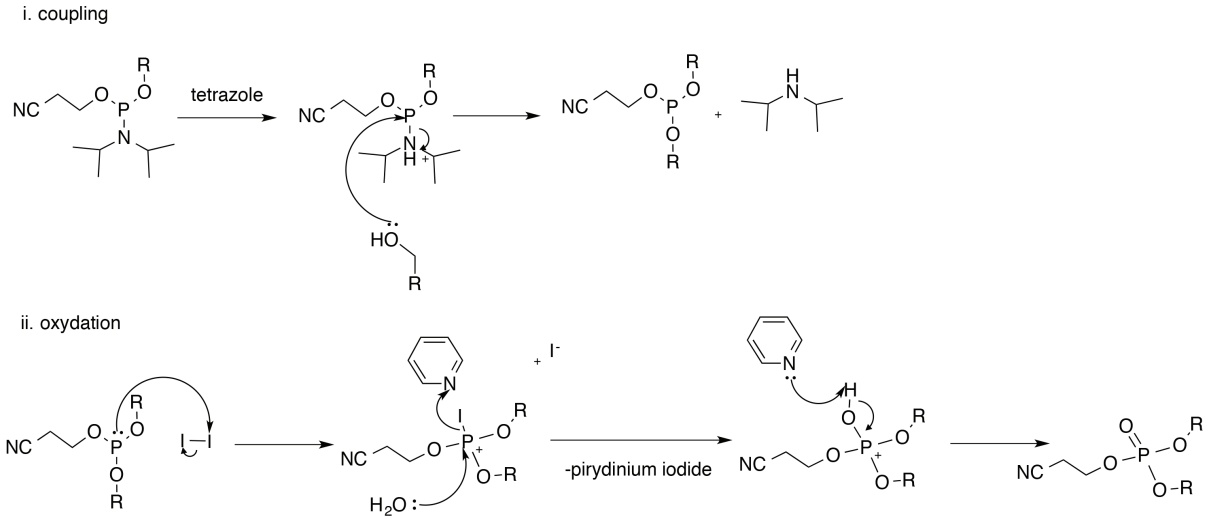

Scheme 2.6 Mechanism of phosphodiester formation.

Hence, 5'O-RFA phosphoramidite was prepared from natural RF and then reacted with a lipid owning free hydroxyl group. The synthesis of a RF-derived phospholipid was envisioned according to the general retrosynthetic strategy depicted in Scheme 2.7.

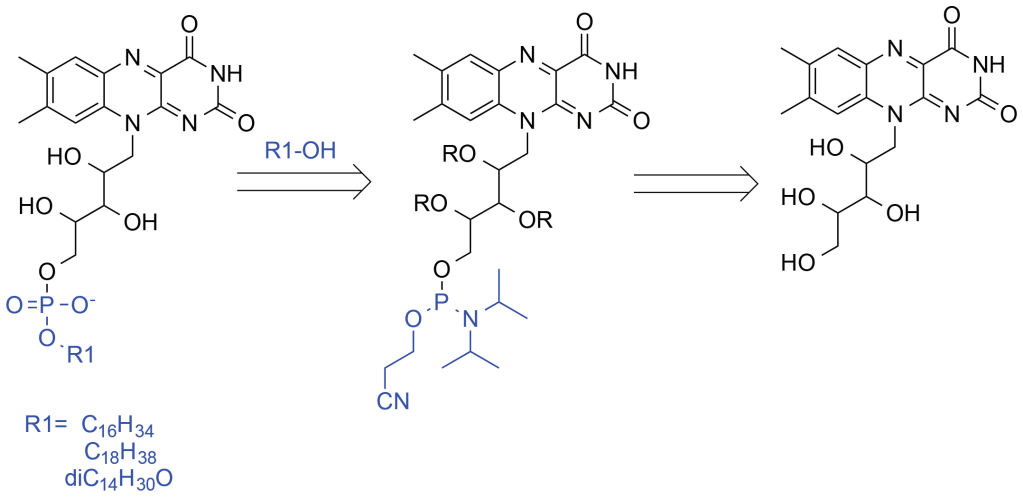

Scheme 2.7 Retrosynthetic scheme of 5'O-RFA preparation.

RF-phosphoramidite was prepared from natural RF in four steps (Scheme 2.8). First of all, a selective protection of the ribitol chain primary alcohol by a dimethoxytrityl group (DMT) was realised. For that purpose, RF was solubilised in dry pyridine and 4,4′-dimethoxytriphenylmethyl chloride, 4-dimethylaminopirydine (DMAP) and triethylamine (TEA) were added.[127] The product **6** was obtained with moderate (35 %) yield mostly due to the poor solubility of RF in pyridine. Next, secondary alcohols were protected through acetate ester groups. This was achieved by dissolving compound **6** in dry pyridine and by addition of 40 equivalents of acetate anhydride. The fully protected RF (compound **7**) was obtained with good yield (90 %). Then DMT group was rapidly cleaved by the treatment with zinc bromide in nitromethane during 20 min to liberate the ribitol primary alcohol. The released DMT-Br was removed by precipitation of the product in ice-cold diethyl ether and subsequent filtration.[127] Finally, RF-phosphoramidite was prepared from compound **8** after a reaction with 2-cyanoethyl-N,N,-diisopropylchlorophosphoramidite in presence of N,N-Diisopropylethylamine (Hünig's base). The formation of desired compound **9** was confirmed by ^{31}P-NMR and mass spectrometry. This highly reactive product was utilised for the next step without purification.

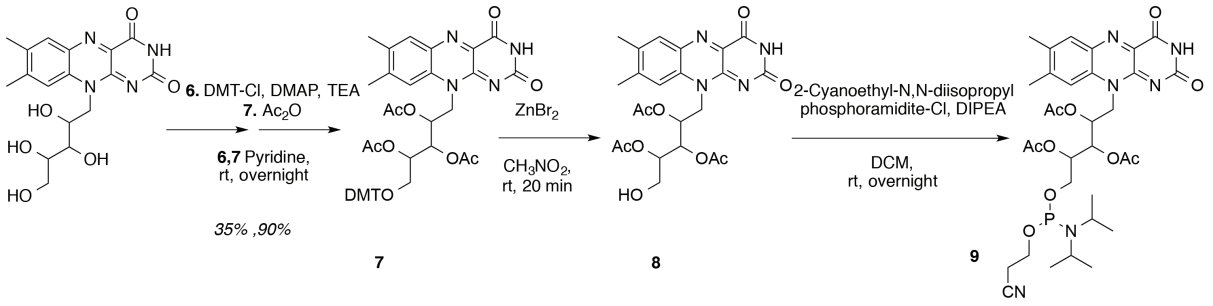

Scheme 2.8 RF-phosphoramidite preparation.

With regard to the choice of the lipid chains, in principle, any free-hydroxyl containing lipid could be coupled with RF-phosphoramidite. In our first trials we utilised single-chain saturated fatty alcohols (palmitoyl – C16-OH and stearyl – C18-OH). The phosphodiester bond formation between RF-phosphoramidite and single chain alcohols was

confirmed by ^{31}P-NMR, but the products were difficult to purify due to high polarity. Thus, we decided to enhance its hydrophobic character by using the double-chain glycerol derivatives instead of single chain. Double chain glyceroester lipids are commercially available; nevertheless they were not adapted to our strategy. Indeed, the final deprotection reaction in our synthetic route will also lead to the cleavage of ester moieties in the lipid. Thus, we prepared an ether glycerol derivative with double myristoyl (C14) chains. The lipid chain length was chosen according to its transition temperature (Tm). For double myristoyl glycerophospholipids Tm is near to the room temperature (23°C) and is easier to manipulate.

Thus 1,2-dimyristoyl-glycerol was prepared from (S)-(+)-1,2-Isopropylideneglycerol (solketal) in four steps (Scheme 2.9). First, the free hydroxyl of solketal (+) was protected with paramethoxyphenol group in the Mitsunobu reaction. For this purpose solketal was dissolved in toluene with paramethoxyphenol (PMP), triphenylphosphine and diethylazodicarboxylate (DEAD). The desired product **10** was obtained with an excellent yield (94 %). Then, an acidic DOWEX resin was used in methanol to cleave the isopropylidene acetal protective group and liberate two hydroxyls. The reaction yielded compound **11,** which did not require further purification. In the next step myristoyl chains were coupled to PMP-glycerol (**11**) by a nucleophilic substitution reaction. Compound **11** was first mixed with a suspension of NaH in anhydrous DMF for 30 min and then bromotetradecan was added to the reaction mixture. The required product **12** was obtained with a good yield of 74%. The PMP removal from the hydroxyl group was achieved with the help of cerium ammonium nitrate (CAN) in acetonitrile/water (80:20) mixture with 61% yield (compound **13**).

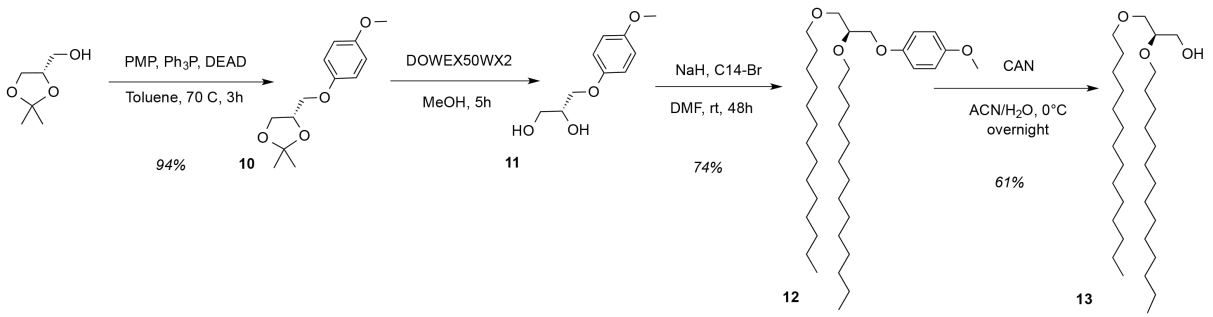

Scheme 2.9 Synthesis of 1,2-dimyristoyl-glycerol.

The phosphodiester coupling between RF-phosphoramidite (**9**) and glycerolipid (**13**) occurred in dry THF with 5-Benzylthio-1H-tetrazole as catalyser (Scheme 2.10). When the appearance of the phosphite triester was confirmed by TLC and ^{31}P NMR, the oxidizing solution (0.2 M iodine in THF/Pyridine/H_2O (2:1:1)) was added to the reaction mixture. The desired compound **14** – a fully protected 5'O-RFA was obtained with 30% yield (for 3 steps). Final cleavage of acetate and cyanoethyl protective groups with the help of sodium methanoate in methanol generated the 5'O-dimyristoyl-phosphoriboflavin abbreviated **RfdiC14** (compound **15**).

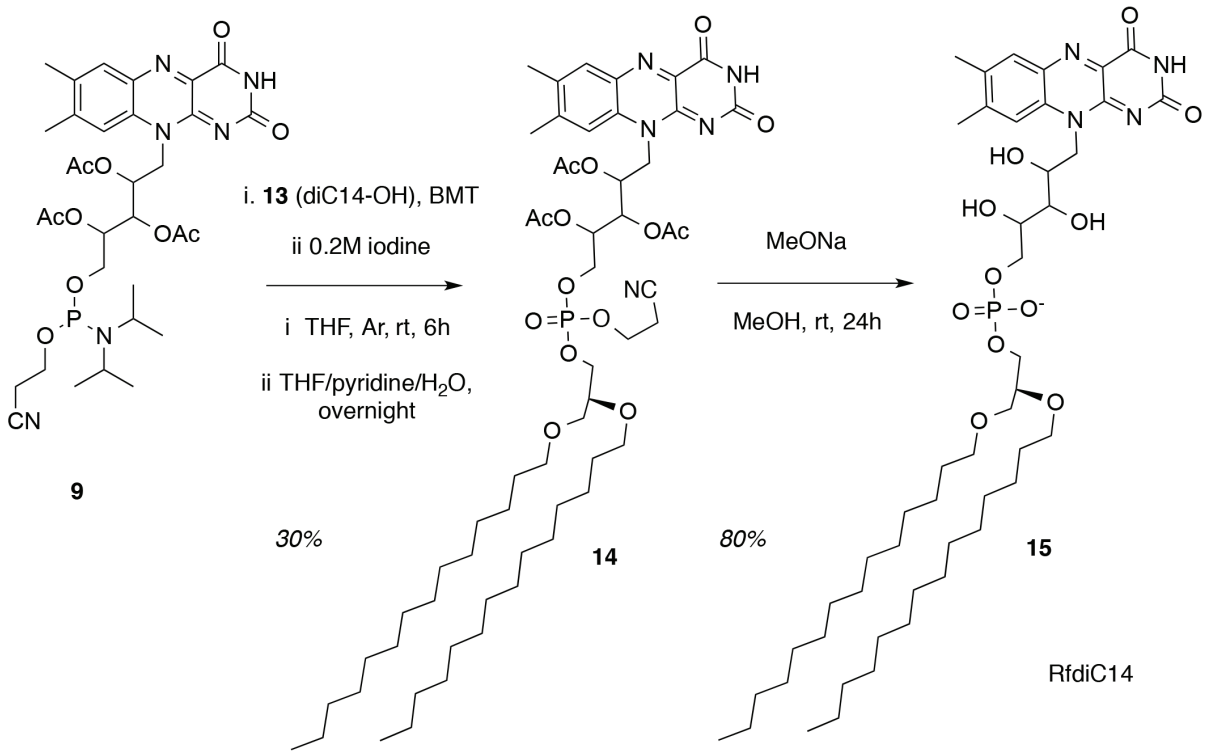

Scheme 2.10 5' O-RFA synthesis.

The obtained amphiphile RfdiC14 displayed good solubility in dichloromethane, chloroform, methanol, ethanol and moderate solubility in water (forming cloudy solution). This might suggest the potential auto-assemblies of RfdiC14, which were studied within the next section.

2.4 5'O-RFA PEGylated derivative

For further *in vivo* evaluation of RF targeting potential, we prepared an analogous derivative of RfdiC14 including a PEG spacer. The molecule consists of a PEGylated lipid coupled to RF moiety at 5'O position. In the literature, PEGylated lipids functionalised with antibodies and peptides were reported. Coupling between a PEG-lipid moiety and a targeting ligand generally occurs as an amide bond (reaction between activated carboxyl groups and amino groups, Figure 2.3.), disulfide bond (reaction between pyridyldithiols and thiols) or thioether bonds (between maleimide derivatives and thiols).[34] Such reactions often take place in water, when PEGylated lipid with an activated functional group is already inserted into the liposome membrane. As this coupling employs surface chemistry, it could be more difficult to perform.

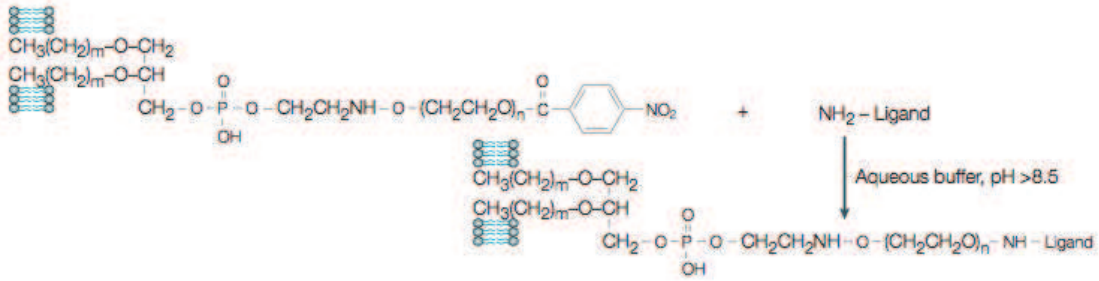

Figure 2.3 Widely employed chemical strategy for PEGylated lipid functionalization.[34]

Many of PEG-lipid conjugates incorporating a functional group for subsequent coupling are commercially available. Among them are DSPE-PEG-Carboxylic acid, DSPE-PEG-Maleimide, DSPE-PEG-Amine, DSPE-PEG-Biotine, DSPE-PEG-Azide etc. However, these strategies are not applicable to RF, as it does not possess any of these functional groups (e.g. azide, amine, carboxylic acid). Moreover, the moderate water solubility of RF is not compatible with such post-liposome formed reactions. Consequently, we decided to attach RF via a Steglich esterification to a commercially available phospholipid that holds an NHS-activated carboxylic acid at the terminal of a PEG spacer - DSPE-mPEG2000-succinyl (1,2-distearoyl-sn-glycero-3-phosphoethanolamine-N-[succinyl (polyethylene glycol)-2000]).[128] The general principle of Steglich esterification is depicted on Scheme 2.11. It is a mild reaction, which allows the conversion of sterically demanding and acid labile substrates. Furthermore, the reaction often takes place in DMF, which ensures better solubility of RF.

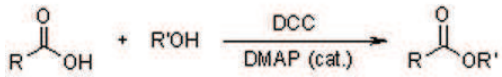

Scheme 2.11 Steglich esterification.

The primary hydroxyl group of RF is considered to be more reactive than the secondary hydroxyls. For this reason we utilised non-protected RF. Moreover, the protection with acetate esters, utilised in previous RF amphiphile synthesis, was not compatible with such reaction (due to the presence of ester moieties in the DSPE-PEG). For the same purpose we could not utilise a phosphoramidite RF analogue developed in previous section. As RF-phosphoramidite holds acetate esters as protective groups, their deprotection after

phosphodiester coupling would at the same time cleave glycerol esters of the phospholipid.

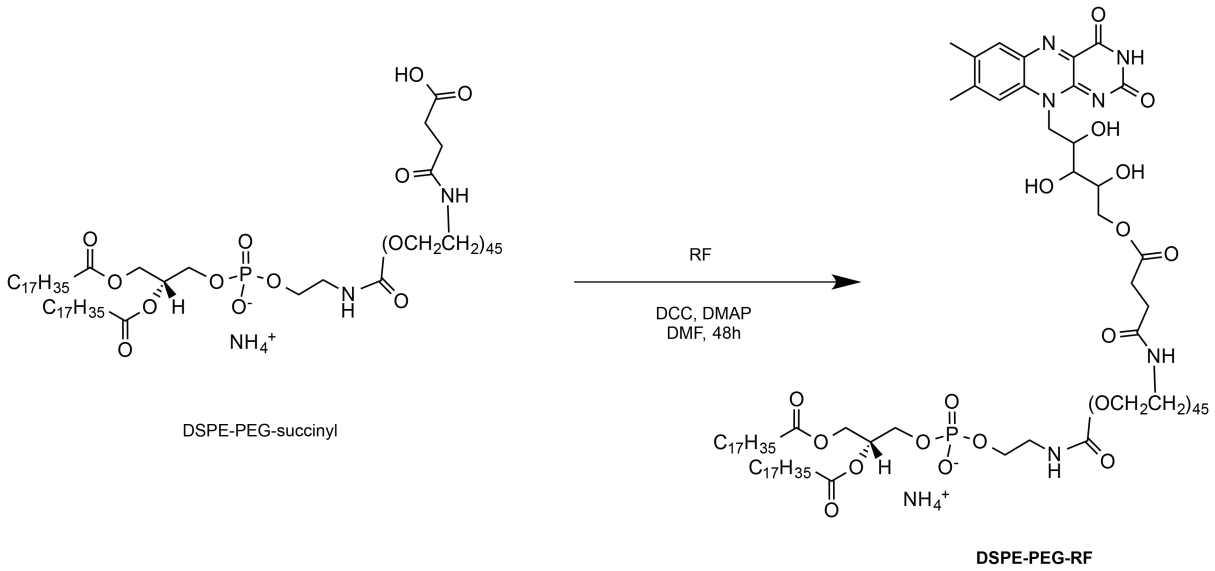

Scheme 2.12 Synthesis of DSPE-PEG-RF.

The synthesis of DSPE-PEG-RF is presented on Scheme 2.12. First, RF and DSPE-PEG-succinyl were solubilised in DMF and mixed. Then stoichiometric amount of DCC (N,N'-Dicyclohexylcarbodiimide) and catalytic amount of DMAP were added to the reaction mixture. The formation of a new product was confirmed by TLC analysis. The product (DSPE-PEG-RF) was analysed and purified by reverse-phase HPLC with a UV-Vis detector set at 265 nm (one of RF absorption maxima). The chromatogram presented on Figure 2.4 shows a peak at 3 min that corresponds to unreacted RF and the second peak at 26 min that corresponds to the DSPE-PEG-RF derivative. However, the unreacted DSPE-PEG was not visible in these conditions due to the absence of its absorbance at 265 nm.

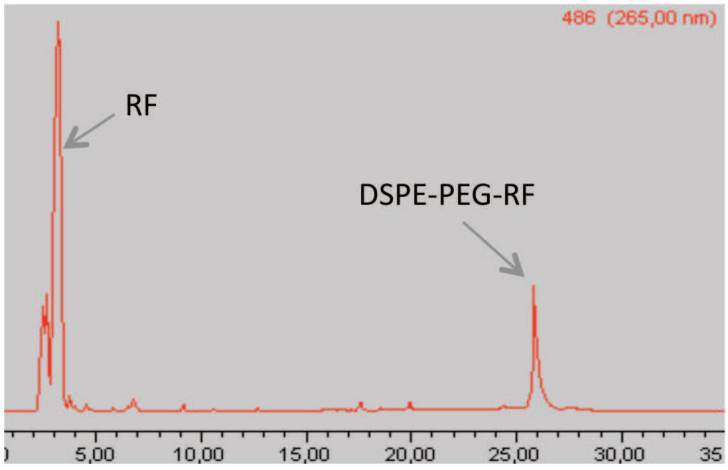

Figure 2.4 Reverse-phase HPLC chromatogram of DSPE-PEG-RF synthesis

After purification, DSPE-PEG-RF was analysed by MALDI-MS (matrix-assisted laser desorption ionisation mass spectrometry). The obtained results are presented on Figure 2.5.A. One could observe two distinct isotopic massifs typical for the size distribution of PEGylated molecules.[129] The first massif corresponds to the unreacted DSPE-PEG in the form of

carboxylic acid (theoretical m/z 2815) and the second massif corresponds to the DSPE-PEG-RF (theoretical m/z 3229). The relative intensity ratio between the compounds was approximately 3:1. Unfortunately, it was not possible to separate these two molecules by reverse-phase HPLC and thus the presence of unreacted DSPE-PEG lipid was taken into account during further preparation of liposomes.

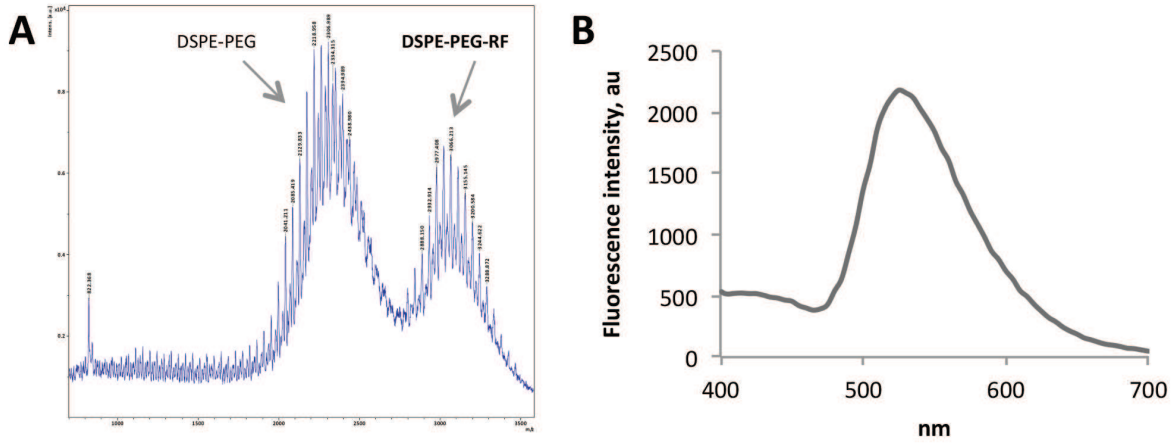

Figure 2.5.A. MALDI mass spectra of DSPE-PEG-RF; B. Fluorescence emission spectra of DSPE-PEG-RF.

Due to the presence of unbound DSPE-PEG it was not possible to calculate properly the reaction yield. Finally, after HPLC purification DSPE-PEG-RF exhibited a fluorescence spectrum similar to the RF with an emission maximum close to 530 nm (Figure 2.5.B.)

The structure of the obtained amphiphile is similar to the commercially available and widely used in the preparation of targeting formulations – DSPE-PEG-Folate® (CAS number 1236288-25-7, Avanti Polar Lipids). In principle, our targeting agent could be easily incorporated into any lipid containing formulation in the same manner that DSPE-PEG-Folate. The possible advantage of targeting with RF over folate is the RF ability for selective binding to both cancerous cells and neoplasic endothelium. On the other hand, RF transporters are not overexpressed in all kinds of tumours and thus, the targeting could be mainly oriented to prostate,[108] breast,[109] epidermic cancers and hepatocellular carcinoma.[110] This newly synthesised PEGylated RF amphiphile was further utilised for the preparation of long-circulating targeted liposomes for *in vivo* testing (Platform B).

2.5 Conclusions

The synthesis of RFA derivatives was complex and challenging, mostly due to the solubility problems of the RF by itself. However, we achieved to synthesise several RFAs with various chemical approaches such as click chemistry, phosphoramidite chemistry and esterification (Figure 2.6).

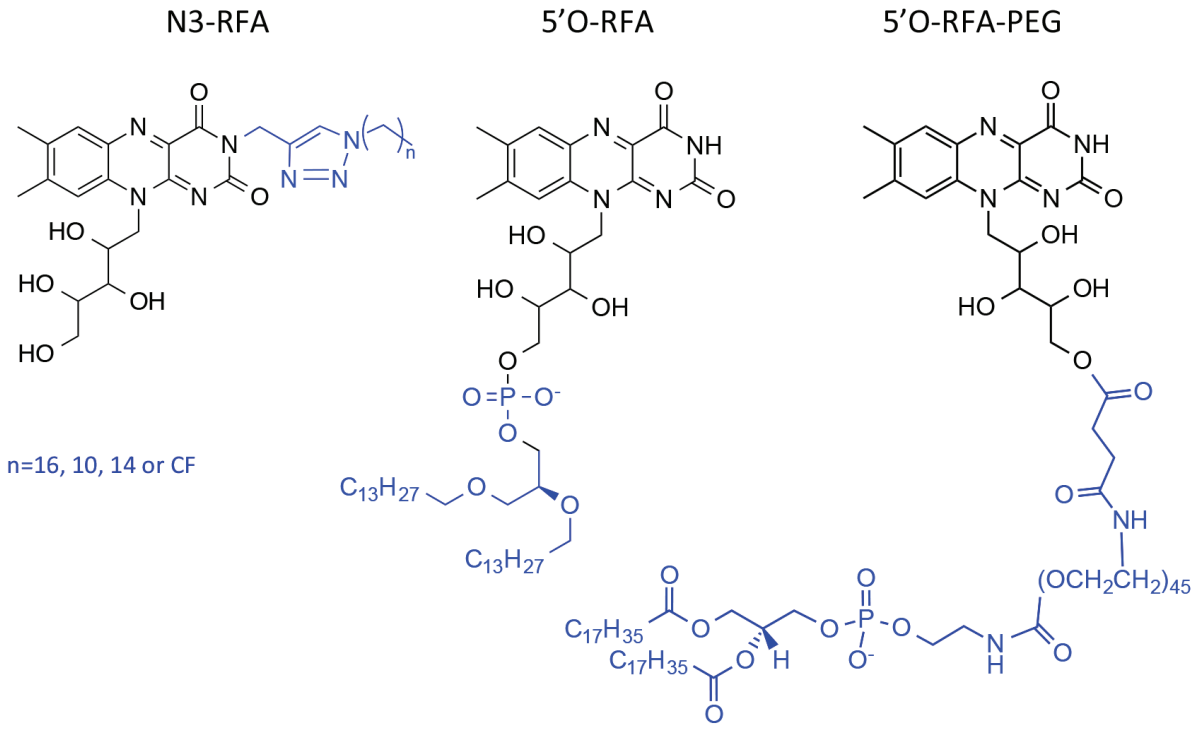

Figure 2.6 Chemical structures of prepared RFAs: N3-RFA; 5'O-RFA; 5'O-RFA-PEG.

The first four prepared derivatives had a single alkyl chain attached with a triazole bond in N3 position. The chosen alkyl chains were lauryl, palmitoyl, stearyl and fluorocarbon chain (with 10 carbons). Unfortunately, all of them were barely soluble in organic solvents and almost insoluble in water. This brought us to the conclusion that free hydroxyl groups of the ribitol chain do not provide enough hydrophilicity to the molecule and additional charged moiety was needed. This is corroborated with the fact that, FMN, a natural phosphorylated RF derivative, is almost 300-fold more water-soluble than RF.

For this reason, we decided to change the synthetic strategy towards phosphoramidite chemistry in 5'O position, which will mimic natural FMN structure. To make the molecule look like headgroup-functionalised phospholipid, we utilised a dimyristoyl glycerol derivative as a hydrophobic moiety. The chain length of the lipid was chosen in accordance with its phase transition temperature (see Chapter V). In other words, myristoyl lipids stay in the liquid state at room temperature. Nevertheless, the described synthetic route is adaptable for the synthesis of almost any phosphoramidite derivatives of RF. Eventually, the key intermediate, RF-phosphoramidite, could serve as a building block for the synthesis of RFA with various chain hydrophobic length and chemistries.

The obtained 5'O-RFA derivative was named RfdiC14. It presents a promising

potential for the auto-assembly formation, since it displays similar to classical phospholipids solubility in chloroform, DCM, methanol and ethanol. Again, similarly to the phospholipids, in buffer RfdiC14 forms a cloudy suspension, which could suggest the formation of vesicles or other self-assemblies.

Due to the particular physicochemical properties of RF, the auto-assemblies of its amphiphiles could give rise to new nanosystems with various properties – stimuli-reponsive, redox, photosensitising and fluorescence. Thus, in the next chapter (III) we will attempt to calculate the theoretical critical packing parameter for RfdiC14 to predict its potential auto-organisation type. We will also study its behaviour in aqueous solution by solid state NMR, cryo electron microscopy (Cryo-EM) and dynamic light scattering (DLS).

On the other hand, we are also going to investigate the influence of RfdiC14 on an artificial membrane by solid state NMR. Finally, the liposomes containing RfdiC14 will be prepared and their physicochemical properties will be compared to normal liposomes. This cancer cell targeted liposomal platform will be utilised in biological evaluation on various cancer cell lines (Chapter IV).

Moreover, we prepared a new RFA derivative holding a PEG spacer between RF and lipid – DSPE-PEG-RF. The molecule was prepared in a single step from commercially available PEGylated lipid. Reverse-phase HPLC did not provide the complete purification from a lipid-PEG precursor, but its presence should not be problematic for subsequent liposome formation. Therefore, the targeting potential of DSPE-PEG-RF will by studied *in vivo* within a model drug delivery nanosystem (Platform B represented by a stable liposome formulation with PEG coating).

3 Chapter III. Study of RFA auto-assemblies

To date, numerous technics exist for the investigation of amphiphile auto-assemblies, their architecture and properties. Among them are theoretical calculations, molecular modelling, NMR spectroscopy, photon correlation spectroscopy (also called dynamic light scattering), infrared and Raman spectroscopies, fluorescence spectroscopy, small-angle neutron scattering, small-angle X-ray scattering, circular dichroism, transmission emission microscopy (TEM), cryo-electron microscopy (cryo-EM), atomic force microscopy, confocal microscopy, differential scanning calorimetry, zeta potential measurements etc.[17]

The combination of various approaches helps to understand supramolecular interactions between amphiphiles, predict and visualise their self-assemblies, study their physicochemical properties and dynamics. In this chapter we will give a brief description of various technics used for the study of RFA self-assemblies and try to characterise and classify the observed structures. Finally, we will make some biological tests to evaluate cellular uptake of RFA self-organised systems.

3.1 Physicochemical characterisation

3.1.1 CPP calculations

First, we aimed to make a theoretical estimation of possible RfdiC14 auto-assemblies. In this context, the calculation of the critical packing parameter (CPP) is a useful and simple tool to predict auto-organisation of an amphiphile. It is based on the evaluation of the relation between the hydrophobic chain length, its volume and hydrophilic area of an amphiphile. The equation for CPP calculation (already presented in the introduction part) is following:

$$CPP = \frac{v}{a_s l_c} \quad (1)$$

Equation 1, where a_S *is the effective area per head group,* v *the volume of the hydrocarbon chain and* l_C *is the maximum effective length that the hydrocarbon chain can undertake.*[2]

The geometrical visualisation of parameters needed for CPP calculation is presented on Figure 3.1. Hydrophobic interactions between amphiphiles are based on the attraction between chains, whereas the overall auto-assembly curvature is determined by the repulsions between polar heads. In a spherical micelle the maximum hydrocarbon chain length represents also its radius. For conventional amphiphiles *v/lc* is considered stable and independent on the chain length. It is equal to 21 Å^2 for single-chain and 42 Å^2 for double-chain amphiphiles.[130] Accordingly, the effective hydrophilic surface area a_s is a cornerstone in amphiphile packing predictions. In this manner, the single-chain amphiphiles with large headgroup areas will have small CPP values (≤1/3) and tend to form spherical micelles. Cylindrical micelles or hexagonal phase are most likely formed by single-chain surfactants with small headgroup areas (CPP=1/3-1/2). In contrast, double-chain lipids with large headgroups, such as phosphatidylcholine, geometrically will be closer to truncated cone and form bilayers (CPP=1/2-1). Small headgroup and double hydrophobic tail could give rise to a

mirror-phase or planar bilayer (CPP=1). The CPP values greater than 1 generally indicate the formation of inverted water-in-oil phase (for the corresponding auto-assembly schemes – see Chapter 1.1, Figure 1.5).[131]

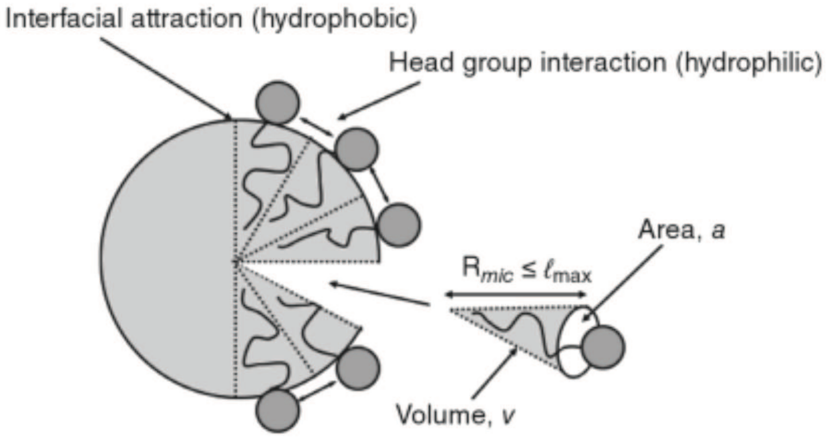

Figure 3.1 Geometrical illustration of CPP.[132]

However, not only geometrical parameters will determine the possible auto-assembly of an amphiphile. The possible interactions between headgroups (electrostatic attraction or repulsion, stacking etc.) should also be taken into account. Thus, strong repulsive interactions between charged headgroups will lead to the formation of micellar-type aggregates, while the contrary (attractive interactions between headgroups) argues for the bilayer-type structures. In this case, the changes in temperature and ionic force, modifying head-to-head interactions, could also influence on the aggregate architecture.[132] In spite of the complexity of factors impacting auto-assembly formation, the CPP still stays a simple method for first theoretical prediction.

In our case, each parameter was obtained using molecular mechanical calculations as described by Khalil R.A. *et al*.[133] The analysis of hydrophobic volume, *v* and the effective chain length, *lc* are presented in Table 3.1. Our calculations found the *v*/*lc* ratio approximately 44,6 Å, which is close to the theoretical value. As expected, the evaluation of effective area per head group, a_s turned to be a complex issue. Consequently, we attempted two different variations of the calculations.

In the first method (M1) the RF headgroup was considered to be totally flexible in its movements around the phosphate backbone, like in the situation with conventional phospholipids. Accordingly, the effective hydrophilic area was estimated with the help of surface accessible solvent parameter (SAS). In this method the small probe is rolling along the atoms of van der Waals spheres detecting the area accessible for the solvent molecule. In this way, the total SAS area of RfdiC14 was estimated and from this value, the area corresponding to the hydrophobic part of RfdiC14 was subtracted. The obtained hydrophilic area was 250 $Å^2$, which gave the CPP=0,18. The obtained CPP value is below 0,33, which should indicate the formation of spherical micelles. The schematic representation on Figure 3.2 illustrates the measures made for this first method (M1).

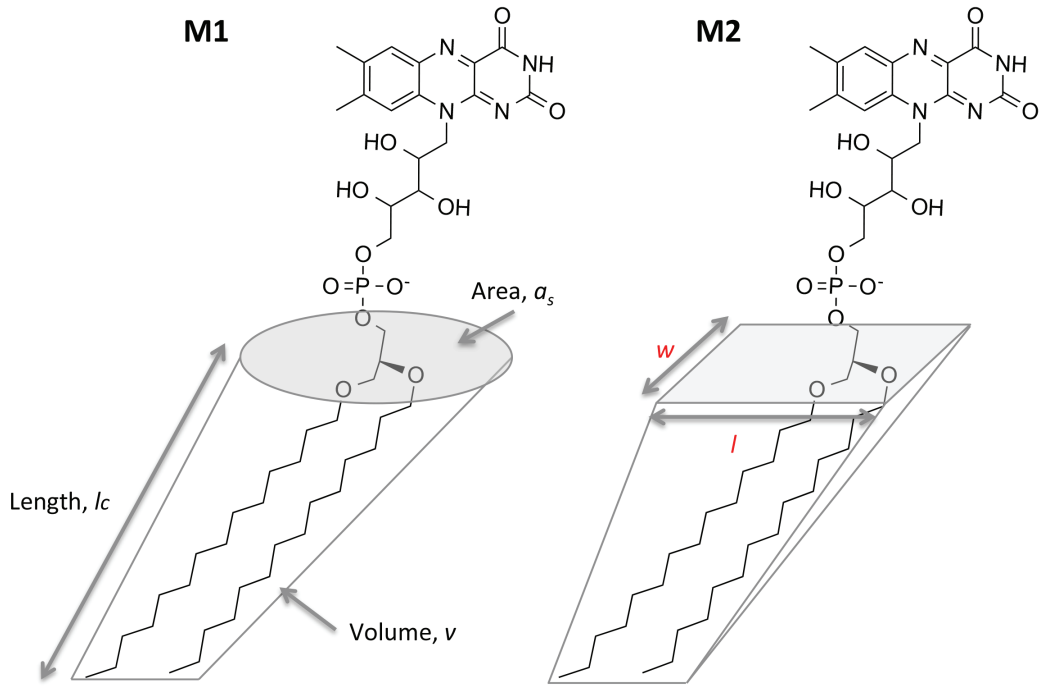

Figure 3.2 Schematic of two methods for CPP estimation

However, this calculation does not take into account the possible interactions between RF headgroups. There is a non-negligible probability of π-π stacking interactions between the planar isoalloxazine rings. Such interactions were already described in RF-functionalised polymeric helices.[100,134] If similar interactions could occur in our case, the calculation of a hydrophilic area should be different. In this second method (M2, Figure 3.2) we supposed, that the effective hydrophilic area could be roughly estimated as a rectangle or parallelogram. This rectangle will approximately represent the space that one RF headgroup could occupy if it is engaged in π-π stacking with two other RF headgroups. Therefore, the length of this rectangle is equal to the length of an isoalloxazine ring (l=12,6 Å) and the width (w) is estimated as twice the distance of possible π-π stacking. The width w, calculated by molecular simulation, measured from 3,6 Å to 4,2 Å. This gives us the possible area between 90,5-105,6 Å^2, which is at least twice smaller than in the previous method. Consequently, with the area decrease CPP changes and becomes from 0,49 to 0,43 (Table 3.1). In contrast to M1 calculations, these values are in between hexagonal and lamellar phase indexes and could indicate ordered structures with complex three-dimensional architectures.

Table 3.1 Parameters for CPP calculations

Method	v, Å^3	lc, Å	a_s, Å^2	CPP
M1	848	19	250	0,18
M2	848	19	91-106	0,49-0,43

Even though CPP calculations could give the first indications on the possible auto-organisation of an amphiphile, these estimations should be considered carefully and verified by several experimental approaches.

3.1.2 Characterisation with DLS

Dynamic light scattering (DLS) is another approach to study auto-assemblies. DLS is also known as photon correlation spectroscopy (PCS), and it is extensively used in size distribution analysis of spherical-shaped nanoparticles. In particular, DLS measures the time-dependant fluctuations of light scattered from particles undergoing Brownian motion. This motion originates from collisions between suspended particles and solvent molecules. The smaller the particles are, the faster their Brownian motion is (Figure 3.3).[30] The velocity of Brownian motion is defined by the translational diffusion coefficient, which is then converted in particle size by mathematical transformation. Thus, DLS gives the average hydrodynamic diameter of the particles in suspension and estimates the width of size distribution or polydispersity index (PDI). PDI is a dimensionless parameter, which ranges from 0 to 1. The smaller is the PDI value the more monodisperse the sample is. For instance, in the characterisation of liposomes a PDI below 0,3 is acceptable. The samples with a PDI higher than 0,7 are considered non-suitable for DLS measurements (Malvern® Instruments Ltd).

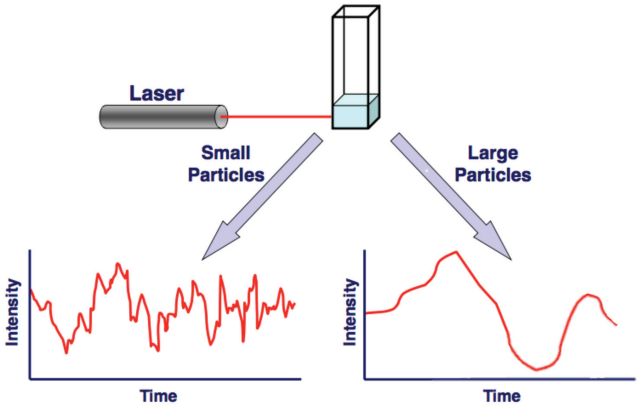

Figure 3.3 General principles of DLS (Malvern® Instruments Ltd)

This method offers the possibility of fast and non-invasive analysis of the particle size distribution in their native dispersion media (water, buffer etc.). However, it is applicable only for spherical submicron particles such as micelles, liposomes, lipid nanoparticles or nanoemulsions. In our case, the RfdiC14 auto-assemblies did not give comprehensive DLS response. The prepared crude solution with 2 mg/mL of RFA displayed very broad size distribution (polydispersity PDI – 0,751) with an average size peak at 210 nm (Table 3.2). After filtration of this solution through 0,22 μm syringe filter we obtained two populations with distinct average sizes: 143 nm and 23 nm. The PDI value after filtration was twice smaller 0,350.

Table 3.2 Results of DLS analysis of RfdiC14 auto-assembly

Sample Name	PDI	Pk 1 Mean Int, d.nm	Pk 2 Mean Int, d.nm
RfdiC14, non-filtered	0,751	210	-
RfdiC14, filtered 0,22 µm	0,350	143	23

The data indicate very heterogeneous population of objects in solution. The filtration seemed to destroy and/or eliminate larger objects, which caused the appearance of two populations. The aggregates of 23 nm are closer in size to micelles and the ones of 143 to

vesicles. However, such broad size distribution is a sign of DLS detection limit. If RFA auto-assemblies are not spherical, these results do not reflect the reality of objects in solution. The hypothesis of non-spherical objects is in accordance with our CPP calculations (M2 method) and solid-state NMR study. Nevertheless, additional techniques are needed to understand and visualise the nature and morphology of possible auto-assemblies. Among such techniques, the cryo electron microscopy (cryo-EM) is a golden standard in nanosystem size and morphology analysis.

3.1.3 Phase behaviour and order parameters

Nuclear magnetic resonance spectroscopy (NMR) is an analytical technique based on the magnetic properties of atomic nuclei. This technique provides information about the structure, dynamics as well as the chemical environment of molecules. Wide line solid-state NMR offers the possibility to study equilibrium and dynamical properties of non-crystalline or amorphous materials, such as polymers, glasses, protein precipitates, membrane proteins, and membrane-forming lipids at the molecular level.[135] It could also bring significant insights about the auto-organisation of non-bilayer lipid aggregates.[136]

The principle of NMR measurements relies on the precessions of nuclear spins (magnetic moments) upon the application of an external magnetic field (B_0). Only the nuclei possessing non-zero spin (^1H, ^2H, ^{13}C, ^{31}P *etc*.) are able to precess in the magnetic field (*i.e*., those having a magnetic moment). In the absence of magnetic field, all nuclear spins are randomly orientated and situated at basic energy level. The application of an external magnetic field makes them to orient in accordance with this field and change their energy state from basic. Orientated spins precess in the magnetic field with a radio frequency (ω_0) particular for each nucleus (Figure 3.4). In a macroscopic sample at ambient temperature the orientation of spins with respect to B_0 is dictated by the Boltzman distribution. This leads to a resultant magnetisation of the sample that is 10^6 weaker than B_0. Observation of the magnetisation is performed using additional radio-frequency fields, B_1, that are oriented perpendicular to B_0. This places the ensemble of magnetic moments and hence the magnetisation outside equilibrium. When the magnetisation returns to equilibrium due to exchanges of energy and entropy with the system it induces a current into a receiving coil placed orthogonal to B_0. The time dependent signal called Free Induction Decay (FID) is recorded, digitised and further Fourier transformed to generate an NMR spectrum of the corresponding nucleus.

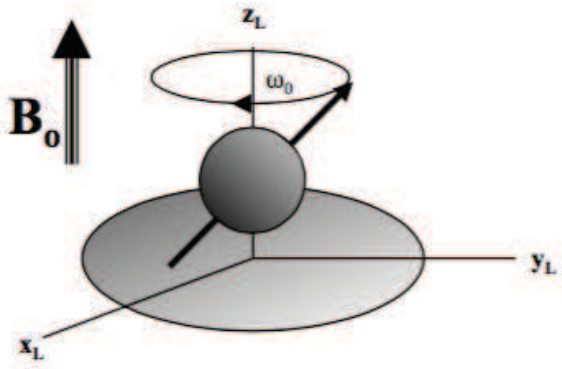

Figure 3.4 Spin precession with a radio frequency ω_0 upon the magnetic field application.

Several external and internal magnetic or electric interactions influence at the nucleus behavior in magnetic field and as a consequence, at its NMR spectrum. External couplings occur between nuclear magnetic moments and its external environment (applied magnetic fields B_0 and B_1) and are referred as *Zeeman interactions*. They are specific for each nucleus and represent the predominant interactions in strong magnetic fields.

Internal interactions appear between studied nucleus and other nuclei neighboring it. They are weaker than Zeeman interactions and depend on the sample state. For instance, in the liquid state due to fast molecular tumbling some interactions are averaged (isotropic) and do not contribute to the NMR spectrum. Consequently, **liquid state NMR** is characterised by only two types of internal interactions – *chemical shielding* also called in chemistry *chemical shift* arising from the inhomogeneous electron shielding around the nucleus and *scalar* or *J-coupling* induced by the interactions between covalently bound nuclei of the same molecule. These interactions result in well-resolved sharp peaks of a few Hz width on the NMR spectra. Chemical shift and J-coupling give important information about molecular structure, but do not describe directly the intermolecular interactions (due to, as already mentioned, fast molecular movement in solution).[137]

In contrast, in solid or crystalline state, molecular tumbling is most of the times absent. Therefore, the interactions here are not averaged (anisotropic) and generate much broader NMR spectra. This could give valuable information about material structure and dynamics. Thus, in addition to already described interactions, one could also observe dipolar and quadrupolar couplings with **solid state NMR (ss NMR).** Dipolar interactions arise between two nuclei in geometrical proximity (intermolecular), when their magnetic moments influence mutually. Quadrupolar couplings are characteristic to the nuclei with spin greater than ½ (^{2}H, ^{14}N *etc*.). These interactions are generated by the coupling between quadrupolar moment of the nucleus and the gradient of electric field created by the external charges (electrons, ions) in anisotropic media. They are not very common, as majority of routinely studied nuclei have spin equal to ½ (^{1}H, ^{13}C, ^{31}P *etc*.). However, quadrupolar couplings are extremely useful in the studies of ^{2}H ss NMR as they dominate all other internal interactions.[138]

Although anisotropic interactions contribute to the peak broadening and lowering the resolution of NMR spectra, they give additional structural and dynamic information.[135,139] For instance, ^{2}H ss NMR provides a direct evidence about organisation of lipid auto-assemblies.

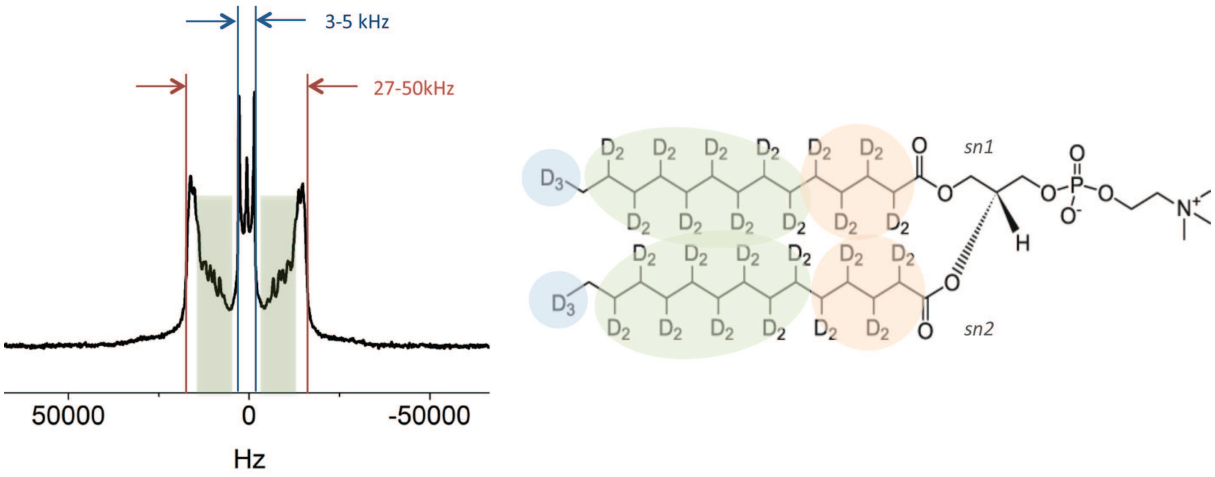

Figure 3.5. Position of deuterated chemical groups on the solid-state ^{2}H NMR spectrum.

It was shown, that by measuring of ^{2}H quadrupolar couplings and relaxation rates, one could access to several important parameters of lipid membranes.[135] Lipid bilayers exist in various phases – liquid disordered phase (*ld*), completely ordered solid phase (*so*) and intermediate liquid ordered phase (*lo*) frequently presented in cholesterol-containing membranes.[140] The phase transitions are induced by the temperature changes and could be observed with ^{2}H-NMR. Introducing of ^{2}H (or deuterium, D) labels at each individual C-D bound within the lipid allows obtaining the information for dynamic membrane systems at atomic level. The position of various carbon-deuterium groups on the spectra of typical phospholipid membrane) is presented in Figure 3.5. Hence, so-called axially asymmetric powder patterns are detected for lipids in *so* state. In contrast, axially symmetric powder patterns are characteristic for liquid disordered phase (*ld*). Both result from the superposition of Pake doublets for each deuterium labelled position (Figure 3.6.B). Such spectral transitions are characteristic for the lamellar phase behaviour.[141]

On the other hand, the ^{2}H spectral lineshapes could predict the formed phase type – lamellar, hexagonal or inverse hexagonal (Figure 3.6.A.). Thus, as one could observe, reverse hexagonal phase gives much more narrow lineshapes than hexagonal and lamellar phases. This is related to the phase geometry and dynamics of acyl chains in each phase.

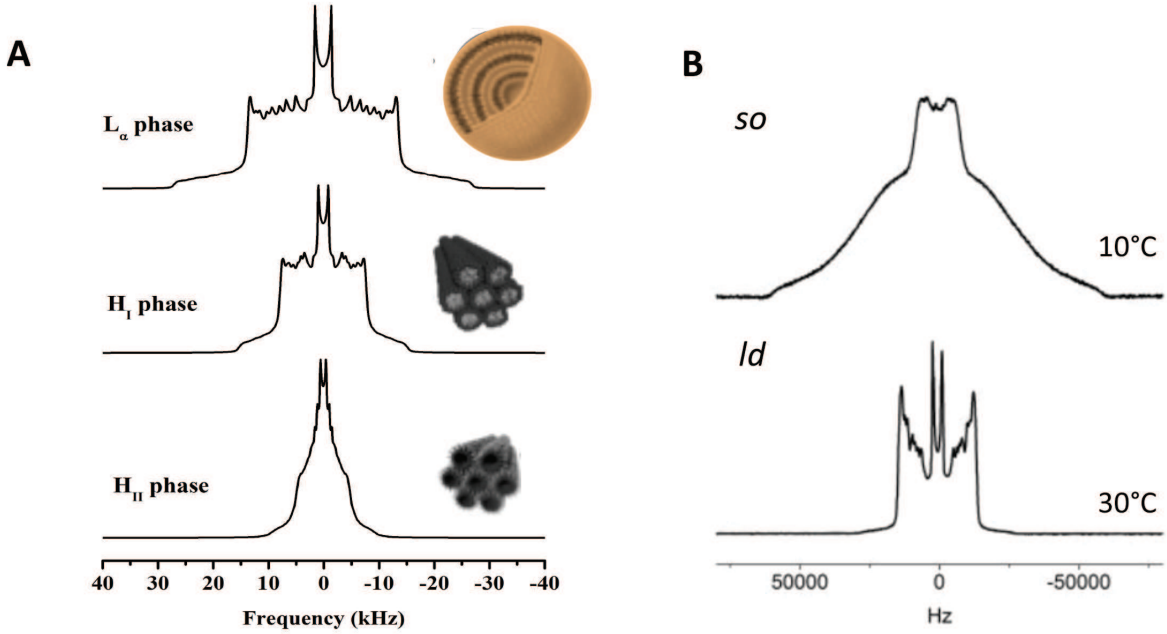

Figure 3.6.A Examples of ^{2}H NMR spectra lineshapes characteristic of lamellar (Lα), hexagonal (H_I) and inverted hexagonal (H_{II}) phases;[142] B. Example of patterns observed in lamellar so (gel, Lβ') and ld (fluid, Lα) state of a phospholipid membrane.

Another important characteristic of lipid bilayer, acyl chain order parameters, could be directly obtained from ^{2}H-NMR quadrupolar splittings.[141] Lipid order parameters represent the orientational mobility of the C–D bond and are dependent on angle between the C–D bond vector and a reference axis of the bilayer.[140,141] Order parameters (SD) vary between 0 and 1, where 0 indicates a fully disordered system as in liquids and 1 means totally ordered such as solids. The CD_2 moieties of the acyl chains, which are closer to the lipid glycerol backbone, are generally more ordered than terminal CD_2 and CD_3.[141]

The phase behaviour and order parameters of RfdiC14 were studied by ^{2}H ss NMR and compared to pure deuterated DMPC-d54. Because RfdiC14 is not ^{2}H labelled, we added a small amount of DMPC-d54 (2,5% molar) to monitor its signal by ^{2}H-NMR.

The deuterium spectra obtained from pure DMPC-d54 are characteristic of a lamellar phase (Figure 3.7). At the temperatures lower than 298K (25°C) there is a mixture of liquid and solid phases. Above 298K the *ld* phase is observed.

In contrast, the ^{2}H-NMR spectra of RfdiC14 in presence of 2,5% DMPC-d54 are completely different. Thus, at 298K the dominant phase is a fluid phase, *ld*, and even at 278K one could still observe a coexistence of liquid-disordered and solid-ordered phases. The complete transition to a gel phase is detected at 258K – nearly 40°C lower than for pure DMPC. This indicated that acyl chains in our RFA auto-assembly are highly disordered, most probably due to steric hindrance arising from bulky headgroups (phosphate plus RF) that act as laterally spacing groups providing more space at the chain level to undergo conformational isomerisation. The acyl chain disorder could be verified by the calculation of previously described order parameters and hydrophobic layer thickness (membranes with disordered acyl chains are thinner).

The isotropic peak observed in the central part of the spectra (Figure 3.7) represent 10% from overall intensity and could be a result of DMPCd54 small micelle or vesicle excluded from membrane auto-assembly.

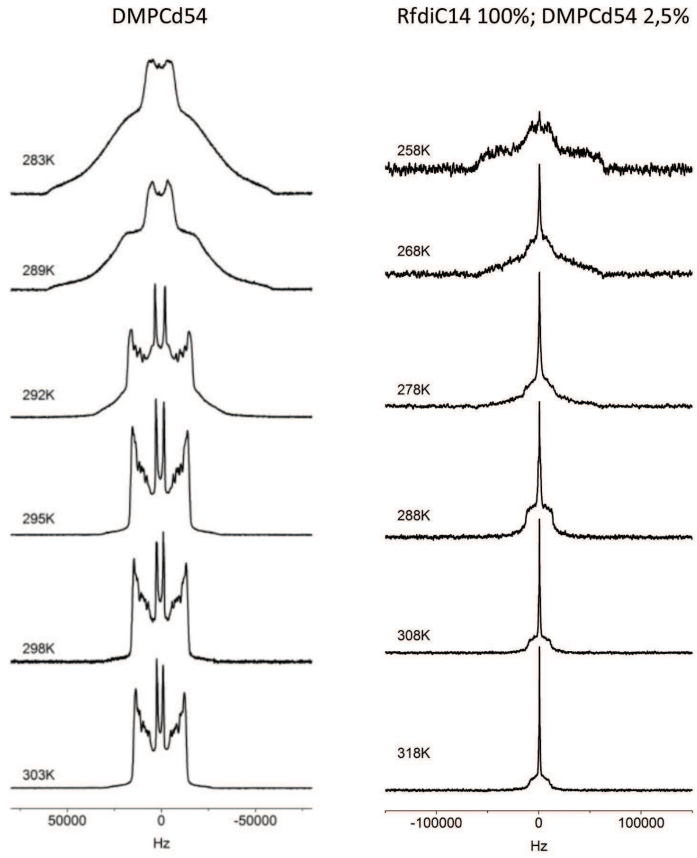

Figure 3.7 2H-NMR spectra of DMPC-d54 (left) and RfdiC14 with 2,5% DMPC-d54

The order parameters of pure DMPC-d54 bilayer at 35°C were calculated. As expected, one could observe (Figure 3.8) a relatively ordered plateau zone for atoms located closer to glycerol backbone (positions 2 to 8). The more disordered part is situated deeply on the bilayer at the level of CD_3 terminals. The two acyl chains *sn-1* and *sn-2* do not have exactly the same position in the bilayer. Thus, for the positions 11, 12 and 13 one could distinguish two slightly different dynamics. The *sn-1* is more dynamic and more profoundly inserted in the bilayer than *sn-2*.[143]

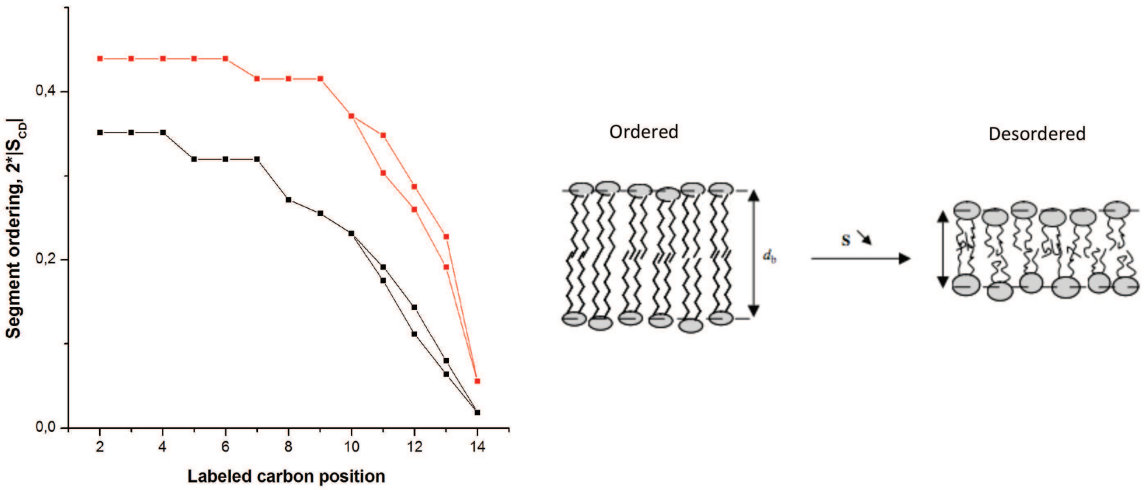

Figure 3.8 Order parameters (right) calculated for DMPC-d54 (red) and RfdiC14 with 2,5% of DMPC-d54 (black) and the illustration (left) of lipid ordered/disordered conformation in relation to bilayer thickness (d_b).[138]

In contrast, the order parameters calculated for RfdiC14 in presence of 2,5 % of DMPC-d54 in fluid phase indicate a marked disorder effect of RFA on the DMPC-d54 chains. The membrane thickness was calculated 20 Å, which is 2 Å smaller than a classic DMPC bilayer. These data confirm our previous hypothesis about disordered acyl chains and as a consequence thinner and more flexible membrane as sketched in Figure 3.8. Most probably, bulky RF headgroups create additional interactions between them such as above-mentioned π-stacking (see CPP calculations section). This may result in lateral spacing of lipid chains hence providing more space at the chain level to undergo conformational isomerisation. These assumptions might be verified by additional ss NMR experiments described in Perspectives section. The visualisation of RFA self-assemblies with cryo-EM microscopy could also bring additional information about membrane architecture and object morphology.

3.1.4 Characterisation with cryo-EM

Cryo-EM is an imaging of radiation-sensitive samples in a transmission electron microscope under cryogenic conditions. The imaging principles of cryo-EM rely on the classical electron microscopy, where the specimen is irradiated with electrons emitted by a source and accelerated in a microscope column. The electrons scattered from the specimen are then focused by the electromagnetic lenses of the microscope. Even though transmission electron microscopy gives images with high resolution (20-40 Å), a high-energy electron beam damages the sample while lower energies would give worse signal-to-noise ratios. Moreover, during the preparation procedure the specimen is dried, which is not optimal for the colloidal systems as they could be modified or even destroyed upon dehydration. The imaging of specimens frozen at liquid nitrogen temperatures resolves these issues. On the one hand, frozen samples are much less damaged by the radiation and on the other hand, the native structures of auto-assemblies in water are preserved.[144]

For our experiments, two solutions with 5 and 2 mg/mL of RfdiC14 were prepared. The auto-assembly formation is a dynamic process, relying on a lot of physical factors (pH,

ionic force, concentration, temperature) and also on the preparation method. For our experiments, we decided to apply a procedure similar to the film method for liposome preparation (Chapter IV, 4.2). Accordingly, RfdiC14 was first dissolved in chloroform and put into a round bottom flask. The solvent was evaporated under gentle nitrogen stream and the resulting RfdiC14 film was redissolved in an appropriate amount of HEPES (20mM, pH=7,4) buffer. The solution was heated at 45°C for 1 hour and then subjected to 5 freeze-thaw cycles with the help of liquid nitrogen. Resulting samples at both concentrations presented cloudy suspension with small amount of particle sedimentation.

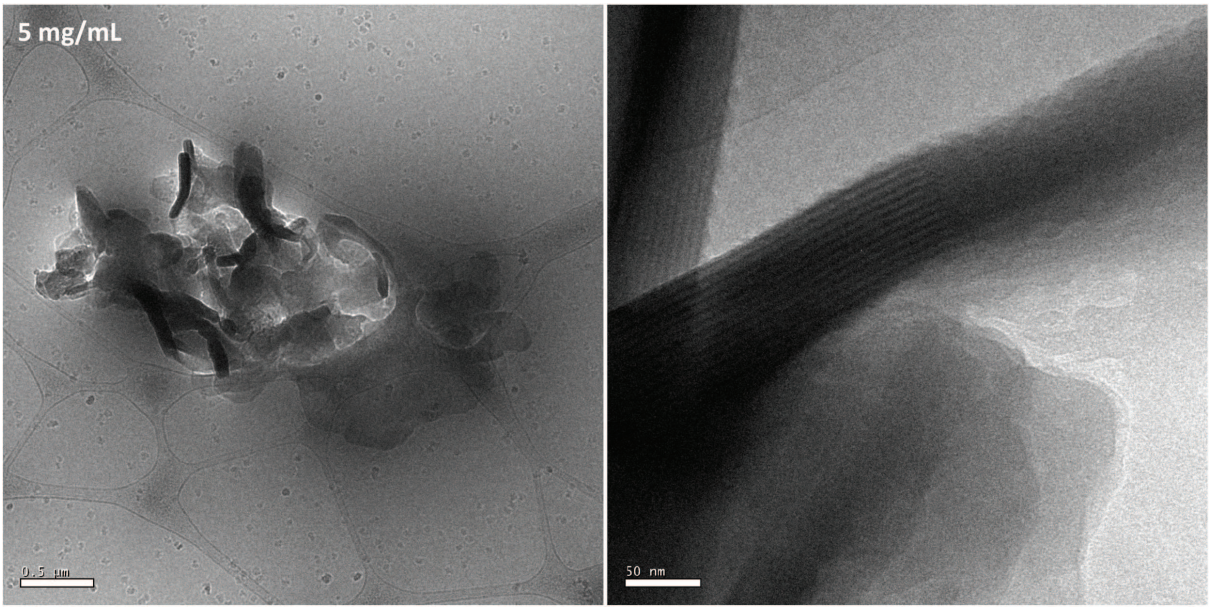

Figure 3.9 Cryo-EM photograph of RFA auto-assemblies at 5mg/mL

The RFA auto-assemblies detected with cryo-EM at 5mg/mL are presented on Figure 3.9 and at the concentration of 2 mg/mL on Figure 3.10. At lower magnification, one could observe 2-3 micrometer size aggregates of irregular shape. The aggregates were three-dimensional and consisted of multiple lamellar structures of a slightly curved shape. The overall architecture of the object and its size was similar for both studied concentrations. Moreover, these objects were observed in all investigated samples with a concentration-correlated abundance. Surprisingly, no signature of an hexagonal pattern was presented in all obtained cryo-EM images.

In the contrary, higher magnification reveals that slightly curved lamellar structures are approximately 44±12 nm thick and consist of very regular bilayers. Each lamellar structure presents from 5 to 9 repetition motifs (layers) presented by white and black bands. This bilayer signature was observed in all images of lamellar structures with a more or less presented curvature. The concentration of 2 mg/mL was more suitable due to the smaller number of objects and thus easier image acquisition. Mean values measured from the images are presented in Table 3.3.

Table 3.3 RFA auto-assembly signature parameters measured in cryo-EM images

Layer thickness, nm			Lamella thickness, nm	Number of layers
Black + white band	**White band**	**Black band**		
5±0,7	2±0,5	3±0,5	44±11,7	7±2

A white band that represents an alkyle chains bilayer has a size slightly lower (2±0,5 nm) than the values found in the literature for a conventional DMPC bilayer (2,5 nm).[145] This measure corresponds to the value calculated from ss NMR study (20 Å), which often gives more precise measurements than cryo-EM. A black band corresponds to the phosphorylated RF moiety. Indeed phosphate is known to give good negative contrast in electron microscopy of lipid vesicles, as it is nearly twice heavier than other atoms in lipids. Combined together, the black and white band repetitions seem to represent double layers of RfdiC14 molecules. From molecular modelling experiments we know that RfdiC14 alone is around 3 nm in size. Thus, the observed layer thickness of 5 nm could nicely correspond to an RfdiC14 bilayer with a slight overlap of myristoyl chains.

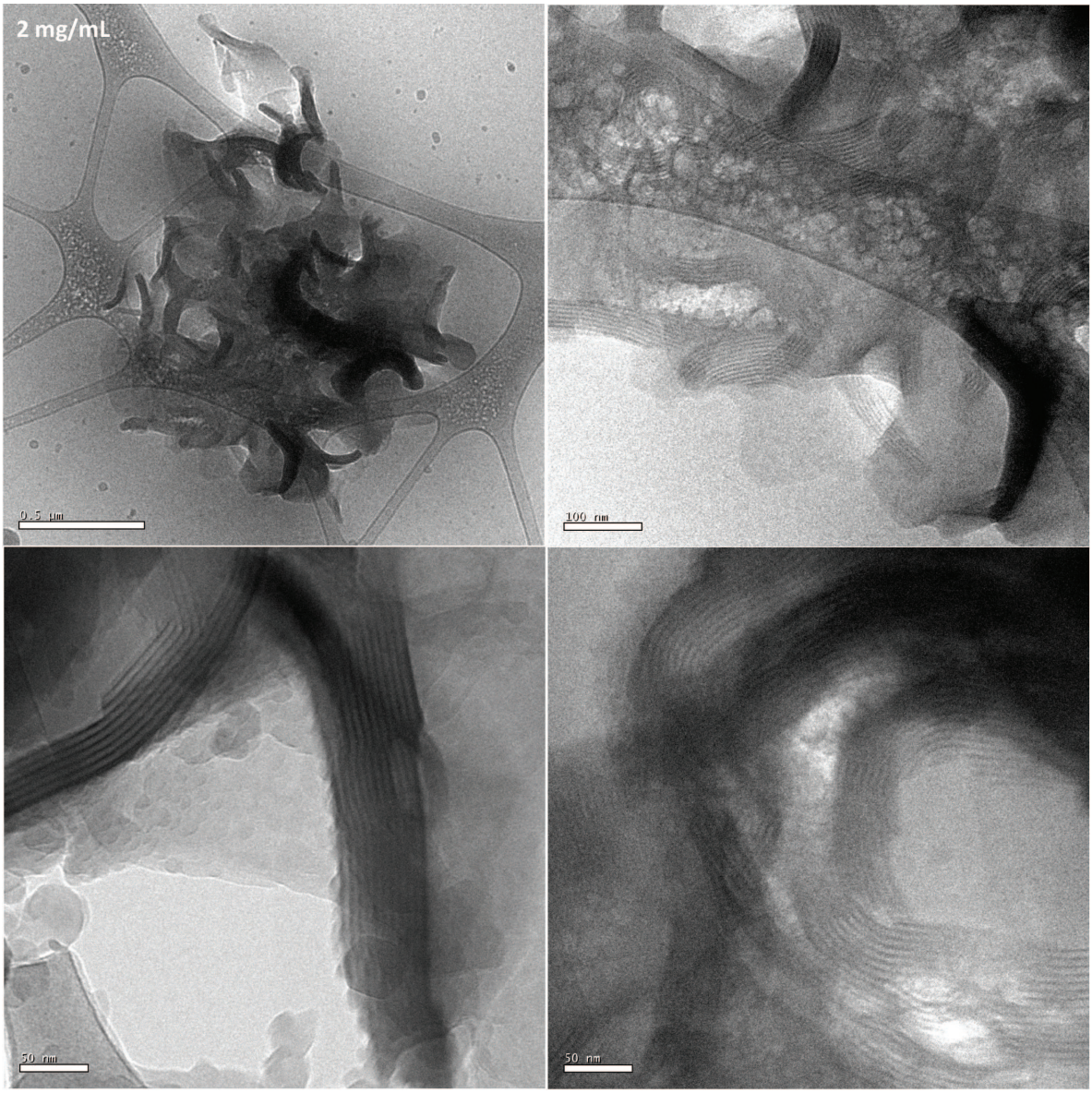

Figure 3.10 Cryo-EM photographs of RFA auto-assembly at 2 mg/mL

However, the observed structures are not similar to a classical lamellar phase of phospholipids that form spherical vesicles. The 5±0,7 nm repetition motif signifies very densely packing of bilayers and their low hydration. These results are in line with the higher acyl chain disorder and lower membrane thickness compared to conventional DMPC membrane (observed with ssNMR). As we already mentioned, this may signify the presence of additional interactions between RF headgroups. Indeed, such strict organization of the lamellas could be a result of π-stacking interactions between the isoalloxazine rings of RF. On the other hand, the presence of a negatively charged phosphate could lead to repulsive electrostatic interactions between RFAs and provoke the curvature of formed lamellas. It also possible that network of hydrogen bonds is formed between ribitol chains and water. These water molecules could be entrapped in the bilayer like in so-called cocheate phases.[146] However, additional experiments are needed to confirm these assumptions.

3.2 Biological evaluation

The uptake of RfdiC14 auto-assemblies was studied on PC3 cell line. PC3 is androgen-independent prostate cancer cell line and represents a variant of highly invasive small cell neuroendocrine carcinoma.[147] Prostate cancer cells were shown to overexpress the riboflavin carrier protein.[115] Moreover, PC3 cell line in particular, displayed a specific uptake of FMN-functionalised iron oxide nanoparticles.[104]

Cells were incubated with an RfdiC14 solution (1 mg/mL) in HEPES buffer at two different concentrations (10 µM and 0,1 µM in 100 µL) for 30 min at 37°C or 4°C. The uptake was monitored by fluorescence microscopy (ex. 450 nm, Figure 3.11) and the obtained images were quantified with ImageJ software (Figure 3.12). Surprisingly, RF internal fluorescence (ex. 450 nm, em. 530 nm) was enough bright enough to distinguish it from cells auto-fluorescence. This is an important advantage of such auto-assembly system, as it does not need additional fluorophores for visualisation. In contrast, for the FMN solution at the same concentration, the fluorescent signal is 'diluted' in cell auto-fluorescence and not visible. Thus, to visualise RF or FMN, they should be conjugated to a fluorescent dye with longer wavelength such as Rhodamine in the study of Phelps *et al* or bound to nanoparticles like in the case of FLUSPIOs[104].

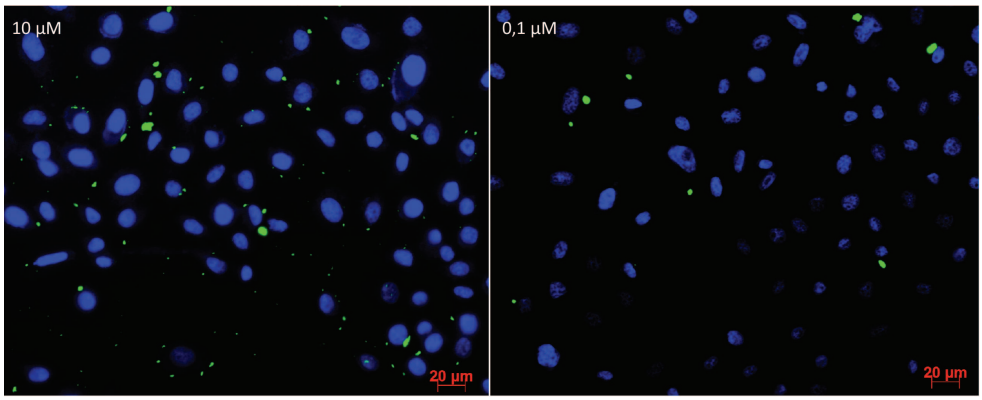

Figure 3.11 Fluorescence microscopy images of RfdiC14 uptake in PC3 cells (RfdiC14 is presented in green, nuclei are marked with DAPI in blue).

Both concentrations showed uptake at 37°C in the form of micrometer size aggregations localised in cytoplasm and perinuclear space (Figure 3.11). The uptake at 4°C was less homogeneous than at 37°C, that explains high standard deviation in quantification (Figure 3.12), however, the mean fluorescence values for both concentrations were not significantly different from the values at 37°C. Thus we could suppose that the uptake is not specific to active RF transporter systems but more likely occurs through macropinocytosis.

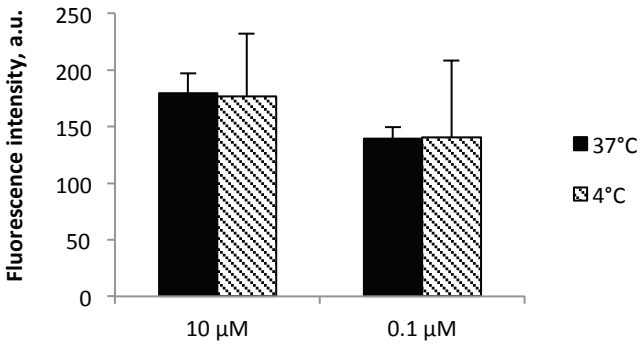

Figure 3.12 RfdiC14 uptake in PC3 cells; values are presented as mean ±SD (n=10)

This result could be explained by the morphology of RFA auto-assemblies. If all RF moieties are involved in bilayer formation and their isoalloxazine rings are not accessible due to intermolecular π-stacking interactions, they could not be recognised by a transporter protein. Moreover, the large, micrometer sized lipid aggregates, that we have seen at cryo-EM images, could be taken up by the cells non-specifically. However, due to their internal fluorescence RFA auto-assemblies could be useful in other applications such as tissue engineering or optoelectronics.

Nevertheless, to ensure specific transporter-RF interactions, several conditions should be accomplished: i. the nanosystem needs to be small and its passive internalisation in the cell should be minimal; ii. RF should be accessible for the interactions with a protein, i.e. situated on the nanosystem surface; iii. the amount of RF on the nanosystem surface should be minimal, which will prevent the interactions between its isoalloxazine rings and increase the accessibility. The above-mentioned aims could be achieved through the insertion of RfdiC14 into the existing nanosized drug delivery systems. This approach will be discussed in the following section (Chapter IV).

3.3 Conclusions

We studied the auto-organisation of prepared RFA with several theoretic (CPP calculations) and practical approaches (NMR, DLS cryo-EM). Like probably for any unconventional amphiphiles, the results were complex and sometimes difficult to interpret.

The CPP calculations indicated the possibility of the formation of either spherical micelles or the auto-assemblies closer to hexagonal and lamellar phases. The latter is possible if one takes into account the potential π-stacking interactions between isoalloxazine rings of RF. The DLS analysis of RfdiC14 in solution did not give any conclusive results, therefore indicating that the formed objects are non-spherical.

In the same way, solid-state NMR experiments revealed very different phase transitions of RfdiC14 auto-assembly from those of conventional lamellar DMPC-d54 bilayers. The system composed from 100:2,5 molar of RfdiC14 and DMPC-d54 showed the transition from liquid to solid gel phase about 40°C lower than for pure DMPC-d54. This indicates the presence of significant disorder in the hydrophobic part, which might be due to the steric hindrance generated by the large RF headgroups that act as laterally spacing groups providing more space at the chain level to undergo conformational isomerisation. This might also signify the presence of additional interactions between RF headroups such as π-stacking or hydrogen bonds with water. Thus, the results indicate the formation of lamellar phase with thinner and disordered hydrophobic part, but possibly highly organised headgroups.

Surprisingly, cryo-EM image analysis was in line with ss NMR and DLS data. We oserved large micrometer sized three-dimensional objects constituted from multiple lamellar structures. The latter were consisted from well-organised layers, 5±0,7 nm in width. The geometrical parameters of these layers brought us to the hypothesis of a bilayer organisation of RfdiC14 with multiple π-stacking interactions between isoalloxazine rings. The proposed bilayer organisation based on ss NMR and cryo-EM data is presented in Figure 3.13.

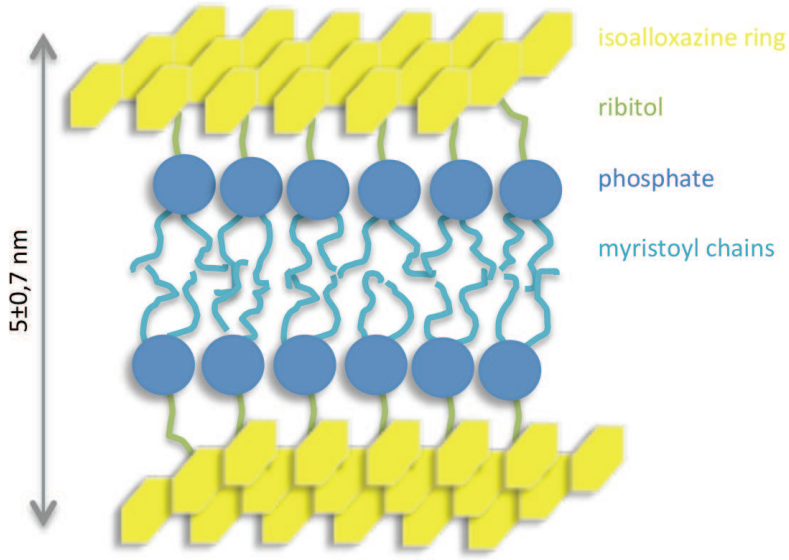

Figure 3.13 Proposed scheme of RfdiC14 bilayer organisation.

The cellular uptake of RfdiC14 auto-assemblies in PC3 cell culture was high, but not specific to an active transporter system and more likely occurred through a passive membrane fusion or macrocytose. The corresponding auto-assemblies exhibited bright fluorescence in cells and did not need any additional fluorescent label for the detection. Therefore, they have a potential in tissue engineering or optoelectronic fields.

4 Chapter IV. Platform A: RFA-functionalised liposomes

In this chapter we aimed to investigate the insertion of our RFA in the established drug delivery systems to render them tumour specific. Due to its double myristoyl chain, RfdiC14 could be inserted into almost any lipid containing formulation such as micelles, liposomes, hexosomes, cubosomes, lipid nanoparticles and nanoemulsions. We chose liposomes as a model system to test the RfdiC14 insertion because of their low toxicity biocompatibility and straightforward preparation method.[29]

These RFA-functionalised liposomes were named Platform A. After establishing the liposome composition, their physicochemical properties will be compared to conventional liposomes. We will analyse the impact of RfdiC14 on the liposome membrane and the efficiency of its insertion.

Liposomes will be labelled with a fluorescent dye for cellular uptake studies and it will also serve as a model of drug. The uptake and toxicity of Platform A will be studied and compared to non-functionalised liposomes in several cell lines including PC3, A431, CT26, MLS and HUVECs.

4.1 Design

4.1.1 Choice of lipids

Lipid composition plays an essential role in liposome physicochemical properties. Classically, liposomes are prepared from phosphatidylcholine (see Chapter I, Liposomes) with various chain lengths. Other lipids such as cholesterol, phosphatidylglycerol, phosphatidylethanolamine, phosphatidylserine etc. could be added in smaller amounts to provide specific properties to the formulation (stability, surface charge, membrane fluidity). Thus the crucial parameters in liposome design are lipid composition, lipid molar ratios and liposome preparation method.

We selected a simple formulation consisting of 1,2-dimyristoyl-sn-glycero-3-phosphocholine (DMPC) and 1,2-dimyristoyl-sn-glycero-3-phosphoglycerol (DMPG) (Figure 4.1). The myristoyl lipids were chosen in accordance to the chain length of RfdiC14. DMPC:DMPG (90:10 molar) formulation was reported in literature as stable and efficient for passive drug delivery *in vitro*[39,40] and *in vivo*.[41] Moreover, it is available on the market as Abelcet® (encapsulated Amphotericin B for injections) indicated for the treatment of invasive fungal infections.[148] Small amounts of DMPG (10% molar), a negatively charged phospholipid, make formulation anionic and thus contributes to its colloidal stability.

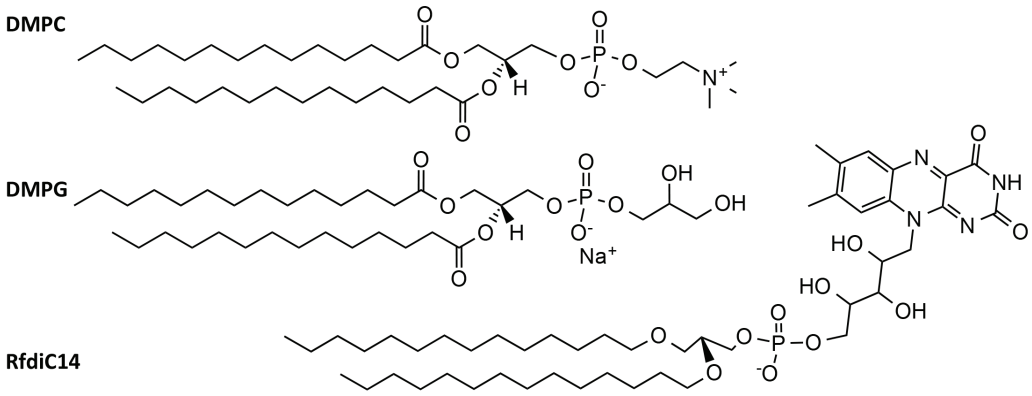

Figure 4.1 Chemical structures of lipids selected for liposome preparation

DMPC:DMPG liposomes were considered as a **control** formulation. The formulation that contained RfdiC14 in 1% molar ratio was termed as **targeted** (DMPC:DMPG:RfdiC14, 90:10:1). This amount of ligand was shown sufficient for cell targeting and at the same time not disturbing the liposome stability.[39,75]

4.1.2 Choice of labelling

Fluorescent dyes are frequently used to label liposomes and serve as model drugs for first formulation studies. RF itself has a visible green fluorescence (ex. 450 nm, em. 530 nm), but its quantum yield is quite low (0,3), compared to other dyes, and the signal overlaps with cell auto-fluorescence. It is important to note, that here we utilise only 1% molar of RfdiC14 and this quantity is not enough for the direct visualisation like in the previous study with RfdiC14 at 100%. Therefore, additional labelling is necessary. Red fluorescent dye Rhodamine is frequently used for the *in vitro* studies due to its high quantum yields (0,6-1) and good water solubility. Moreover, Rhodamine was already employed in uptake studies of RF conjugates.[117,149]

For the liposomes labelling in general, and for the labelling with Rhodamine in particular, two options exist. One could either encapsulate a water-soluble fluorophore in the aqueous phase of liposomes or insert a fluorophore-lipid conjugate in liposome bilayer.

For the first approach we chose a water-soluble Rhodamine B (RhB) dye presented in Figure 4.2. The RhB encapsulated in aqueous phase of liposomes could also serve as a model water-soluble drug. The liposomes labelled with RhB were named as *control* and *targeted* according to their composition (control without and targeted with 1% molar of RFA). Their respective schematic illustrations are presented in Figure 4.2. However, water-soluble components are known to have quite low encapsulation rate in liposomes compared to the molecules inserted in liposome bilayer

Therefore, as alternative to RhB, we took a lipid conjugate – Rhodamine Lissamine PE (LRhPE) or 1,2-dimyristoyl-sn-glycero-3-phosphoethanolamine-N-(lissamine rhodamine B sulfonyl) presented on Figure 4.2. Accordingly, the liposome labelling with fluorophore lipid conjugates should increase their fluorescent signal. Indeed rhodamine concentration in both control and targeted liposomes labelled with LRhPE was around 8 times

more important than in the RhB formulations (Table 4.1). The formulations encapsulating LRhPE were named as *control LRhPE* and *targeted LRhPE* liposomes. Their compositions are displayed on Figure 4.2.

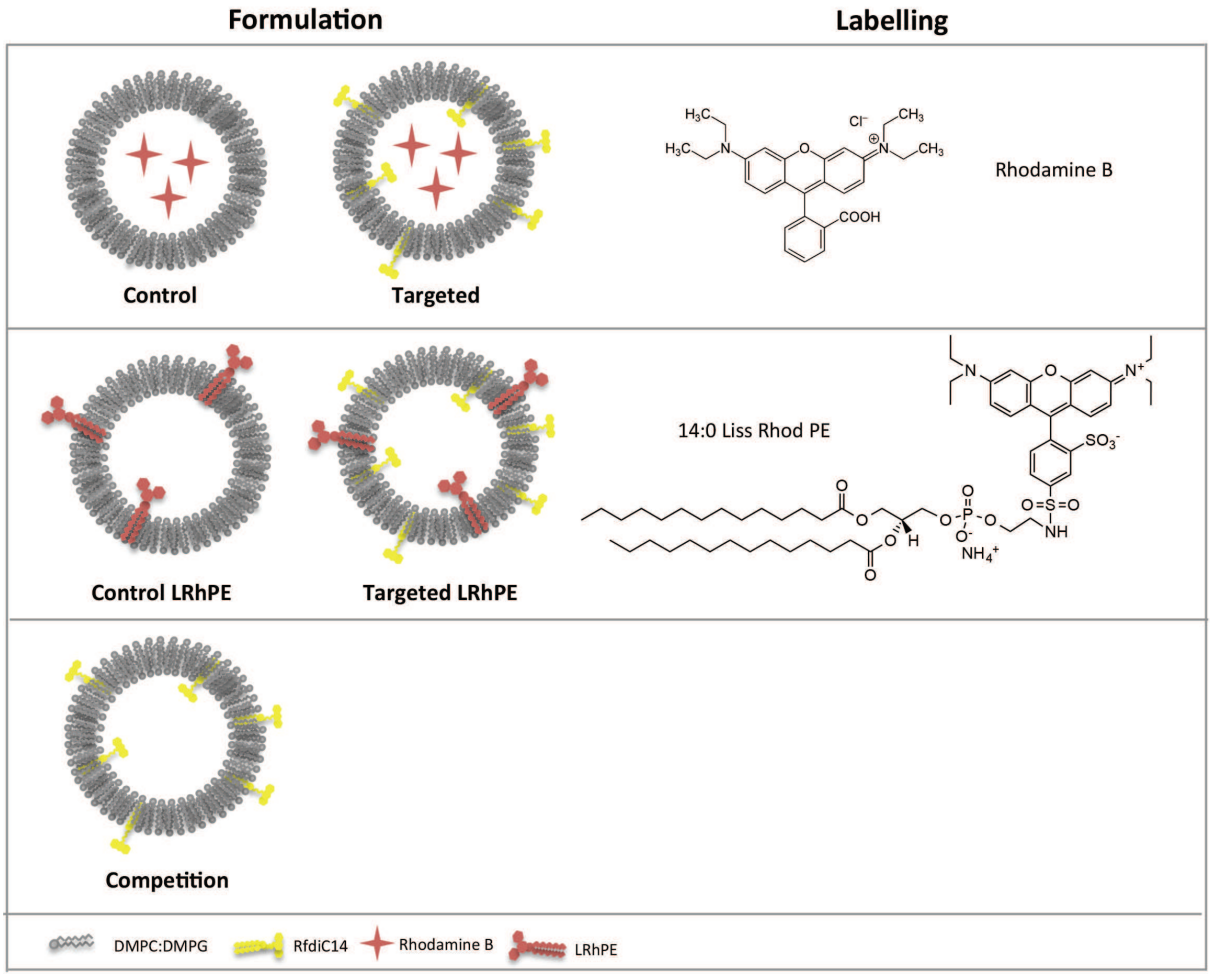

Figure 4.2 Schematic representation of prepared formulations and dyes utilised for their labelling.

We also prepared a formulation of targeted liposomes without any labelling to perform competitive binding studies *in cellulo*. These liposomes were named *competition* liposomes (Figure 4.2).

4.2 Preparation

There are several methods for liposome preparation. They could be divided in two main categories: i. the ones based on swelling of initially dried, pre-organised lipids and then their mechanical dispersion and manipulation of bilayers; ii. the ones involving a co-solvent in which lipids are soluble or additional "helper" non-bilayer-forming amphiphiles. Each method has its advantages and limitations.[17]

For our experiments we utilised the film hydration method, which is quite simple and straightforward. In this method lipids are first dissolved in organic solvent, generally chloroform, mixed in appropriate amounts and this solution is deposed into a round-bottom flask. After organic solvent evaporation, a thin lipid film is formed on the flask walls. The subsequent hydration of this film with a buffer generates large multilamellar vesicles that could be transformed into unilamellar by various techniques (sonication, freeze-thawing, extrusion etc.).

The general preparation method is depicted in Figure 4.3 and the detailed compositions of prepared formulations are presented in Table 4.1. The lipid film was dried overnight *in vacuo* and then hydrated at 40°C with HEPES buffer (25 mM) containing 1 mM of RhB. After hydration, the obtained MLV were subjected to 3 freeze-thaw cycles, extruded through 100 nm polycarbonate membrane and purified from non-encapsulated RhB by a size-exclusion chromatography on G25 Sephadex column. This preparation method displayed an excellent batch-to-batch reproducibility for both control and targeted formulations.

For the preparation of LRhPE liposomes, 0,3 % molar of lipid-dye conjugate were added into the initial lipid blend. There was no RhB in the hydration buffer for the preparation of LRhPE and competition liposomes.

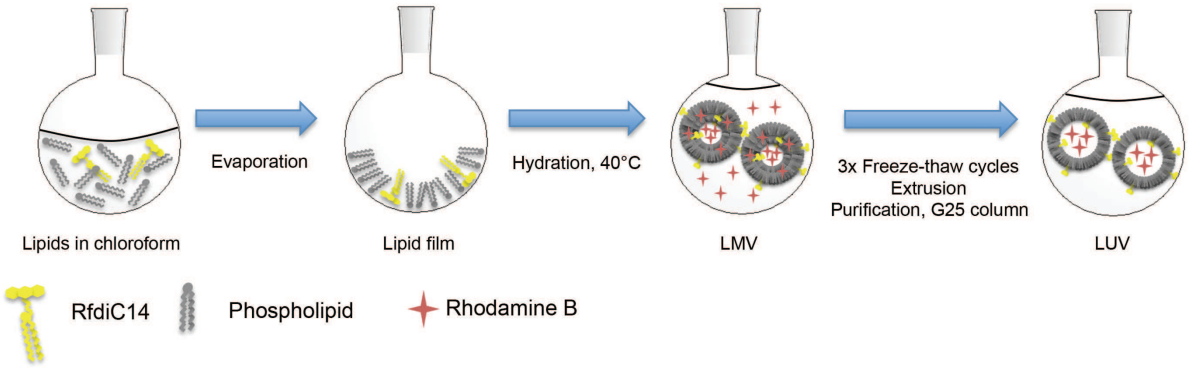

Figure 4.3 Schematic for liposome preparation steps

To ensure the proper insertion of RfdiC14 in liposome membrane through its myristoyl chains, it was dissolved in chloroform and mixed with other lipids during the lipid film preparation (Figure 4.3). The total lipid amount was 20 μmol in 1 mL and thus 0,2 μmol of RfdiC14 were utilised for the targeted liposome preparation.

We also attempted the post-insertion of RfdiC14 in pre-formed liposomes by their incubation with an appropriate amount of RfdiC14 in buffer and subsequent purification with G25 Sephadex column. However, it was difficult to achieve because of RfdiC14 auto-

organisation and aggregation in buffer.

Indeed, amphiphiles are generally subjected to a competition between the insertion in a membrane and their own auto-assembly in solution. To achieve a sufficient and stable membrane anchoring, a certain balance should be respected. On the one hand, an amphiphile should be sufficiently lipophilic to avoid desorption from the membrane and on the other hand, very high hydrophobicity might result in kinetically stable self-assemblies and thus limit its partition with a membrane.[150] We hypothesise that in our case, the previously observed RFA self-assemblies in buffer are quite stable. Once they are formed, RfdiC14 will preferentially tend to remain there, rather than insert into a liposome membrane. In the contrary, mixing of small amounts of RfdiC14 with other phospholipids will avoid the formation of above-mentioned self-assemblies and ensure its stable bonding to the liposome membrane.

4.3 Characterisation

4.3.1 Hydrodynamic diameter and zeta potential measurements

All prepared liposomes were analysed and compared in terms of their size distribution, polydispersity, zeta potential, encapsulation efficiency and stability. These parameters as well as liposome composition are described in Table 4.1.

Table 4.1 Physicochemical characteristics of prepared liposomes

Name	Lipids	Hydrodynamic diameter, nm	PDI	Zeta Potential, mV	Rhodamine, µM
Control liposomes	DMPC:DMPG 90:10	115±5	0,10	-52±2	5,7
Targeted liposomes	DMPC:DMPG:RfdiC14 90:10:1	115±2	0,06	-51±3	5,1
Competition liposomes	DMPC:DMPG:RfdiC14 90:10:1	130±3	0,11	-57±1	-
Control LRhPE liposomes	DMPC:DMPG:LRhPE 90:10:0,3	131±1	0,08	-58±2	46,8
Specific LRhPE liposomes	DMPC:DMPG:RfdiC14: LRhPE 90:10:1:0,3	124±1	0,06	-61±1	46,4

Hydrodynamic diameter of liposomes and their size distribution were measured by DLS. Both control and targeted liposomes presented similar diameters - 115±5 nm and narrow size distribution (Figure 4.4). As discussed in chapter I this is the optimal size for a drug delivery system. The polydispersity index (PDI) was good – 0,10 for control and 0,06 for targeted formulations indicated homogeneous liposome populations. Interestingly, the size of obtained LRhPE liposomes was slightly higher than those with encapsulated RhB.

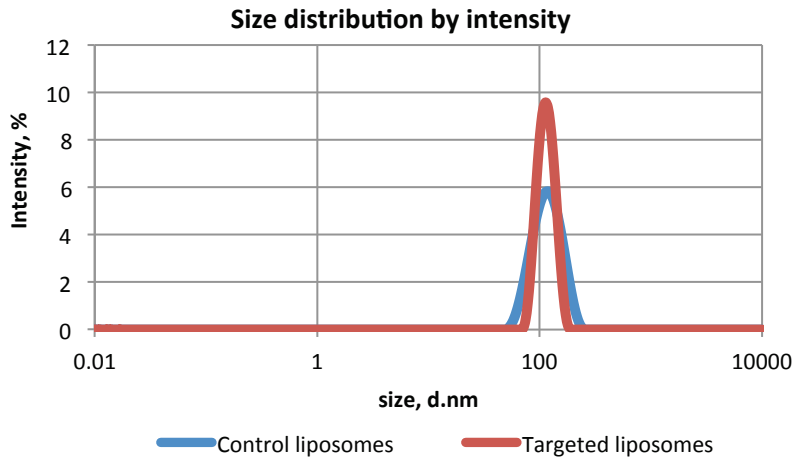

Figure 4.4 Size distribution by intensity of control and targeted liposomes

Competition liposomes were around 130 nm in diameter and had zeta potential of -57

mV, slightly higher than targeted and control (Table 4.1). Taking into account that these measures did not differ from batch to batch we suppose that the smaller size of the control and targeted liposomes could be caused by the RhB presence.

All studied formulations were anionic and presented a highly negative zeta potential without significant differences between control (-52±2 mV) and targeted liposomes (-51±3 mV). Such zeta potential values could be explained by the presence of negatively charged DMPG lipid. Probably due to this important negative charge, the liposomes exhibited a good colloidal stability in buffer during at least three weeks. This assumption is based on hydrodynamic size measurements at different time points presented on the Figure 4.5.

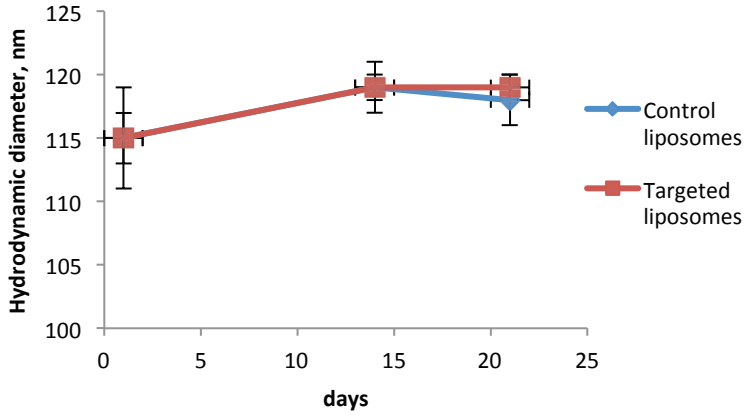

Figure 4.5 Hydrodynamic size stability of control and targeted liposomes (average of 3 measurements, ±SD)

4.3.2 TEM and cryo-EM

DLS size measurements were confirmed by transmission electron microscopy (TEM) with negative staining. Although negative staining is not the best method to visualise liposomes, due to the drying step that could destroy them, it was still possible to see round-shaped structures around 80-100 nm in diameter for both formulations.

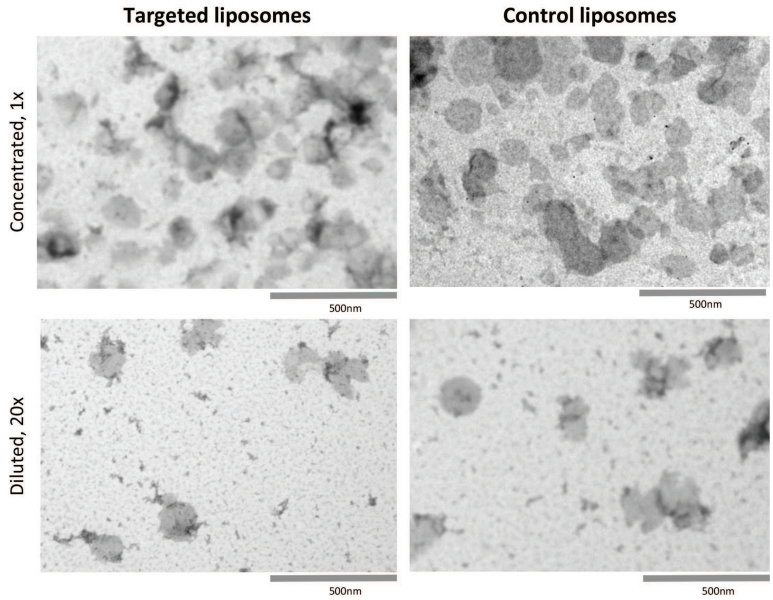

Figure 4.6 TEM photographs of targeted (left) and control (right) liposomes, negative staining with uranyl acetate (0.5 %)

Cryo-EM analysis gave images with much better resolution. On the Figure 4.7, one could observe unilamellar vesicles with mean diameter of 88±16 nm and a couple of smaller objects of 45 nm. Because DLS detects the hydrodynamic diameter it is generally larger than the one measured with Cryo-EM. Moreover, we could visualise a population of smaller vesicles (45 nm), which is difficult to detect with DLS (because of their lower scattering).

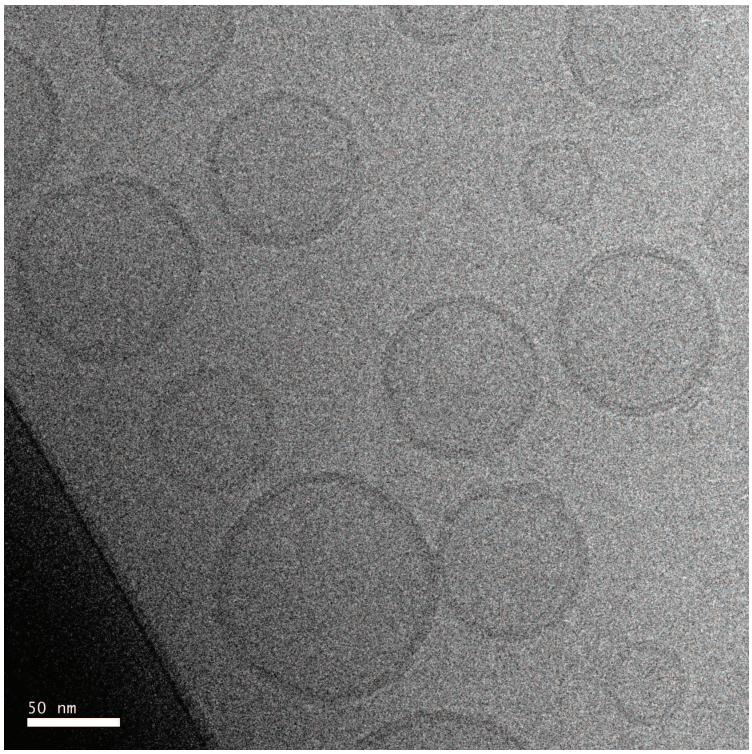

Figure 4.7 Cryo-EM photograph of targeted liposomes; scale bar 50 nm.

4.3.3 Fluorescence spectroscopy

One of the key advantages of RF as a targeting ligand is the intrinsic fluorescence of the molecule (ex. 450 nm, em. 530 nm). Hence, the presence of RfdiC14 in the formulation could be easily controlled and quantified by fluorescence spectroscopy in contrast to sophisticated and indirect quantification with immunoprecipitation, HPLC (high pressure liquid chromatography) and radioactivity measurements commonly utilised for Ab, peptides and proteins. On the Figure 4.8 one can observe a single emission peak at 580 nm for control liposomes, which corresponds to the rhodamine emission maxima, and two emission peaks for targeted liposomes - 530 nm and 580 nm, which demostrate the presence of both fluorophores – RF and rhodamine respectively.

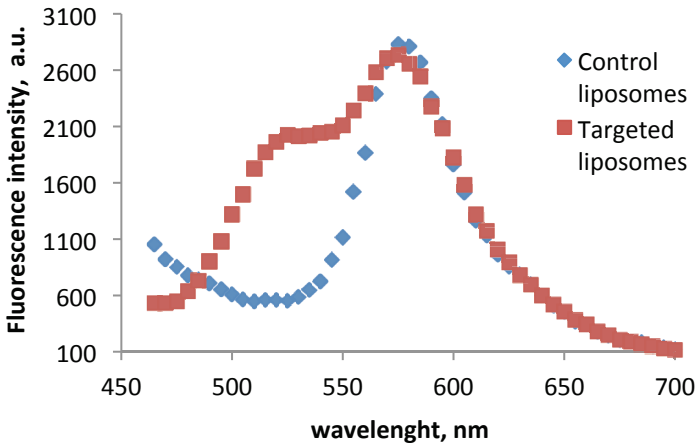

Figure 4.8 Fluorescence emission spectra of control (blue triangles) and targeted (red squares) liposomes.

The exact amount of each fluorophore in the formulation was calculated with the help of calibration curves - $y=5987x$ (R^2=0.9939) for RF and $y=17888x$ (R^2=0.98918) for rhodamine, where y represents the fluorescence intensity and x – the concentration in μM (Figure 4.9). The insertion efficiency of RfdiC14 was always close to 100% with respect to the starting composition (0.2 μmol of RF for 20 μmol of total lipid content represents the desired 1% molar). This signifies that RfdiC14 was efficiently entrapped in the lipid bilayer.

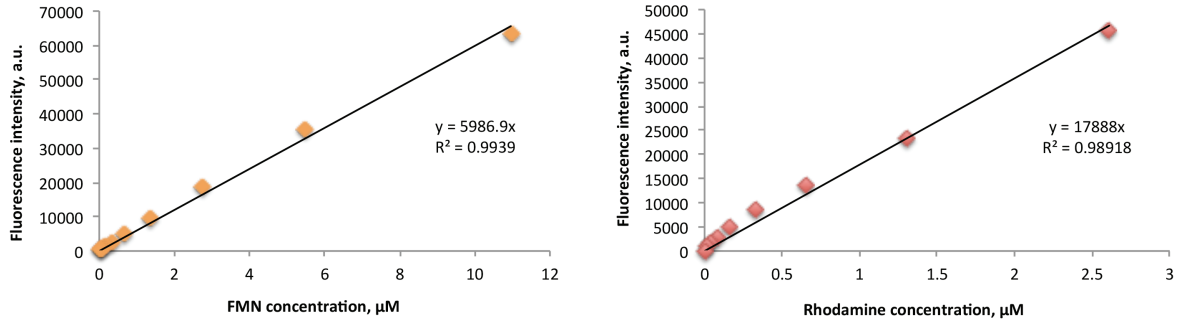

Figure 4.9 Calibration curves for riboflavin (left) and rhodamine (right) in buffer.

We utilised the same calibration curve for RhB and LRhPE. The RhB concentration was nearly the same in control and targeted formulations – 5,7 and 5,1 μM respectively (Table 4.1). As mentioned previously, liposomes labelled with rhodamine-lipid conjugate, presented a higher concentration of rhodamine. It was 46,8 and 46,4 μM for control and targeted LRhPE liposomes respectively. Thus, we can conclude that RfdiC14 could be efficiently inserted into the DMPC:DMPG liposome membrane with a 1% molar ratio and did not influence the liposome size, polydispersity, zeta potential, stability or encapsulation efficiency.

4.3.4 Solid state NMR

As described earlier, the deuterium ss NMR gives an access to the information about lipid phase type and transition, order parameters and hydrophobic layer thickness. We already studied the phase behaviour of our RFA derivative (RfdiC14) alone. Therefore, here we aimed to investigate its influence on the bilayer dynamics and order parameters of DMPC:DMPG membrane after RFA insertion in 9% molar ratio.

For this purpose two formulations were prepared: DMPC-d54:DMPG (90:10 molar) and DMPC-d54:DMPG:RfdiC14 (90:10:10). Similarly to pure DMPC-d54, the ^{2}H-NMR spectres of both formulations indicate the presence of lamellar phase. Below the 288K the lamellar phase is in the gel state with small amount of liquid phase that increases with the temperature. In spectra of membrane in the presence or absence of RfdiC14 one could note an isotropic line close to 0 ppm indicating the presence of a small quantity of lipids in the isotropic phase (nearly 3% at 308K). In the presence of 9% RfdiC14 the global line shapes do not change much on the entire studied temperature range

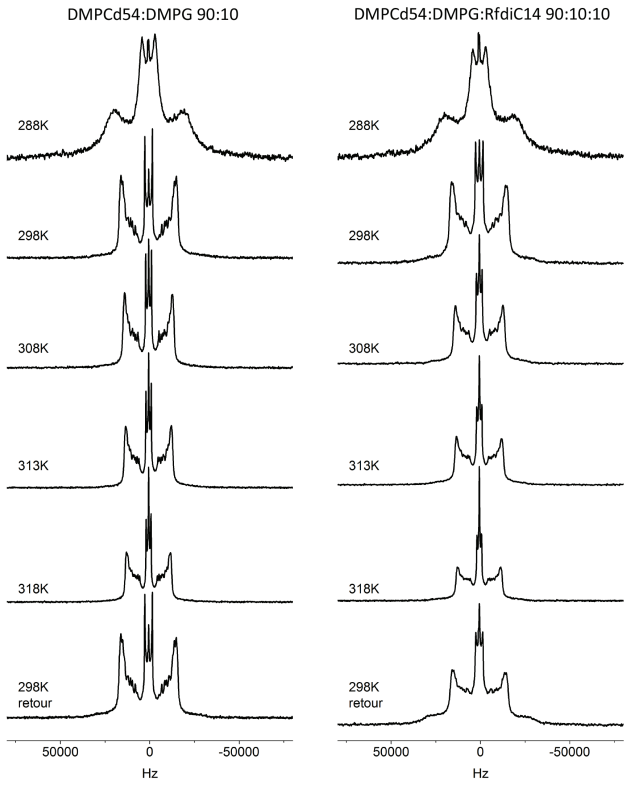

Figure 4.10 ^{2}H-NMR spectra of DMPC-d54 (left) and DMPCd54:DMPG:RfdiC14 (right)

The calculation of order parameters for both membranes (not shown) does not reveal significant differences, thus the dynamics of DMPC:DMPG acyl chains is not markedly impacted by the presence of 9% RfdiC14.

Because hydrated RfdiC14 has a thermotropism with a low lamellar gel-to-fluid phase transition (*vide supra*), one could expect an effect on that of a DMPC:DMPG membrane. The above results indicate that 9% of RfdiC14 is not enough to perturb significantly the DMPC:DMPG membrane.

In summary, an amphiphile derivative of RF - RfdiC14 could be inserted into lipid-containing nanosystem due to its myristoyl chains. In this section we prepared and characterised various liposomal formulations with RfdiC14. We showed, that it could be efficiently entrapped in liposome membrane and quantified by a fluorescence spectroscopy. The RfdiC14 functionalised liposomes did not exhibit significant differences in terms of size, zeta-potential, morphology or stability compared to conventional non-functionalised liposomes (control).

The obtained targeted formulation (Platform A) could be utilised for the delivery of cytostatic drugs and/ or imaging agents. Hence, in the next section we are going to evaluate the internalisation profile of our platform A in comparison to control liposomes in various cell lines.

4.4 Biological evaluation

4.4.1 Cellular uptake

In this section we aimed to evaluate the internalisation of liposomes containing 1% molar of RfdiC14 (targeted) and compare it to classical, non-functionalised liposomes (control) (see Table 4.1).

The uptake of control and targeted liposomes was studied in cancerous cell lines – PC3, A431, MLS, CT26 and a primary culture of human umbilical vein endothelial cells (HUVEC). As already mentioned in a previous chapter, PC3 is androgen-independent prostate cancer cell line[147] that display specific uptake of RF-functionalised nanosystems.[104] A431 is an epidermoid carcinoma cell line and an established model of solid tumours.[151] MLS is human epithelial ovarian carcinoma cell line and CT26 is murine colon carcinoma cell line that represents highly aggressive and highly leaky tumour model *in vivo*.[152] HUVECs are the cells derived from the umbilical cord veins endothelium. They are used as a laboratory model to investigate the function and pathology of endothelial cells.[153] In our study HUVECs were utilised as model of activated endothelial cells that could mimic tumour neovasculature.

The choice of cell lines was based on previous published (PC3 and HUVECs) and unpublished results (A431) that indicated specific uptake of RF-functionalised systems. CT26 and MLS were taken as additional cell lines to verify the specificity of RF targeting in other tissues.

4.4.1.1 PC3 cells

PC3 cells were incubated with control and targeted liposomes (50 nM in 100 μL, RhB concentration) for 30 min at 37°C and 4°C. The uptake was accessed by a fluorescence microscopy through the fluorescence signal of RhB (ex. 554 nm, em. 605 nm) and quantified with ImageJ software. At 37°C the uptake of targeted liposomes was 5,5 times significantly higher ($p<0.001$) than for the control ones – 93±30 and 17±11 a.u. respectively (Figure 4.11. B) At 4°C the active transport mechanism are blocked and only unspecific membrane binding occurs. In our case the internalisation targeted liposomes decreased to 78% ($p<0.001$) at 4°C compared to 37°C. This indicates that targeted liposomes were predominantly internalised in an active, transporter-mediated manner.

The competitive binding experiments were performed to evaluate the role of RF in the observed enhanced uptake of targeted liposomes. For this purpose cells were pre-incubated with 20x excess of competition liposomes (targeted liposomes without encapsulated RhB, Table 4.1) for 15 min at 37°C or 4°C followed by the normal 30 min incubation with targeted liposomes. Under these conditions we observed a significant 31% decrease ($p<0.01$) in the uptake of targeted liposomes at 37°C and only 10% decrease at 4°C. These data greatly support our hypothesis of an active transport mediated by RF-transporter system and the importance of RfdiC14 in the improvement of liposome uptake. Moreover, the diffusive fluorescence signal from RhB in cells may signify that it is released from liposomes into the cytoplasm (Figure 4.11 A).

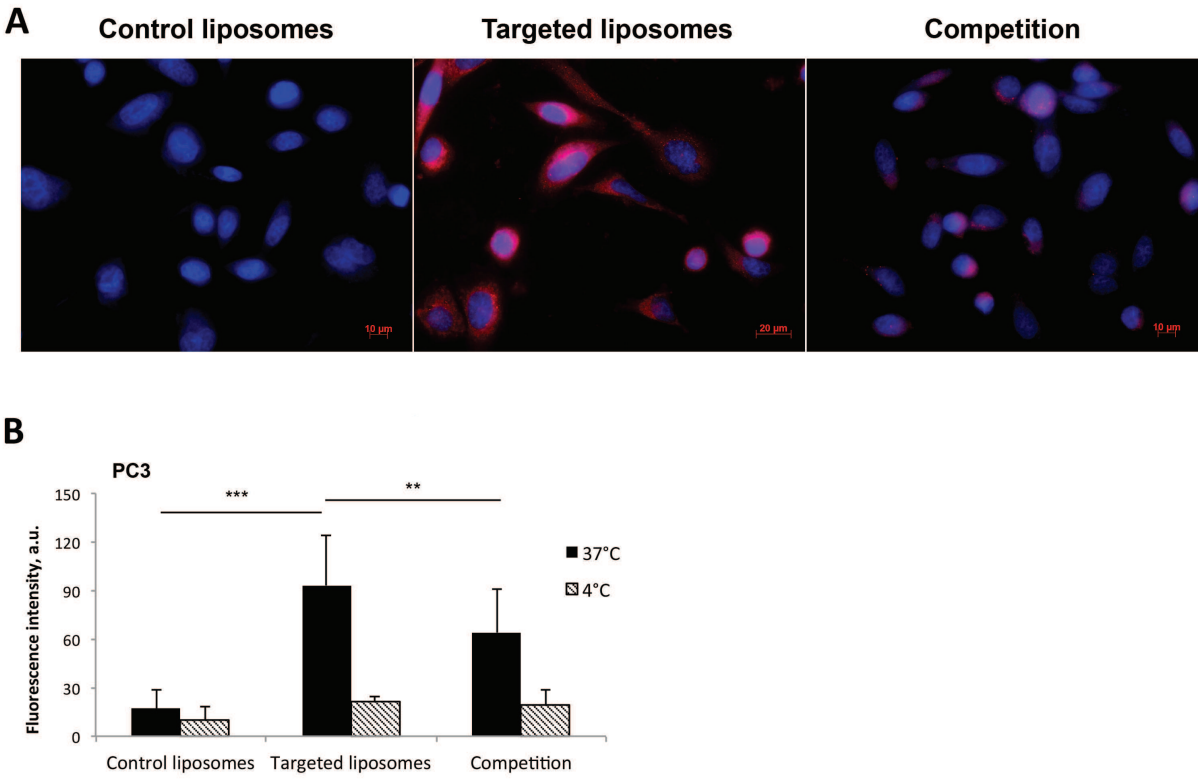

*Figure 4.11 A. Fluorescence microscopy images of liposomes uptake in PC3 cells, RhB is red, cell nuclei marked with DAPI are blue; B. Uptake of liposomes in PC3 cells; results presented as mean ±SD from 3 individual experiments with n=10 images for each condition; ***p<0.001, **p<0.01.*

In order to confirm the results obtained with microscopy, we performed flow cytometry study of liposomes uptake in PC3 cell line. This complementary approach allows analysing high number of cells and precise measurement of their fluorescence signal.

As for the fluorescence microscopy experiment, PC3 cells were incubated for 30 min at 37°C with control or targeted liposomes. For the competition experiment before standard incubation, cells were pre-incubated with a 20 times excess of competition liposomes. In this experiment we also added two additional negative controls like incubation with FMN and with competition liposomes to make sure that the excess of RF fluorescence did not interfere with RhB.

It is important to not confuse competition liposomes (without RhB) with the competition experiment, where we evaluate the uptake of targeted liposomes (contain RhB) after the pre-incubation with competition liposomes. Thus, competition liposomes by themselves as well as FMN should not exhibit any signal in RhB channel and this was confirmed by the experimental data (Figure 4.12). The signal in RhB channel for FMN and competition liposomes was similar to the cell auto-fluorescence level. In contrast the signal from targeted liposomes was 28 times higher than the basic cell fluorescence level and 2.7 times higher uptake ($p<0.01$) compared to control liposomes. Similarly to the fluorescence microscopy study, competitive binding experiment revealed a 40% decrease in targeted liposomes accumulation.

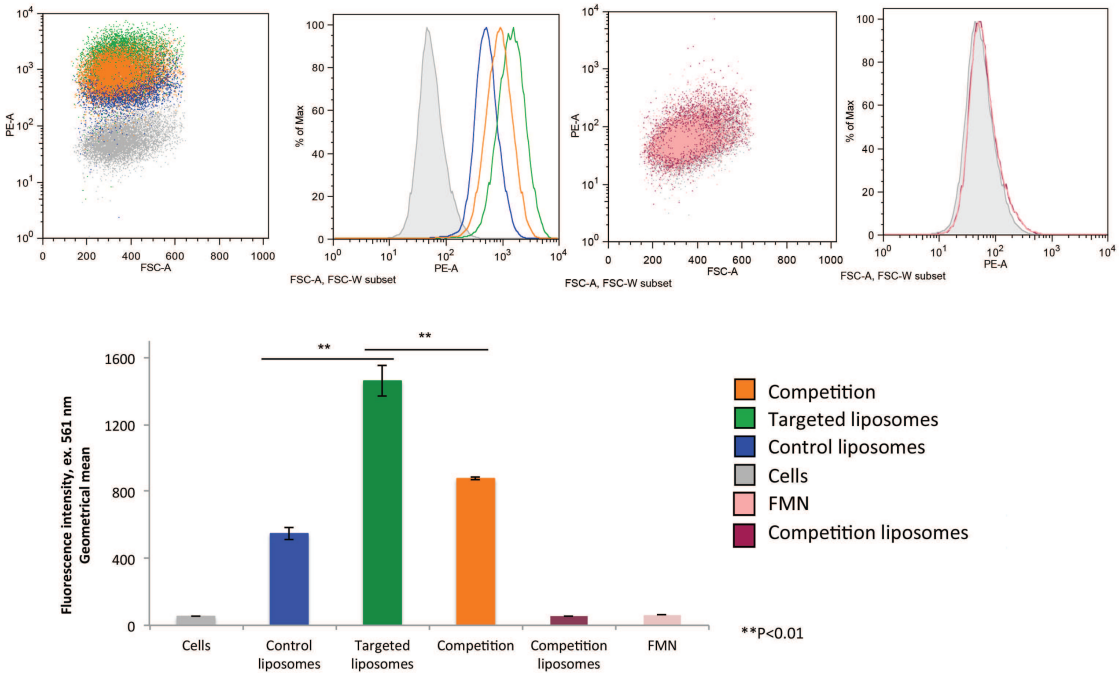

*Figure 4.12 Flow cytometry study of liposome uptake in PC3 cells (ex. 561 nm, em. 578 nm); results presented as mean ±SD from 3 individual experiments with threshold of 50,000 cells for each condition, **p<0.01.*

Hence, targeted RfdiC14 functionalised liposomes exhibited a significantly higher uptake compared to non-targeted control. The important internalisation decrease at 4°C (78%- and after pre-incubation with competition liposomes (40%) signifies that the uptake occurs in an active manner with potential involvement of RF transporters.

On the contrary, targeted liposomes with lipid derivative of RhB – Lissamine Rhodamine PE (Table 4.1) exhibited a tiny uptake increase (7%) in PC3 cells (Figure 4.13). The internalisation of LRhPE was presented by small clusters in contrast to the diffusive signal obtained from targeted liposomes with the encapsulated RhB (Figure 4.11). The moderate uptake could be due to the potential stacking interactions between LRhPE and RfdiC14 on the liposomes surface (because of the similarity in their chemical structures). This could disturb RF interactions with the transporter.

Moreover, rhodamine itself is able to promote cellular internalisation. For instance, Biswas and co-workers[154] showed an improved uptake of rhodamine-123 conjugated on the surface of the liposomes in HeLa and B16F10 cells. This signifies that rhodamine is able to create interactions with cell receptors and, due to the similarity in their structures, could also act as a RF competitor.

Therefore, LRhPE liposome labelling strategy is probably more suitable for utilisation with targeting ligands, which are not directly attached to the lipid but rather have a spacer moiety between the ligand and the liposome membrane. The spacer could prevent stacking between the ligand and the dye and avoid the unspecific interactions with the receptor. For example, O'Halloran T.V. *et al.*[155] showed an enhanced uptake of liposomes functionalised with DSPE-PEG3350-folate and labelled with LRhPE in KB and HeLa cell lines. Hence, to

avoid the issues associated with LRhPE, for all other cell experiments we utilised only liposomes with encapsulated RhB.

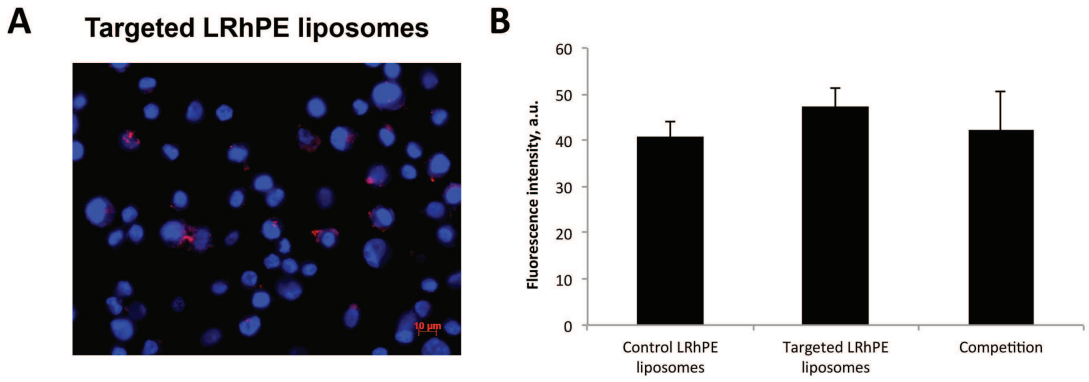

Figure 4.13 A. Fluorescence microscopy image of LRhPE liposomes uptake in PC3 cells; B. uptake of LRhPE liposomes in PC3 cells; LRhPE is red, cell nuclei marked with DAPI are blue results are presented as mean ±SD from n=10 images.

4.4.1.2 A431 and HUVECs

The experimental conditions and liposome concentrations for A431 cell line and HUVECs were exactly the same that for PC3 cells. A431 cell line displayed a 16 times higher uptake of targeted liposomes (62±23 a.u.) compared to control (4±1 a.u.) at 37°C, $p<0.001$ (Figure 4.14). Compared to the cancer cell lines, HUVECs showed a higher liposome internalization for both targeted and control formulations at 37°C. However, the uptake of RfdiC14 functionalised liposomes was still twice higher than the control (358±20 compared to 149±12 a.u respectively), $p<0.001$. The competitive binding experiment showed a significant ($p<0.01$) decrease in targeted liposomes uptake - 37% for A431 and 20% for HUVEC after the pre-incubation with 20-fold excess of RfdiC14-containing non-fluorescent liposomes. The uptake of targeted liposomes significantly decreased ($p<0.01$) at 4°C for both A431 and HUVEC indicating an active transport mechanism.

Although the cellular uptake of RF-liposomes varies among PC3, A431 cell lines and HUVECs, probably due to different densities of RF transporter expression, the results clearly show that RfdiC14 increases liposome uptake and that the internalisation is active and RF specific. Our results are in accordance with the study of Jayapaul *et al* describing FMN – functionalised iron oxide nanoparticles specific for prostate cancer cells and tumour neovasculature *in vitro*[104] and *in vivo*.[103]

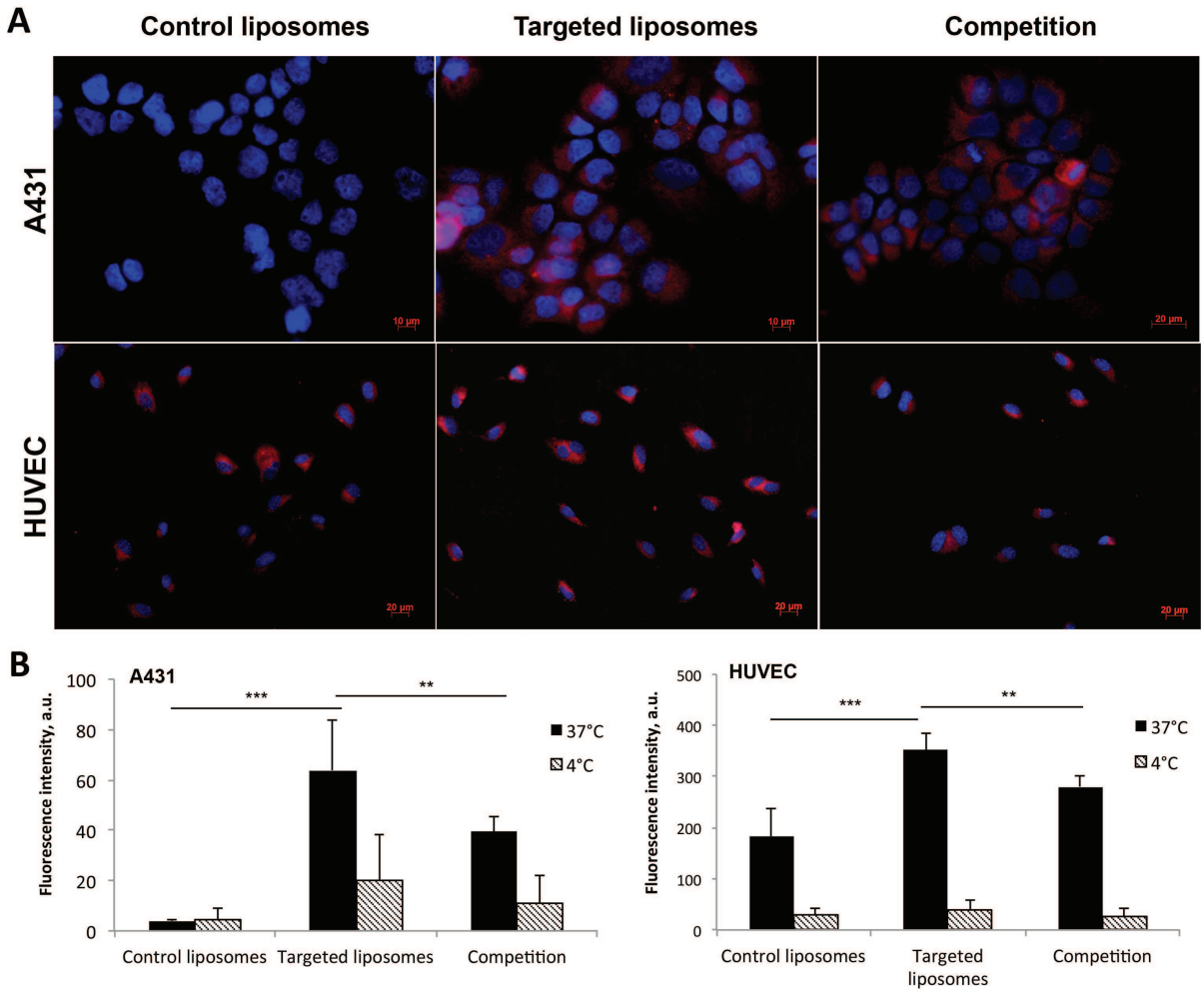

*Figure 4.14 Fluorescence microscopy images of liposomes uptake in A431 cells and HUVECs; RhB is red, cell nuclei marked with DAPI are blue; B. Uptake of liposomes in PC3 cells; results presented as mean ±SD from 3 individual experiments with n=10 images for each condition; ***p<0.001, **p<0.01.*

4.4.1.3 CT26 and MLS

Encouraged by these positive results, we studied the uptake in two additional cell lines – CT26 and MLS. However, the uptake of targeted and control liposomes in both cell lines were not significantly different (Figure 4.15). This may indicate that the RF transporter expression is not homogeneous in all cancerous tissues and RF could target only certain cancers. It might even be an advantage compared to other vitamin-based targeting agents such as folate, which receptor is overexpressed in the majority of tumours.

It is also possible, that in these two cell lines the unspecific uptake by membrane fusion or phagocytosis is prevalent. As a consequence, one is not able to distinguish RF-induced internalisation from the unspecific one.

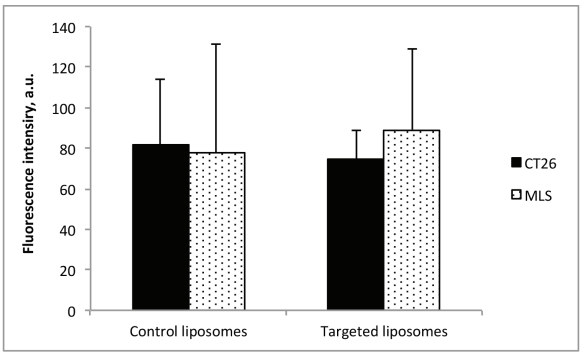

Figure 4.15 Liposome uptake in MLS and CT26 cell lines; results presented as mean ±SD from 3 individual experiments with n=10 images for each condition.

Thus, according to our studies and the literature,[103,110,116] RF-functionalised liposomes could be useful to target prostate, breast, hepatocellular and epidermoid carcinomas as well as tumour vasculature. The RF targeting *in vivo* could be a very complex approach due to the presence of two types of RF transporter proteins – RCP (RF carrier protein) a soluble protein generally presented in plasma and RFVT- a family of membrane proteins, expressed according in plasma and RFVT- a family of membrane proteins, expressed according to cell type and metabolic state. The exact targeting route of RF-conjugated nanoparticles and macromolecules is still poorly understood. Thus, RfdiC14 could be also used as a tool for lipid nanosystems functionalisation and investigation of the RF targeting and internalisation pathways.

4.4.2 Cytotoxicity study

Finally, we performed a standard cell viability test (MTT test) to evaluate the toxicity of RfdiC14 liposomes towards cells. The cells were incubated either with three concentrations of control and targeted liposomes: 50 nM – 1x, 150 nM – 3x and 250 nM – 5x for 72 hours. Then cells were incubated with MTT and blue formazan crystals formed by the living cells were solubilised in DMSO. The relative viability was expressed in % and calculated by the ratio between formazan absorbance of treated and control (untreated) cells. The data indicate an absence of specific toxicity associated with RfdiC14 as there is no significant difference between cell viability after treatment with targeted or control liposomes in all three concentration tested. The 40-60% decrease in viability at 3x and 5x concentration is most probably associated with the general toxicity of RhB administrated in high doses.[156]

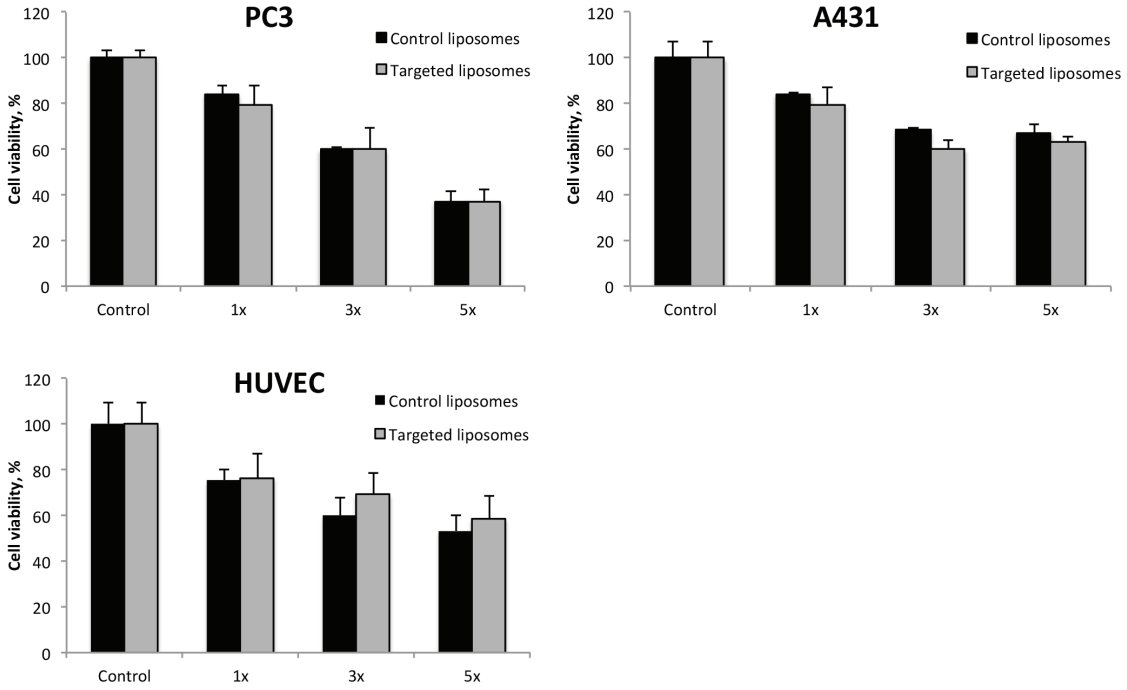

Figure 4.16 Liposome toxicity in various cells; results are presented as mean ±SD from 3 individual experiments.

4.5 Conclusions

In this chapter, we studied the insertion of RfdiC14 in the clinically relevant liposome formulation (**Platform A**). For the morphological and cell uptake studies, liposomes were prepared with 1% molar ratio of RfdiC14. Our results did not show any significant differences between control (DMPC:DMPG, 90:10 molar) and targeted (DMPC:DMPG:RfdiC14, 90:10:1 molar) formulations in terms of size, polydispersity, zeta potential or morphology. Additionally, solid ^{2}H-NMR studies did not show any substantial influence of RfdiC14 on the DMPC:DMPG membrane fluidity or order coefficient. For further cellular uptake studies, RhB or LRhPE were encapsulated in liposomes.

The uptake studies in PC3, A431 cancer cells and HUVECs showed an enhanced internalisation of targeted liposomes compared to control. The data indicate that the internalisation occurred through an active transport system due to the significant decrease in targeted liposomes uptake at 4°C in all cell lines. Moreover, competitive binding experiments proved the importance of RfdiC14 in the internalisation, as after incubation with competition liposomes the uptake of targeted liposomes significantly decreased in PC3, A431 cells and HUVECs. In contrast, two other cancerous cell lines (CT26, MLS) did not show specific, transporter-mediated uptake of targeted liposomes, probably due to the absence of specific receptors.

Thus, RfdiC14 could be efficiently inserted into the lipid containing nanosystems and rendered them tumour-specific in several types of cancer. Moreover, taking into account that the exact mechanism of RF internalisation and transport still remains unclear, such nanosystems could be also utilised as a pharmacological tool to study the function of RF-transporters and their signalling pathways.

However, the utilisation of conventional liposomes *in vivo* is limited by their short circulation time and opsonisation by plasma proteins. A hydrophilic polymer coating (e.g. PEG) is generally utilised to avoid these issues. Thus, to evaluate RF targeting efficiency *in vivo*, polymer coated liposome formulation and a new RF amphiphile with a polymer spacer between RF and lipid (**Platform B**) was prepared. Its synthesis was previously described in Chapter II (2.4).

5 Chapter V. Platform B: RFA-functionalised long-circulating liposomes

Platform B is a model drug delivery nanosystem aimed to study the potential of RFA to target cancerous cells *in vivo*. It is represented by a stable liposome formulation with polymer coating and RF-amphiphile as a targeting moiety (DSPE-PEG-RF). Based on previous *in vitro* results (described in Chapter IV), two xenograft tumour models, A431 and PC3, were selected.

A431 is derived from human epidermal carcinoma and frequently utilised as a model for the studies dealing with epidermal growth factor receptor.[157] A431 subcutaneous xenografts grow rapidly in mice and like a lot of solid tumours, they suffer from high interstitial pressure and very restricted stromal compartement, which limits passive drug accumulation.[158] The EPR effect in such tumours is restricted. Thus, the development of an active targeting strategy that will ensure cell binding is extremely important.

PC3 is a model of androgen-irresponsive prostate cancer, which shares common features with human prostatic small cell neuroendocrine carcinoma.[147] PC3 cells do not express prostate-specific antigen and thus the development of targeted therapies for these cells is very useful. Although orthotropic prostate cancer models are more precise because they develop in host organ environment, subcutaneous xenografts are still a good option for the first pre-clinical trials.[159]

The tumour accumulation and biodistribution of DSPE-PEG-RF-functionalised liposomes was assessed by two different imaging modalities – photoacoustic imaging (PAI) and fluorescence molecular tomography (FMT) combined with micro-computer tomography (μCT). Accordingly, appropriate liposome labels were selected for each imaging modality. Indocyanine green (ICG) was chosen for photoacoustic visualisation of tumour accumulation and lipid derivative of cyanine (DiR) was chosen for the biodistribution studies with μCT/FMT system. Both are near-infrared dyes, which upon liposome preparation are located in the lipid bilayer. Therefore, two separate liposome formulations, Platform B1 and Platform B2, were prepared. They shared the same lipid composition, but had different labelling.

Due to the limited number of available animals we assigned one liposome type per one tumour model. As a consequence, Platform B1, encapsulating ICG, was evaluated in A431 tumours by PAI. Platform B2, encapsulating DiR, was evaluated in PC3 tumour model with μCT/FMT imaging modality.

First of all, in this section we will show the optimisation of liposome formulation and the implementation of liposome platform incorporating the corresponding RF amphiphile. The appropriate choice of lipids and liposome labelling will be discussed. Then, the delivery efficiency of RFA-functionalised liposomes (targeted) will be studied *in vitro* and *in vivo*. We are going to present the potential of targeted ICG liposomes (Platform B1) as optoacoustic contrast agent and visualise their accumulation in A431 tumour xenografts over time. The longitudinal biodistribution of targeted DiR liposomes (Platform B2) was visualised by a combined μCT/FMT imaging system in PC3 tumour model.

5.1 Introduction on PA and µCT/FMT imaging modalities

5.1.1 Photoacoustic imaging

PAI is a combination of optic and acoustic imaging also referred as optoacoustic. The main features of PAI as imaging modality are: ability to gather functional and molecular information in real-time, absence of ionizing radiation, high spatial resolution and clinically relevant imaging depths.[160]

In this technique, short laser pulses (~5 to 50 ns) are transmitted to the tissue and generate a thermoelastic expansion of an absorber in NIR (near infrared) range. This selective absorption and thermoelastic response create acoustic waves detected by an ultrasound transducer at the tissue surface (Figure 5.1.B).[161]

Photoacoustic (PA) effect was discovered by Alexander G. Bell in 1880s, but its biomedical application was not feasible till the development of enough intense and reliable light sources in 1980s. Since then, a lot of efforts were put by the scientific community for the development of PAI imaging devices and their biomedical applications. Examples of such preclinical studies include the research dealing with: non-fluorescent pigments (red blood cells & melanin), angiogenesis and anti-angiogenic response, microcirculation physiology and pathology, drug response for screening, brain functions and biomarkers. The clinical studies involving PAI include: breast and prostate cancer detection, guided sentinel lymph node needle/core biopsy for breast cancer staging, neonatal and adult brain imaging, blood flow, oxygenation, and tissue metabolism imaging, early response to chemotherapy and many others.[162]

The contrast in PAI is achieved with intrinsic absorbers such as haemoglobin, melanin, DNA, RNA etc.) and exogenous absorbers like gold nanoparticles or organic near-infrared dyes.

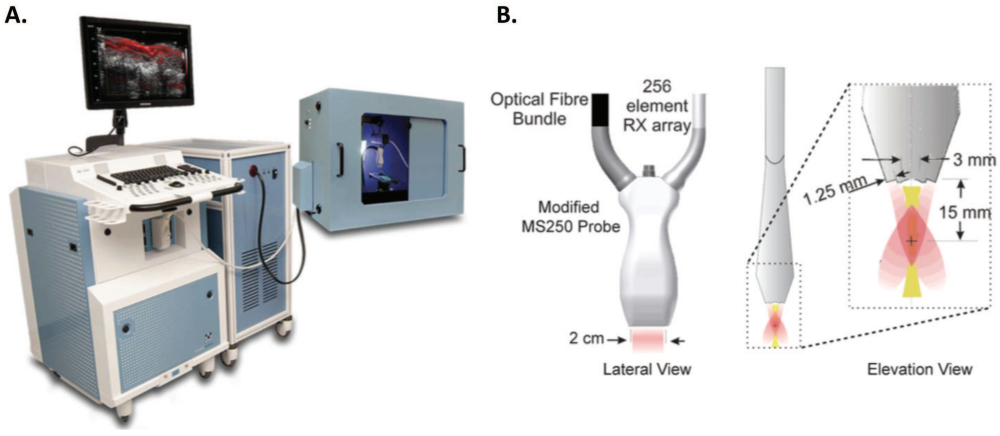

Figure 5.1.A. Photograph of PAI Vevo®LARZ system; B. scheme explaining PAI transducer construction: separate cable/fibre-optic packages are used for optical and acoustic elements. Laser excitation in the range from 680 to 970 nm goes through optical fibre bundle. The generated by the tissue ultrasound response is collected by 256 element RX array and transferred to a scanner that reconstructs PA signal.[161,163]

Compared to conventional optical imaging, PAI penetration depth is much deeper,

because the optical contrast is determined by acoustic waves. Moreover PAI works in NIR 'therapeutic' window (670-900 nm) where tissue absorption is limited and thus the detection of NIR tracers is facilitated. The exceptions are oxygenated and deoxygenated haemoglobin in blood as well as melanin in skin that possess high absorption wavelength (750, 850 and 700 nm respectively). This gives an additional feature to PAI – the detection of oxygen saturation (sO_2) in blood and organs.[161,164] For our studies we used PAI Vevo®LAZR system (FujiFilm Visualsonics, Netherlands) presented on Figure 5.1.A.

5.1.2 Combined µCT/FMT imaging

FMT allows longitudinal and non-invasive determination of fluorescence signal distribution *in vivo*.[165] In the FMT setup, a laser beam illuminates the subject with an injected fluorescent probe at a particular wavelength. The light propagates in the subject and the emitted fluorescence is captured by an objective lens and recorded with a CCD camera. The wavelengths are distinguished by the corresponding bandpass filters installed on the camera lens.[166]

FMT is widely used in preclinical studies to access the biodistribution of novel probes, study disease progression and visualise angiogenesis, apoptosis, inflammation *etc*. with specific fluorescent probes. Another advantage of FMT is the possibility of 3D reconstruction of the fluorescence signal in organs and tissues in depths of several centimetres. The FMT combination with anatomical imaging modality such as μCT is highly beneficial for image reconstruction and improved signal to organ localisation. μCT anatomical data fused with FMT fluorescence map allow the precise reconstruction of organs and tissues in 3D volume and thus, a more accurate determination of fluorescence signal (Figure 5.2).[165,167]

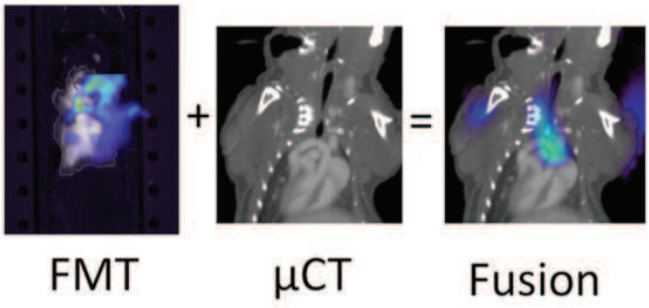

Figure 5.2 Schematic presenting µCT/FMT hybrid system (from poster 10.1594/ecr2011/C-2265).

Gremse F. *et al.*[167] optimised data treatment and reconstruction protocols for μCT/FMT imaging by taking into account the intrinsic tissue absorption. Tissue and organ absorption is highly dependent on their relative blood volume (rBV). rBV varies a lot among different tissues – e.g. 2% for muscle, 30% for liver and 100% for pure blood. As the majority of the probes are injected intravenously, rBV of the organ greatly influences on emitted fluorescence signal (e.g., the more the organ is perfused, the more signal comes from blood and not from the organ). Thus, an absorption map was developed to determine accurately the fluorescence signal coming from strongly perfused organs such as heart, kidneys and liver. In our studies we utilised the reconstruction protocol,[165] where μCT and FMT data were fused automatically and upon reconstruction each organ or tissue had its own optimised absorption coefficient.

5.2 Platform design

Once injected intravenously liposomes could be subject to various transformations – opsonisation by plasma proteins, rapid cleavage by macrophages, fast lipid disassembly and content release, which could significantly affect their drug carrier properties. For this purpose it is extremely important to control liposome size, charge, surface chemistry and stability.[30,34,36] Moreover, it is important to choose a suitable label for the efficient study of liposome biodistribution *in vivo*. The perfect liposome label should be stably entrapped in the formulation, possess a low detection limit and good biocompatibility. Due to their low tissue absorption, high quantum yield and generally low toxicity, near-infrared dyes are the most adapted candidates for the liposome labelling.[168]

In this section, we will first attempt to find an appropriate lipid composition for our *in vivo* studies. We will also discuss the choice of different near-infrared dyes for the Platform B1 and B2 labelling – indocyanine green (ICG) and a lipid derivative of cyanine – DiR (1,1'-Dioctadecyl-3,3,3',3'-Tetramethylindotricarbocyanine Iodide) respectively.

5.2.1 Composition optimisation

When designing a liposome formulation, one should take into account several important parameters. The choice of lipids and their molar ratios will have a direct impact on liposome characteristics – size, morphology, surface charge and stability. These parameters are influenced on the one hand, by the chemical nature of phospholipids – headgroup charge, alkyl chain length, unsaturation, and on the other hand, by the addition of supplementary lipids such as cholesterol or polymer-lipid conjugates.

To find an appropriate formulation for our *in vivo* studies, we prepared eight different liposome formulations with variable lipid compositions and molar ratios (Table 5.1). The chemical structures of lipids used for this study are presented in Figure 5.3. The lipid concentration (20 mM in 1 mL) as well as buffer parameters (HEPES 10mM, pH=7,4, sucrose 9,25% m/v) and preparation protocol were kept constant. All formulations were prepared by the film hydration method with subsequent extrusion through 800, 400, 200 and 100 nm polycarbonate membranes and purification by size-exclusion column chromatography as described in section 4.2. The main features (hydrodynamic size, zeta potential, PDI and phosphorus content) of each formulation are presented in Table 5.1.

Table 5.1 Prepared liposome formulations.

Name	Lipids	Hydrodynamic size, nm	PDI	Zeta Potential, mV	P content, mg/ml	PDI after 7 days
L1	OSPC:SOPG:DOPE-PEG 88:10:2	155±6	0,29	-11,9±3	2,3	nd
L2	OSPC:SOPG:DOPE-PEG 85:10:5	123±2	0,09	-15,6±1,7	2,6	0,18
L3	OSPC:Chol:SOPG:DOPE-PEG 65:20:10:5	125±14	0,26	-5,7±4,9	1,79	0,50
L4	OSPC:Chol:DOPE-PEG 69:30:1	131±57	0,63	-5,7±2,1	nd	nd
L5	OSPC:Chol:DOPE-PEG 68:30:2	199±47	0,40	-5,3±2,2	nd	nd
L6	OSPC:Chol:DOPE-PEG 65:30:5	125±3	0,11	-12,0±2,1'	1,72	0,18
L7	DPPC:Chol:DOPE-PEG 65:30:5	124±2	0,10	-13,6±1,6	1,52	0,15
L8	DPPC:Chol:DSPE-PEG 65:30:5	132±1	0,06	-17,0±1,0	1,88	0,11

The average size distribution of liposomes is known to change over time. Upon storage, liposomes tend to fuse and grow into bigger vesicles, which could lead to liposome damage and drug leakage. Moreover, the major constituents of liposomes - phospholipids are known to undergo oxidative reactions. Therefore, the prepared formulations were monitored and compared in terms of their PDI variations and encapsulated drug leakage.

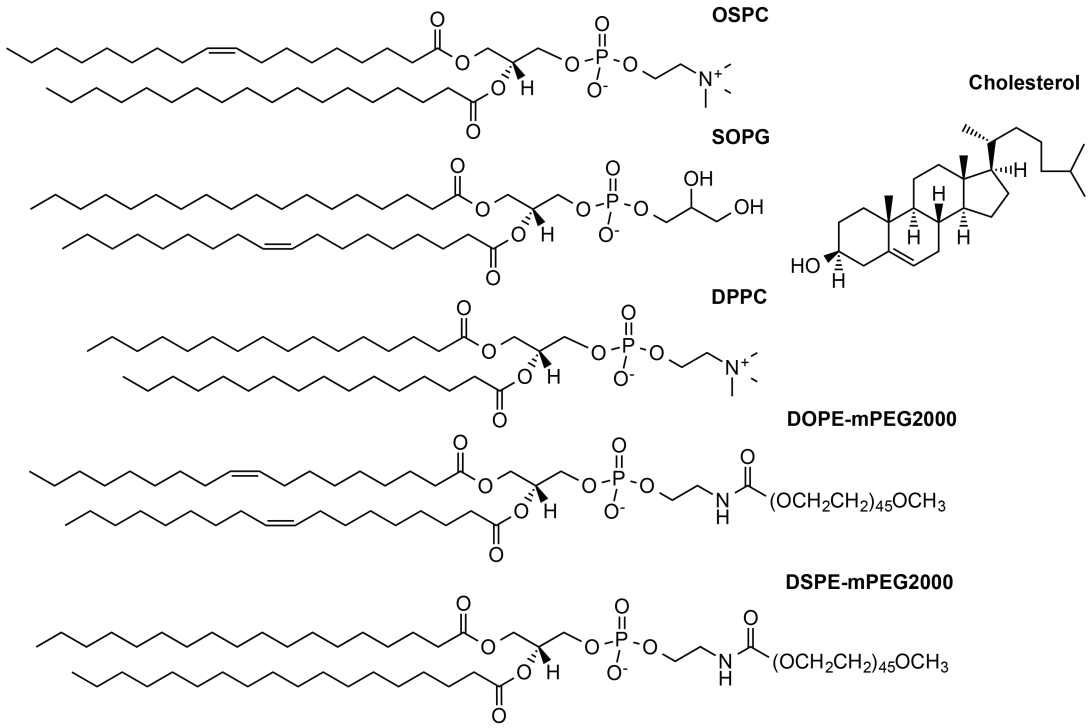

Figure 5.3. Chemical structures of lipids utilised for liposome preparation.

The encapsulated drug leakage of liposomes was studied in several formulations by a calcein leakage assay.[169] Calcein is a fluorophore (ex. 495, em. 515 nm) that autoquenches at high concentrations (70-100 mM). Thus, when encapsulated in liposomes it does not emit fluorescence. If the liposome membrane is damaged, calcein leaks out and starts emitting fluorescence, because of the dilution in the surrounding buffer (Figure 5.4.A.). The detailed calculations of calcein leakage % are presented in the experimental procedures section.

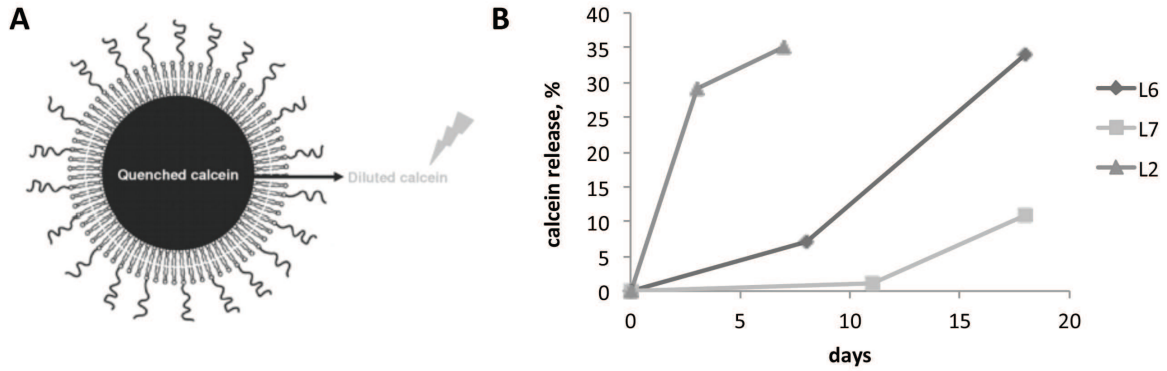

Figure 5.4.A. Schematic of calcein leakage assay; B. Calcein release in different liposomal formulations over time.

Liposomal formulations L2, L6 and L7 were prepared in presence of 70 mM of calcein and the increase in fluorescence at 515 nm was monitored over time. The results are shown in Figure 5.4.B and will be discussed further.

5.2.1.1 Alkyl chain length and unsaturation

The synthesised DSPE-PEG-RF amphiphile has two saturated stearyl (C18) chains. Thus, the lipids for basic formulation, where DSPE-PEG-RF could be inserted, should present more or less a similar chain length. A similar acyl chain length in the formulation helps to create more homogeneously packed membrane and thus should improve the liposome stability. The alkyl chain length, unsaturation, charge, and headgroup species directly influence the lipid phase transition temperature (Tm). Tm is extremely important in the liposome preparation process and its *in vivo* behaviour.[17]

As discussed previously, phase Tm is represented by the temperature that induces change in the lipid physical state from the ordered gel phase, where the acyl chains are fully extended and closely packed (*so*), to the disordered liquid crystalline phase, where the acyl chains are randomly oriented and fluid (*lo*). Within the increase in the acyl length, van der Waals interactions become stronger requiring more energy to disrupt the ordered packing, therefore the phase transition temperature increases. Likewise, a *cis* double bond or unsaturation, introduced in the hydrocarbon chain, puts a kink in it and decreases a temperature required for disrupting an ordered packing arrangement.[17,148]

*Table 5.2 Examples of lipids, their phase transition temperature and net charge**

Name	Fatty Acid	Transition Temperature (°C)	Net Charge at pH 7.4
DMPC	14:0	23	0
DPPC	16:0	41	0
DSPC	18:0	55	0
DOPC	18:1	-20	0
OSPC	18:1-18:0	9	0
DMPE	14:0	50	0
DPPE	16:0	63	0
DOPE	18:1	-16	0
DMPG•Na	14:0	23	-1
DPPG•Na	16:0	41	-1
DOPG•Na	18:1	-18	-1
SOPG•Na	18:0-18:1	N/A	-1
DSPE-mPEG-2000•Na	18:0	N/A	-1

*adapted from Avanti Polar Lipids website http://avantilipids.com

The saturated stearyl chains possess a high phase transition temperature (55°C), compared to other lipids (Table 5.2), which could make liposome preparation more complex (risk of the encapsulated material degradation during heating). Moreover, pure DSPE liposomes will be too rigid. Consequently, the release of their content once reached the targeted cells might be difficult.[148] For this reason, we chose lipids with lower phase transition temperature and, at the same time, appropriate chain length such as monounsaturated OSPC and SOPG, bisunsaturated DOPE-mPEG2000; and saturated DSPE-mPEG2000 and DPPC (Figure 5.3). DMPC and DMPG utilised in previous formulations were not considered due to the short alkyl chain length (only 14 carbons).

The minimal calcein leakage was observed during at least 10 days in L7 formulation. In contrast, fast calcein release occurred in L2 formulation and a slower, but more important release, in L6 liposomes. This could be explained by the higher stability of saturated DPPC lipid over OSPC, which possesses one double bond and thus is more susceptible to lipid oxidation. Lipid oxidation causes permeability changes within liposome bilayer and may induce drug leakage and adverse phospholipid-drug reactions.[170]

Another advantage of DPPC utilisation for targeted liposomes is the possibility of thermosensitive release in the tumour site.[171] The transition temperature of DPPC is close to tumour hyperthermia which is around 40-42°C.[172] Consequently, the accumulation of DPPC liposomes in the tumour tissue could induce changes in membrane state from gel to liquid crystalline phase and subsequent drug release. Several research groups reported DPPC thermosensitive liposomes efficient for drug delivery and control release.[173–175] DPPC is also used in thermosensitive liposomal formulation of doxorubicin (ThermDox®) which is under clinical trials.[148]

5.2.1.2 Cholesterol content

Mosca M. *et al*.[176] showed that cholesterol was able to prevent lipid oxidation by stabilising the bilayer under transition temperature of other lipids. Thus, DPPC in combination with cholesterol (L7) was more beneficial compared to OSPC (L6). Because at room temperature DPPC is in the gel state, it could keep membrane intact much longer.

Indeed, cholesterol is widely known to improve liposome stability and prolong its shelf-life. It increases the rigidity of the membrane by feeling the gaps in the bilayer and helping to maintain the membrane in the ordered gel state. Moreover, this is due to fewer interactions with plasma high- and low-density lipoproteins (HDL and LDL) and decreased leakage of liposome convent *in vivo*.[33]

We found that 30% molar of cholesterol were optimal for our formulations. Indeed, the formulations containing this amount of cholesterol (L4-L8) generally were more stable and monodisperse compared to the ones without cholesterol. However, not only membrane rigidity, but also surface chemistry contributes to the colloidal stability of liposomes. This could be achieved by the addition of negatively charged lipids such as phosphatidylglycerols and/or hydrophilic polymer-lipid conjugates (i.e. DSPE-PEG or DOPE-PEG).

5.2.1.3 PEG-conjugates and surface charge

For the optimisation study we choose DOPE-PEG2000 as PEGylated lipid. It possesses low transition temperature known for monounsaturated lipids and thus the liposomes could be prepared without additional heating. Various amounts of DOPE-PEG2000 in the formulation were tested – from 1 to 5% molar ratio. The data show that 1-2% of DOPE-PEG2000 produce highly polydispersed liposomes (PDI from 0,29 to 0,63).

Dos Santos N. *et al*.[177] demonstrated the prolonged circulation time and optimal PEG coverage could be achieved with 2-5% molar of DSPE-PEG2000 in DSPE liposomes. In our case, the classically utilised[148,178] 5% molar of PEGylated lipid gave better results in terms of polydispersity (PDI from 0,06 to 0,26) and liposome stability during storage compared to 1%.

In contrast, utilisation of a charged phospholipid – SOPG in 10% molar ratio was not beneficial for liposome stability, for instance the twice increase of PDI after 7 days of storage at +4°C was observed for L2 and L3 formulations. In contrast, 30% molar of cholesterol in combination with 5% molar of DOPE-PEG2000 prevented liposome aggregation in buffer (formulation L7).

The hydrodynamic size was similar for the three most monodisperse formulations (PDI<0,2) – L2, L6, L7 with an average of 124±1 nm. Their zeta potentials were also very close – in average -13,7±1,7 mV. Such negative zeta potential could be explained by the presence of charged DOPE-PEG2000 and is in accordance with previous findings.[179] The negative zeta potential contributes to the colloidal stability of liposomes. However, some studies suggest that negatively charged liposomes could induce the activation of complement system and thus rapid elimination from the blood flow.[33] Nevertheless, PEGylated anionic liposomes still circulate for a longer time than non-PEGylated ones.[180]

In summary, L7 was selected as the most potent formulation for *in vivo* tests in terms

of size and drug leakage. However, to exclude the risk of lipid oxidation we prepared a similar formulation (L8) with saturated DSPE-PEG2000 lipid instead of DOPE-PEG2000. The L8 liposomes had an hydrodynamic diameter around 132 nm (PDI 0,06) and a negative zeta potential of 17±1 mV. This lipid composition DPPC:Chol:DSPE-PEG (65:30:5 molar) is very similar to clinically utilised liposomal doxorubicin (Doxil®).[178] The L8 formulation was employed for all further experiments.

5.2.1.4 Control of total P content

We also controlled the phosphorus content in each formulation to calculate the dose of liposome injection *in vivo*. The animal testing regulations in Europe require the precise quantities of formulation designated for injection. Generally, in the case of liposomes the total amount of phospholipids per kg of animal is necessary. The dose, found in the literature[83,87] as non-toxic for an injection in mice, was 10 mg/kg of body weight. Therefore, we adapted our liposome preparation procedure to reach this amount of phospholipids per injection.

The total phosphorus content (mg/mL) in liposomes was determined with the classic Rouser method.[181] It was around 2 mg/mL for the prepared formulations and depended on liposome dilution upon purification on the size-exclusion chromatography column (Table 5.1). It is important to note, that in the case of utilisation of cholesterol, total phosphorus content is lower, than for other formulations, as cholesterol does not have a P in its structure. However, the total initial concentration of lipids stays the same.

The average nude mouse weight is about 20 g, thus per one mouse the maximum of 0,2 mg of lipids should be injected. Taking into account the optimal injection volume of 100 μL per mouse, the concentration in solution should be 0,2 mg/100 μL or 2 mg/mL. This concentration and corresponding preparation method were conserved for all our *in vivo* experiments.

5.2.2 Choice of labelling

5.2.2.1 PAI

Contrast enhancement in PAI could be achieved with the help of metal nanoparticles (e.g. gold nanorods) or organic chromophores and fluorophores. Gold nanoparticles are the current standard in PAI, due to their strong and photostable signal. However, they could induce some toxicity issues and long tissue retention. Thus, clinically approved fluorophores, like ICG or methylene blue, could be the molecules of choice, even though their optoacoustic signal is lower.[160]

ICG is a clinically approved near-infrared (NIR) dye utilised in ophthalmology for visualisation of retinal blood vessels. It is non-toxic and non-ionising, has an absorption maximum around 780-800 nm (depending on the environment) and fluoresces in NIR window (Figure 5.5). However, ICG fluorescence is not linear with the concentration. In blood, ICG binds to plasma proteins and is rapidly excreted. It is also unstable in buffer solutions and has non-linear fluorescence quantum yield versus concentration.[182,183] The encapsulation of ICG in liposomes showed a significant improvement of its circulation lifetime, stability and optical properties.[184–186]

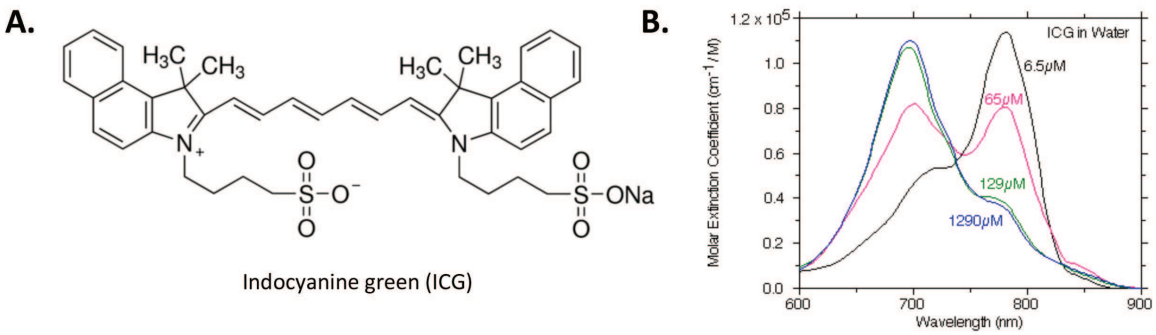

Figure 5.5.A. Chemical structure of ICG. B. ICG extinction coefficient in water.

Recently, Beziere N. *et al.*[184] reported PEGylated ICG-loaded liposomes (LipoICG) as potent optoacoustic contrast agent. Their homemade LipoICG was found more stable *in vitro* and circulated longer *in vivo* compared to free ICG. Moreover, the photoacoustic (PA) signal generated by LipoICG was stronger than the one from gold nanoparticles. The authors employed spectral unmixing techniques to distinguish ICG signal from intrinsic haemoglobin and melanin absorption and monitored LipoICG accumulation in subcutaneous tumour xenografts in mice. This new contrast agent represents a great promise in optoacoustic imaging for visualising vascular permeability and lymphatic system in tumours.

Hence, we decided to encapsulate ICG for monitoring the RFA-functionalised liposome (Platform B1) accumulation with photoacoustic imaging in A431 tumour xenografts in mice.

5.2.2.2 μCT/FMT

FMT works in NIR range – 635 - 790 nm excitation wavelength to exclude interferences with tissue auto-fluorescence. The fluorophores used for FMT imaging could be divided into two groups: inorganic such as quantum dots or upconverting phosphors or organic such as cyanine derivatives, porphyrins or squaraines.[187] Among all these fluorophores only ICG is clinically approved so far. However, ICG fluorescence emission is not linear with the concentration changes and it possesses a very low quantum yield comparable to other dyes. Thus, commercially available and widely used dyes such as AlexaFluor700, Cy7 or DiR have 25, 28 and 28% quantum yield, whereas ICG has only 1,3%.[187]

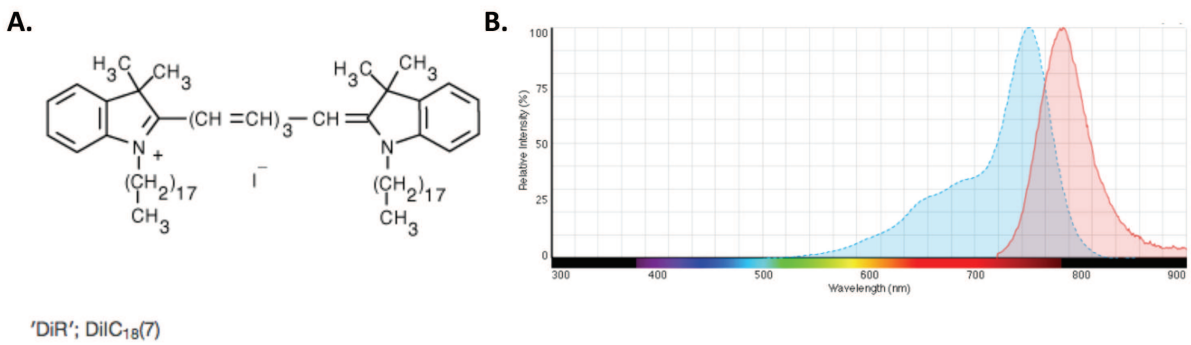

Figure 5.6.A. DiR chemical structure; B. DiR absoption and fluorescence emission spectra.

DiR or 1,1'-dioctadecyl-3,3,3',3'-tetramethylindotricarbocyanine iodide is a lipid

derivative of cyanine (Figure 5.6). It is utilised for membrane labelling and cell tracking *in vitro*[188] and *in vivo*.[188–190] DiR is excited at 750 nm and emits strong fluorescent signal at 782 nm, when located in lipid environment. In contrast, DiR fluorescence in water is weak (Life technologies).

Due to its high quantum yield and good stability in lipid environment, DiR is an excellent candidate for the preparation of NIR fluorescent liposomes. Therefore, we decided to use it for the labelling of Platform B2 designed to study the biodistribution of RFA-functionalised liposomes in PC3 tumour model.

5.3 Platform B1: RFA-functionalised ICG liposomes for PAI

5.3.1 Preparation and characterisation

5.3.1.1 Physicochemical properties

Two batches of liposomes – control and targeted were prepared (Figure 5.7). The control ICG liposomes consisted from the lipid mixture corresponding to described earlier L8 formulation. ICG was dissolved in HEPES buffer used for lipid film hydration. ICG is a mainly water-soluble fluorophore, but in liposomes it is generally situated in the lipid bilayer due to its amphiphilic nature. This could be visualised by the changes in ICG absorption spectra (Figure 5.9) as it is sensitive to the ICG environment.

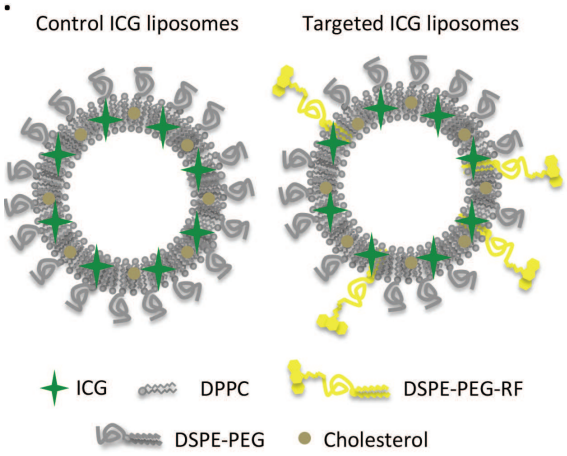

Figure 5.7. Scheme of control and targeted ICG liposomes.

Control liposomes were 97±1 nm in size (PDI 0,09) and had a negative zeta potential of -18±1 mV (Table 5.3). In targeted liposomes DSPE-PEG2000 was replaced by our PEGylated RF amphiphile - DSPE-PEG2000-RF. As already discussed, even after purification by HPLC, the product presented a mixture of unreacted DSPE-PEG2000-COOH (which will be in the form of $–COO^-$) and the desired amphiphile DSPE-PEG2000-RF (environ 3:1 mass ratio). Therefore, 5% molar of such mixture in liposome composition represents approximately 3,75% for DSPE-PEG2000-COO^- and 1,25 % for DSPE-PEG2000-RF. Like we mentioned in the section 4.2 – 1% molar of ligand in liposomes is sufficient for its targeting efficiency.[39,75]

The prepared targeted ICG liposomes were slightly bigger in size than control ones – 112±1 nm (PDI 0,11) and had a more negative zeta potential of -26±1 mV (Table 5.3). This could be explained by the presence of additional negative charges brought by the carboxylic acid moiety of DSPE-PEG2000-COO^-. Overall the presence of ICG decreased the mean hydrodynamic size of liposomes compared to formulation L8. This is not surprising as encapsulated drug molecules were shown to influence the physicochemical properties of liposomes (i.e. mean hydrodynamic diameter).[30]

Table 5.3 Physicochemical properties of ICG liposomes

Name	Lipids	Size, nm	PDI	Zeta Potential, mV	ICG, µM
Control ICG liposomes	**DPPC:Chol:DSPE-PEG 65:30:5**	**97±1**	**0,09**	**-18±1**	**97**
Targeted ICG liposomes	**DPPC:Chol:DSPE-PEG-RF 65:30:5**	**112±1**	**0,11**	**-26±1**	**112**

The presence of RF in the formulation was confirmed spectroscopically. On the fluorescence emission spectra (Figure 5.8) one could observe a characteristic for a RF peak at 530 nm in targeted ICG liposomes and the beginning of an ICG emission in NIR region in both targeted and control formulations.

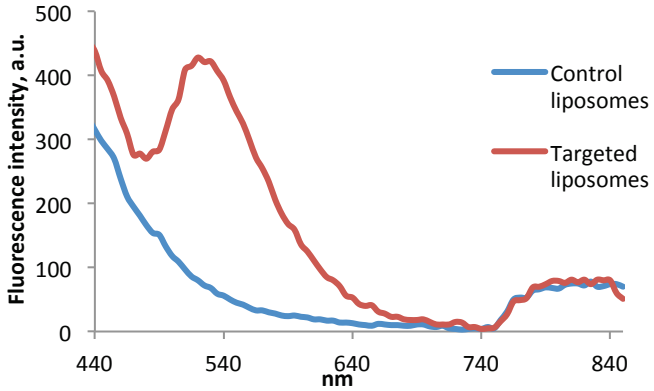

Figure 5.8 Fluorescence spectra of control and targeted liposomes

Because ICG fluorescence signal is not linear with the concentration, it was quantified by the absorption. Liposomes were dissolved with 10% DMSO in buffer and ICG absorbance was measured at 780 nm. The exact amount of ICG and RF in the formulation was calculated with the help of calibration curves - $y=59087x$ (R^2=0.9939) for RF and $y=21604x$ (R^2=0.9591) for ICG, where y represents fluorescence intensity for RF and Abs for ICG and x - concentration in μM. Control liposomes contained a slightly lower amount of encapsulated ICG than targeted liposomes (97 μM and 112 μM respectively).

Although we know that the competitive binding phenomenon *in vivo* is quite complex and the limited injection dose in terms of total phospholipid content makes this experiment difficult to realise, we also prepared competition liposomes. These DSPE-PEG-RF containing liposomes were free from labelling and had an average hydrodynamic diameter of 132±1 nm (PDI 0,09) and a negative zeta potential of -35±1 mV.

In summary, DSPE-PEG-RF was successfully inserted in liposomal formulation with an encapsulated ICG. Compared to control formulation, our RFA derivative induced only small changes in zeta potential towards more negative values. Such negative zeta potential could, on the one hand, enhance the colloidal stability of liposomes, but on the other hand, decrease cellular uptake due to steric repulsions (cell membranes are also negatively charged). Nevertheless, in the case of active targeting, this situation may be even beneficial, as it may

contribute to the decrease of unspecific interactions between cells and liposomes.

5.3.1.2 *in vitro stability evaluation*

Lipid surrounding modifies ICG absorption spectra with a shift from 780 towards 800 nm and change in the ratio between its two absorption maxima. Incubation in 50% FBS (foetal bovine serum) and interaction with serum proteins also induces changes in ICG optical properties. Thus, the absorption maximum for liposomes in serum is at 800 nm and it is approximately 20% higher than in buffer. The variations of ICG and ICG liposomes absorption spectra are presented on Figure 5.9.A.

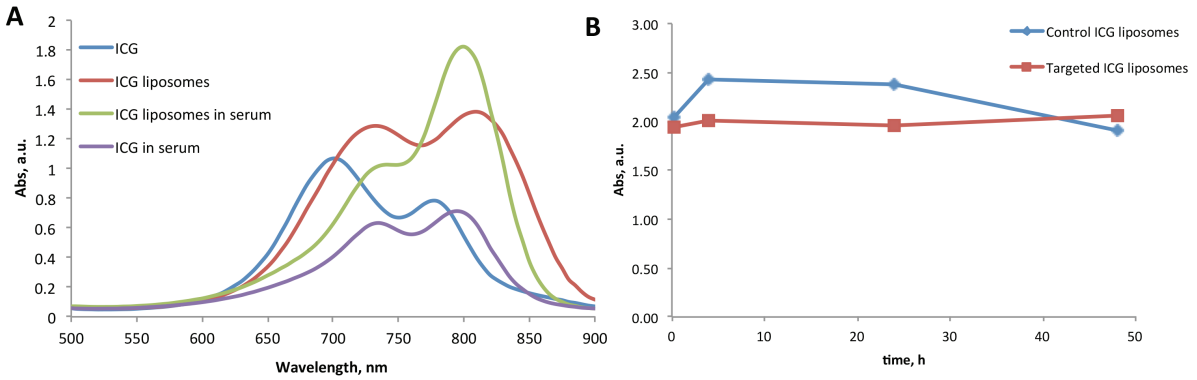

Figure 5.9.A. ICG absorbance spectra in different conditions (the results are similar for control and targeted liposomes); B. Absorbance at 800 nm at various time points after liposomes incubation with 50% FBS at 37°C.

We also monitored liposome stability in 50% FBS at 37°C over time (15 min, 4h, 24h and 48h). The results presented on Figure 5.9.B. indicate no significant changes in ICG absorption after incubation with FBS during 48h for both control and targeted liposomes. The size distribution and zeta potential of liposomes before and after incubation with FBS were also analysed. For the control ICG liposomes the average hydrodynamic size was slightly higher (+5 nm) and PDI increased 2,7 times. Zeta potential of control ICG liposomes became twice more negative – from -18 mV to -36 mV. As for the targeted ICG liposomes, their mean hydrodynamic size increased slightly, zeta potential did not changed, but PDI increased 3,7 times.

Table 5.4 Liposome properties after incubation with 50% FBS

Name	Size, nm	PDI	Zeta Potential, mV
Control ICG liposomes	103±1	0,24	-36±3
Targeted ICG liposomes	110±2	0,41	-24±2

Probably, the presence of RF generates more interactions with serum proteins and thus could reduce targeted liposomes circulation time compared to control. However, a recent study from Hadjidemetriou M. and co-workers[191] indicates, that the *in vitro* stability tests do not always reflect the situation *in vivo*. They tested 3 different types of liposomes – bare, PEGylated and PEGylated with a targeting agent (IgG). The liposomes were either injected in CD-1 mice and recovered from the blood or incubated with CD-1 mouse serum. After *in vitro*

incubation, liposomes displayed protein coronas organised in fibrillar network on the liposomes surface. The protein coronas from liposomes injected *in vivo* were similar, but in contrast to the *in vitro* study, the surface was not completely covered with proteins. Cellular binding studies showed reduced uptake for all types of liposomes after protein corona formation. Nevertheless, targeted liposomes showed significantly enhanced cellular internalisation compared to non-targeted after both, *in vivo* and *in vitro* protein corona formations.

Hence, a targeting agent on the surface of long-circulating liposomes is always a risk. Blood half-life of such nanosystems could be reduced and as a consequence, passive accumulation in the tumour site via EPR effect could be also decreased. However, targeted nanosystems still remain an essential alternative for fragile or highly active biomolecules delivery such as nucleic acids or proteins that need cellular internalisation to accomplish their therapeutic activity.[77]

5.3.2 Biological evaluation

5.3.2.1 in vitro

The targeting efficiency of DSPE-PEG-RF derivative was evaluated *in vitro* on A431 cell lines. This experiment was aimed to control the targeting performance of DSPE-PEG-RF *in vitro*, before proceeding with an *in vivo* study. Although, ICG is a promising fluorophore for *in vivo* studies, it is not always suitable for *in vitro* because of its high fluorescence emission wavelength (>800 nm), which required special microscopy equipment. For this reason, we encapsulated Rhodamine B in the control and targeted liposomes to perform uptake studies in A431 cells. Liposomes were prepared in the same way that was previously described for non-PEGylated formulations (section 4.2).

A431 cells were incubated with control and targeted PEGylated liposomes (50 nM in 100 μL, RhB concentration) for 30 min at 37°C. The uptake was observed by fluorescence microscopy and quantified by RhB fluorescence signal (ex. 554, em. 605). DSPE-PEG-RF containing liposomes showed a 5,9 times significantly higher ($p<0,001$) uptake compared to control liposomes – 95±18 and 16±2 a.u. respectively (Figure 5.10). The competitive binding studies, where cells were pre-incubated with 20 fold excess of competition liposomes showed a significant decrease (26%, $p<0,001$) in targeted liposome uptake. These data suggest the internalisation of DSPE-PEG-RF liposomes higher than control, specific to RF transporters and is in agreement with previous study of RfdiC14 inserted into DMPC:DMPG formulation.

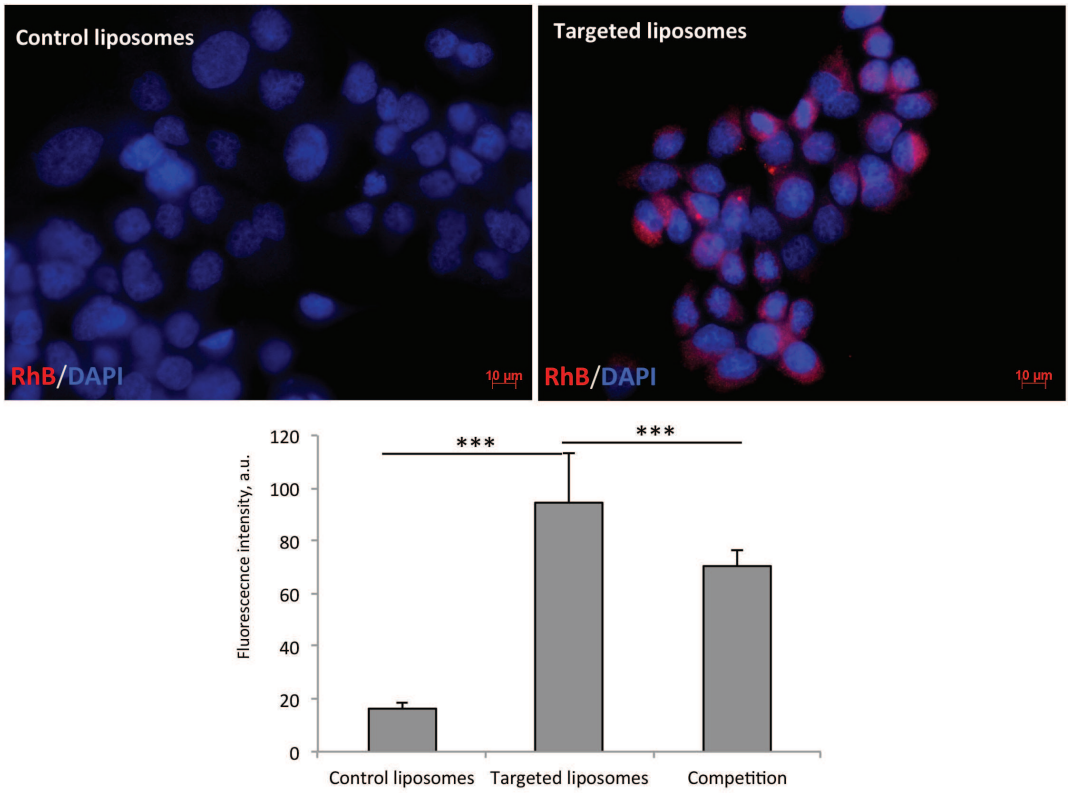

*Figure 5.10 Fluorescence microscopy images of PEGylated liposomes uptake in A431 cells (up): RhB is red, cell nuclei marked with DAPI are blue; uptake quantification (down), results presented as mean from 3 individual experiments with n=10 images for each condition; ***p<0.001.*

5.3.2.2 Phantoms

Phantom in imaging is a specially designed object that is scanned with an imaging device to evaluate, analyse, and tune the device performance. Studies in phantoms are always performed before the transition to a living subject, to calibrate the imaging device and minimise risks for animals/patients. Phantoms should be adapted for the needs of each imaging modality and represent major features (i.e. density, light scattering and absorption, ultrasound response etc.) of a target tissue. There are two major classes of phantoms – synthetic and biological. The first is represented by various tissue-mimicking polymeric materials such as silicones, polyester resins or hydrogels. The second includes whole blood, meat, gelatine-embedded cells or animal cadavers. New imaging contrast agents are also first evaluated in phantoms, to validate their performance in contrast enhancement, signal-to-noise ratio and stability.[192,193]

The optoacoustic properties of prepared Platform B1 were investigated in various phantoms. Polymeric blood-vessel mimicking tubes were chosen to evaluate optoacoustic signal from liposomes upon dilution and register their absorption spectra. Chicken breast phantom was used to detect the PA (photoacoustic) signal in biological tissue and to test the depth of signal penetration.

For this purpose, liposome stock solution was diluted to obtain the concentration range from 2000 to 2 pmols in 35 μL. These solutions were injected in blood vessel-mimicking tubes and the tubes were subjected to PAI in combination with conventional ultrasound (US).

The intensity of PA signal from ICG liposomes in the tubes was acquired in the range from 680 to 970 nm (Figure 5.11.A). The maximum PA intensity of ICG liposomes was observed after laser irradiation around 806 nm and shifted upon dilution to 800 nm. The PA signal displayed in red in Figure 5.11.B. was overlaid with US signal from tubes (grey). PA average intensity was calculated in the selected regions of interest (ROI) and then plotted against ICG concentration. Liposomes were still detectable at 2 pmol concentration. The concentration/PA signal dependence was logarithmic and expressed by the equation $y=0.2872ln(x) + 0.3643$, where y represents PA signal intensity and x – the quantity of ICG liposomes in pmol.

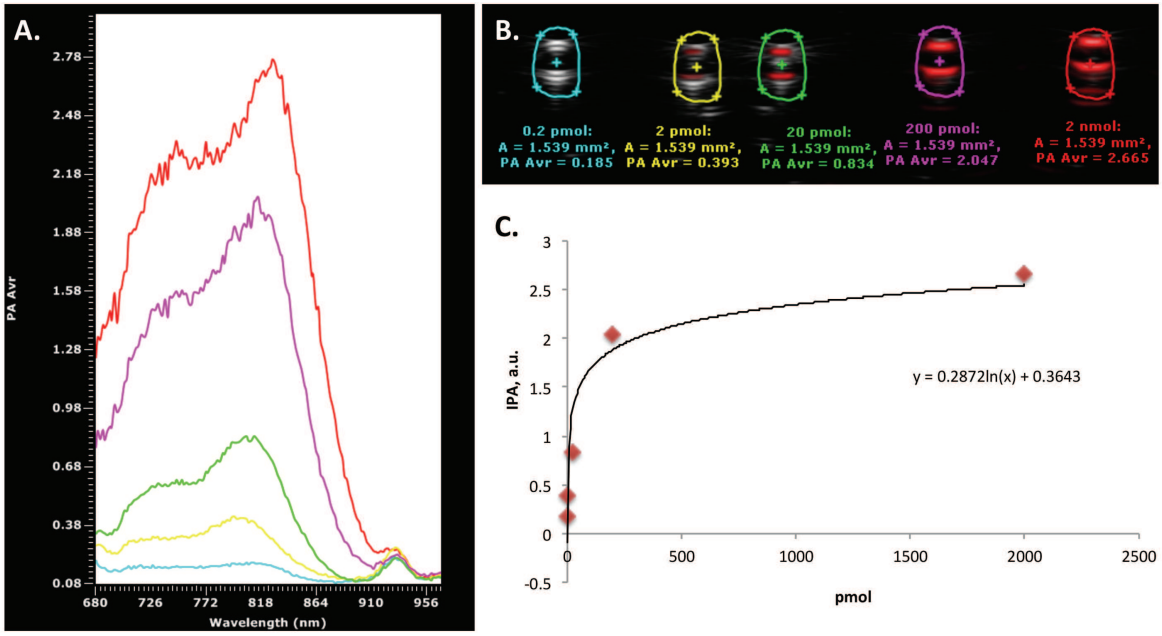

Figure 5.11.A. PA spectra of ICG liposomes at various concentrations, colours correspond to ROIs from B.; B. Overlay of US (grey) and PA (red) images from ICG liposomes at various concentrations; C. Logarithmic dependence between Intensity of PA signal (IPA) and ICG liposome concentration (pmol).

After the determination of the maximum absorption wavelength and concentration sensitivity, we moved to biological tissue phantom. To determine the maximum depth of signal penetration, 2 nmol of ICG liposomes in 50 μL were injected at various depths in the chicken breast phantom. Similarly to the previous study, the PA signal was overlaid with ultrasound image. We could observe an exponential decline in PA signal intensity with the increase injection depth (d, mm), which is typical for a biological tissue. Thus, ICG liposome signal was clearly resolved till the depth of 10 mm and the fitted exponential decay was in accordance with previous results published from Repenko T. *et al*.[194]

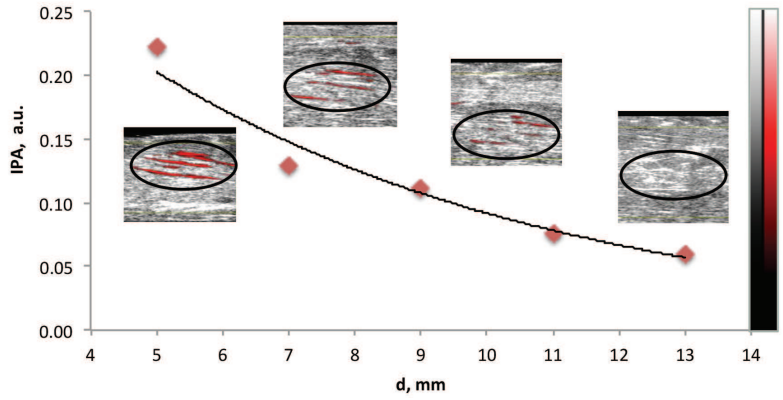

Figure 5.12 Depth-dependence of IPA signal from ICG liposomes in chicken breast phantom.

These data are particularly useful for the *in vivo* studies as they indicate working concentration range, method sensitivity and depth of PA signal detection.

5.3.2.3 in vivo

Control and targeted ICG encapsulating liposomes were evaluated in A431 tumour xenograft model. For this purpose, 15 female nude mice were injected with A431 cells (5 mln) in the right flank. The xenografts were left to grow over approximately 2 weeks untill the tumours reached the volume around 500 mm^3. Then, anesthetised (2% isoflurane) animals were injected intravenously (i.v.) with 100 μL of a liposome solution with a total amount of ICG 6 nmol for both targeted and control formulations. For the competitive binding experiment 15 min prior to inject targeted liposomes, 35 μL of competition liposomes (DSPE-PEG-RF containing formulation without ICG) were injected. The quantity of DSPE-PEG-RF in this solution was 10 times greater than in targeted liposomes.

The animals were divided in 3 groups: 5 for control liposomes, 5 for targeted and 5 for competition. All tumours were pre-scanned with PA Vevo® LAZR system at 800 nm before liposomes injection and then 15 min, 4h, 24h and 48h after injection. Tumours were scanned in 3D with the help of an automated motor system. After the last scan, animals were sacrificed and organs were collected.

The obtained PA data were analysed with Vevo® LAZR software. For each time point, tumours were reconstructed in 3D and the mean PA signal per tumour volume was calculated in PS% (Photoacoustic signal %). PS% is a relative value indicating general photoacoustic signal increase. For each mouse, the signal from pre-scanned tumour was subtracted from the PS% at each time point.

When comparing tumour accumulation of normal and targeted liposomes, one should expect the most interesting results at early time points.[186] After 24h in the circulation normal PEGylated liposomes should reach their peak in tumour accumulation via EPR effect.[184] In contrast, targeted liposomes should bind to their receptor (neovasculature or tumour cells) much faster.[89] From our *in vitro* experiments and other studies[103,104], we know, that RF and its derivatives bind to both cancerous cells and endothelial cells within the tumour.

Thus, at early time points 15 min and 4h we indeed observed an important increase in

PS% in the targeted group compared to control (Figure 5.13). The average increase PS% targeted group is 8% in 15 min and reaches 24% at 4h. In contrast, the control group shows moderate 4% increase in 15 min, that doubles to 8% in 4h. Consequently, if we assume, that the PA signal at 800 nm comes only from the ICG, the accumulation of targeted liposomes seems to be twice higher than control after 15 min in the circulation and 3-fold higher after 4h in the circulation ($p<0.05$). The competitive binding experiment showed only slight, but not significant decrease in the PS% at both time points compared to targeted group. Most probably due to high variability of PS% among studied animals, which does not allow to detect subtle differences in the uptake.

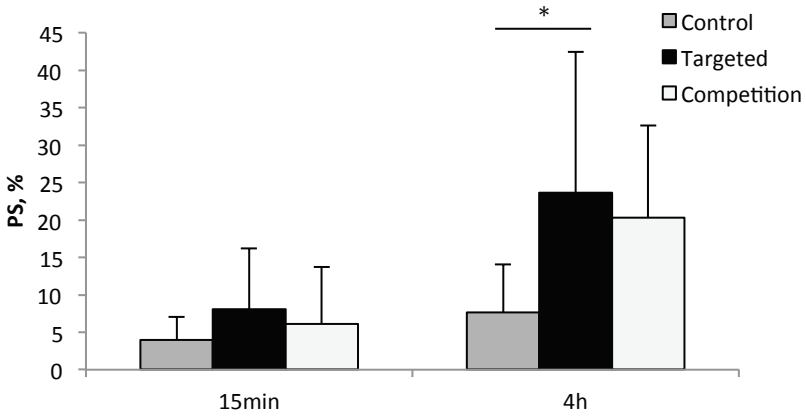

*Figure 5.13 Average PS% in 3D scans of tumours 15 min and 4h after injection of liposomes (values presented as mean ±SD from n=5 animals in each group, *p<0,05)*

However, as one could observe at Figure 5.13 the PA signal variability within the tumours is very important. This is possibly due to the fact that at 800 nm we can detect not only ICG absorbance, but also the absorbance from oxygenated and deoxygenated haemoglobin. Thus, overall PA signal will be dependent on tumour perfusion with blood. The Figure 5.14.A demonstrates 2D PA image of the tumour from targeted group next to corresponding US image at pre-scan, 15 min and 4h after injection. We observe the increase of PA signal with time mostly on the periphery of the tumour, probably next to tumour-supplying blood vessels. But this technique, unfortunately, does not allow distinguishing between blood and ICG liposomes absorbance.

To differentiate the blood absorption from ICG signal, we performed a spectral unmixing experiment for additional animals (2 in each group). This technique is able to extract the absorbance spectrum of a particular compound from the intrinsic blood spectra.[184] For this purpose, PA data were registered at various wavelengths – 700, 750, 800, 850 and 900 nm in 2D tumour slices and 750, 800, 850 nm in the 3D tumour volume. Vevo® LAZR system could acquire the data sequentially at various wavelengths and then unmix them automatically, if the spectrum of each compound is known. ICG liposomes spectrum was already acquired during phantom studies and the spectra of both forms of haemoglobin are pre-set in the system.

An absorption maximum of the compound determines the wavelength of choice for the unmixing. Thus, the absorption maximum of oxygenated haemoglobin (OxyHemo) is 750 nm, deoxygenated (deOxyHemo) – 850 nm, melanin – 700 nm, 800 nm – ICG liposomes. 900

nm was utilised for the additional control, as the more wavelengths are acquired, the more precise result is possible. However, to unmix ICG liposomes from blood only 3 wavelengths should be sufficient - 750, 800, 850 nm. As a consequence, for the 3D tumour unmixing we utilised only those three, to reduce the time of images registration and maximise the workflow.

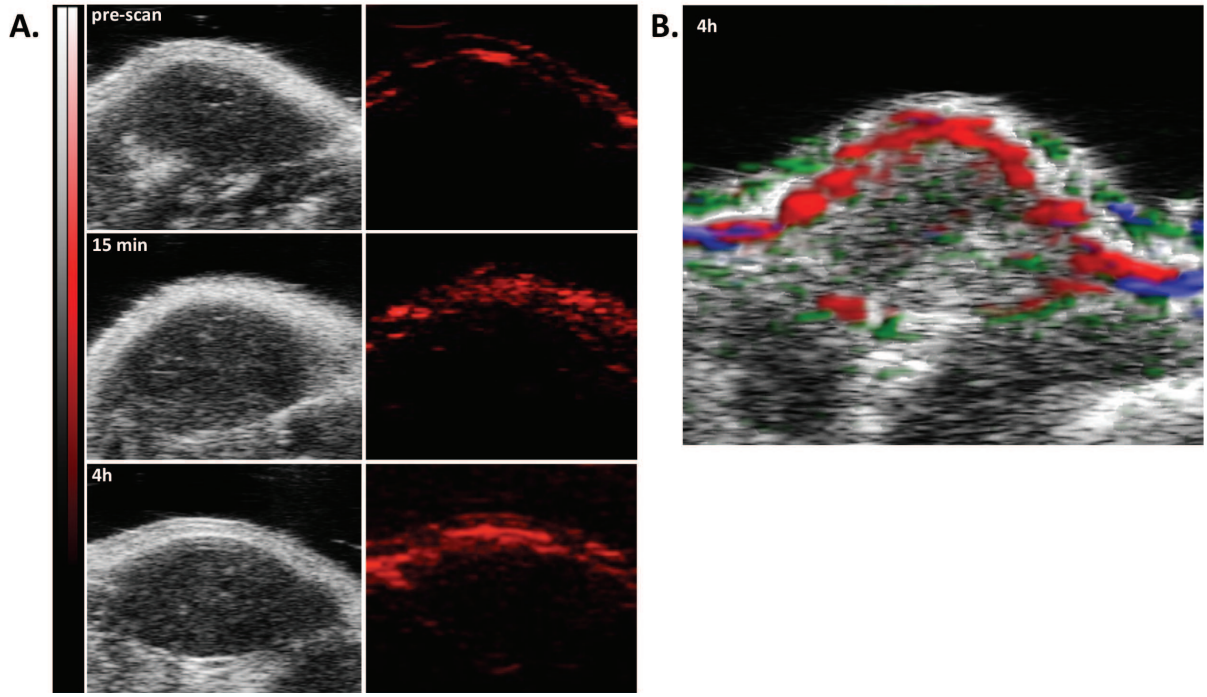

Figure 5.14.A 2D slice of tumour before (pre-scan) and after injection of targeted ICG liposomes (15 min and 4h); US image is on the left and corresponding PA signal on the right; B. merge of US and PA unmixed images of 2D slice of tumour 4h after targeted ICG liposomes injection (green – targeted ICG liposomes, red – OxyHemo, blue – deOxyHemo)

The example of obtained unmixed image is presented on Figure 5.14.B. After 4h from the injection of targeted liposomes, we observe ICG signal co-localised with major blood vessels that supply the tumour and the surrounding areas. These results are in accordance with the observations from Song W. *et al*[195], where ICG liposomes were heterogeneously distributed in the tumour tissue and mainly localised close to blood vessels.

To analyse the differences in the tumour accumulation of control and targeted liposomes we compared mean ICG intensity of PA signal (IPA) between groups in the selected region of interest (ROI). Our version of Vevo®LAZR software could not calculate the unmixed signal in 3D volume. For this reason, we took the average PA signal in the ROI from at least twenty-five 2D slices in different positions of the tumour (Figure 5.15). The signal from OxyHemo and deOxyHemo was grouped in general 'blood' signal. We could observe an important increase in PA signal intensity for targeted liposomes at 15 min, 4h and even 24h after injection compared to control. At 48h the values were similar for both groups.

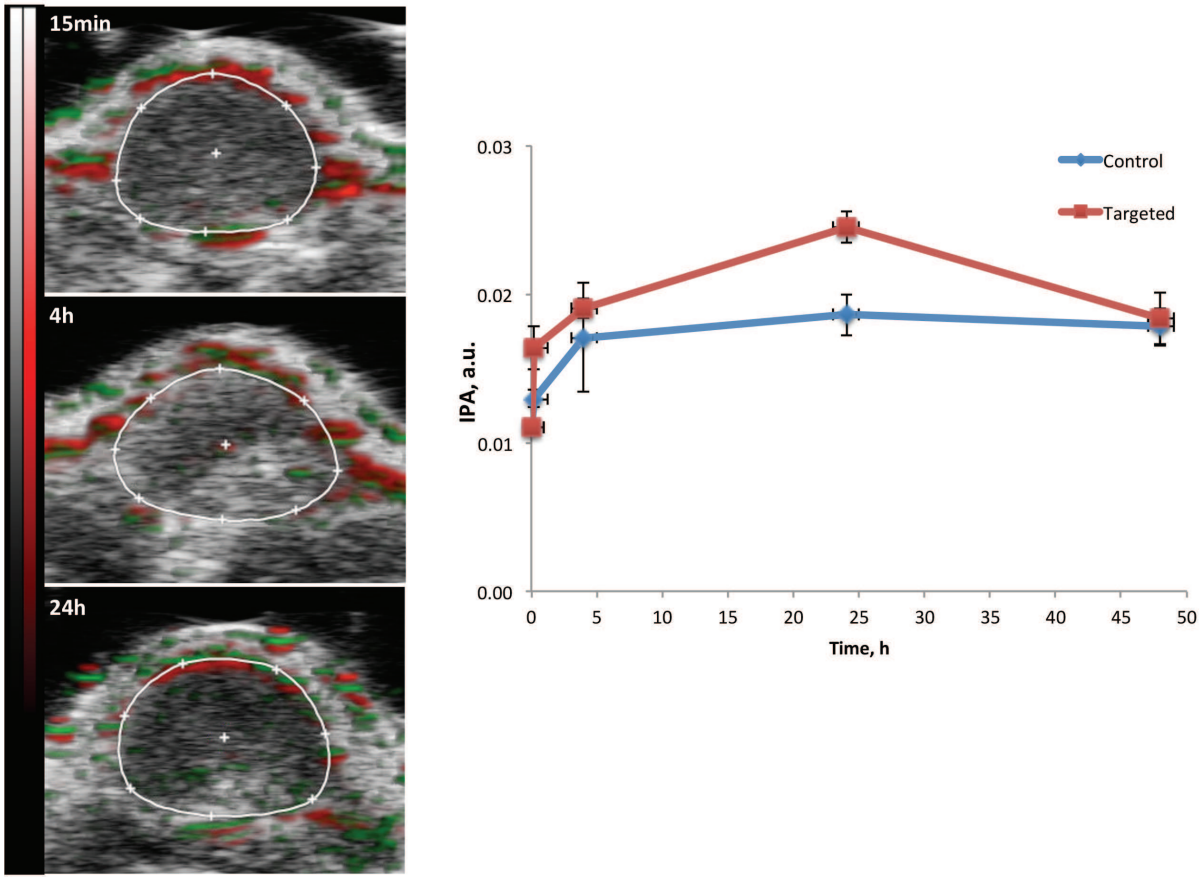

Figure 5.15 merge of US and PA unmixed images of 2D slice of tumour 15min, 4h and 24h after ICG liposomes injection (green – targeted ICG liposomes, red - blood) (left); average PA signal intensity in the tumour over time after liposomes injection (n=4) (right)

The mean values for each time point were obtained from 2 animals in each group and thus could not be considered as significantly different. However, this still gives us important information about tumour accumulation of DSPE-PEG-RF functionalised liposomes. We could see that the targeting agent does not seem to disturb the blood circulation of liposomes as the signal for both formulations increases over time. We also observed a heterogeneous signal distribution in the tumour tissue for both control and targeted liposomes. Taking into account that RF binds to both endothelial and cancerous cells, this targeting strategy could be interesting in the evaluation of tumour vascularisation. Moreover, with this system one could monitor in real time the *in vivo* drug delivery into both vascular and stromal compartments of the tumour.

5.4 Platform B2: RFA-functionalised DiR liposomes for µCT/FMT

5.4.1 Preparation and characterisation

Similarly to the platform B1, two formulations encapsulating DiR were prepared – control and targeted. The preparation procedure and lipid molar ratios were the same that for L8 formulation described earlier. Schematic representation of prepared formulations is depicted in Figure 5.16. To ensure a proper encapsulation of DiR in liposomal membrane, it was dissolved in chloroform and added to the initial lipid mixture in 0,5 % molar ratio.

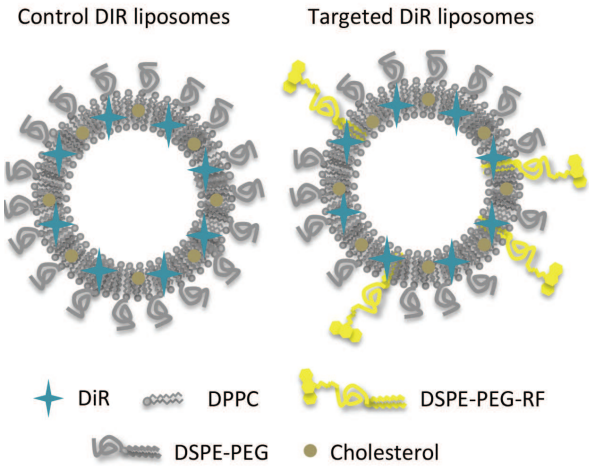

Figure 5.16. Scheme of control and targeted DiR liposomes.

Control DiR liposomes had a mean hydrodymanic diameter of 137±2 nm (PDI 0,06) and a negative zeta potential of -18±1 mV. Targeted DiR liposomes had slightly greater size of 141±1 (PDI 0,07) and a more important zeta potential of -33±1 mV. The average hydrodynamic size of DiR liposomes is 30-40 nm bigger than the ones of ICG liposomes. On the other hand they are quite close to the mean size of bare L8 formulation, indicating that ICG, but not DiR, influences physicochemical properties of liposomes. In accordance with previous results, zeta potential of targeted DiR liposomes is more important than the one of control DiR formulation due to DSPE-PEG-COO^-.

Table 5.5 Physicochemical characteristics of DiR liposomes

Name	Lipids	Size, nm	PDI	Zeta Potential, mV	DiR, µM
Control DiR liposomes	DPPC:Chol:DSPE-PEG:DiR 65:30:5:0,5	137±2	0,06	-18±1	38
Targeted DiR liposomes	DPPC:Chol:DSPE-PEG-RF:DiR 65:30:5:0,5	141±1	0,07	-33±1	37

The TEM photograph of targeted DiR liposomes indicates the presence of regular, spherical liposomes with the mean diameter close to 100 nm. As previously described, the

presence of RF amphiphile and DiR in the liposomes was confirmed and quantified spectroscopically. At the fluorescence emission spectra one can observe a characteristic emission of RF at 530 nm for targeted liposomes and the DiR emission peak at 782 nm for both formulations. In contrast to ICG, DiR emission peak exhibited three times higher intensity than the emission peak of RF. The calibration curves were: $y=59087x$ (R^2=0.9939) for RF and $y=7200x$ (R^2=0.9916) for DiR, where y represents the fluorescence intensity and x – the concentration in μM. The DiR concentration in control and targeted liposomes were almost identical 38 μM and 37 μM respectively). DiR liposomes exhibited decent size stability during storage (no significant size and PDI increase after 2 weeks storage at 4°C).

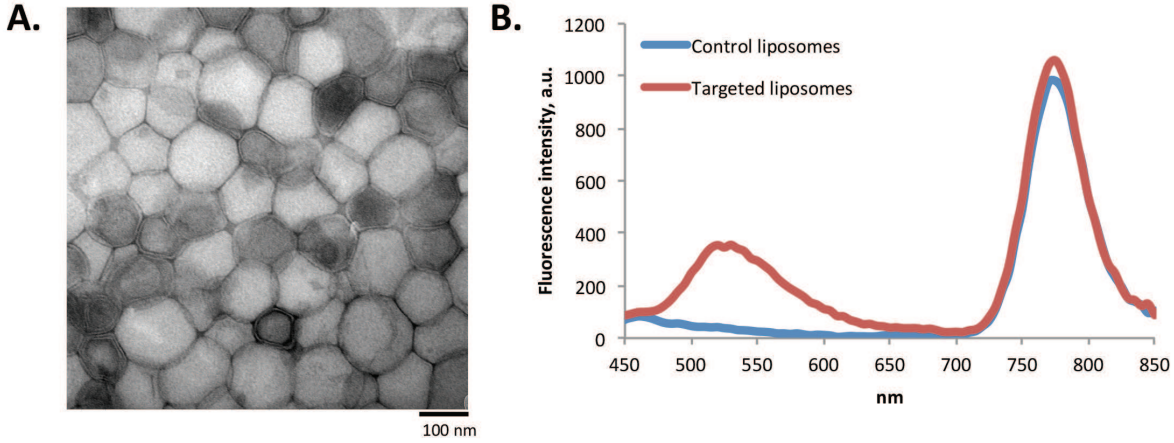

Figure 5.17 A. TEM photograph of targeted DiR liposomes (scale bar 100 nm); B. Fluorescence emission spectra of targeted and control DiR liposomes.

For further *in vitro* and *in vivo* experiments we used the same competition liposomes (DSPE-PEG-RF containing liposomes without any labelling) that were prepared in Platform B1 section.

In conclusion, we prepared and characterised control and targeted liposomes with a lipophilic derivative of cyanine - DiR. DiR dye is less studied, compared to ICG (employed for Platform B1), but it possesses an excellent quantum yield in hydrophobic environments and thus could be complementary to the ICG study. Obtained liposomes exhibited bright fluorescence in the NIR range, were around 139 nm in size and had good stability during storage. Similarly to Platform B1, targeted DiR formulation displayed slightly higher zeta potential than control due to the presence of negatively charged DSPE-PEG-COO^- lipids.

5.4.2 Biological evaluation

5.4.2.1 in vitro

The internalisation of control and targeted DiR liposomes was studied on PC3 cell line to confirm the targeting potential of DSPE-PEG-RF before subsequent *in vivo* testing.

PC3 cells were incubated with 1 nmol of control or targeted liposomes (1 nmol of DiR in 100 μL) for 30 min at 37°C. After incubation the uptake was evaluated by fluorescence microscopy (ex. 750, em. 780 nm). In contrast to RhB containing liposomes, the uptake of DiR liposomes seemed less diffusive. On Figure 5.18 we can observe numerous aggregations

situated in the perinuclear space. The quantification of DiR fluorescence revealed six times significantly higher signal from targeted liposomes compared to controls ($p<0,001$). The competitive binding studies with 100-fold FMN excess (competition 1) or 20-fold excess of non-fluorescent DSPE-PEG-RF liposomes (competition 2) demostrated an uptake decrease of targeted liposomes in both cases. The pre-incubation with 100-fold FMN excess showed significant 88% drop in the internalisation ($p<0,01$). Whereas the pre-incubation with 20-fold excess of competition liposomes diminished the uptake for 54% and due to high variability of the internalisation between cells this difference was unfortunately non-significant.

Nevertheless, the data indicate that targeted liposomes uptake in PC3 cells is higher than control and specific to RF. The difficulties with the "competition 2" experiment could be due to the insufficient amount of RF on the competition liposome surface or high fluorescence quantum yield of DiR dye which does not allow the detection of subtle uptake differences. For the *in vivo* studies, the utilisation of FMN as competitor is not optimal because of short circulation time and rapid renal clearance of the molecule.

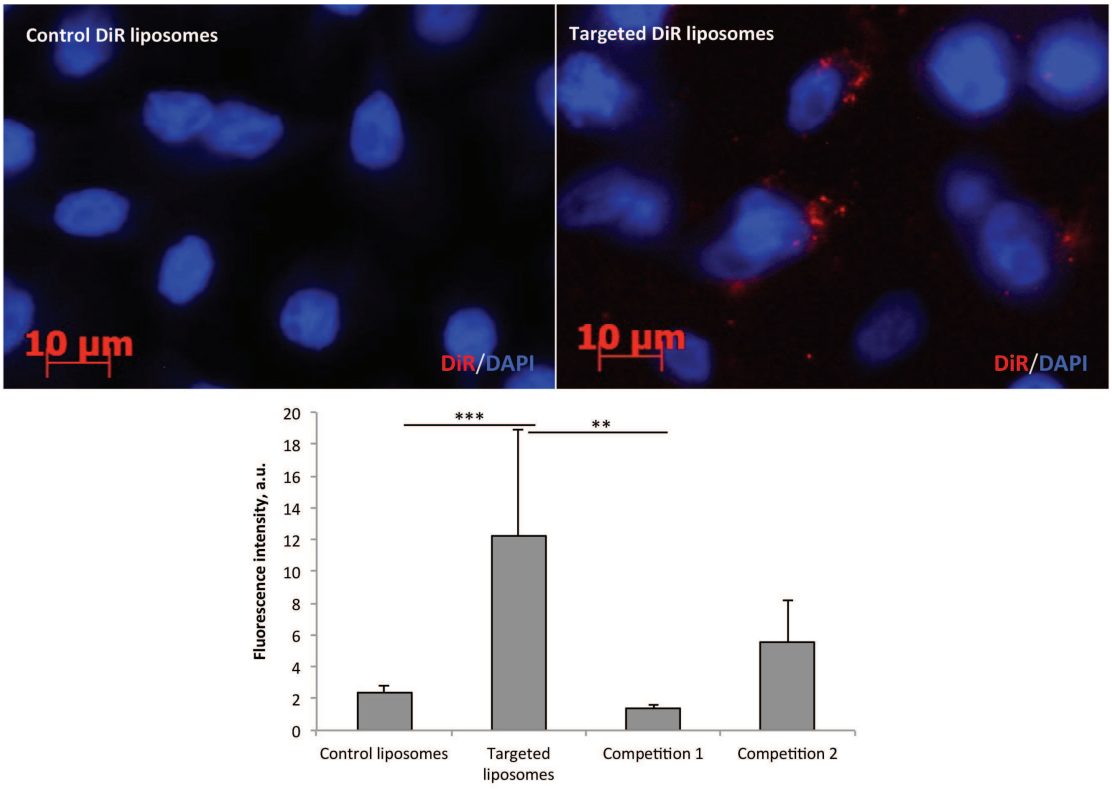

*Figure 5.18 Fluorescence microscopy images of PEGylated DiR liposomes uptake in PC3 cells (up): DiR is red, cell nuclei marked with DAPI are blue; uptake quantification (down), results presented as mean from 3 individual experiments with n=10 images for each condition; ***p<0,001, **p<0,01.*

Thus, the synthesised DSPE-PEG-RF amphiphile enables efficient and specific liposome uptake in PC3 cell line. The obtained results are very similar to those with RfdiC14 functionalised liposomes. Hence, the PEGylation of liposome surface and the spacer between RF and DSPE do not seem to influence on RF interactions with its transporter protein. With these positive results it was possible to proceed for the evaluation of DSPE-PEG-RF targeting efficiency *in vivo*.

5.4.2.2 Phantoms

The fluorescence signal intensity generated by targeted DiR liposomes was evaluated in block shaped FMT phantom by combined μCT/FMT imaging (Figure 5.19). This polymeric phantom was specifically designed to access and reconstruct the fluorescence signal in 3D. The phantom absorption is very close to those of biological tissues.

The liposome stock solution was diluted to give 0,01, 0,03 and 0,06 nmol in 100 μL. For the increased accuracy, 1 % lipid emulsion (Lipovenoes) was added to liposomal solutions to give the same scattering coefficient to the solution as the rest of the phantom. 5% of μCT contrast agent (Imeron) were added to the solution to facilitate image analysis.[167]

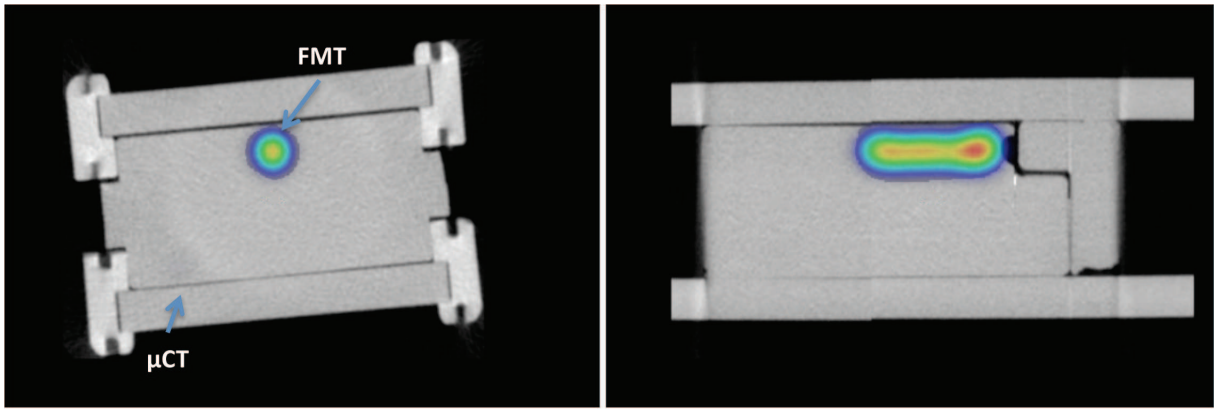

Figure 5.19 Up and side view of phantom image obtained from µCT and FMT fusion.

The solutions were installed in the cylindrical inclusion of the phantom and scanned with μCT/FMT system at 750 nm ex. channel. The 3D reconstruction of the solution volume in phantom based on µCT images yielded fluorescence intensity values for each concentration. The obtained values were plotted against DiR liposomes quantity in nmol (Figure 5.20). We could observe a linear dependence between DiR liposomes concentration and the emitted fluorescence, described by the following equation - $y = 4311.2x + 23.3$ ($R^2 = 0.99238$), where y represents the fluorescence signal intensity and x – the quantity of DiR liposomes in nmol.

The obtained results were utilised for the quantification of DiR liposomes accumulation in the various organs during the *in vivo* biodistribution study.

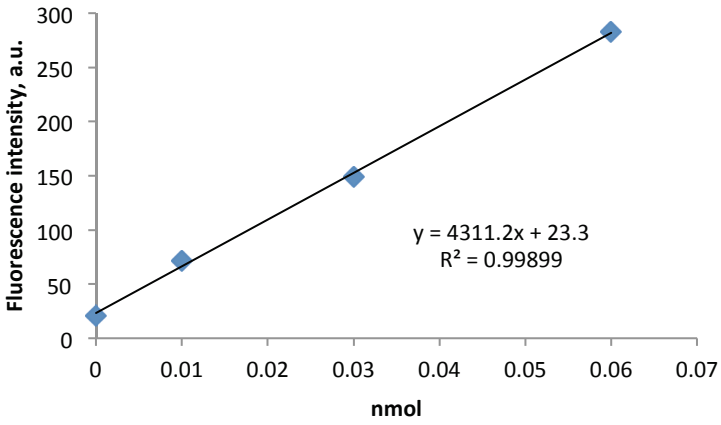

Figure 5.20 μCT/FMT study of DiR liposomes in phantom, fluorescence (ex. 750 nm) signal intensities are plotted against DiR liposomes quantity (nmol).

5.4.2.3 in vivo

Control and targeted DiR encapsulating liposomes were evaluated in PC3 tumour xenograft model. For this purpose 9 male nude mice were injected with PC3 cells (3 mln) in the right flank. The xenografts were grown for 3 to 5 weeks until the tumours reached the volume around 50-100 mm^3. Compared to A431 xenografts, PC3 ones were growing very slowly and heterogeneously and by the end of the experiment were much smaller.

The animals were divided in three groups: 3 for control liposomes, 3 for targeted and 3 for competition. The animals were injected i.v. with 100 μL of liposomes solution with total amount of DiR 2,5 nmol for both targeted and control formulations. Similarly to the previous study, for the competitive binding experiment 15 min prior to inject targeted liposomes, 35 μL of competition liposomes, with the 10-fold excess of DSPE-PEG-RF compared to targeted liposomes.

We performed a whole-body μCT with subsequent FMT scans (ex. 750 nm) for all animals after 15 min, 4h, 24h and 48h from liposomes injection. After the last scan, animals were sacrificed, organs were collected and scanned in the FMT to obtain 2D reflectance images. μCT scans were merged with FMT images and then the main organs such as tumour, heart, lungs, liver, kidneys and bladder were reconstructed with Imalytics Preclinical 2.0© software. The mean fluorescence, quantified from each reconstructed in 3D organ, was then calculated into pmol of the DiR using a scale factor based on a phantom calibration of the probe (see section 2.4.2).

The first analysis of 2D whole-body fluorescence reflectance scans could indicate general trends in probe biodistribution. They are not as accurate as 3D fluorescence evaluation, but could give first insights of the accumulation profile. On Figure 5.21 the 2D scans of one animal from each group at various time points after injection are presented. One can observe the accumulation of DiR liposomes in the tumour over time (black oval region marked on the picture) without noticeable differences between groups. Concerning healthy organs – at the early time points the signal comes mainly from major blood vessels and highly perfused organs like kidneys, brain or heart. After 24h from the injection a bright fluorescence

is observed in the liver area, which is a common situation for the liposomes.[30,196] However, the 2D reflectance scans give only qualitative information about superficial fluorescence signal.[89,165] The more precise accumulation profile in 3D then assessed by the superposition of μCT with FMT scans and subsequent organ segmentation.

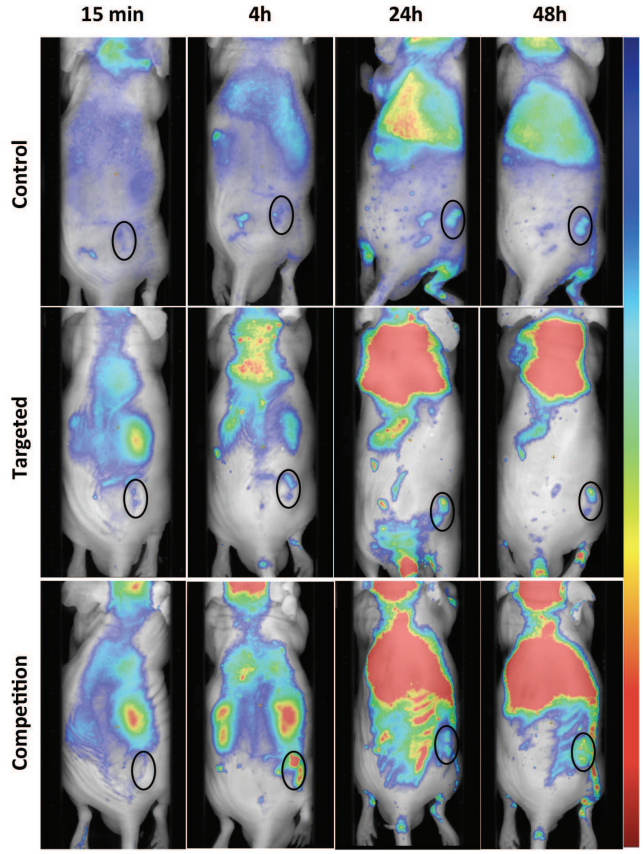

Figure 5.21 2D reflectance images of DiR liposomes accumulation over time (dark cicle indicates tumour location).

Organ segmentation was based on 3D μCT scans and performed using Imalytics Preclinical 2.0© software. Figure 5.22 shows various steps of segmentation in 2D and the Figure 5.23 shows these steps in generated 3D μCT scan, superposition of segmented organs with the μCT and FMT scans. Finally the fluorescent signal from each organ was quantified in 3D, then averaged from animals within groups. The average fluorescent signal was recalculated in pmol of DiR and compared between organs over time.

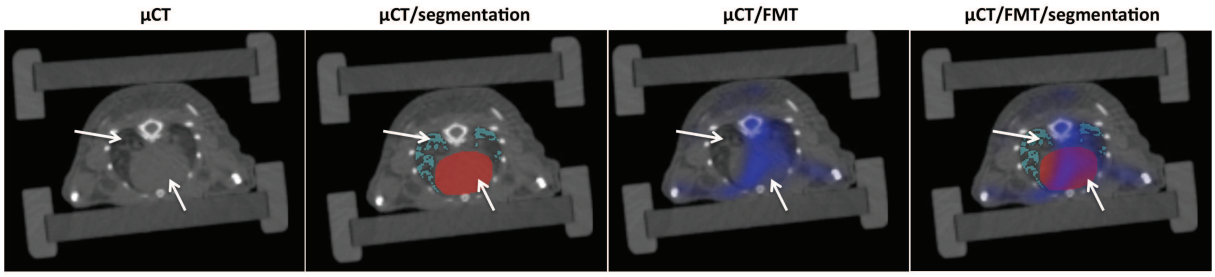

Figure 5.22 Various steps of organ segmentation in transverse view of a mouse; heart (red) and lungs (light blue) are marked with white arrows. µCT contrast is grey and fluorescent signal appears in a shape of dark blue cloud.

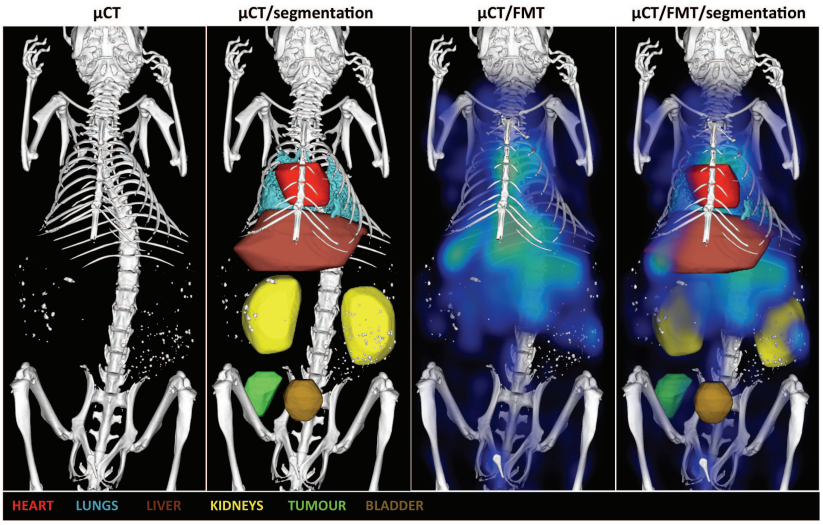

Figure 5.23 Various steps of organ reconstruction and fluorescence quantification in 3D. Segmented organs are presented in various colours: heart – red, lungs – light blue, liver – brown, kidneys – yellow, tumour – green, bladder – beige. Fluorescent signal appears in the form of diffuse blue clouds.

The 3D quantification of liposomes signal in healthy organs is presented on Figure 5.24. In general, the pharmacokinetic profile of targeted liposomes was similar to control. The highest concentration was observed in the liver for all time points and in the heart at 15 min after injection. The signal from the heart dropped after 24h but was still present at 48h indicating that liposomes are slowly removed from the circulation over time. Due to the high perfusion of the kidneys, an important signal was also observed there. However, the liposomes size does not permit kidneys excretion and thus there was almost no fluorescence in bladder. This also indicates the absence of free dye dissociating from liposomes. The high amount of liposomes in the liver at early time points could be explained by the important blood perfusion of this organ. The liver accumulation seemed slightly higher at 48h for control liposomes compared to specific, ones but this difference was not significant. Although compared to conventional liposomes the PEGylation limits opsonisation and macrophages uptake,[33] liver still remains a major organ for liposomes excretion.[196]

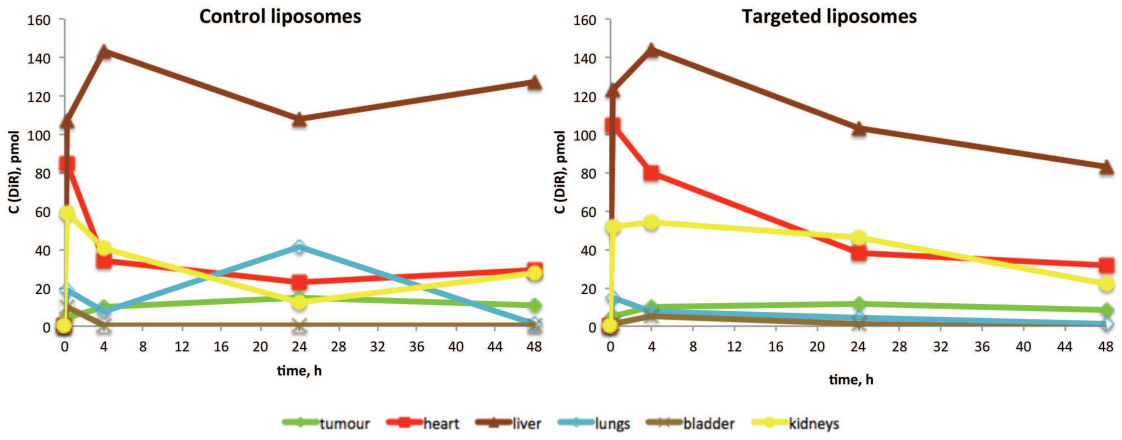

Figure 5.24 Results from longitudinal fluorescence quantification in various organs after i.v. DiR liposomes injection (n=3 for each group).

As for the tumour, the 3D fluorescence quantification did not show significant differences in the accumulation of control and targeted liposomes (Figure 5.25). This is probably because PC3 xenografts in our experiment were small, slowly growing and poorly vascularised. This indicates the absence of functional EPR effect and thus low accumulation of liposomes in the tumour. As already mentioned in the introduction part, the EPR effect relies on vessel density in the tumours, their porosity and orientation, tumour stroma thickness and interstitial pressure. The vascularisation in xenographts generally starts from tumours of at least 3 mm in diameter. In our case, the tumours were around 3-5 mm in diameter, which was possibly not the optimal size for this model.

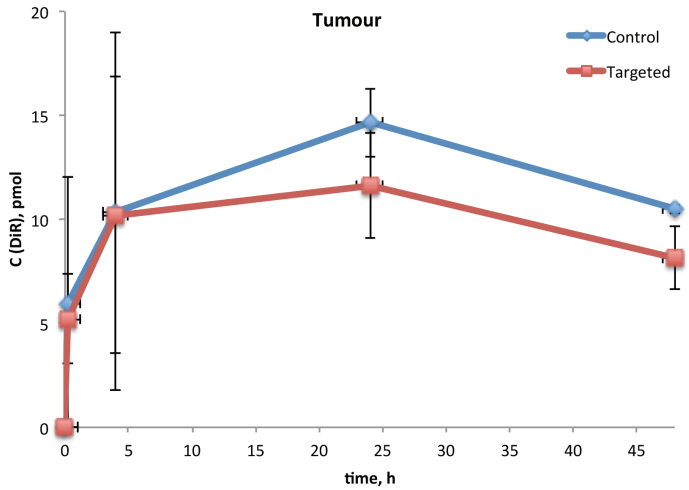

Figure 5.25 Results from longitudinal fluorescence quantification in PC3 tumour xenografts after i.v. DiR liposomes injection (n=3 for each group).

At early time points, 15 min and 4h, the signal from the tumour was highly variable in each group, probably due to heterogeneous blood supply of the tumours. At 24 and 48h targeted liposomes exhibited even slightly lower signal that the control group. This might be due to their faster elimination caused by the presence of a targeting ligand on the surface, which is known to be one of the most important issues of targeted nanosystems.[75,77]

In our study, the ratio between tumour and liver accumulation was around 1/10 for both groups, which signifies quite poor tumour to healthy organ accumulation. In contrast, the more rapidly growing or the more leaky xenografts could provide better tumour accumulation trough the EPR effect. For instance, Kunjachan S. *et al.*[89] showed more important accumulation of a polymeric drug carrier in the highly leaky murine tumour model (CT26, murine colon carcinoma) compared to healthy organs such as liver and spleen. Thus, sufficient number of blood vessels in tumour and functional EPR effect are extremely important factors for nanomedicine biodistribution and tumour accumulation.

Similarly to the study with A431 tumours, the competitive binding experiments did not give any noticeable differences in the signal, probably due to the high variability between animals in each group and/or insufficient amount of competition liposomes.

After mice were sacrificed, the organs were excised, collected and their 2D fluorescence reflectance images were taken. The results presented on Figure 5.26 display a

high liposome accumulation in the liver and spleen probably resulting from the macrophage uptake. Kidneys, tumour, intestine and skin also showed comparable accumulation. In contrast, heart, muscle and testis displayed almost no signal.

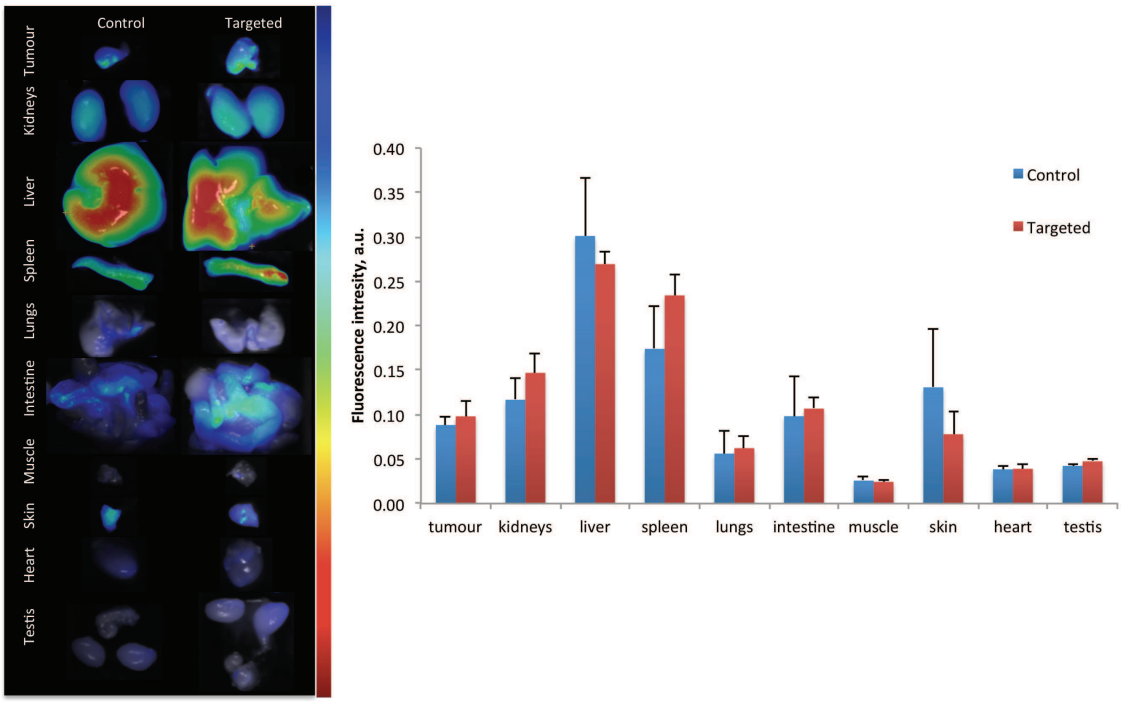

Figure 5.26 ex vivo 2D fluorescence reflectance images of various organs and PC3 tumour xenografts from control and targeted group (left); mean fluorescence intensity from ex vivo organs and PC3 tumours (results presented as mean from n=3 animals ±SD) (right).

Hence, the monitoring of liposomes pharmacokinetics over 48h showed no significant differences between the control and targeted formulations, indicating that DSPE-PEG-RF on the liposome surface does not influence their biodistribution. The accumulation in the tumour was similar for both formulations and lower compared to other pre-clinical studies.[89,197] This may be due to the insufficient vasculature of PC3 tumour model in our study. Some papers suggest the injection of PC3 cells inoculated in Matrigel®[198] to ensure better and faster growth of the xenografts. Otherwise, we could have also tested the orthotropic prostate cancer model,[159] which should reflect better the clinical situation.

The resected tumours were embedded in TissueTec® and frozen at -80°C. The histological analysis of tumour cryo-sections showed (Figure 5.27) a more important co-localisation of targeted liposomes with endothelial cells (marked with Rhodamine-Lectin) compared to control liposomes ($p<0,01$). Co-localisation of liposomes with endothelial cells was compared by Pearson coefficient calculated with Fiji Software©. Even though the overall tumour accumulation was not different for control and targeted liposomes, vascular targeting with DSPE-PEG-RF does work for PC3 tumours. Therefore, one could suggest, that the vascular targeting is responsible for moderate tumour accumulation. However, the diffusion of targeted liposomes inside the tumour tissue looks similar to the diffusion of control liposomes. Thus, the binding site barrier, one of the major problems for antibody targeting,[199] does not seem to occur with DSPE-PEG-RF.

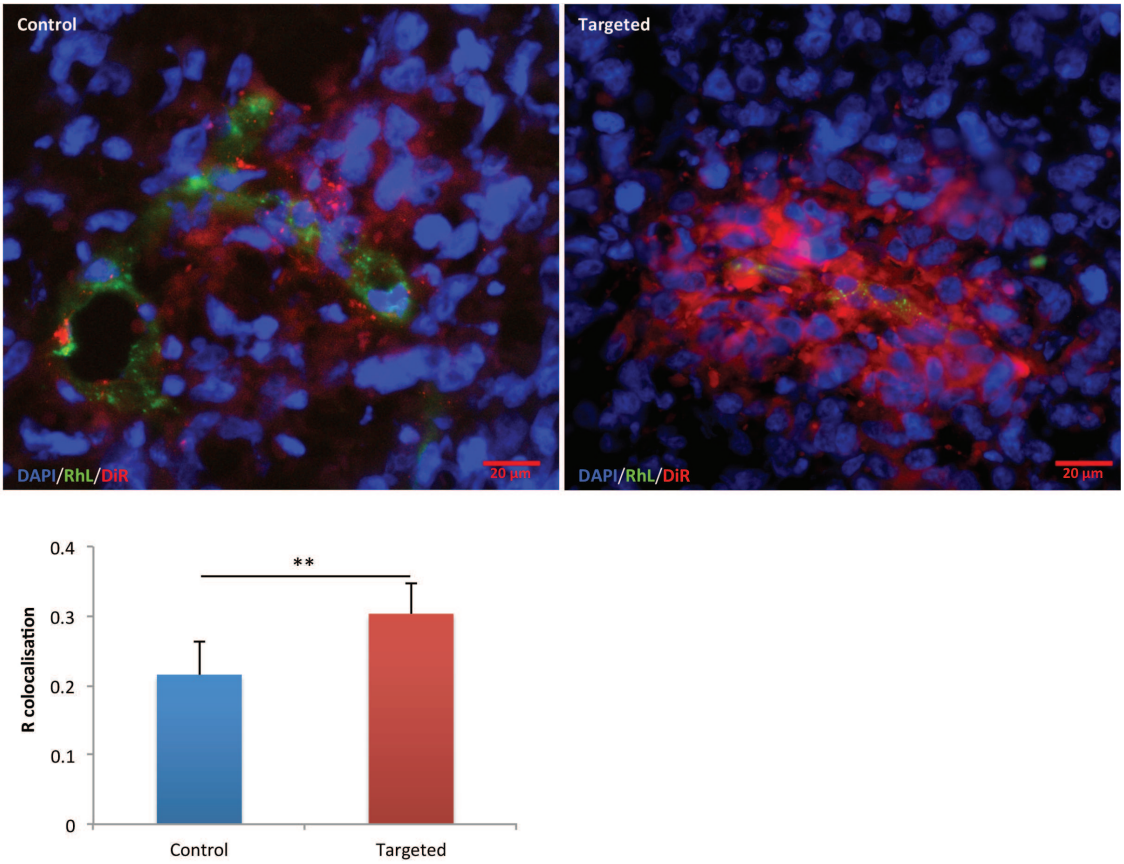

*Figure 5.27 Fluorescence microscopy images from tumour cryo-sections (up), nuclei are stained in blue with DAPI, endothelial cells in green with Rhodamine-Lectin and DiR liposomes are presented in red; Quantification of co-localisation between endothelial cells and DiR liposomes, results are presented as mean from n=3 tumours and 10-15 images for each tumour, ±SD, **p<0,01.*

In summary, the study of DiR liposomes biodistribution in PC3 tumour model showed similar pharmacokinetics profile for targeted and control formulations. Hence, 48h from intravenous injection, liposomes were mainly accumulated in the liver and spleen. The overall accumulation in the tumour xenografts was poor, compared to healthy organs and may be due to the insufficient tumour size and vascularisation. However, the histological analysis of frozen tumour sections revealed a higher co-localisation of targeted liposomes with endothelial cells compared to control. Thus, similarly to A431 tumour model, vascular targeting seems to be prevalent here. This could be beneficial for the intracellular delivery of therapeutics in tumour vasculature.

In perspective, the study should be repeated with more developed PC3 tumours and this would probably show the differences in accumulation of targeted liposomes. The more important number of animals is also required to limit the variations within groups. The PC3 cells could be either injected together with artificial extracellular matrix (Matrigel®) or implanted orthotopically into prostate tissue to ensure a faster tumour growth and vascularisation. Moreover, other prostate tumour models such as LNCaP, CWR-22 or LuCap-23 might be tested.[159,200]

5.5 Conclusions

To perform *in vivo* evaluation of the RFA targeting potential, we selected the appropriate liposome formulation in terms of stability and reproducibility. DSPE-PEG-RF was successfully inserted in the formulation with near-infrared dyes encapsulated as model drugs (ICG or DiR). The obtained targeted labelled liposomes (Platform B1 and B2) were extensively characterised and compared to control (without DSPE-PEG-RF) formulation. Our analysis revealed slight differences in size (in the case of ICG liposomes) and zeta potential between targeted and control liposomes, which yet did not drastically impact their stability or biological efficacy.

The prepared targeted formulations were first evaluated *in vitro* in two cell lines A431 and PC3, where they showed enhanced, specific uptake compared to control. These results are in line with previous findings describing non-PEGylated targeted liposome formulation (liposomes with RfdiC14). Consequently, the PEG spacer between RF and lipid does not influence RF targeting efficiency, which is sometimes a risk for such conjugates.

The studies in biological phantoms showed stable and quantifiable signal from both types of labelling. Thus ICG liposomes generated good photoacoustic signal comparable with the literature.[184] DiR liposomes exhibited strong fluorescence in linear correlation with the probe concentration, detected by dual μCT/FMT imaging systems.

Finally, the targeting efficiency of DSPE-PEG-RF functionalised liposomes was evaluated in two diverse xenograft tumour models – A431 and PC3 with two different imaging modalities – PAI and μCT/FMT. The tumour accumulation and organ distribution were studied longitudinally during 48h. We found an enhanced accumulation of targeted ICG liposomes in the A431 tumour xenografts at early time points (15 min and 4h). The probe distribution was non homogeneous within the tumour tissue and mostly present in the areas close to tumour-supplying blood vessels.

The biodistribution of targeted DiR liposomes was not different from the control formulation – major organs of liposome accumulation were liver and spleen. This indicates similar blood circulation times and clearance mechanisms. PC3 tumour xenografts presented poor liposomes accumulation and there was no significant difference between of targeted and control formulations. However, we believe this could be a result of slow growth and insufficient vascularisation of PC3 xenografts. Nevertheless, the vascular targeting of DSPE-PEG-RF was shown in tumour cryo-sections by more important co-localisation of targeted liposomes with endothelial cells compared to control. This enhanced vascular targeting might reduce the overall tumour accumulation of targeted liposomes. However, due to high variability of 3D fluorescence signal within the groups the results are difficult to interpret. Additional study with higher number of animals per group and more pronounced PC3 xenograft size is required.

Even though the obtained results appeared complex and not 100% positive, these are the first *in vivo* assays on RF targeted liposomes. As found in the literature RF functionalised nanoparticles[104,118] and conjugates[116,117,119] were so far only evaluated *in vitro*. The exception is FAD-USPIO nanoparticles[103] that showed an enhanced vascular uptake in prostate tumour

xenografts (LnCap) at early time points (1h and 3h), which is in line with our results. However, due to the major differences in average size, surface chemistry and pharmacokinetics the comparison of FAD-USPIOs and our targeted liposomes is difficult. Thus, our first investigations on RF-functionalised long circulating liposomes could give useful insights for extended and more systematic pre-clinical evaluation.

6 Chapter VI. General conclusions and perspectives

RF is an extremely pluripotent molecule, which opens new avenues in nanotechnology field.

In this study we synthesised and characterised six new amphiphile derivatives of RF (RFA). For that purpose three types of coupling chemical reaction were employed – Huisgen reaction, phosphoramidite coupling and Steglich esterification. The modification of RF into an amphiphile was performed in two different positions N3 and 5'O. The prepared derivatives are presented on Figure 6.1.

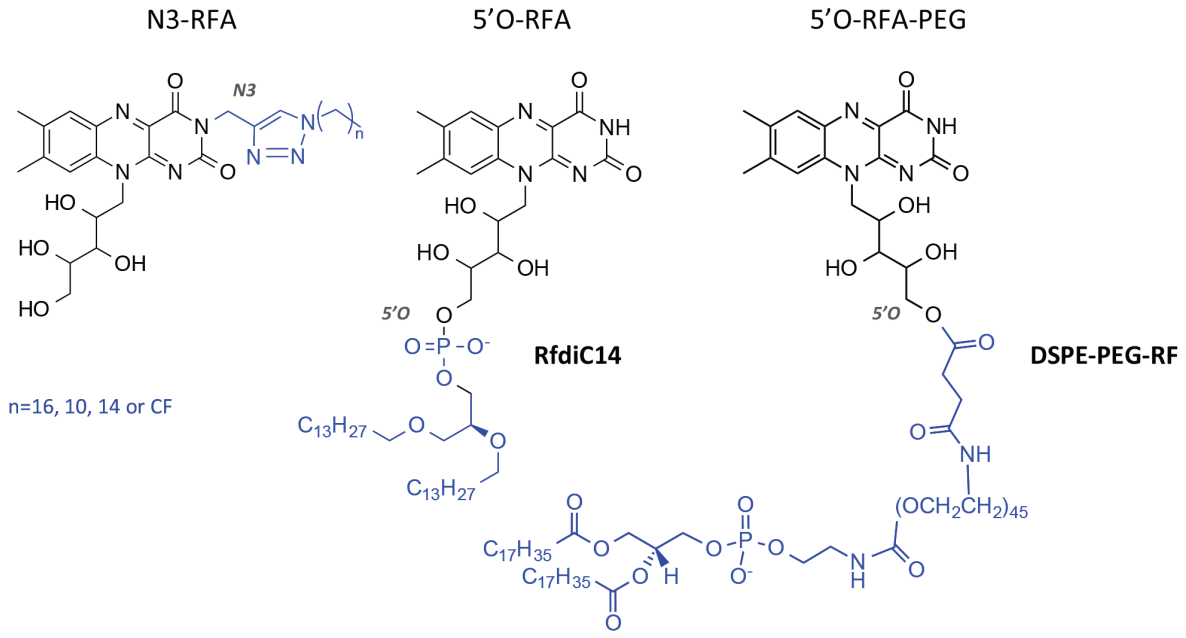

Figure 6.1 Chemical structures and abbreviations of synthesised RFA

The first strategy yielded four RF derivatives with various alkyl chains attached to the N3 position with a triazole bond. Unfortunately, all N3-RFAs displayed a very weak solubility in water and organic solvents. The second strategy was more successful. It employed the attachment of a lipid moiety through a phosphodiester bond to the 5'O end of RF's ribitol chain. The prepared 5'O-RFA, named RfdiC14, exhibited similar chemical structure and solubility than conventional phospholipids. Consequently, it was an excellent candidate for auto-assembly formation. We also prepared a similar derivative, which held a PEG spacer between RF and the lipid moiety. This molecule, designated for the *in vivo* studies, was named DSPE-PEG-RF.

The **auto-assembly** formation of RfdiC14 was studied by means of various physicochemical technics including CPP calculations, DLS analysis, ss NMR experiments and cryo-EM imaging. Each technic contributed to the overall understanding of the RfdiC14 self-assembly behaviour. In summary, the results indicate the formation of three-dimensional micrometre-sized objects constituted from multiple lamellar structures. The latter represent highly organised densely packed bilayer morphology with a repetition motif of 5±0,7 nm. The

ssNMR studies revealed more important disorder in the RfdiC14 bilayers compared to classical phospholipid membranes and thinner hydrophobic portion (20 Å). This might be a consequence of lateral spacing of lipid chains induced by additional interactions between bulky RF-headgroups. Among the potential interactions we suppose the π-stacking between the isoalloxazine rings and a network of hydrogen bonds between ribitol chains and water. The possible model of RfdiC14 bilayer organisation and cryo-EM photographs are presented on Figure 6.2.

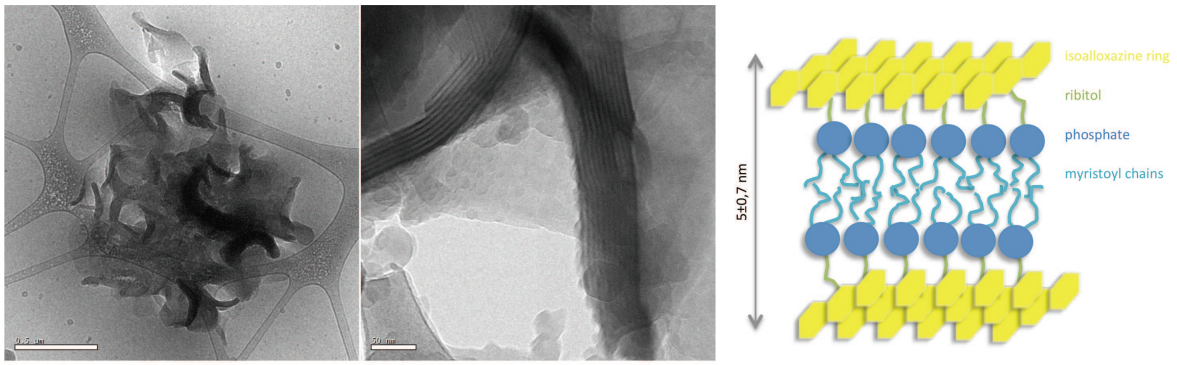

Figure 6.2 Cryo-EM photographs of RfdiC14 auto-assemblies at different magnifications (left, scale bars 0,5 µm, 50 nm) and cartoon suggesting RfdiC14 bilayer organization (right).

As RF transporters were shown overexpressed in certain types of cancer and in metabolically active cells, RF could serve as a tumour targeting ligand. Therefore, several RFAs were inserted into model liposome formulations to evaluate the targeting potential of RF *in vitro* and *in vivo*. The prepared RF-functionalised drug delivery platforms are summarised in the Figure 6.3.

Platform A was designated for the first *in vitro* studies. RfdiC14 was inserted into simple DMPC:DMPG liposome formulation, which was labelled with various rhodamine derivatives. We showed, that RfdiC14 insertion in small amounts does not influence the physicochemical properties of liposomes. Targeted liposomes labelled with lipid derivative of rhodamine (LRhPE) did not display specificity in cell uptake. In contrast, targeted liposomes, encapsulating rhodamine B, revealed enhanced and specific uptake in PC3, A431 cell lines and HUVECs compared to control. RfdiC14 could be eventually inserted into any lipid contained formulation such as lipid nanoparticles, cubosomes, hexosomes, nanoemultions etc. and render it tumour specific. The prepared RFA could also serve as a pharmacological tool to study RF transport mechanisms.

Platform B was prepared for the *in vivo* evaluation. In this case, long-circulating liposomes (PEGylated) with optimised lipid composition were prepared. DSPE-PEG-RF was utilised as a RF-presenting targeting moiety. Liposomes were labelled with NIR dyes – either ICG (platform B1) or DiR (platform B2) and tested in two tumour models. The accumulation of platform B1 in tumour tissue was monitored with photoacoustic imaging in A431 xenographt model. We observed slight improvement in the tumour accumulation of targeted liposomes compared to control. The signal was not homogeneous within the tumour tissue and mostly situated near to blood vessels. The biodistribution studies of platform B2 were performed by µCT/FMT combined imaging system in PC3 tumour model. The overall

biodistribution of the RF-targeted liposomes was comparable to control and there was no significant difference in their tumour accumulation. Though, this could due to slow growth of PC3 xenographs and insufficient vascularisation. Nevertheless, histological analysis revealed enhanced vascular targeting with RFA-functionalised liposomes. In summary, these initiate *in vivo* studies of RFA-functionalised drug delivery platforms could give useful insights for further investigations.

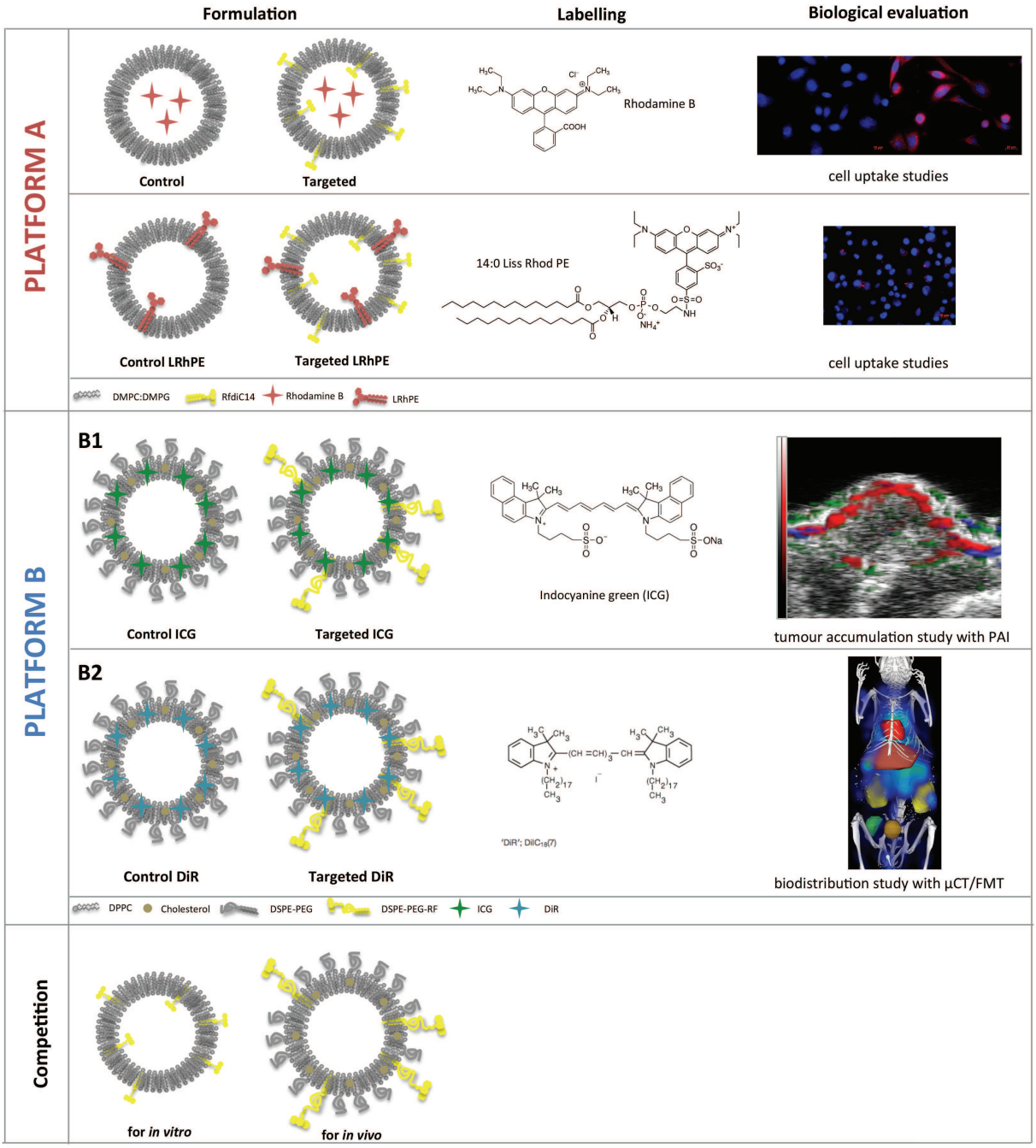

Figure 6.3 Summary of prepared RFA-functionalised platforms

In perspective of this work it would be interesting to explore further the potential of synthesised RFAs.

Concerning RFA insertion in lipid-based nanosystems, an in-depth evaluation of

platform B with additional *animal experiments* could be performed. For instance, with more important number of animals and higher concentration of platform B1 liposomes in A431 tumour model, one could probably find more substantial differences in tumour accumulation. On the other hand, in PC3 tumour model the xenographts were slowly growing and poorly vascularised. Therefore, this study might be repeated with the utilisation of Matrigel® for increased tumour growth or with an orthotropic model.

So far, we explored only two cancer models – prostate and epidermic. However, we know from the literature, that RF transporters are also overexpressed in breast cancer[109] and hepatocellular carcinoma.[110] Therefore, the studies of RFA targeting potential could also continue in this direction. One might start from several cellular uptake experiments in breast cancer (e.g. MCF7, MDA etc.) and hepatocellular carcinoma cell lines (e.g. Huh7, HEPG2 *etc*.) and then proceed to animal trials.

Moreover, at the *cellular level* one could also explore the RFA internalisation pathway by endosome tracking. Another possibility is to encapsulate in the RFA-functionalised liposomes a drug, which alone is not able to enter cells. A nucleic acid such as microRNA or siRNA could be an excellent candidate for this study. The therapeutic site of these molecules is situated in the cytosol and thus requires an endosomal escape.

Finally, the insertion of RFA in other lipid-based nanosystems such as nanoparticles or nanoemulsions to render them tumor specific could be envisioned.

Concerning *RFA auto-assemblies, their investigation* could continue in two major directions. Firstly, further structural characterisation of formed lamellar objects is needed. One could perform molecular modelling simulations, additional ss NMR investigations, SAXS and DSC which would help to better understand the bilayer architecture and confirm our hypothesis about π-stacking interactions between RF headgroups. Secondly, the impact of RFA self-assemblies on RF physicochemical properties would be considered - fluorescence analysis, redox potential and photosensitizing. Indeed, several studies showed that the integration of RF in supramolecular systems such as hydrogels,[102] polymeric helices[100] or carbon nanotubes[106] creates stimuli-responsive objects with interesting physicochemical properties. This could be also the case for our RFA auto-assemblies.

Finally, from a *chemical point of view*, one could suggest to synthesise additional RFA derivatives with different lipids introduced in other positions on RF template. These modifications may have important consequences on the auto-assembly formation.

7 Experimental section

7.1 Chemicals and Analytical Conditions

Reagents and solvents were purchased from Sigma Aldrich, Glen Research or Alfa Aesar and were utilised without further purification. Phospholipids were purchased from Bachem or Avanti Polar Lipids (USA). Fluorescent dyes were purchased from Sigma Aldrich (Germany), except DiR purchased from Life Technologies (Carlsbad, California, USA). Cell culture media and additives were from Gibco®/Life Technologies (Carlsbad, California, USA).

For the flash chromatography, silica gel 60 (particle size: 45 μm, Biotage) was utilized. Aluminum plates coated with silica gel 60 F254 (Merck) were used for thin layer chromatography (TLC). The TLC plates were analysed with visible/UV light or revealed with phosphomolybdic acid solution (10 %).

All synthesised compounds were characterized using ^{1}H, ^{13}C and ^{31}P NMR spectroscopy (apparatus Bruker Avance DPX-300, ^{1}H at 300 MHz, ^{13}C at 75 MHz, and ^{31}P at 121 MHz or Bruker Avance DPX-400, ^{1}H at 400 MHz, ^{13}C at 100 MHz, and ^{31}P at 162 MHz). The NMR chemical shifts are reported in parts per million relative to the tetramethylsilane, using the deuterium signal of the solvent ($CDCl_3$, MeOD or deuterated dimethylsulfoxide DMSO-d_6) as a heteronuclear reference for ^{1}H. The ^{1}H NMR coupling constants, J's, are reported in Hz.

Electrospray ionization mass spectra (Full ESI-MS) were performed by the "Mass Spectrometry Platform" at IECB (Bordeaux, France) on Agilent 6560 ESI-IMS-Q-TOF apparatus. For the PEGylated sample an Ultraflex III MALDI-TOF-TOF instrument (Bruker Daltonics GmbH, Bremen, Germany) equipped with a Smartbeam 2 laser with a repetition rate up to 200Hz (500 lazer shots) was used. The obtained mass spectrum was analysed with Flex-analysis version 4.0 software (Bruker Daltonics GmbH, Bremen, Germany).

HPLC separation and analysis were performed with Waters® Alliance 2695 (Waters® Corporation, USA) apparatus equipped with the UV-detector Waters® 486, USA and analysed with Millennium 32 software (Waters® Corporation, USA). The reverse phase analytical C8 column (Macherey-Nagel, GmbH&Co, KG) was used for all separations.

7.2 Synthesis

7.2.1 Click chemistry

7.2.1.1 Preparation of RF-Ac-propargyl (1, 2)

2', 3', 4', 5'-tétra-O-acétylriboflavin (1)

RF (2 g, 5.31 mmol) was solubilised in AcOH/Ac_2O mixture (80 mL 1/1 v/v) under argon atmosphere. Then perchloric acid (1.2 eq, 641 mg, 6.37 mmol) was added and the reaction mixture was heated at 50°C. After 2h the reaction was cooled down with ice and 80 mL of water were added. The product was extracted with DCM (3 x 120 mL). The combined organic

layers were washed with water (3 x 120 mL) and brine (3 x 120 mL), dried over Na_2SO_4, filtered and evaporated under reduced pressure. The obtained yellow solid displayed sufficient purity and was utilised without purification. Yield: 2.76g (5.07 mmol, 95%)

^{1}H NMR (300 MHz, $CDCl_3$): δ (ppm) = 1.78 (s, 3H, CH_3, Ac), 2.10 (s, 3H, CH_3, Ac), 2.24 (s, 3H, CH_3, Ac), 2.31 (s, 3H, CH_3, Ac), 2.47 (s, 3H, CH_3), 2.58 (s, 3H, CH_3), 4.23-4.48 (m, 2H, CH_2-N), 4.91 (m, 1H, CH-O), 5.15 (m, 1H, CH-O), 5.40-5.50 (m, 2H, CH_2-O), 5.66-5.71 (m, 1H, CH-O), 7.58 (s, 1H, CH_{ar}), 8.05 (s, 1H, CH_{ar}), 8.52 (s, 1H, NH).

^{13}C NMR (75 MHz, $CDCl_3$): δ (ppm) = 19.5 (CH_3), 20.4 (CH_3), 20.8 (CH_3, Ac), 20.9 (CH_3, Ac), 21.1 (CH_3, Ac), 21.5 (CH_3, Ac), 45.0 (CH_2-N), 61.9 (CH_2-O), 68.9 (CH-O), 69.4 (CH-O), 70.4 (CH-O), 115.5 (CH_{ar}), 131.2 (CH_{ar}), 132.9 (C_{ar}), 134.6 (C_{ar}), 135.9 (C_{ar}), 137.0 (C_{ar}), 148.26 (C=N), 150.70 (C=N), 154.38 (C=O), 159.33 (C=O), 169.9 - 170.68 (C=O, Ac).

*3-propargyl-2', 3', 4', 5' - tétra-O-acétylriboflavin (**2**)*

Compound 1 (1 g, 1.83 mmol) was dissolved in anhydrous DMF under argon atmosphere and heated to 55°C. Then DBU (3 eq, 837 mg, 5.5 mmol) and propargyl bromide (2 eq, 915 mg, 3.67 mmol) were added. After 48h the organic solvent was evaporated under reduced pressure. Water (100 mL) was added to the crude product, which was further extracted 3 times with ether (100 mL) and washed with brine (100 mL). Combined organic layers were dried over Na_2SO_4, filtered and the solvent was evaporated under reduced pressure. The crude product was purified on silica gel column (Ethyl acetate/Hexane, 8/2 to 10/0, v/v) to afford an orange solid. Yield: 1g, (1.72 mmol, 94%).

^{1}H NMR (300 MHz, $CDCl_3$): δ (ppm) = 1.74 (s, 3H, CH_3, Ac), 2.08 (s, 3H, CH_3, Ac), 2.17-2.19 (m, 1H, C≡CH), 2.23 (s, 3H, CH_3, Ac), 2.32 (s, 3H, CH_3, Ac), 2.45 (s, 3H, CH_3), 2.56 (s, 3H, CH_3), 4.22-4.45 (m, 2H, CH_2-N), 4.84-4.85 (m, 2H, CH_2-C≡C), 5.40-5.56 (m, 2H, CH_2-O), 5.65-5.68 (m, 1H, CH-O), 7.56 (s, 1H, CH_{ar}), 8.05 (s, 1H, CH_{ar}).

7.2.1.2 Preparation of lipid chain azides (3a-d)

*1-azidooctadecane (**3a**)*

Sodium azide (3 eq, 1.17 g, 17 mmol) and octadecane bromide (2 g, 5.99 mmol) were dissolved in 22 mL of anhydrous DMF. The reaction mixture was heated to 80°C and stirred during 24h. Then the solution was cooled down and 100 mL of ethyl acetate were added. The organic layer was washed with water (2 x 25 mL) and brine (25 mL) and subsequently dried over Na_2SO_4, filtered and evaporated under reduced pressure. The crude product was purified by silica gel chromatography (Hexane/Ethyl acetate, 99/1, v/v) to afford compound 3a as oil. Yield: 1.25 g (4.25 mmol, 71%).

^{1}H NMR (300 MHz, $CDCl_3$): δ (ppm) = 0.88-0.94 (m, 3H, CH_3), 1.27-1.40 (m, 30H, 15 × CH_2), 1.66 (m, 2H, CH_2-C-N_3), 3.25-3.30 (m, 2H, CH_2-N_3).

*1-azidohexadecane (**3b**)*

The protocol was similar to the previous one (compound **3a)**. Briefly, hexadecane (2 g, 6.55 mmol) and sodium azide (3 eq, 1.28 g, 19 mmol) were solubilised in anhydrous DMF (24 mL) and stirred for 24h. After the work-up procedure and purification on silica gel column (Hexane/Ethyl acetate, 99/1, v/v) the desired product **3b** was obtained. Yield: 1.67 g (6.22 mmol, 95%).

^{1}H NMR (300 MHz, $CDCl_3$): δ (ppm) = 0.88-0.92 (m, 3H, CH_3), 1.30 (m, 26H, 13 × CH_2), 1.57-1.64 (m, 2H, CH_2-CH_3), 3.25-3.30 (m, 2H, CH_2-N_3).

*1-azidododecane (**3c**)*

The protocol was similar to the previous one (compound **3a)**. Briefly, dodecane (2 g, 8.03 mmol) and codium azide (3 eq, 1.56 g, 24 mmol) were solubilised in anhydrous DMF (29 mL) and stirred for 24h. After the work-up procedure and purification on silica gel column (Hexane/Ethyl acetate, 99/1, v/v) the desired product **3c** was obtained. Yield: 1.67 g (7.90 mmol, 98%).

^{1}H NMR (300 MHz, $CDCl_3$): δ (ppm) = 0.88-0.92 (m, 3H, CH_3), 1.30 (m, 18H, 9 × CH_2), 1.57-1.64 (m, 2H, CH_2-CH_3), 3.25-3.30 (m, 2H, CH_2-N_3).

*heptadecafluoro-1-azidododecane (**3d**)*

The protocol was similar to the previous one (compound **3a)**. Briefly, heptadecafluorodecane iodide (0.5 g, 0.87 mmol) and Sodium azide (3 eq, 170 mg, 2.61 mmol) were solubilised in anhydrous DMF (15 mL) and stirred for 24h. After the work-up procedure and purification on silica gel column (Hexane/Ethyl acetate, 99/1, v/v) the desired product **3c** was obtained. Yield: 322 mg (0.65 mmol, 75%).

^{1}H NMR (300 MHz, $CDCl_3$): δ (ppm) = 2.29-2.47 (m, 2H, CH_2-N_3), 3.69-3.64 (m, 2H, CF_2-CH_2).

7.2.1.3 Click chemistry coupling (4a-4d)

*3-octadecane-triazole-2', 3', 4', 5' - tetra-O-acetylriboflavin (**4a**)*

Compound **2** (300 mg, 0.53 mmol) was solubilised in anhydrous DMSO (30 mL) under argon atmosphere. Then 1-azidooctadecane **3a** (2.3 eq, 359 mg, 1.22 mmol) and CuI (1.5 eq, 151 mg, 0.79 mmol) were added and the reaction mixture was heated to 80°C during 3h. Next the solution was cooled down to RT and 80 mL of water were added. The crude product was extracted with 3 x 150 mL of ether and the combined organic layers were washed with NH_4Cl until the appearance of a yellow fluorescent colour. The solution was dried with Na_2SO_4, filtered and was evaporated under reduced pressure. Purification by silica gel chromatography (DCM/MeOH, 99/1 to 80/20, v/v) afforded the desired product **4a** as an orange solid. Yield: 233 mg (0.27 mmol, 50%).

^{1}H NMR (300 MHz, $CDCl_3$): δ (ppm) = 0.84-0.90 (m, 3H, CH_3, chain), 1.23-1.24 (d, 34H,

17 × CH_2,chain), 1.72 (s, 3H, CH_3, Ac), 1.79-1.89 (m, 2H, N-CH_2, triazole), 2.06 (s, 3H, CH_3, Ac), 2.21 (s, 3H, CH_3, Ac), 2.29 (s, 3H, CH_3, Ac), 2.44 (s, 3H, CH_3), 2.52 (s, 3H, CH_3), 4.20-4.29 (m, 2H, CH_2-N), 4.40-4.45 (m, 1H, CH-O), 4.86 (m, 1H, CH-O), 5.38-5.45 (m, 2H, CH_2-O), 5.63-5.66 (m, 1H, CH-O), 7.53 (s, 1H, CH_{ar}), 7.67 (s, 1H, CH_{ar}), 8.01 (s, 1H, CH, triazole).

*3-hexadecane- triazole -2', 3', 4', 5' - tetra-O-acetylriboflavin (**4b**)*

The protocol was similar to the one used for the compound **4a**. Briefly, compound **2** (170 mg, 0.30 mmol), 1-azidohexadecane (**3b**) (2.3, 182 mg, 0.69 mmol) and CuI (1.5 eq, 85 mg, 0.45 mmol) were solubilised in anhydrous DMSO (16 mL) and stirred at 80°C for 3h. After the work-up procedure and purification on silica gel column (DCM/MeOH, 99/1 to 80/20, v/v) the desired product **4b** was obtained. Yield: 170 mg (0.20 mmol, 66%).

^{1}H NMR (300 MHz, $CDCl_3$): δ (ppm) = 0.84-0.88 (m, 3H, CH_3, chain), 1.23-1.24 (s, 30H, 15 × CH_2,chain), 1.72 (s, 3H, CH_3, Ac), 1.79-1.89 (m, 2H, N-CH_2, triazole), 2.06 (s, 3H, CH_3, Ac), 2.21 (s, 3H, CH_3, Ac), 2.29 (s, 3H, CH_3, Ac), 2.44 (s, 3H, CH_3), 2.52 (s, 3H, CH_3), 4.20-4.29 (m, 2H, CH_2-N), 4.40-4.45 (m, 1H, CH-O), 4.86 (m, 1H, CH-O), 5.38-5.45 (m, 2H, CH_2-O), 5.63-5.66 (m, 1H, CH-O), 7.53 (s, 1H, CH_{ar}), 7.67 (s, 1H, CH_{ar}), 8.01 (s, 1H, CH, triazole).

*3-dodecane- triazole -2', 3', 4', 5' - tetra-O-acetylriboflavin (**4c**)*

The protocol was similar to the one used for the compound **4a**. Briefly, compound **2** (300 mg, 0.53 mmol), 1-azidododecane (**3b**) (2.3, 257 mg, 1.22 mmol) and CuI (1.5 eq, 151 mg, 0.79 mmol) were solubilised in anhydrous DMSO (30 mL) and stirred at 80°C for 3h. After the work-up procedure and purification on silica gel column (DCM/MeOH, 99/1 to 80/20, v/v) the desired product **4c** was obtained. Yield: 197 mg (0.25 mmol, 47%).

^{1}H NMR (300 MHz, $CDCl_3$): δ (ppm) = 0.85-0.90 (m, 3H, CH_3, chain), 1.23-1.24 (s, 22H, 11 × CH_2,chain), 1.74 (s, 3H, CH_3, Ac), 1.81-1.88 (m, 2H, N-CH_2, triazole), 2.08 (s, 3H, CH_3, Ac), 2.23 (s, 3H, CH_3, Ac), 2.31 (s, 3H, CH_3, Ac), 2.44 (s, 3H, CH_3), 2.52 (s, 3H, CH_3), 4.22-4.30 (m, 2H, CH_2-N), 4.41-4.47 (m, 1H, CH-O), 4.92 (m, 1H, CH-O), 5.40-5.49 (m, 2H, CH_2-O), 5.63-5.68 (m, 1H, CH-O), 7.55 (s, 1H, CH_{ar}), 7.68 (s, 1H, CH_{ar}), 8.02 (s, 1H, CH, triazole).

*3-(heptadecafluoro-10-azidodecane)- triazole -2', 3', 4', 5'- tetra-O-acetylriboflavin (**4d**)*

The protocol similar to the one used for the compound **4a**. Briefly, compound **2** (125 mg, 0.22 mmol), heptadecafluoro-1-azidodecane (**3b**) (2.3, 241 mg, 0.49 mmol) and CuI (1.5 eq, 61 mg, 0.32 mmol) were solubilised in anhydrous DMSO (24 mL) and stirred at 80°C for 3h. After the work-up procedure and purification on silica gel column (DCM/MeOH, 99/1 to 80/20, v/v) the desired product **4d** was obtained. Yield: 109 mg (0.10 mmol, 47%).

^{1}H NMR (300 MHz, $CDCl_3$): δ (ppm) = 0.84-0.89 (m, 3H, CH_3, chain), 1.24 (s, 4H, 2 × CH_2, chain), 1.74 (s, 3H, CH_3, Ac), 1.81-1.88 (m, 2H, N-CH_2, triazole), 2.08 (s, 3H, CH_3, Ac), 2.23

(s, 3H, CH_3, Ac), 2.31 (s, 3H, CH_3, Ac), 2.44 (s, 3H, CH_3), 2.52 (s, 3H, CH_3), 4.24-4.38 (m, 2H, CH_2-N), 4.41-4.47 (m, 1H, CH-O), 4.92 (m, 1H, CH-O), 5.40-5.49 (m, 2H, CH_2-O), 5.63-5.68 (m, 1H, CH-O), 7.55 (s, 1H, CH_{ar}), 7.68 (s, 1H, CH_{ar}), 8.02 (s, 1H, CH, triazole).

7.2.1.4 Final deprotection (5a-5d)

*3-octadecane- triazole -riboflavin (**5a**)*

Compound **4a** (233 mg, 0.27 mmol) was dissolved in 16 mL of MeOH and sodium methoxide (1.85 eq, 27 mg, 0.49 mmol) was added. The reaction was stirred 24h in RT (rt) under argon atmosphere. Then ± 3 g of silica were added to stop the reaction and methanol was evaporated under reduced pressure. The desired product **5a** was obtained after purification by silica gel chromatography (DCM/MeOH, 98/2 to 50/50). Yield: 155 mg (0.22 mmol, 82%).

^{1}H NMR (300 MHz, $CDCl_3$): δ (ppm) = 0.84-0.90 (m, 3H, CH_3, chain), 1.24 (s, 34H, 17 × CH_2,chain), 1.73 (m, 2H, N-CH_2, triazole), 2.41 (s, 3H, CH_3), 2.50 (s, 3H, CH_3), 4.24-4.28 (m, 2H, CH_2-N), 4.51 (m, 1H, CH-O), 4.80-4.82 (m, 1H, CH-O), 4.90 (m, 1H, CH-O), 5.15 (m, 2H, CH_2-O), 7.95 (s, 1H, CH_{ar}), 7.87 (s, 1H, CH_{ar}), 8.14 (s, 1H, CH, triazole).

Mass observed: 732.5 (M^{+23}).

*3-hexadecane- triazole -riboflavin (**5a**)*

The protocol was similar to the one used for the compound **5a**. Briefly, compound **4b** (170 mg, 0.20 mmol and sodium methoxide (1.85 eq, 20 mg, 0.37 mmol) were solubilised in MeOH (12 mL) and stirred at rt for 24h. Then ± 3 g of silica were added to stop the reaction and methanol was evaporated under reduced pressure. After purification (DCM/MeOH, 98/2 to 50/50) the desired product **5b** was obtained. Yield: 141 mg (0,20 mmol, 100%).

^{1}H NMR (300 MHz, $CDCl_3$): δ (ppm) = 0.81-0.85 (m, 3H, CH_3, chain), 1.19-1.21 (s, 30H, 15 × CH_2,chain), 1.73 (m, 2H, N-CH_2, triazole), 2.41 (s, 3H, CH_3), 2.50 (s, 3H, CH_3), 4.24-4.28 (m, 2H, CH_2-N), 4.51 (m, 1H, CH-O), 4.80-4.82 (m, 1H, CH-O), 4.92 (m, 1H, CH-O), 5.14 (m, 2H, CH_2-O), 7.95 (s, 1H, CH_{ar}), 7.96 (s, 1H, CH_{ar}).

Mass observed: 704.5 (M^{+23}).

*3-dodecane- triazole -riboflavin (**5c**)*

The protocol was similar to the one used for the compound **5a**. Briefly, compound **4c** (197 mg, 0.25 mmol and sodium methoxide (2.3 eq, 32 mg, 0.58 mmol) were solubilised in MeOH (20 mL) and stirred at rt for 24h. Then ± 3 g of silica were added to stop the reaction and methanol was evaporated under reduced pressure. After purification (DCM/MeOH, 98/2 to 50/50) the desired product **5c** was obtained. Yield: 109 mg (0.18 mmol, 70%).

^{1}H NMR (300 MHz, $CDCl_3$): δ (ppm) = 0.81-0.86 (m, 3H, CH_3, chain), 1.20 (s, 22H, 11 × CH_2,chain), 1.72-1.76 (m, 2H, N-CH_2, triazole), 2.41 (s, 3H, CH_3), 2.50 (s, 3H, CH_3), 4.24-4.29 (m, 2H, CH_2-N), 4.51 (m, 1H, CH-O), 4.80-4.82 (m, 1H, CH-O), 4.92 (m, 1H, CH-O),

5.14 (m, 2H, CH_2-O), 7.95 (s, 1H, CH_{ar}), 7.96 (s, 1H, CH_{ar}).

Mass observed: 648,4 (M^{+23}).

*3-(heptadecafluoro-1-dodecane)- triazole-riboflavin (**5d**)*

The protocol was similar to the one used for the compound **5a**. Briefly, compound **4d** (109 mg, 0.10 mmol and sodium methoxide (1.85 eq, 10 mg, 0.19 mmol) were solubilised in MeOH (10 mL) and stirred at rt for 24h. Then ± 1.5 g of silica were added to stop the reaction and methanol was evaporated under reduced pressure. After purification (DCM/MeOH, 98/2 to 50/50) the desired product **5c** was obtained. Yield: 36 mg (0.04 mmol, 39%).

^{1}H NMR (300 MHz, $CDCl_3$): δ (ppm) = 0.84-0.89 (m, 3H, CH_3, chain), 1.24 (s, 4H, 2 × CH_2, chain), 1.73 (m, 2H, N-CH_2, triazole), 2.41 (s, 3H, CH_3), 2.50 (s, 3H, CH_3), 4.24-4.28 (m, 2H, CH_2-N), 4.51 (m, 1H, CH-O), 4.80-4.82 (m, 1H, CH-O), 4.90 (m, 1H, CH-O), 5.15 (m, 2H, CH_2-O), 7.95 (s, 1H, CH_{ar}), 7.97 (s, 1H, CH_{ar}), 7.96 (s, 1H, CH_{ar}), 8.14 (s, 1H, CH, triazole).

Mass observed: 904.2 (M^{+23}).

7.2.2 Phosphoramidite chemistry

7.2.2.1 RF-phosphoramidite preparation (6-9)

*5'-O-(4,4'-dimethoxytrityl)-riboflavin (**6**)*

Compound **6** was synthesized as described previously (Rublack N. et al. J of Nucl Ac, V 2011, ID 805253). Briefly, riboflavin (807 mg, 2.14 mmol) was dissolved in dry pyridine (100 mL) under argon atmosphere. Then TEA (3.6 eq, 1 mL, 7.7 mmol), DMAP (0.05 eq, 13 mg, 0.1 mmol) and 4,4' - dimethoxytritylchloride (1.3 eq, 915 mg, 2.7 mmol), were added. The reaction mixture was stirred overnight at RT. To stop the reaction 15 ml of methanol were added and organic solvents were evaporated under reduced pressure. The crude product was dissolved in DCM (50 mL), then filtered, evaporated and purified by silica gel column chromatography (DCM/MeOH/TEA 97/2/1 v/v/v) to afford an orange solid. Yield: 510 mg (0.75 mmol, 35 %).

^{1}H NMR (300 MHz, DMSO-d_6): δ (ppm) = 2.39 (s, 3H, CH_3), 2.41 (s, 3H, CH_3), 3.05-3.18 (m, 2H, CH_2-O), 3.72 (s, 6H, 2 × CH_3-O, DMT), 3.92 (s, 1H, CH-O), 4.23 (s, 1H, CH-O), 4.63 (m, 1H, CH_2-N), 4.94 (m, 1H, CH_2-N), 6.86 (m, 4H, DMT), 7.45-7.17 (m, 9H, DMT), 7.83 (s, 1H, CH_{ar}), 7.90 (s, 1H, CH_{ar}), 11.37 (s, 1H, NH).

^{13}C NMR (75 MHz, $CDCl_3$): δ (ppm) = 29.7 (CH_3), 45.7 (CH_2-N), 55.2 (CH_3-O, DMT), 68.5 (CH-O), 76.6 (CH-O), 77.2 (CH-O), 81.4 (C, DMT), 113.1 (CH_{ar}), 127.0-129.1 (CH_{ar}, DMT), 139.4 (C_{ar}), 147.3-158.6 (C_{ar}, DMT), 159.4 (C_{ar}).

*5'-O-(4,4'-dimethoxytrityl)- 2', 3', 4'- tri-O-acetylriboflavin (**7**)*

Compound **6** (510 mg, 0.75 mmol) was dissolved in dry pyridine (75 mL) and then cooled in an ice bath (0°C) under argon atmosphere. Acetic anhydride (40 eq, 2.8 mL, 30 mmol) was added dropwise and the reaction mixture was stirred overnight at RT. To stop the reaction 3

mL of methanol were added and organic solvents were evaporated under reduced pressure. The crude product was purified by silica gel column chromatography (Ethyl acetate/Hexane 8/2 v/v) to give the desired compound as orange solid. Yield: 545 mg (0.68 mmol, 90 %).

^{1}H NMR (300 MHz, DMSO-d$_6$): δ (ppm) = 1.49 (s, 3H, CH_3 Ac), 2.01 (s, 3H, CH_3 Ac), 2.27 (s, 3H, CH_3 Ac), 2.39 (s, 3H, CH_3), 2.41 (s, 3H, CH_3), 3.08-3.03 (m, 1H, CH_2-O), 3.26-3.22 (m, 1H, CH_2-O), 3.73 (s, 6H, 2 × CH_3-O, DMT), 4.79 (s, 1H, CH_2-N), 4.84 (s, 1H, CH_2-N), 5.25 (m, 2H, CH-O), 5.49 (m, 1H, CH-O), 6.87 (m, 4H, DMT), 7.33-7,2 (m, 9H, DMT), 7.65 (s, 1H, CH_{ar}), 7.90 (s, 1H, CH_{ar}), 11.42 (s, 1H, NH)

^{13}C NMR (75 MHz, CDCl$_3$): δ (ppm) = 19.3 (CH_3), 20.3 (CH_3 Ac), 21.1 (CH_3 Ac), 21.4 (CH_3 Ac), 45.1 (CH_2-N), 55.1 (CH_3-O, DMT), 60.7 (CH_2-O), 62.4 (CH-O), 70.1 (CH-O), 72.4 (CH-O), 81.3 (C, DMT), 113.1 (CH_{ar}, DMT), 115.7 (CH_{ar}), 126.8-131.3 (CH_{ar}, DMT), 132.49 (CH_{ar}), 132.6 (CH_{ar}, DMT), 134.5 (C_{ar}), 134.6 (C_{ar}), 135.4-139.5 (C_{ar}, DMT), 144.4 (C=N), 148.1-158.5 (C_{ar}, DMT), 159.6 (C=O), 170.1 (C=O, Ac), 170.3 (C=O, Ac), 170.6 (C=O, Ac).

*2', 3', 4' - tri-O-acetylriboflavin (**8**)*

Compound **7** (545 mg, 0.68 mmol) was dissolved in nitromethane (20 mL) and anhydrous $ZnBr_2$ (9 eq, 1.27 g, 5.6 mmol) was added. After 10 min the reaction was quenched by addition of ammonium acetate (100 mL, 1 M in water). Then, 100 mL of DCM were added and the organic layer was separated, washed with brine (2 × 40 mL) and dried over sodium sulfate. After evaporation of DCM under reduced pressure, the crude product was extracted several times with ice-cold diethyl ether to remove residual DMT. The desired compound was obtained as yellow powder (323 mg) and utilised for the next step without further purification.

*5'-(2-cyanoethyl-N,N-diisopropyl)- 2', 3', 4'- tri-O-acetylriboflavin-phosphoramidite (**9**)*

All starting materials were dried overnight under high vacuum. The glassware and molecular sieves were dried overnight in an oven at 200°C. Under argon atmosphere compound **8** (323 mg) was dissolved in 6 mL of dry DCM containing molecular sieves. To this solution freshly distilled DIPEA (0.55 mL) and 2-cyanoethyl-*N*,*N*-diisopropylchlorophosphoramidite (1.2 eq, 0.17 mL, 0.78 mmol) were added. After overnight stirring at RT, the reaction was stopped with 0.5 mL of methanol. The reaction mixture was evaporated under reduced pressure, then diluted in ethyl acetate (10 mL) with TEA (0.5 mL) and washed with brine (2 × 20 mL). Combined organic layers were dried over Na_2SO_4 and solvents were removed under reduced pressure. The presence of the desired compound was confirmed by ^{31}P NMR and ESI-MS analysis and the product (241 mg) was utilised without purification. Prior to the next reaction step the product was stored overnight in a vacuum desiccator with phosphorus pentoxide.

^{31}P NMR (121 MHz, CDCl$_3$): δ (ppm) = 152.2, 152.4 (two diasteroisomers).

Mass observed: 701.3 (M^{-1}).

7.2.2.2 Preparation of glyceroether (10-13)

*5-O-paramethoxyphenyl-(S)-solketal (**10**)*

(*S*)-(+)-1,2-Isopropylideneglycerol (0.96 mL 7.50 mmol), paramethoxyphenol (3 eq, 2.79 g, 22.5 mmol) and triphenylphosphine (1.3 eq, 2.56 g, 9.75 mmol) were dissolved in dry toluene (35 mL). Then diethylazodicarboxylate 40% in toluene (1.3 eq, 4.4 mL, 9.75 mmol) was added dropwise. After stirring 3h at RT, the reaction mixture was diluted in water. The aqueous layer was extracted with diethyl ether (2 x 10 mL) and the combined organic layers were washed with brine (2 x 15 mL), dried over Na_2SO_4 and concentrated under reduced pressure. The crude product was purified by silica gel chromatography (ethyl acetate/hexane 10/90 v/v) to afford the desired product as a yellow oil (1.69 g, 94 %).

^{1}H NMR (300 MHz, $CDCl_3$): δ (ppm) = 1.40 (s, 3H, CH_3), 1.41 (s, 3H, CH_3), 3.77 (s, 3H, CH_3-O, PMP), 3.89 (dd, *J=8.8; 5.9Hz*, 2H, CH_2-O), 4.01 (dd, *J=9.5; 5.5Hz*, 1H, CH-O), 4.13-4.20 (m, 1H, CH_2-O), 4.50-4.43 (m, 1H, CH_2-O), 6.84 (m, 4H, CH_{ar})

^{13}C NMR (75 MHz, $CDCl_3$): δ (ppm) = 25.3 (CH_3), 26.8 (CH_3), 55.7 (CH_3-O, PMP), 66.8 (CH_2-O), 69.5 (CH_2-O), 77.2 (CH-O), 109.7 (C), 115.4 (CH_{ar} PMP), 152.7 (C_{ar}, PMP), 154.0 (C_{ar}, PMP).

*5-O-paramethoxyphenyl-(S)-glycerol (**11**)*

Compound **10** (1.69 g, 7.0 mmol) was dissolved in methanol (50 mL) and DOWEX 50WX2 resin (3.30 g) was added. The reaction mixture was stirred overnight at RT then filtered and methanol was evaporated under reduced pressure. TLC (ethyl acetate/hexane 70/30 v/v) and ^{1}H-NMR analysis of crude product showed the desired compound with sufficient purity. The product (1.32 g, white powder) was utilized without further purification.

^{1}H NMR (300 MHz, $CDCl_3$): δ (ppm) = 3.69-3.88 (m, 5H, CH_3-O, CH_2-O), 3.94-4.02 (m, 2H, CH_2-O), 4.05-4.12 (m, 1H, CH-O), 6.84 (m, 4H, CH_{ar}).

^{13}C NMR (75 MHz, $CDCl_3$): δ (ppm) = 55.7 (CH_3-O, PMP), 63.7 (CH_2-O), 69.8 (CH_2-O), 70.4 (CH_2-O), 77.2 (CH-O), 114.6 (CH_{ar} PMP), 115.4 (CH_{ar} PMP), 152.7 (C_{ar}, PMP), 154.0 (C_{ar}, PMP).

*5-O-paramethoxyphenyl-(S)-1,2-O-dimyristoylglycerol (**12**)*

PMP-protected compound **11** (1.32 g) was added to a suspension of NaH 60 % (4 eq, 0.89 g, 26.6 mmol) in dry DMF (67 mL). After stirring for 30 min at RT, 1-Bromotetradecane (6 eq, 12 mL, 39.9 mmol) was slowly added. The reaction mixture was stirred overnight at RT. To stop the reaction 20 mL of MeOH were added and the crude product was diluted with water (20 mL). The aqueous layer was extracted with diethyl ether (3 x 20 mL) and the combined organic layers were washed with brine (2 x 30 mL), dried over Na_2SO_4 and removed under reduced pressure. The crude product was purified by silica gel chromatography (hexane/ethyl acetate 90/10) to afford the desired product as a white solid (2.73 g, 66 %).

^{1}H NMR (300 MHz, $CDCl_3$): δ (ppm) = 0.86 (m, 6H, 2 × CH_3), 1.25 (s, 44H, 22 × CH_2),

1.59 (m, 4H, 2 × CH_2), 3.38-3.65 (m, 6H, 3 × CH_2-O), 3.70-3.79 (m, 4H, CH_3-O, CH-O), 3.93-4.06 (m, 2H, CH_2-O), 6.82 (m, 4H, CH_{ar}).

^{13}C NMR (75 MHz, $CDCl_3$): δ (ppm) = 14.1 (CH_3), 22.7-31.9 (CH_2), 55.7 (CH_3-O, PMP), 68.6 (CH_2-O), 70.3 (CH_2-O), 70.8 (CH_2-O), 71.7 (CH_2-O), 77.2 (CH-O), 114.5 (CH_{ar} PMP), 115.5 (CH_{ar} PMP), 153.0 (C_{ar}, PMP), 153.7 (C_{ar}, PMP).

(S)-1,2-O-dimyristoylglycerol (compound **13**)

Compound **12** 2.73 g (4.62 mmol) was dissolved in ACN/H_2O 8:2 mixture (45 mL) and then put on ice bath. 6.65 g of ceric ammonium nitrate (2.6 eq, 12 mmol) were added subsequently and the reaction mixture was stirred overnight. After a work-up procedure (brine 2 x 30 mL, sodium sulfate) the crude product was purified by silica gel chromatography (hexane/ethyl acetate 90/10 v/v) to give a white powder (1.37 g, 61 %).

^{1}H NMR (300 MHz, $CDCl_3$): δ (ppm) = 0.88 (m, 6H, 2 × CH_3), 1.25 (s, 44H, 22 × CH_2), 1.57 (m, 4H, 2 × CH_2), 2.01 (s, 1H, OH), 3.41-3.75 (m, 9H, 4 × CH_2-O,CH-O).

^{13}C NMR (75 MHz, $CDCl_3$): δ (ppm) = 14.1 (CH_3), 22.7-31.9 (CH_2), 63.1 (CH_2-OH), 70.4 (CH_2-O), 70.9 (CH_2-O), 71.8 (CH_2-O), 77.2 (CH_2-O), 78.2 (CH-O).

Mass observed: 485.5 (M^{+1}).

7.2.2.3 Phosphodiester coupling (14)

*5'-O-(1'', 2''-dimyristoyl-cyanoethylphosphoryl)-2', 3', 4'-tri-O-acetylriboflavin (**14**)*

To afford compound **14** all starting materials were dried overnight with a high vacuum pump. The glassware and molecular sieves were dried overnight in an oven at 200°C. Under argon atmosphere compound **9** (241 mg) was dissolved in 3 mL dry THF containing molecular sieves. Then a solution of 200 mg of compound **13** (1.2 eq, 0.41 mmol) in THF (3 mL) and 4.4 mL of 5-benzylthio-1H-tetrazole (1.3 eq, 0.44 mmol) were added. After stirring 6 h at RT, an oxidizing solution (20 mL, 0.2 M iodine in THF/Pyridine/H_2O 2/1/1) was added. The reaction was stirred overnight at RT and stopped by adding a solution of sodium bisulfite (5 % in water) until the brown color had vanished. The reaction mixture was diluted with ethyl acetate (20 mL) and the organic layer was washed with sodium bicarbonate (2 x 20 mL), brine (2 x 20 mL) and finally dried with Na_2SO_4. The solvents were evaporated under reduced pressure. The crude product was purified by silica gel column chromatography (Ethyl acetate 100 %) to afford a yellow powder. Yield: 227 mg (0.21 mmol, 30 %).

^{1}H NMR (300 MHz, $CDCl_3$): δ (ppm) = 0.87 (t, *J=6,6 Hz*, 6H, 2 × CH_3, chains), 1.24 (s, 44H, 22 × CH_2, chains), 1.52 (m, 4H, 2 × CH_2, chains), 1.79 (s, 3H, CH_3, Ac), 2.20 (s, 3H, CH_3, Ac), 2.34 (s, 3H, CH_3, Ac), 2.44 (s, 3H, CH_3), 2.58 (s, 3H, CH_3), 2.80 (t, *J=6,1 Hz,* 2H, CH_2-CN), 3.37-3.46 (m, 2H, CH_2-O), 3.49 (m, 2H, CH_2-O), 3,55 (m, 2H, CH_2-O), 3,55 (m, 1H, CH-O), 4.49-4.03 (m, 7H, 3 × CH_2-O, 1 × CH_2-N), 4,87 (m, CH_2-N), 5.41 (m, 1H, CH-O), 5.49 (m, 1H, CH-O), 5.62 (m, 1H, CH-O), 7.60 (s, 1H), 8.03 (s, 1H), 8.39 (s, 1H, NH).

^{13}C NMR (75 MHz, $CDCl_3$): δ (ppm) = 14.1 (CH_3, chains), 19.4 (CH_3), 20.3 (CH_3, Ac), 21.0 (CH_3, Ac), 21.4 (CH_3, Ac), 22.6-31.9 (CH_2, chains), 45.1 (CH_2-N), 62.2 (CH_2-O), 67.8 (CH_2-O), 69.3 (CH_2-O), 70.2 (CH_2-O), 70.7 (CH_2-O), 71.8 (CH_2-O), 76.9 (CH-O), 77.2 (CH-O), 115.7 (CH_{ar}), 116.6 (CH_{ar}), 128.6 (CH_{ar}), 129.0-137.0 (C_{ar}), 148.2 (C=N), 154.8 (C=N), 159.2 (C=O), 169.8 (C=O, Ac), 170.2 (C=O, Ac), 170.2 (C=O, Ac).

^{31}P NMR (121 MHz, $CDCl_3$): δ (ppm) =1.88, 1.98 (two diasteroisomers).

Mass observed: 1102.6 (M^{+1}).

7.2.2.4 Final deprotection (15)

*5'-O-(1'', 2''-dimyristoyl-phosphoryl)- riboflavin (**14**)*

Compound **9** (227 mg, 0.21 mmol) was dissolved in 5 mL of methanol and 51 mg of sodium methoxide (3.5 eq, 0.75 mmol) were added. After stirring for 24h at RT the reaction was stopped by the addition of 4 g of dry silica. The solvent was evaporated under reduced pressure and the crude product was purified by silica gel column chromatography (DCM/MeOH/TEA 95/5/1 v/v/v) to afford compound **15** as a yellow powder. Yield: 151 mg (0.17 mmol, 80 %).

^{1}H NMR (400 MHz, $CDCl_3$/MeOD 2:1): δ (ppm) = 0.84 (t, *J = 6.7 Hz*, 6H, 2 × CH_3, chains), 1.22 (s, 44H, 22 × CH_2, chains), 1.31 (TEA, t, *J = 7.3 Hz*, 9H, 3 × CH_3) 1.53 (m, 4H, 2 × CH_2, chains), 2.42 (s, 3H, CH_3), 2.53 (s, 3H, CH_3), 3.13 (TEA, q, *J = 7.3 Hz*, 6H, 3 × CH_2) 3.35-3.62 (m, 9H, 4 × CH_2-O,CH-O, chains), 3.81-3.95 (m, 4H, 2 × CH_2-O), 4.12 (m, 1H, CH-O), 4.81 (m, 1H, CH-O), 4.93 (m, 1H, CH_2-N), 5.13 (m, 1H, CH_2-N), 7.96 (m, 2H, CH_{ar}).

^{13}C NMR (100 MHz, $CDCl_3$/MeOD 2:1): δ (ppm) = 8.8 (CH_2, TEA), 14.2 (CH_3, chains), 19.5 (CH_3), 21.5 (CH_3), 23.0-32.7 (CH_2, chains), 46.6 (CH_2-N, TEA), 47.6 (CH_2-N), 48.8 (CH_2-N), 52.8 (CH_2-O), 58.6 (CH_2-O), 65.4 (CH_2-O), 67.4 (CH_2-O), 70.8-73.0 (CH_2-O, CH-O, chains, RF), 77.9-78.3 (CH-O, chains, RF), 117.7 (CH_{ar}), 132.0 (CH_{ar}), 132.8 (C_{ar}), 135.7 (C_{ar}), 138.0 (C_{ar}), 149.1 (C=N), 151.1 (C=N), 157.5 (C=O), 161.0 (C=O).

^{31}P NMR (162 MHz, $CDCl_3$): 1.86.

Mass observed: 923.5 (M^{+1}).

7.2.3 Preparation of PEGylated RF-lipid

*DSPE-PEG-riboflavin (**16**)*

400 μL of stock solution (25 mg/mL in chloroform) of DSPE-PEG2000-succinyl (10 mg, 0.34 μmol) were put in a round-bottom flask and the solvent was evaporated under gentle nitrogen stream. Riboflavin (20 eq, 2.5 mg, 6.8 μmol) was solubilized in anhydrous DMF and added to DSPE-PEG-succinyl. Then catalytic amount of DMAP and stoichiometric amount of DCC and were added and the reaction mixture was left under N_2 and continuous magnetic stirring. After 48h DMF was evaporated by lyophilisation (Dura-Dry™ MP from FTS Systems™), the crude product was dissolved in H_2O/ACN 50:50 mixture and purified by HPLC on reverse

phase analytical C8 column. Solvent A was H_2O/ACN/TFA 50:50:0.1 and solvent B - H_2O/ACN/TFA 50:50:0.1, with the gradient from 0-100% B in 25 min and then 100-0% B in 5 min. The product was detected by the UV-detector at 265 nm. Gathered fractions were lyophilised and analysed with MALDI-TOF-TOF mass spectrometry.

Mass observed: 3288; 2438.

7.3 Nanosystem preparation and characterisation

7.3.1 General protocol for liposome preparation

Liposomes were prepared with the standard film hydration method. The final concentration of lipids was 20 mM. Briefly, lipids were dissolved in chlorofom, mixed in appropriate proportions in the round-bottom flask and the solvent was evaporated under vaccuo. The flask was then put into a lyophilisator (Dura-Dry™ MP from FTS Systems™), overnight to remove any residual solvent traces. The film was hydrated with 1 mL of 25 mM HEPES buffer (pH=7.4) or 10 mM HEPES buffer (pH=7.4) with 9,25% sucrose containing the fluorescent dye to encapsulate (1 mM of rhodamine B, 70 mM of calcein or indocyanine green, all from Sigma Aldrich, Germany) for 1 h at the temperature at least 20°C above the Tm of utilised lipids. Hydrated films were then subjected to 5 freeze-thaw cycles with the help of liquid nitrogen and a water bath (same temperature than for hydration). Obtained MLV were then extruded 11 times trough 800, 400, 200 and finally 100 nm polycarbonate membranes (Avanti Polar Lipids, USA). To separate liposomes from free fluorescent LUVs, they were purified by size-exclusion chromatography with pre-packed PD10 columns (Sephadex G25 resin, GE Healthcare, UK) or a glass column packed with Sephadex G75 resin (Sigma Aldrich, Germany). Liposome solutions were stored at 4°C.

7.3.2 Size and charge measurement

Size, distribution and Zeta Potential measurements of control and specific liposomes were performed in triplicate by dynamic light scattering (DLS) using a Zetasizer Nano ZS (Malvern Instruments Ltd, Malvern, Worcestershire, UK) at 25°C. Calculations of size distribution based on light scattering intensity were performed by the Zetasizer Nano software from the correlation functions using the general purpose algorithm (Malvern dispersion technology software, version 7.03). The liposomal stock dispersions were diluted by a factor 15 with a 25 or 10 mM HEPES buffer before measurements performed by DLS.

7.3.3 TEM

Liposome size and morphology were analyzed with Philips EM 400 T transmission electron microscope (Eindhoven, The Netherlands) operating at an acceleration voltage of 60 kV. Samples in 25 or 10 mM HEPES were adsorbed on formvar-carbon-coated nickel grids (Maxtaform, 200 mesh, Plano, Wetzlar, Germany) for 10 min and then stained with uranyl acetate (0.5 %, Science Services GmbH, Munich, Germany) for 5 s. After staining the grids were washed in distilled water and dried. Morada 11 megapixel camera and iTEM software (both Olympus, Münster, Germany) were used for image record and analysis.

7.3.4 Cryo-EM

The RfdiC14 auto-assemblies were prepared with the same method as described earlier for the liposome preparation (section 7.3.1). Two concentrations of RfdiC14 were utilised – 2 mg/mL and 5 mg/mL.

Cryo-EM analysis was performed as described earlier.[201] For the sample preparation, 5 μL of sample aliquot was deposited onto an EM grid coated with a perforated carbon film (Ted Pella, Redding, CA, USA), the excess liquid was blotted off with a filter paper, and the grid was then quickly plunged into liquid ethane using a Leica EM- CPC cryo-chamber. EM grids were stored in cryo-boxes under liquid nitrogen until use, and then mounted in a Gatan 626 cryo-holder and transferred in a Tecnai F20 micro- scope operated at 200 kV. Images were recorded with an USC1000-SSCCD Gatan camera. The size of the objects was measured with ImageJ software (U. S. National Institutes of Health, Bethesda, Maryland, USA).

7.3.5 Fluorescence spectroscopy and absorbance

Liposome fluorescence intensity and absorbance were measured with Tecan Infinite 200 Pro (Tecan Trading AG, Switzerland) and analysed with Tecan i-control, v. 1.7.1.12 software. Fluorescence calibration curves were prepared for Riboflavin (ex. 450 nm, em. 530 nm), Rhodamine B and LRhPE (ex. 554 nm, em. 583nm), DiR (ex. 750 nm, em. 782 nm) in water. The concentration of the fluorescent agent in each batch of liposomes was determined with the following equations: $y=59087x$ (R^2=0.9939) for Riboflavin, $y=17888x$ (R^2=0.98918) for Rhodamine B, $y=7200x$ (R^2=0.9916) for DiR, where y represents the fluorescence intensity and x - the concentration in μM. ICG was quantified by its absorbance at 800 nm after liposomes dilution with 10% DMSO. The calibration curve was characterised by the following equation $y=21604x$ (R^2=0.9591), where y represents the ICG absorbance at 800 nm and x – its concentration in μM.

7.3.6 Phospholipid dosage

The total phospholipid content in liposomal preparations was determined with Rouser method.[181] For the standard curve 7 dilutions of sodium phosphate (stock 1mM) were prepared containing 0, 5, 10, 20, 40, 80 and 160 nmol of phosphorus. Liposomes (25 μL of stock solution) in duplicate and standards were transferred into clean glass tubes and the solvent was completely evaporated. After cooling down, 300 μL of perchloric acid (70% in H_2O) were added to each tube and the samples were heated to 180°C during 30 min. Then the solutions were cooled down and 1,4 mL of miliQ water were added. Finally, 200 μL of ammonium molybdate (2,5% in H_2O) and 200 μL of freshly prepared 10% solution of ascorbic acid were added to each tube. The samples were placed in the boiling water bath for 5 min and then cooled down on ice. The absorbance from each solution was read at 797 nm and the P content in mg/mL was calculated according to the calibration curve. The calibration curve was made for each new measurement.

7.3.7 Calcein leakage assay

To perform calcein leakage assay, calcein was encapsulated in the aqueous phase of liposomes at the self-quenching concentration 70 mM. After purification at chosen time

points during storage, liposome suspension was diluted 100 times and 100 μL of diluted solution were put to the black flat bottom 96 well plates (Greiner-Bio-One GmbH, Germany). Two solutions with the same dilution were prepared – sample and control. To the control solution of liposomes 0,1% of Triton x-100 was added. Then the fluorescence signal of calcein (ex. 490 nm, em. 530 nm) was read in triplicate from both solutions with Tecan Infinite 200 Pro (Tecan Trading AG, Switzerland) and analysed with Tecan i-control, v. 1.7.1.12 software. The fluorescence of the control solution was considered as 100% because all liposomes were destroyed with Triton 100x. The % of calcein leakage was calculated with the following equation: $\%\ calcein\ leakage = F_{lip}/F_{tot}*100\%$, where F_{lip} is the fluorescence of the sample and F_{tot} is the fluorescence of the control.

7.3.8 In vitro stability study

Liposomal suspensions or free ICG were diluted with an appropriate buffer 1/5 and then mixed with 50% v/v of FBS (Gibco®/Life Technologies, USA). The solutions were kept at 37°C under continuous agitation (300 rpm) for several days. The ICG absorbance spectra was analysed before incubation and 15 min, 4h, 24h and 48h after incubation started. The size and zeta potential of liposomes were analysed at 24h time point after purification with pre-packed PD10 columns (Sephadex G25 resin, GE Healthcare, UK) to exclude non-bound serum proteins.

7.3.9 solid state NMR

7.3.9.1 sample preparations

Three sets of samples were prepared: DMPC:DMPG (90:10); DMPC:DMPG:RfdiC14 (90:10:10) and RfdiC14:DMPC (100:2,5) with the total lipid concentration of 20 mM. For all samples DMPC-d54 (Avanti Polar Lipids, USA) with fully deuterated acyl chains was utilised. Lipids were dissolved in chloroform, mixed in appropriate proportions and the solvent was evaporated under gentle nitrogen stream. The obtained lipid films were taken up in 500 μL of MiliQ water, hydrated at 45°C for 30 min and then subjected to 5 freeze-thaw cycles. After the last cycle samples were frozen in liquid nitrogen and lyophilised (Dura-Dry™ MP from FTS Systems™). The obtained powder was taken up in 100 μL of light water (containing 2-3 ppm of deuterium, CortectNet, France) for solid NMR studies. Then again 3 freeze-thaw cycles occurred (10 min at 45°C/stirring/freezing in liquid nitrogen) before the transfer to 4 mm zircon oxide rotors (CortectNet, France).

7.3.9.2 NMR

The NMR spectrometer RMN 800 MHz SB Bruker (Wissembourg, France) equipped with the probe CP-MAS SB 1H/BB able to rotate at magic angle was used for the solid NMR studies. The echo solid sequence (90°-τ-90°-τ-Acq) was employed for the deuterium observations. The pulses at 90° were 2,88 μs, the echo delays (τ) were 40 μs with the registering from 4k points. The repeating time was 2s with the acquisitions number from 1 to 12k according to the sample. The temperature varied from 20 to 50 ± 5°C. The obtained signals were filtered with a decreasing exponential function of the constant between 100 and 500 Hz and then subjected to Fourier transformation from the top of echo spin. Finally, the

data were analysed with the help of Topspin 3.2 software (Bruker, USA).

7.3.10 CPP calculations

To calculate the CPP value of RfdiC14, hydrocarbon chain volume *v* and effective length of the hydrocarbon chain *lc* were computed with the *Calculate Molecular Properties* module of Discovery Studio 3.1 suite (Accelrys software Inc., San Diego, USA).[202] In the first method (M1), the effective area of head group *as* was calculated with the same module applied on a restricted part of the RfdiC14. The 3D SASA (solvent accessible surface area) property of RF head group was used to approximate the effective area *as*. In the case of the second method (M2), a first short 2 ns equilibration (at 300K and 1 bar) of 2 RfdiC14 was performed to adjust the π - π stacking interactions (distance). The mean distance between each atom of two π-stacked isoalloxazine rings was measured to obtain the width (*w*). All molecular dynamic simulations were performed with GROMACS 5.0 software[203] and the gromos9653a6 forcefield.[204]

7.4 Cellular uptake experiments

7.4.1 Cell culture

A431 (human epidermal cervix carcinoma) and PC3 (human prostate carcinoma), CT26 (murine colon carcinoma) and MLS (human epithelial ovarian carcinoma) cell lines as well as HUVEC (human umbilical vein endothelial cells) *primary culture* (all ATCC, USA) were maintained at 37°C, under humidified air with 5 % CO_2, in RMPI, McCoy`s medium or Endopan 3 L-Glutamine medium (HUVECs) supplemented with 10 % (v/v) foetal bovine serum (except HUVECs) and 100 U/mL of penicillin G and 100 U/mL of streptomycin (cell culture media and additives were from Gibco®/Life Technologies, Carlsbad, California). Cells were cultivated in standard 75 cm^2 flasks and splitted each 3-5 days (up to 10 passages maximum).

7.4.2 Fluorescent microscopy

Cells in maintenance medium were trypsinised and seeded into 24-well culture plates at optimum confluence. Incubations were conducted at 50 nM (Rhodamine B) or with 20 nM (DiR) of control or targeted liposomes in serum-containing maintenance medium for 30 minutes. For the competitive binding experiment cells were pre-incubated with 20 fold excess of targeted liposomes without any dyes for 15 min and then, without washing, targeted liposomes were added and incubated for 30 min. For the 4°C uptake studies cells were pre-incubated in the refrigerator for 30 min. After incubation with liposomes, cells were washed three times in 1× PBS to remove free liposomes and fixed with 4 % PFA. The cell nuclei were stained with DAPI standard protocol (Life Technologies). Cellular uptake was monitored by fluorescence microscopy with an Axio Imager M2 microscope and a high-resolution AxioCam MRm Rev.3 camera under 20× or 40× magnifications. Various channels were studied – DAPI (ex. 365 nm, em. 455 nm) to visualise nuclei, GFP (ex. 450 nm, em. 530 nm) to visalise RfdiC14, dsRed (ex. 554 nm, em. 605 nm) observe liposome uptake trough Rhodamine B or Cy7 (ex. 750 nm, em. 782 nm) for DiR fluorescence. For each individual

well from 10 to 20 images were collected and the fluorescence intensity was then quantified with ImageJ software (U. S. National Institutes of Health, Bethesda, Maryland, USA). All uptake experiments were conducted in triplicate.

7.4.3 Flow cytometry

The incubation conditions were the same as for the fluorescence microscopy experiments. Briefly, cells were trypsinised, counted, and then incubated in Eppendorf tubes (0.4 million cells/mL) with 50 nM of liposomes (Rhodamine B) for 30 min at 37°C. Then, tubes were centrifuged and the cell pellet was washed 3 times with PBS to remove free liposomes. For the competition experiment cells were pre-incubated with a 20-fold excess of targeted liposomes without Rhodamine B for 15 min. Finally, cells were re-suspended in PBS buffer in flow cytometry tubes and the measurements were performed using a FACS Canto II™ (Becton Dickinson) flow cytometer. Fluorescence was monitored with two channels – green channel FITC (ex. 495 nm, em. 519 nm) and orange channel – PE (ex. 561 nm, em. 578 nm). 50,000 cells were counted for each condition tested. The data were analysed and quantified using the FACS Diva Software (Becton Dickinson).

7.4.4 Cytotoxicity test

The cytotoxicity of control and specific liposomes was accessed using a standard MTT (Life Technologies) test following the manufacturer's description. Briefly, cells in maintenance medium were seeded in 96 well plates and incubated for 72 h with liposomes in 1x, 3x and 5x concentrations (50, 150 and 250 nM, respectively). After incubation, cells were washed with maintenance medium without serum and 50 μL of MTT (5 mg/mL) solution per well were added. Cells were incubated 2h a 37°C and the MTT solution was removed. Formed by live cells blue formazan crystals were solubilized with 200 μL DMSO per well. The blue formazan absorbance was read at 570 nm with Tecan Infinite 200 Pro. The cell viability was calculated using the following formula: Viability % = (A_{570nm} for the treated cells/A_{570nm} for the control cells) × 100 %, where A_{570nm} is the absorbance value. Each assay was repeated in triplicate.

7.4.5 Statistics

All data are presented as the mean ± standard deviation. Two-tail Student test and variance analysis were used to determine significance among groups. A value of $P<0.05$ was considered to show significant differences.

7.5 In vivo studies

All *in vivo* experiments were approved by the local and national regulatory authorities and by ethical animal welfare committee under the number AZ - 87-51.04.2010.A278. Eight-week old CD1-nu/nu mice (Charles River Laboratories, Wilmington, USA) weighing ~25 g were fed with chlorophyll-free food pellets and water *ad libitum*. Mice were housed in ventilated cages and placed in controlled room with adapted conditions. A431 human epidermal cervix carcinoma cells and PC3 human prostate carcinoma cells were cultured as described in section 4.1. Mice were injected with A431 ($5x10^6$ cells / 100 μL) and PC3

tumour cells ($3x10^6$ cells / 100 μL) by subcutaneous inoculation into the dorsolateral right flank. A tumour size of ~5-8 mm was obtained within 10-14 days for A431 cells and ~3-4 mm within 30–40 days for PC3. The animals were conditionally inhalation-anaesthetized during all experimental operations.

7.5.1 Photoacoustic imaging

PAI was performed on the Vevo® LAZR system equipped with a LZ250 transducer (FUJIFILM VisualSonics, Amsterdam, The Netherlands) as described previously.[194] The Vevo® LAZR system features peak energies of 45 +/- 5 mJ, with pulse duration of 4-6 ns at adjustable wavelengths between 680 – 970 nm (2 nm step size). In combination with photoacoustic (PA) signal, high-resolution ultrasound (US) images were acquired at 21 MHz. Both these conditions were maintained for the phantom and *in vivo* experiments.

7.5.1.1 Phantom studies

To investigate the depth detection limit of ICG liposomes, 50 μL of liposomes stock solution (100 μM) were injected intramuscularly into chicken breasts at different depths. For all experiments the imaging parameters were kept constant. For the measurements in blood vessel mimicking plastic tubing phantoms, a 100 μM solution of ICG liposomes was diluted 5 times by a factor of 10 to obtain final ICG content of 2000, 200, 20, 2 and 0,2 pmol. The dilutions were injected into PE plastic tubes, aligned parallel in a custom build rack and immersed in water (as background). As a control, one of the tubes was filled with HEPES buffer solution. The immersed tubes were then subjected to simultaneous PA and US imaging providing PA excitation spectra at various concentrations. At the maximum wavelength merged US/PA images of the plastic tubes were recorded.

7.5.1.2 Animal studies

Control and targeted ICG liposomes (100 μL with 6 nmol ICG in each) were injected into the tail vein of 15 CD-1 nude female mice bearing A431 tumours of size of ~5-8 mm in diameter. Animals were divided in 3 groups – control, targeted and competition with n=5 in each group. For the competitive binding studies, 30 μL of competition liposomes (10x excess) were injected 15 min prior to targeted liposomes injection. The anaesthetised (2.5 % mixture of isoflurane / O_2) animal was placed in the Vevo® Imaging Station system and the tumour was first located with a high-resolution US. Then the tumours were scanned in 3D with the help of an automated motor system. The PA signal was acquired at 800 nm excitation wavelengths together with US signal. For several animals (n=2 in each group) the PA signal was also acquired at multiple excitation wavelengths in the NanoStepper mode - 700, 750, 800, 850 and 900 nm in 2D tumour slices, and 750, 800, 850 nm in the whole 3D tumour volume. All tumours were scanned prior to liposome injection and at 0.25, 4, 24, and 48 h after injection. After the last scan animals were sacrificed and the organs collected. The tumour segmentation, PA signal intensity calculations and spectral unmixing were performed with Vevo® LAZR software.

7.5.2 µCT/FMT imaging

7.5.2.1 Phantom studies

Phantom studies for the probe calibration were performed in a block shaped FMT phantom[165] (33x40x15 mm^3, absorption 0.1 cm^{-1}, scattering 8 cm^{-1}), containing a cylindrical inclusion (diameter 3 mm, length 1 cm). The inclusion was filled with varying concentrations of fluorescencent DiR liposomes (ex 750 nm, em 782 nm). 5% CT contrast agent (Imeron 400, Bracco Imaging, Konstanz, Germany) was added to liposomes solutions to facilitate the segmentation of the inclusion in the µCT images. 1% of Lipovenoes (20% stock) were also added to mimic tissue absorption. The phantom was subjected to the μCT imaging (Tomoscope DUO; μCT Imaging, Erlangen, Germany) with subsequent 3D FMT scans (FMT2500; PerkinElmer). Based on μCT data, the cylindrical inclusion in phantom was segmented using Imalytics Research Workstation (Philips Technologie GmbH Innovative Technologies, Aachen, Germany) and the fluorescence signal from FMT was quantified in the segmented volume.

7.5.2.2 Animal studies

Control and targeted DiR liposomes (100 μL with 2,5 nmol DiR in each) were injected into the tail vein of 9 CD-1 nude male mice bearing PC3 tumours of size of ~3-4 mm in diameter. Animals were divided in 3 groups – control, targeted and competition with n=3 in each group. For the competitive binding studies, 30 μL of competition liposomes (10x excess) were injected into the tail vein 15 min prior to targeted liposomes injection. The anaesthetised (2.5 % mixture of isoflurane / O_2) animals were placed on a multi-modal imaging mice holder (CT-imaging, Erlangen, Germany), which is manually adjusted to keep the mice with the tumours projecting at the right side. High-resolution dual-energy μCT and subsequent image reconstruction were performed as described previously.[89,165] After the μCT scan, without changing the position and orientation of mouse, it was transferred to the FMT. Process parameters such as excitation wavelength and calibration agent were preset by the FMT based on earlier phantom experiments. The FMT machine detected and set automatically the laser scanning depth of imaging holder. Whole body images of the mice were first captured using FRI. The 3D FMT scans were subsequently performed in the region of interest selected from 2D FRI images. All animals were subjected to μCT and subsequent 3D FMT imaging at 0.25, 4, 24, and 48 h. After the final scanning, Rhodamine-lectin (Axxora, LLC, 1mg/ml; 70μL) was injected into the tail vein, and mice were sacrificed for *ex vivo* biodistribution validation. The μCT and FMT image data sets were fused as described previously.[165] Based on μCT data, tumours and healthy organs were interactively segmented using Imalytics Research Workstation. Fluorescence signals from FMT were overlaid with corresponding organ-segmented μCT images, and the concentration of control and targeted DiR liposomes in organs was quantified. The mean DiR content for each segmented organ was calculated on the basis of phantom experiments and was normalised to its respective average volume.

7.5.3 Tumour cryo-sections and staining

Histological stainings were performed to visualise the tumour micromorphology and compare the tumour accumulation of different liposomal formulations. Thus, snap-frozen 8

μm-thick sections were prepared and stained using DAPI (Sigma Aldrich, Germany) for nuclei. Blood vessels were already stained with Rhodamine-lectin. Sections were mounted on microscopy slides and fixed using Mowiol (Sigma Aldrich, Germany). Fluorescence microscopy imaging was performed using an Axio Imager M2 microscope and a high-resolution AxioCam MRm Rev.3 camera, at different magnifications. The images were acquired in various positions of the tumour and within various depths. The data were further post-processed using Image J software (U. S. National Institutes of Health, Bethesda, Maryland, USA) and the co-localisation was analysed with Fiji Colocalization Test tool (U. S. National Institutes of Health, Bethesda, Maryland, USA).

7.5.4 Statistics

All data are presented as the mean ± standard deviation. Two-tail Student test was used to determine significance among groups. A value of $P<0.05$ was considered to show significant differences.

8 Summary in French

La Riboflavine (RF) est une vitamine essentielle pour la croissance et le développent cellulaire. Elle possède des propriétés physico-chimiques particulières comme la fluorescence, le potentiel redox et la photosensibilisation.[98]

Dans l'organisme, la RF est transformée en FMN et FAD par action de l'ATP. Ces dérivés sont des co-facteurs qui associés aux flavoenzymes sont impliqués via la chaîne respiratoire dans le métabolisme des sucres, des acides aminés, des lipides ainsi que dans celui d'autres vitamines hydrosolubles. La RF est ainsi une vitamine essentielle mais elle n'est pas synthétisée *in situ*. Les mammifères ont un système de transporteurs spécifiques à la RF et ses dérivés. Ce système comprend plasma protéine porteuse de la RF (RCP ou RF carrier protein)[205] et une famille de protéines de la membranaires (SLC52).[120] Ce dernier se compose de trois protéines transmembranaires, qui ont été récemment découvertes et de leur structure cristalline n'est pas encore résolu. La RCP est surexprimée pendent la grossesse pour assurer le développent foetal, mais aussi dans le cas de certains cancers comme cancer de la prostate, cancer du sein et le carcinome hepatocellulaire.[109,110,114,115] Ceci suggère l'utilisation de la RF comme un agent de ciblage pour ces cancers.

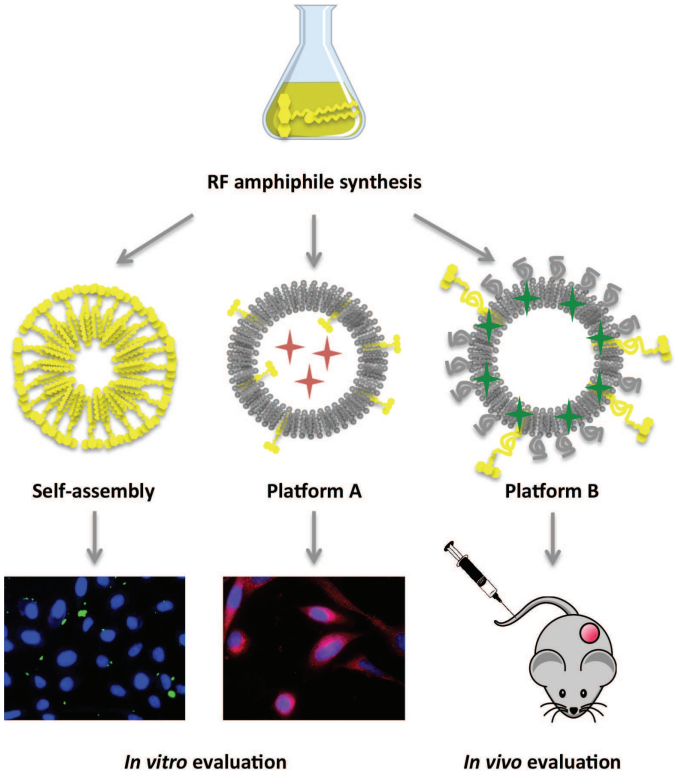

Figure 8.1 Stratégie générale de l'étude

Grace à ces propriétés intéressantes, le RF a été utilisée dans la conseption des divers nano-systemes tells que les hydrogels,[101,102] les deniméres,[99] les helices polymeriques,[100] les nanotubes de carbone[106] et les nanoparticules d'oxides de fer.[103–105] Quelques équipes ont tenté d'utiliser la RF comme un ligand pour la deliverance ciblée de pricipes actifs[116–119] et l'imagerie.[103,104] Ces systèmes on été basés sur la liaison covalente avec la RF[116–119] ou sur les interactions électrostatiques.[103,104] Toutefois, sauf émulsions orales de la RF laurate, peu est

connu sur les dérivés amphiphiles de la RF (RFA) et de leur auto-organisation.[111] En raison de la simplicité et la grande polyvalence des systèmes auto-assemblés, la préparation des RFA et l'étude de leurs assemblages supramoléculaires sont d'un grand intérêt.

Dans ce projet nous avons eu pour le but dans un premier temps de synthétiser les dérives amphiphiles de la RF et étudier les auto-assemblages. Dans un second temps, d'insérer ces dérivés dans les systèmes du délivrance modèle et étudier le potentiel de la RFA en tant que l'agent du ciblage actif (Figure 8.1).

Pour la préparation d'un amphiphile il est important de considérer certain équilibre hydrophile / hydrophobe dans la molécule. En raison de sa structure chimique, RF a déjà des propriétés amphiphiles inhérents – le noyau isoalloxazine responsable de l'hydrophobie et de la chaîne ribitol responsable hydrophile. Cependant, la molécule ne soit pas connue de former des auto -assemblages en elle même. Par conséquent, nous avons choisi de greffer les divers chaines lipidiques pour renforcer son caractère hydrophobe.

La RF, du fait de sa structure, possède différentes fonctions chimiques qui peuvent être modifiées et sur lesquelles les chaînes hydrophobes seront introduites. Les modifications vont donc pouvoir être localisées sur l'amine de la fonction uréido du noyau isoalloxazine (N3) ou sur l'hydroxyle primaire de la partie ribitol (5'O). Les deux stratégies de synthèse sont présentées à la Figure 8.2.

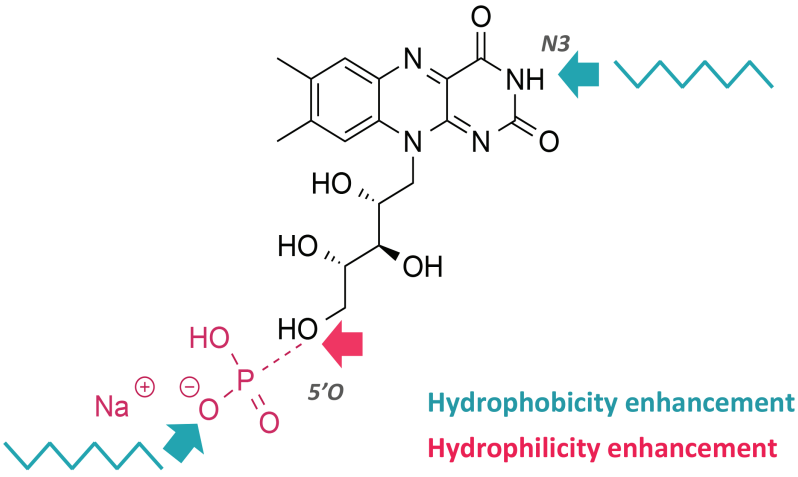

Figure 8.2 Strategies pour la preparation des RFAs.

Bien que, la modification chimique de RF pourrait conduire à la perte de l'affinité vis-à-vis de ses transporteurs, elle sera toujours reconnue par la RCP. En revanche, Witte A. *et al*.[99] ont montré que les conjugués N3 ont une plus grande affinité de liaison à la RCP par rapport à la série 5'O. Bien que, la position 5'O semble d'être moins avantageuse, l'internalisation cellulaire efficace a été signalé pour ses conjugués aussi.[117,119]

Dans cette étude, nous avons synthétisés et caractérisés six nouveaux dérivés amphiphiles de la RF en utilisant les deux positions différentes de modification - N3 et 5'O. A cet effet, trois types de chimie ont été employés – la réaction de Huisgen, le couplage phosphoramidite et l'estérification. Les dérivés préparés sont présentés sur la Figure 8.3.

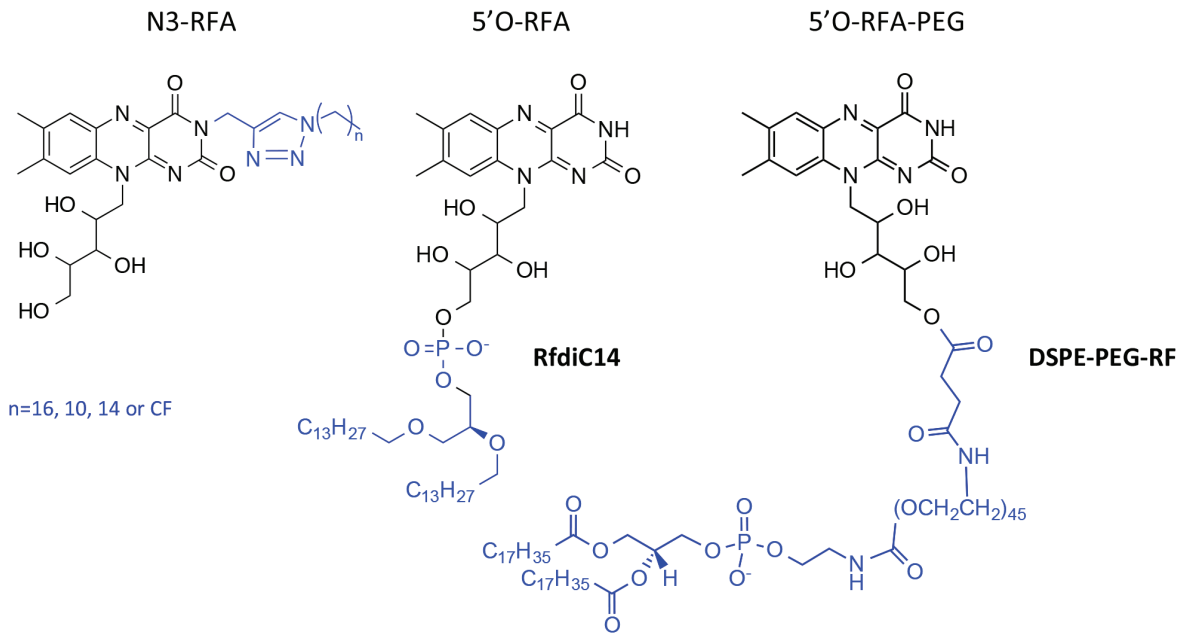

Figure 8.3 Les structures chimiques des RFAs synthesizées

La première stratégie a abouti à quatre dérivés de la RF avec les différentes chaînes alkyle attachés position de N3 par un lien triazole. Malheureusement, tous les N3-RFA ont eu une très faible solubilité dans l'eau et les solvants organiques. La deuxième stratégie a été plus productive. Ici on a utilisé la liaison phosphodiester entre un lipide de choix et l'extrémité 5'O de la chaîne ribitol. Le derivé preparé (RfdiC14) a été très similaire à des phospholipides classiques par sa structure chimique et sa solubilité. Par conséquent, il était un excellent candidat pour la formation des auto-assemblages. Nous avons également préparé un produit dérivé similaire, qui a eu une spaceur PEG entre la RF et la partie lipidique. Cette molécule, désignée pour les études *in vivo*, a été nommé DSPE-PEG-RF.

La formation des auto-assemblages par la RfdiC14 a été étudiée au moyen de différentes techniques physico-chimiques, y compris les calculs du CPP (critical packing parameter), l'analyse DLS, les expériences de la RMN du solide et l'imagerie cryo-EM. Chaque technique a contribué à la compréhension globale de l'architecture et du comportement des auto-assemblages de la RfdiC14. En résumé, les résultats indiquent une formation des objets micrométriques en trois dimensions constitués de plusieurs structures lamellaires. Ces derniers représentent une morphologie de bicouche très dense et bien organisée, avec un motif de répétition de 5 ± 0,7 nm. Les études de la NMR du solide révélé un désordre plus important dans les bicouches de la RfdiC14 par rapport aux phospholipides membranaires classiques et une partie hydrophobe plus mince (20 Å). Ceci peut être une conséquence de l'espacement latéral de chaînes lipidiques induite par des interactions supplémentaires entre les têtes encombrantes de la RF. Parmi les interactions potentielles on suppose que le π-stacking entre les anneaux isoalloxazines et les liaisons hydrogène dans la partie de ribitol. Le modèle possible d'organisation en bicouche de la RfdiC14 et des images cryo-EM sont présentés sur la Figure 8.4.

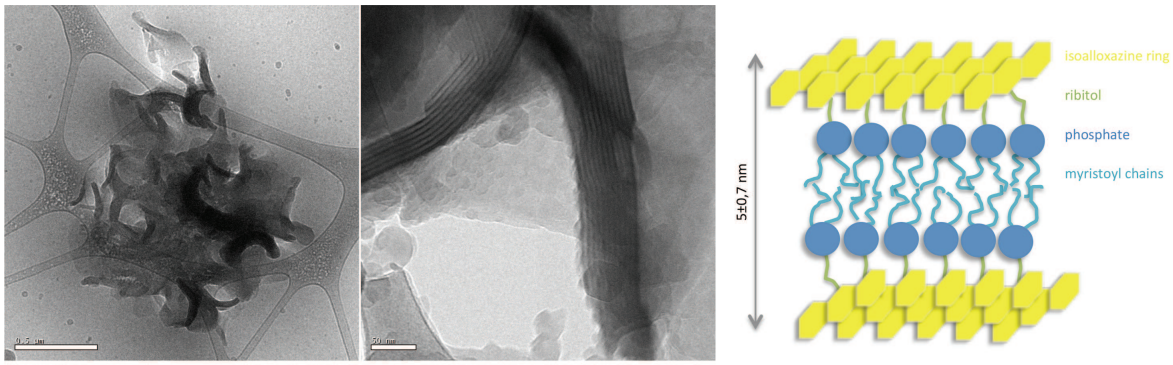

Figure 8.4 Photographies cryo-EM des auto-assemblages de la RfdiC14 à différents grossissements (gauche, barres d'échelle 0,5 um, 50 nm) et un dessin suggérant organisation bicouche RfdiC14 (droite)

Comme les transporteurs de la RF ont été montrés surexprimés dans certains types de cancers et dans les cellules métaboliquement actives, la RF pourrait servir en tant que ligand de ciblage tumoral. Par conséquent, quelques RFAs ont été insérés dans des liposomes modèles pour évaluer leur potentiel de ciblage *in vitro* et *in vivo*. Les plateformes à délivrance ciblée fonctionnalisés avec les divers RFAs sont résumées dans le Figure 8.5.

Plateforme A a été désigné pour les premières études *in vitro*. La RfdiC14 a été inséré dans des liposomes constitués du DMPC:DMPG (90 :10 molaire), qui ont été marqués avec les dérivés de la rhodamine. Nous avons pu montrer, que l'insertion de la RfdiC14 en faibles quantités (1% molaire) n'a aucune influence sur les propriétés physico-chimiques des liposomes. Liposomes ciblés marqués avec un dérivé lipidique de la rhodamine (LRhPE) n'ont pas montré une spécificité de l'internalisation cellulaire. En revanche, les liposomes ciblés, encapsulant la rhodamine B, ont révélé une internalisation plus importante et spécifique à la RF dans les lignées cellulaires A431, PC3 et les cellules HUVEC par rapport au control. Par conséquent, la RfdiC14 pourrait être éventuellement inséré dans les diverses formulations lipidiques comme les nanoparticules lipidiques, les cubosomes, les hexosomes, les nanoemultions *etc*. pour les apporter une spécificité tumorale. La RfdiC14 pourrait également servir comme un outil pharmacologique pour étudier les mécanismes de transport de RF.

Plateforme B a été préparé pour l'évaluation *in vivo*. Dans ce cas, on a préparé les liposomes à la circulation prolongée (PEGylés) avec la composition lipidique optimisée. DSPE-PEG-RF a été inséré dans les liposomes pour servir de l'agent de ciblage actif. Les liposomes ont été marqués avec les fluorophores emmétant dans le proche infrarouge - soit indocyanine vert ou ICG (pour plateforme B1), soit dérivé lipidique de la cyanine ou DiR (plateforme B2) et testées dans deux modèles tumoraux. L'accumulation de la plateforme B1 dans le tissu tumoral a été évaluée par l'imagerie photo-acoustique dans le modèle de xénogreffe A431. Nous avons observé une légère amélioration dans l'accumulation dans la tumeur des liposomes ciblés par rapport aux liposomes control. Le signal était non homogène au sein du tissu tumoral et le plus souvent situé à proximité de vaisseaux sanguins. Les études de biodistribution de la plateforme B2 ont été effectuées par le système d'imagerie combinée (µCT/FMT) dans le modèle tumoral PC3. La biodistribution de liposomes ciblés et contrôles était similaire et il n'y avait pas de différence significative dans leur accumulation au sein des

tumeurs PC3. Cela peut être une conséquence de la croissance ralenti des xénogreffes PC3 et leur vascularisation insuffisante. Néanmoins, l'analyse histologique a révélé l'accumulation preferentielle des liposomes ciblés à la RF au niveau des neovaisseaux sanguins. En résumé, ces études initiales pour l'évaluation de la plateforme de délivrance fonctionnalisées avec la RFA pourraient donner des indications utiles pour les futures recherches.

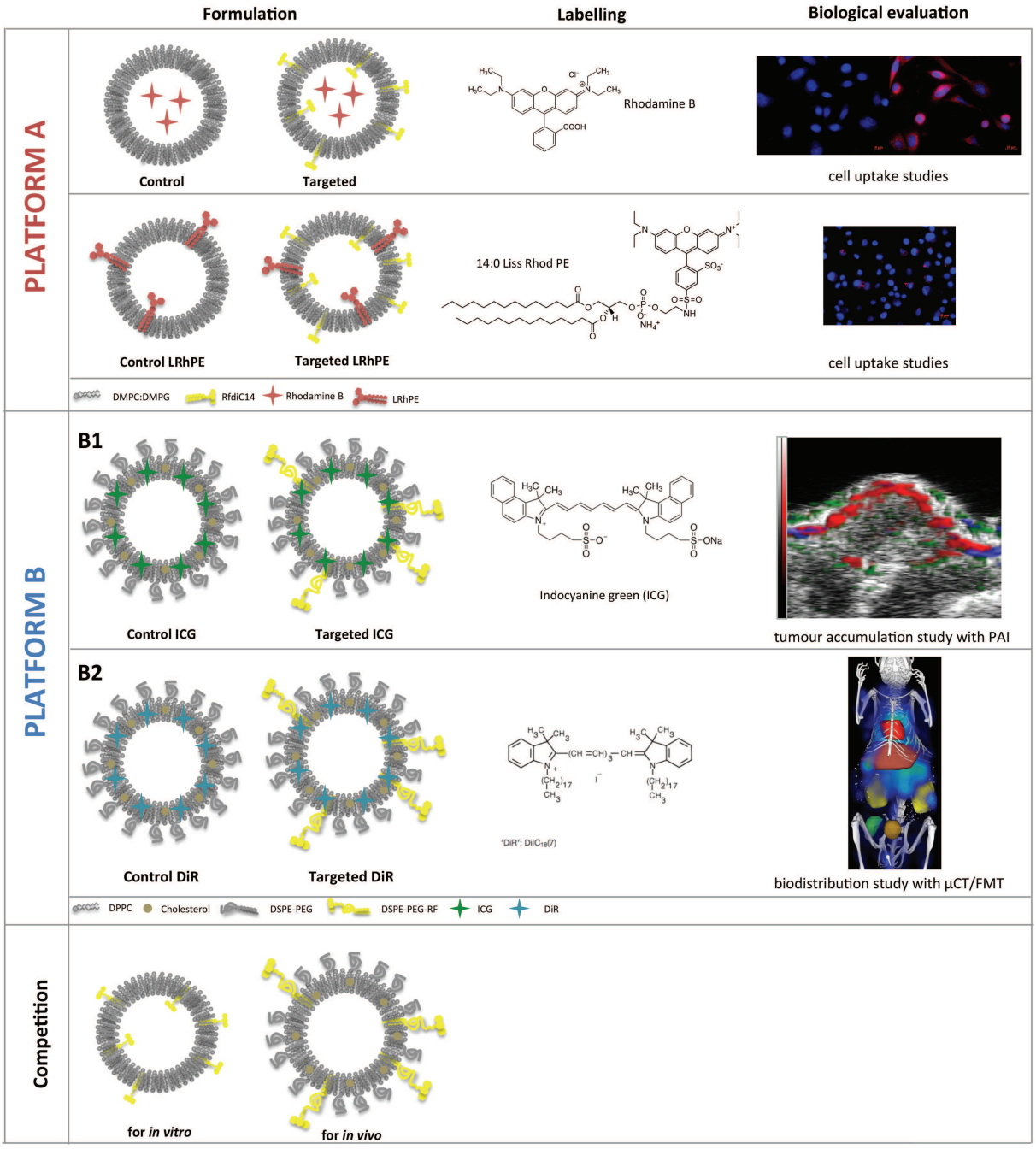

Figure 8.5 Plateformes fonctionnalisées à la RF

9 References

1. Yu, G., Jie, K. & Huang, F. Supramolecular Amphiphiles Based on Host–Guest Molecular Recognition Motifs. *Chem. Rev.* (2015). doi:10.1021/cr5005315
2. Santos, S. dos, Medronho, B., Santos, T. dos & Antunes, F. E. in *Drug Delivery Systems: Advanced Technologies Potentially Applicable in Personalised Treatment* (ed. Coelho, J.) 35–85 (2013).
3. Lipids in Water. *biowiki.ucdavis.edu* at <http://biowiki.ucdavis.edu/Biochemistry/Lipids/Lipids_in_Water>
4. Jie, K., Zhou, Y., Yao, Y. & Huang, F. Macrocyclic amphiphiles. *Chem. Soc. Rev.* **44,** 3568–3587 (2015).
5. Kral, T. *et al.* Lipopolythiourea/DNA interaction: A biophysical study. *Biophys. Chem.* **148,** 68–73 (2010).
6. Allain, V., Bourgaux, C. & Couvreur, P. Self-assembled nucleolipids: from supramolecular structure to soft nucleic acid and drug delivery devices. *Nucleic Acids Res.* **40,** 1891–1903 (2012).
7. Tonelli, G. *et al.* Amino acid-nucleotide-lipids: effect of amino acid on the self-assembly properties. *Langmuir ACS J. Surf. Colloids* **29,** 5547–5555 (2013).
8. Raouane, M. *et al.* Synthesis, Characterization, and in Vivo Delivery of siRNA-Squalene Nanoparticles Targeting Fusion Oncogene in Papillary Thyroid Carcinoma. *J. Med. Chem.* **54,** 4067–4076 (2011).
9. Latxague, L., Patwa, A., Amigues, E. & Barthélémy, P. Glycosyl-Nucleolipids as New Bioinspired Amphiphiles. *Molecules* **18,** 12241–12263 (2013).
10. Richard, C. *et al.* Amphiphilic perfluoroalkyl carbohydrates as new tools for liver imaging. *Int. J. Pharm.* **379,** 301–308 (2009).
11. Galantini, L. *et al.* Bile salts and derivatives: Rigid unconventional amphiphiles as dispersants, carriers and superstructure building blocks. *Curr. Opin. Colloid Interface Sci.* (2015, in press), doi:10.1016/j.cocis.2015.08.004
12. Chae, P. S., Laible, P. D. & Gellman, S. H. Tripod Amphiphiles for Membrane Protein Manipulation. *Mol. Biosyst.* **6,** 89–94 (2010).
13. Moroi, Y. *Micelles: Theoretical and Applied Aspects* (ed. Springer US), ISBN - 13: 9781489907028 (2013).
14. Diamant, H. & Andelman, D. Onset of Self-Assembly in Polymer-Surfactant Systems. *Europhys. Lett. EPL* **48,** 170–176 (1999).
15. Yu, D., Huang, F. & Xu, H. Determination of critical concentrations by synchronous fluorescence spectrometry. *Anal. Methods* **4,** 47–49 (2012).
16. Krister Holmberg, Bo Jönsson, Bengt Kronberg, *et al*. Surfactants and Polymers in Aqueous Solution, 2nd Edition, ISBN: 978-0-471-49883-4 (2002).
17. Walde P. Preparation of Vesicles (Liposomes). *Encyclopedia of Nanoscience and Nanotechnology* **9***,* 43-79 (2012).
18. Garavito, R. M. & Ferguson-Miller, S. Detergents as tools in membrane biochemistry. *J. Biol. Chem.* **276,** 32403–32406 (2001).
19. Letchford, K. & Burt, H. A review of the formation and classification of amphiphilic block copolymer nanoparticulate structures: micelles, nanospheres, nanocapsules and polymersomes. *Eur. J. Pharm. Biopharm.* **65,** 259–269 (2007).
20. KRAFT, J. C., FREELING, J. P., WANG, Z. & HO, R. J. Y. Emerging Research and Clinical Development Trends of Liposome and Lipid Nanoparticle Drug Delivery Systems. *J. Pharm. Sci.* **103,** 29–52 (2014).

21. Dumitriu, S. *Polymeric Biomaterials, Revised and Expanded*, ISBN-13: 978-0824705695, (2001).
22. Aulton, M. E. & Taylor, K. M. G. *Aulton's Pharmaceutics: The Design and Manufacture of Medicines*, ISBN: 978-0-7020-4290-4 (2013).
23. Müller-Goymann, C. C. Physicochemical characterization of colloidal drug delivery systems such as reverse micelles, vesicles, liquid crystals and nanoparticles for topical administration. *Eur. J. Pharm. Biopharm.* **58,** 343–356 (2004).
24. Chen, Y., Ma, P. & Gui, S. Cubic and Hexagonal Liquid Crystals as Drug Delivery Systems. *BioMed Res. Int.* **2014,** e815981 (2014).
25. Wilson, C. G. & Crowley, P. J. *Controlled Release in Oral Drug Delivery*, ISBN 978-1-4614-1004-1 (2011).
26. Negrini, R. & Mezzenga, R. pH-responsive lyotropic liquid crystals for controlled drug delivery. *Langmuir ACS J. Surf. Colloids* **27,** 5296–5303 (2011).
27. Lopes, L. B., Speretta, F. F. F. & Bentley, M. V. L. B. Enhancement of skin penetration of vitamin K using monoolein-based liquid crystalline systems. *Eur. J. Pharm. Sci. Off. J. Eur. Fed. Pharm. Sci.* **32,** 209–215 (2007).
28. Zeng, N. *et al.* Lipid-based liquid crystalline nanoparticles as oral drug delivery vehicles for poorly water-soluble drugs: cellular interaction and in vivo absorption. *Int. J. Nanomedicine* **7,** 3703–3718 (2012).
29. Akbarzadeh, A. *et al.* Liposome: classification, preparation, and applications. *Nanoscale Res. Lett.* **8,** 102 (2013).
30. Laouini, A. *et al.* Preparation, Characterization and Applications of Liposomes: State of the Art. *J. Colloid Sci. Biotechnol.* **1,** 147–168 (2012).
31. Mishra, G. P., Bagui, M., Tamboli, V. & Mitra, A. K. Recent Applications of Liposomes in Ophthalmic Drug Delivery. *J. Drug Deliv.* **2011,** e863734 (2011).
32. Chang, H.-I. & Yeh, M.-K. Clinical development of liposome-based drugs: formulation, characterization, and therapeutic efficacy. *Int. J. Nanomedicine* **7,** 49–60 (2012).
33. Immordino, M. L., Dosio, F. & Cattel, L. Stealth liposomes: review of the basic science, rationale, and clinical applications, existing and potential. *Int. J. Nanomedicine* **1,** 297–315 (2006).
34. Torchilin, V. P. Recent advances with liposomes as pharmaceutical carriers. *Nat. Rev. Drug Discov.* **4,** 145–160 (2005).
35. Deshpande, P. P., Biswas, S. & Torchilin, V. P. Current trends in the use of liposomes for tumor targeting. *Nanomed.* **8,** (2013).
36. Çağdaş, M., Sezer, A. D. & Bucak, S. in *Application of Nanotechnology in Drug Delivery* (ed. Sezer, A. D.) (2014).
37. Liu, H. *et al.* Virosome, a hybrid vehicle for efficient and safe drug delivery and its emerging application in cancer treatment. *Acta Pharm. Zagreb Croat.* **65,** 105–116 (2015).
38. Ito, A., Shinkai, M., Honda, H. & Kobayashi, T. Medical application of functionalized magnetic nanoparticles. *J. Biosci. Bioeng.* **100,** 1–11 (2005).
39. Hodenius, M. *et al.* Fluorescent magnetoliposomes as a platform technology for functional and molecular MR and optical imaging. *Contrast Media Mol. Imaging* **7,** 59–67 (2012).
40. Soenen, S. J. H. *et al.* The labeling of cationic iron oxide nanoparticle-resistant hepatocellular carcinoma cells using targeted magnetoliposomes. *Biomaterials* **32,** 1748–1758 (2011).
41. Ketkar-Atre, A. *et al.* In vivo hepatocyte MR imaging using lactose functionalized

magnetoliposomes. *Biomaterials* **35,** 1015–1024 (2014).
42. Guo, H. *et al.* Theranostic magnetoliposomes coated by carboxymethyl dextran with controlled release by low-frequency alternating magnetic field. *Carbohydr. Polym.* **118,** 209–217 (2015).
43. Kaur, G., Garg, T., Rath, G. & Goyal, A. K. Archaeosomes: an excellent carrier for drug and cell delivery. *Drug Deliv.* 1–16 (2015). doi:10.3109/10717544.2015.1019653
44. Réthoré, G. *et al.* Archaeosomes based on synthetic tetraether-like lipids as novel versatile gene delivery systems. *Chem. Commun. Camb. Engl.* 2054–2056 (2007).
45. Benvegnu, T., Lemiègre, L. & Cammas-Marion, S. New generation of liposomes called archaeosomes based on natural or synthetic archaeal lipids as innovative formulations for drug delivery. *Recent Pat. Drug Deliv. Formul.* **3,** 206–220 (2009).
46. Higa, L. H., Corral, R. S., Morilla, M. J., Romero, E. L. & Petray, P. B. Archaeosomes display immunoadjuvant potential for a vaccine against Chagas disease. *Hum. Vaccines Immunother.* **9,** 409–412 (2013).
47. Müller, R. H., Mäder, K. & Gohla, S. Solid lipid nanoparticles (SLN) for controlled drug delivery – a review of the state of the art. *Eur. J. Pharm. Biopharm.* **50,** 161–177 (2000).
48. Üner, M. & Yener, G. Importance of solid lipid nanoparticles (SLN) in various administration routes and future perspectives. *Int. J. Nanomedicine* **2,** 289–300 (2007).
49. Tam, Y. Y. C., Chen, S. & Cullis, P. R. Advances in Lipid Nanoparticles for siRNA Delivery. *Pharmaceutics* **5,** 498–507 (2013).
50. Ganta, S., Talekar, M., Singh, A., Coleman, T. P. & Amiji, M. M. Nanoemulsions in Translational Research—Opportunities and Challenges in Targeted Cancer Therapy. *AAPS PharmSciTech* **15,** 694–708 (2014).
51. Sutradhar, K. B. & Amin, M. L. Nanoemulsions: increasing possibilities in drug delivery. *Eur. J. Nanomedicine* **5,** 97–110 (2013).
52. Anton, N. & Vandamme, T. F. Nano-emulsions and micro-emulsions: clarifications of the critical differences. *Pharm. Res.* **28,** 978–985 (2011).
53. Lovelyn, C. Current State of Nanoemulsions in Drug Delivery. *J. Biomater. Nanobiotechnology* **02,** 626–639 (2011).
54. Ganta, S. *et al.* EGFR Targeted Theranostic Nanoemulsion for Image-Guided Ovarian Cancer Therapy. *Pharm. Res.* **32,** 2753–2763 (2015).
55. Muzammil Afzal, S., Naidu, V. G. M., Harishankar, N. & Kishan, V. Albumin anchored docetaxel lipid nanoemulsion for improved targeting efficiency - preparation, characterization, cytotoxic, antitumor and in vivo imaging studies. *Drug Deliv.* 1–9 (2015). doi:10.3109/10717544.2015.1030715
56. Shukla, P. *et al.* Nanoemulsion based concomitant delivery of curcumin and etoposide: impact on cross talk between prostate cancer cells and osteoblast during metastasis. *J. Biomed. Nanotechnol.* **10,** 3381–3391 (2014).
57. Hallouard, F. *et al.* Iodinated nano-emulsions as contrast agents for preclinical X-ray imaging: Impact of the free surfactants on the pharmacokinetics. *Eur. J. Pharm. Biopharm.* **83,** 54–62 (2013).
58. Blanazs, A., Armes, S. P. & Ryan, A. J. Self-Assembled Block Copolymer Aggregates: From Micelles to Vesicles and their Biological Applications. *Macromol. Rapid Commun.* **30,** 267–277 (2009).
59. Movassaghian, S., Merkel, O. M. & Torchilin, V. P. Applications of polymer micelles for imaging and drug delivery. *Wiley Interdiscip. Rev. Nanomed. Nanobiotechnol.* (2015). doi:10.1002/wnan.1332
60. Burt, H. M., Zhang, X., Toleikis, P., Embree, L. & Hunter, W. L. Development of

copolymers of poly(d,l-lactide) and methoxypolyethylene glycol as micellar carriers of paclitaxel. *Colloids Surf. B Biointerfaces* **16,** 161–171 (1999).
61. Bian, X. *et al.* Development of PLGA-based itraconazole injectable nanospheres for sustained release. *Int. J. Nanomedicine* **8,** 4521–4531 (2013).
62. Yousaf, A. M. *et al.* Enhanced oral bioavailability of fenofibrate using polymeric nanoparticulated systems: physicochemical characterization and in vivo investigation. *Int. J. Nanomedicine* **10,** 1819–1830 (2015).
63. Yang, J., Liu, H. & Zhang, X. Design, preparation and application of nucleic acid delivery carriers. *Biotechnol. Adv.* **32,** 804–817 (2014).
64. Kim, Y. *et al.* Polymersome delivery of siRNA and antisense oligonucleotides. *J. Control. Release Off. J. Control. Release Soc.* **134,** 132–140 (2009).
65. Kim, H.-O. *et al.* A biodegradable polymersome containing Bcl-xL siRNA and doxorubicin as a dual delivery vehicle for a synergistic anticancer effect. *Macromol. Biosci.* **13,** 745–754 (2013).
66. Ge, X. *et al.* PEG-PCL-DEX polymersome-protamine vector as an efficient gene delivery system via PEG-guided self-assembly. *Nanomed.* **9,** 1193–1207 (2014).
67. Zhang, X. & Wang, C. Supramolecular amphiphiles. *Chem. Soc. Rev.* **40,** 94–101 (2010).
68. Zhang, J. & Ma, P. X. Cyclodextrin-based supramolecular systems for drug delivery: Recent progress and future perspective. *Adv. Drug Deliv. Rev.* **65,** 1215–1233 (2013).
69. Kobayashi, H., Watanabe, R. & Choyke, P. L. Improving Conventional Enhanced Permeability and Retention (EPR) Effects; What Is the Appropriate Target? *Theranostics* **4,** 81–89 (2013).
70. Torchilin, V. Tumor delivery of macromolecular drugs based on the EPR effect. *Adv. Drug Deliv. Rev.* **63,** 131–135 (2011).
71. Maeda, H. The enhanced permeability and retention (EPR) effect in tumor vasculature: the key role of tumor-selective macromolecular drug targeting. *Adv. Enzyme Regul.* **41,** 189–207 (2001).
72. Matsumura, Y. & Maeda, H. A new concept for macromolecular therapeutics in cancer chemotherapy: mechanism of tumoritropic accumulation of proteins and the antitumor agent smancs. *Cancer Res.* **46,** 6387–6392 (1986).
73. Fang, J., Nakamura, H. & Maeda, H. The EPR effect: Unique features of tumor blood vessels for drug delivery, factors involved, and limitations and augmentation of the effect. *Adv. Drug Deliv. Rev.* **63,** 136–151 (2011).
74. Huynh, E. & Zheng, G. Cancer nanomedicine: addressing the dark side of the enhanced permeability and retention effect. *Nanomed.* 1–3 (2015). doi:10.2217/nnm.15.86
75. Noble, G. T., Stefanick, J. F., Ashley, J. D., Kiziltepe, T. & Bilgicer, B. Ligand-targeted liposome design: challenges and fundamental considerations. *Trends Biotechnol.* **32,** 32–45 (2014).
76. Jin, S.-E., Jin, H.-E. & Hong, S.-S. Targeted delivery system of nanobiomaterials in anticancer therapy: from cells to clinics. *BioMed Res. Int.* **2014,** 814208 (2014).
77. Lammers, T., Hennink, W. E. & Storm, G. Tumour-targeted nanomedicines: principles and practice. *Br. J. Cancer* **99,** 392–397 (2008).
78. Bae, Y. H. & Park, K. Targeted drug delivery to tumors: myths, reality and possibility. *J. Control. Release Off. J. Control. Release Soc.* **153,** 198–205 (2011).
79. Jain, A. *et al.* Galactose engineered solid lipid nanoparticles for targeted delivery of doxorubicin. *Colloids Surf. B Biointerfaces* **134,** 47–58 (2015).

80. Guo, B. *et al.* In vitro and in vivo studies of galactose-modified liver-targeting liposomes. *J. Drug Target.* **21,** 257–264 (2012).
81. de Miguel, L., Noiray, M., Surpateanu, G., Iorga, B. I. & Ponchel, G. Poly(γ-benzyl-l-glutamate)-PEG-alendronate multivalent nanoparticles for bone targeting. *Int. J. Pharm.* **460,** 73–82 (2014).
82. Gmeiner, W. H. & Ghosh, S. Nanotechnology for cancer treatment. *Nanotechnol. Rev.* **3,** 111–122 (2015).
83. Paoli, E. E. *et al.* Accumulation, internalization and therapeutic efficacy of neuropilin-1-targeted liposomes. *J. Control. Release Off. J. Control. Release Soc.* **178,** 108–117 (2014).
84. Oliveira, S., Heukers, R., Sornkom, J., Kok, R. J. & Van Bergen En Henegouwen, P. M. P. Targeting tumors with nanobodies for cancer imaging and therapy. *J. Controlled Release* **172,** 607–617 (2013).
85. Chames, P., Van Regenmortel, M., Weiss, E. & Baty, D. Therapeutic antibodies: successes, limitations and hopes for the future. *Br. J. Pharmacol.* **157,** 220–233 (2009).
86. Bothun, G. D. *et al.* Multicomponent folate-targeted magnetoliposomes: design, characterization, and cellular uptake. *Nanomedicine Nanotechnol. Biol. Med.* **7,** 797–805 (2011).
87. Gabizon, A. *et al.* In Vivo Fate of Folate-Targeted Polyethylene-Glycol Liposomes in Tumor-Bearing Mice. *Clin Cancer Res* ***9****;* 6551 (2003)
88. Leamon, C. P., Cooper, S. R. & Hardee, G. E. Folate-liposome-mediated antisense oligodeoxynucleotide targeting to cancer cells: evaluation in vitro and in vivo. *Bioconjug. Chem.* **14,** 738–747 (2003).
89. Kunjachan, S. *et al.* Passive vs. Active Tumor Targeting using RGD-and NGR-modified Polymeric Nanomedicines. *Nano Lett.* **14,** 972–981 (2014).
90. McNeeley, K. M., Karathanasis, E., Annapragada, A. V. & Bellamkonda, R. V. Masking and triggered unmasking of targeting ligands on nanocarriers to improve drug delivery to brain tumors. *Biomaterials* **30,** 3986–3995 (2009).
91. Yang, Y. *et al.* Dual-modified liposomes with a two-photon-sensitive cell penetrating peptide and NGR ligand for siRNA targeting delivery. *Biomaterials* **48,** 84–96 (2015).
92. Davis, M. E. *et al.* Evidence of RNAi in humans from systemically administered siRNA via targeted nanoparticles. *Nature* **464,** 1067–1070 (2010).
93. Hrkach, J. *et al.* Preclinical Development and Clinical Translation of a PSMA-Targeted Docetaxel Nanoparticle with a Differentiated Pharmacological Profile. *Sci. Transl. Med.* **4,** (2012).
94. Krishnan, V. & Rajasekaran, A. K. Clinical Nanomedicine: A Solution to the Chemotherapy Conundrum in Pediatric Leukemia Therapy. *Clin. Pharmacol. Ther.* **95,** 168–178 (2014).
95. Reynolds, J. G. *et al.* HER2-targeted liposomal doxorubicin displays enhanced anti-tumorigenic effects without associated cardiotoxicity. *Toxicol. Appl. Pharmacol.* **262,** 1–10 (2012).
96. Matsumura, Y. *et al.* Phase I and pharmacokinetic study of MCC-465, a doxorubicin (DXR) encapsulated in PEG immunoliposome, in patients with metastatic stomach cancer. *Ann. Oncol. Off. J. Eur. Soc. Med. Oncol. ESMO* **15,** 517–525 (2004).
97. Riboflavin. Monograph. *Altern. Med. Rev. J. Clin. Ther.* **13,** 334–340 (2008).
98. Massey, V. The chemical and biological versatility of riboflavin. *Biochem. Soc. Trans.* **28,** 283–296 (2000).
99. Witte, A. B. *et al.* Biophysical Characterization of a Riboflavin-conjugated

Dendrimer Platform for Targeted Drug Delivery. *Biomacromolecules* **13,** 507–516 (2012).
100. Iida, H., Mizoguchi, T., Oh, S.-D. & Yashima, E. Redox-triggered switching of helical chirality of poly(phenylacetylene)s bearing riboflavin pendants. *Polym. Chem.* **1,** 841–848 (2010).
101. Bairi, P., Chakraborty, P., Mondal, S., Roy, B. & Nandi, A. K. A thixotropic supramolecular hydrogel of adenine and riboflavin-5'-phosphate sodium salt showing enhanced fluorescence properties. *Soft Matter* **10,** 5114–5120 (2014).
102. Manna, S., Saha, A. & Nandi, A. K. A two component thermoreversible hydrogel of riboflavin and melamine: Enhancement of photoluminescence in the gel form. *Chem. Commun. Camb. Engl.* 4285–4287 (2006). doi:10.1039/b608234c
103. Jayapaul, J. *et al.* Riboflavin carrier protein-targeted fluorescent USPIO for the assessment of vascular metabolism in tumors. *Biomaterials* **33,** 8822–8829 (2012).
104. Jayapaul, J. *et al.* FMN-coated fluorescent iron oxide nanoparticles for RCP-mediated targeting and labeling of metabolically active cancer and endothelial cells. *Biomaterials* **32,** 5863–5871 (2011).
105. Tsvetkova, Y. *et al.* Refinement of adsorptive coatings for fluorescent riboflavin-receptor-targeted iron oxide nanoparticles. *Contrast Media Mol. Imaging* (2015). doi:10.1002/cmmi.1657
106. Ju, S.-Y. & Papadimitrakopoulos, F. Synthesis and redox behavior of flavin mononucleotide-functionalized single-walled carbon nanotubes. *J. Am. Chem. Soc.* **130,** 655–664 (2008).
107. Lee, T., Tsai, M. H. & Lee, H. L. Riboflavin Chelated Luminescent Metal–Organic Framework: Identified by Liquid-Assisted Grinding for Large-Molecule Sensing via Chromaticity Coordinates. *Cryst. Growth Des.* **12,** 3181–3190 (2012).
108. Johnson, T. *et al.* Biochemical characterization of riboflavin carrier protein (RCP) in prostate cancer. *Front. Biosci. Landmark Ed.* **14,** 3634–3640 (2009).
109. Karande, A. A., Sridhar, L., Gopinath, K. S. & Adiga, P. R. Riboflavin carrier protein: a serum and tissue marker for breast carcinoma. *Int. J. Cancer J. Int. Cancer* **95,** 277–281 (2001).
110. Rao, P. N. *et al.* Elevation of serum riboflavin carrier protein in hepatocellular carcinoma. *Hepatol. Res. Off. J. Jpn. Soc. Hepatol.* **35,** 83–87 (2006).
111. Xuan, Z. *et al.* Exploration of the protection of riboflavin laurate on oral mucositis induced by chemotherapy or radiotherapy at the cellular level: what is the leading contributor? *Int. J. Mol. Sci.* **14,** 4722–4733 (2013).
112. Hu, X. *et al.* Biocompatible riboflavin laurate long-acting injectable nanosuspensions allowing sterile filtration. *Drug Deliv.* **21,** 351–361 (2014).
113. Matricardi, P., Di, M. C. & Villani, C. Novel polymer platform to prepare nanohydrogel. Patent WO/2015071873/A1(2015).
114. Yao, Y. *et al.* Identification and comparative functional characterization of a new human riboflavin transporter hRFT3 expressed in the brain. *J. Nutr.* **140,** 1220–1226 (2010).
115. Johnson, T. *et al.* Biochemical characterization of riboflavin carrier protein (RCP) in prostate cancer. *Front. Biosci. Landmark Ed.* **14,** 3634–3640 (2009).
116. Thomas, T. P., Choi, S. K., Li, M.-H., Kotlyar, A. & Baker, J. R. Design of riboflavin-presenting PAMAM dendrimers as a new nanoplatform for cancer-targeted delivery. *Bioorg. Med. Chem. Lett.* **20,** 5191–5194 (2010).
117. Marlin, F. *et al.* Flavin Conjugates for Delivery of Peptide Nucleic Acids. *ChemBioChem* **13,** 2593–2598 (2012).

118. Witte, A. B. *et al.* Atomic Force Microscopy Probing of Receptor–Nanoparticle Interactions for Riboflavin Receptor Targeted Gold–Dendrimer Nanocomposites. *J. Phys. Chem. B* **118,** 2872–2882 (2014).
119. Holladay, S. R. *et al.* Riboflavin-mediated delivery of a macromolecule into cultured human cells. *Biochim. Biophys. Acta* **1426,** 195–204 (1999).
120. Yonezawa, A. & Inui, K. Novel riboflavin transporter family RFVT/SLC52: identification, nomenclature, functional characterization and genetic diseases of RFVT/SLC52. *Mol. Aspects Med.* **34,** 693–701 (2013).
121. Monaco, H. L. Crystal structure of chicken riboflavin-binding protein. *EMBO J.* **16,** 1475–1483 (1997).
122. Kolb, H. C., Finn, M. G. & Sharpless, K. B. Click Chemistry: Diverse Chemical Function from a Few Good Reactions. *Angew. Chem. Int. Ed.* **40,** 2004–2021 (2001).
123. Ritter, S. C. & König, B. Signal amplification and transduction by photo-activated catalysis. *Chem. Commun.* 4694–4696 (2006). doi:10.1039/B610696J
124. Caelen, I., Kalman, A. & Wahlström, L. Biosensor-based determination of riboflavin in milk samples. *Anal. Chem.* **76,** 137–143 (2004).
125. Li, Z. & Bittman, R. Synthesis and Spectral Properties of Cholesterol- and FTY720-Containing Boron Dipyrromethene Dyes. *J. Org. Chem.* **72,** 8376–8382 (2007).
126. Russell, M. A., Laws, A. P., Atherton, J. H. & Page, M. I. The mechanism of the phosphoramidite synthesis of polynucleotides. *Org. Biomol. Chem.* **6,** 3270–3275 (2008).
127. Rublack, N. *et al.* Synthesis of Specifically Modified Oligonucleotides for Application in Structural and Functional Analysis of RNA. *J. Nucleic Acids* **2011,** (2011).
128. Neises, B. & Steglich, W. Simple Method for the Esterification of Carboxylic Acids. *Angew. Chem. Int. Ed. Engl.* **17,** 522–524 (1978).
129. Enjalbal, C. *et al.* MALDI-TOF MS Analysis of Soluble PEG Based Multi-Step Synthetic Reaction Mixtures with Automated Detection of Reaction Failure. *J. Am. Soc. Mass Spectrom.* **16,** 670–678 (2005).
130. Nagarajan, R. Molecular Packing Parameter and Surfactant Self-Assembly: The Neglected Role of the Surfactant Tail†. *Langmuir* **18,** 31–38 (2002).
131. Hiemenz, P. C. & Rajagopalan, R. *Principles of Colloid and Surface Chemistry, Third Edition, Revised and Expanded*, ISBN 9780824793975 (1997).
132. Kronberg, B., Holmberg, K. & Lindman, B. *Surface Chemistry of Surfactants and Polymers*. (2014).
133. Khalil, R. A. & Zarari, A. A. Theoretical estimation of the critical packing parameter of amphiphilic self-assembled aggregates. *Appl. Surf. Sci.* **318,** 85–89 (2014).
134. Iida, H., Iwahana, S., Mizoguchi, T. & Yashima, E. Main-Chain Optically Active Riboflavin Polymer for Asymmetric Catalysis and Its Vapochromic Behavior. *J. Am. Chem. Soc.* **134,** 15103–15113 (2012).
135. Brown, M. F., Lope-Piedrafita, S., Martinez, G. V. & Petrache, H. I. in *Modern Magnetic Resonance* (ed. Webb, G. A.) 249–260 (2008).
136. Thurmond, R. L., Lindblom, G. & Brown, M. F. Curvature, order, and dynamics of lipid hexagonal phases studied by deuterium NMR spectroscopy. *Biochemistry (Mosc.)* **32,** 5394–5410 (1993).
137. Canet D., Bouguet-Bonnet S., Leclerc S. *RMN Express. Résonance Magnétique Nucléaire : spins 1/2, état liquide*, ISBN-13 978-2-8143-0048-4 (2011).
138. Dufourc, E. J. Solid state NMR in biomembranes. *Chemical Biology* (eds. Larijani, B., Rosser, C. A. & Woscholski, R.) 113–131 (2006).
139. Dybowski*, C. & Bai, S. Solid-State NMR Spectroscopy. *Anal. Chem.* **80,** 4295–4300 (2008).

140. Beck, J. G., Mathieu, D., Loudet, C., Buchoux, S. & Dufourc, E. J. Plant sterols in 'rafts': a better way to regulate membrane thermal shocks. *FASEB J.* **21,** 1714–1723 (2007).
141. Vermeer, L. S., de Groot, B. L., Réat, V., Milon, A. & Czaplicki, J. Acyl chain order parameter profiles in phospholipid bilayers: computation from molecular dynamics simulations and comparison with 2H NMR experiments. *Eur. Biophys. J. EBJ* **36,** 919–931 (2007).
142. Grelard, A. *et al.* Hepatitis B subvirus particles display both a fluid bilayer membrane and a strong resistance to freeze drying: a study by solid-state NMR, light scattering, and cryo-electron microscopy/tomography. *FASEB J.* **27,** 4316–4326 (2013).
143. Davis, J. H. The description of membrane lipid conformation, order and dynamics by 2H-NMR. *Biochim. Biophys. Acta* **737,** 117–171 (1983).
144. Milne, J. L. S. *et al.* Cryo-electron microscopy: A primer for the non-microscopist. *FEBS J.* **280,** 28–45 (2013).
145. Kučerka, N., Nieh, M.-P. & Katsaras, J. Fluid phase lipid areas and bilayer thicknesses of commonly used phosphatidylcholines as a function of temperature. *Biochim. Biophys. Acta BBA - Biomembr.* **1808,** 2761–2771 (2011).
146. Laroche, G., Dufourc, E. J., Dufourcq, J. & Pézolet, M. Structure and dynamics of dimyristoylphosphatidic acid/calcium complexes by 2H NMR, infrared, spectroscopies and small-angle x-ray diffraction. *Biochemistry (Mosc.)* **30,** 3105–3114 (1991).
147. Tai, S. *et al.* PC3 Is a Cell Line Characteristic of Prostatic Small Cell Carcinoma. *The Prostate* **71,** 1668–1679 (2011).
148. Chang, H.-I. & Yeh, M.-K. Clinical development of liposome-based drugs: formulation, characterization, and therapeutic efficacy. *Int. J. Nanomedicine* **7,** 49–60 (2012).
149. Phelps, M. A., Foraker, A. B., Gao, W., Dalton, J. T. & Swaan, P. W. A novel rhodamine-riboflavin conjugate probe exhibits distinct fluorescence resonance energy transfer that enables riboflavin trafficking and subcellular localization studies. *Mol. Pharm.* **1,** 257–266 (2004).
150. Patwa, A., Gissot, A., Bestel, I. & Barthélémy, P. Hybrid lipid oligonucleotide conjugates: synthesis, self-assemblies and biomedical applications. *Chem. Soc. Rev.* **40,** 5844–5854 (2011).
151. Graness, A., Hanke, S., Boehmer, F. D., Presek, P. & Liebmann, C. Protein-tyrosine-phosphatase-mediated epidermal growth factor (EGF) receptor transinactivation and EGF receptor-independent stimulation of mitogen-activated protein kinase by bradykinin in A431 cells. *Biochem. J.* **347,** 441–447 (2000).
152. Castle, J. C. *et al.* Immunomic, genomic and transcriptomic characterization of CT26 colorectal carcinoma. *BMC Genomics* **15,** 190 (2014).
153. Park, H.-J. *et al.* Human umbilical vein endothelial cells and human dermal microvascular endothelial cells offer new insights into the relationship between lipid metabolism and angiogenesis. *Stem Cell Rev.* **2,** 93–101 (2006).
154. Biswas, S., Dodwadkar, N. S., Sawant, R. R., Koshkaryev, A. & Torchilin, V. P. Surface modification of liposomes with rhodamine-123-conjugated polymer results in enhanced mitochondrial targeting. *J. Drug Target.* **19,** 552–561 (2011).
155. Chen, H., Ahn, R., Bossche, J. V. den, Thompson, D. H. & O'Halloran, T. V. Folate-mediated intracellular drug delivery increases the anticancer efficacy of nanoparticulate formulation of arsenic trioxide. *Mol. Cancer Ther.* **8,** 1955–1963 (2009).
156. Kaji, T., Kawashima, T., Sakamoto, M., Kurashige, Y. & Koizumi, F. Inhibitory effect of rhodamine B on the proliferation of human lip fibroblasts in culture. *Toxicology* **68,**

11–20 (1991).
157. Robinson, S., Dean, B. & Petty, B. Characterization of the a431 tumor xenograft as an invivo model for testing epidermal growth factor-receptor antagonists. *Int. J. Oncol.* **1,** 293–298 (1992).
158. Hofmann, M. *et al.* Lowering of Tumor Interstitial Fluid Pressure Reduces Tumor Cell Proliferation in a Xenograft Tumor Model. *Neoplasia N. Y. N* **8,** 89–95 (2006).
159. Park, S. I., Kim, S. J., McCauley, L. K. & Gallick, G. E. Pre-Clinical Mouse Models of Human Prostate Cancer and their Utility in Drug Discovery. *Curr. Protoc. Pharmacol. Editor. Board SJ Enna Ed.--Chief Al* **51,** 14.15–14.15.27 (2010).
160. Luke, G. P., Yeager, D. & Emelianov, S. Y. Biomedical applications of photoacoustic imaging with exogenous contrast agents. *Ann. Biomed. Eng.* **40,** 422–437 (2012).
161. Needles, A. *et al.* Development and initial application of a fully integrated photoacoustic micro-ultrasound system. *IEEE Trans. Ultrason. Ferroelectr. Freq. Control* **60,** 888–897 (2013).
162. Photoacoustic Imaging, a Fast-Developing Imaging Technique for Biomedicine at <http://health.embs.org/editorial-blog/imaging-listening-sound-light-photoacoustic-imaging-fast-developing-imaging-technique-biomedicine/>
163. Bohndiek, S. E., Bodapati, S., Van De Sompel, D., Kothapalli, S.-R. & Gambhir, S. S. Development and Application of Stable Phantoms for the Evaluation of Photoacoustic Imaging Instruments. *PLoS ONE* **8,** e75533 (2013).
164. Yin, M., Lakshman, M. & Foster, F. S. Quantitative functional assessment of tumour microenvironment using contrast enhanced ultrasound and photoacoustic imaging. in *Ultrasonics Symposium (IUS), 2013 IEEE International* 1833–1836 (2013).
165. Gremse, F. *et al.* Hybrid μCT-FMT imaging and image analysis. *J. Vis. Exp. JoVE* (2015). doi:10.3791/52770
166. Cristobal, G., Schelkens, P. & Thienpont, H. *Optical and Digital Image Processing: Fundamentals and Applications*, ISBN: 9783527635245 (2013).
167. Gremse, F. *et al.* Absorption Reconstruction Improves Biodistribution Assessment of Fluorescent Nanoprobes Using Hybrid Fluorescence-mediated Tomography. *Theranostics* **4,** 960–971 (2014).
168. Mérian, J., Gravier, J., Navarro, F. & Texier, I. Fluorescent nanoprobes dedicated to in vivo imaging: from preclinical validations to clinical translation. *Mol. Basel Switz.* **17,** 5564–5591 (2012).
169. Slepushkin, V. A. *et al.* Sterically Stabilized pH-sensitive Liposomes INTRACELLULAR DELIVERY OF AQUEOUS CONTENTS AND PROLONGED CIRCULATION IN VIVO. *J. Biol. Chem.* **272,** 2382–2388 (1997).
170. Borst, J. W., Visser, N. V., Kouptsova, O. & Visser, A. J. W. G. Oxidation of unsaturated phospholipids in membrane bilayer mixtures is accompanied by membrane fluidity changes. *Biochim. Biophys. Acta BBA - Mol. Cell Biol. Lipids* **1487,** 61–73 (2000).
171. Ta, T. & Porter, T. M. Thermosensitive liposomes for localized delivery and triggered release of chemotherapy. *J. Controlled Release* **169,** 112–125 (2013).
172. Wust, P. *et al.* Hyperthermia in combined treatment of cancer. *Lancet Oncol.* **3,** 487–497 (2002).
173. Affram, K., Udofot, O. & Agyare, E. Cytotoxicity of gemcitabine-loaded thermosensitive liposomes in pancreatic cancer cell lines. *Integr. Cancer Sci. Ther.* **2,** 133–142 (2015).
174. Zhang, K. *et al.* Aptamer-modified Temperature-sensitive Liposomal Contrast Agent for MR Imaging. *Biomacromolecules* (2015). doi:10.1021/acs.biomac.5b00250
175. Dicheva, B. M. *et al.* Enhanced Specificity and Drug Delivery in Tumors by cRGD -

Anchoring Thermosensitive Liposomes. *Pharm. Res.* (2015). doi:10.1007/s11095-015-1746-7
176. Mosca, M., Ceglie, A. & Ambrosone, L. Effect of membrane composition on lipid oxidation in liposomes. *Chem. Phys. Lipids* **164,** 158–165 (2011).
177. Santos, N. Dos *et al.* Influence of poly(ethylene glycol) grafting density and polymer length on liposomes: Relating plasma circulation lifetimes to protein binding. *Biochim. Biophys. Acta BBA - Biomembr.* **1768,** 1367–1377 (2007).
178. Soundararajan, A., Bao, A., Phillips, W. T., Perez, R. & Goins, B. A. 186Re-Liposomal Doxorubicin (Doxil): In Vitro Stability, Pharmacokinetics, Imaging and Biodistribution in a Head and Neck Squamous Cell Carcinoma Xenograft Model. *Nucl. Med. Biol.* **36,** 515–524 (2009).
179. Garbuzenko, O., Zalipsky, S., Qazen, M. & Barenholz, Y. Electrostatics of PEGylated micelles and liposomes containing charged and neutral lipopolymers. *Langmuir ACS J. Surf. Colloids* **21,** 2560–2568 (2005).
180. Lu, W.-L. *et al.* A pegylated liposomal platform: pharmacokinetics, pharmacodynamics, and toxicity in mice using doxorubicin as a model drug. *J. Pharmacol. Sci.* **95,** 381–389 (2004).
181. Rouser, G., Fkeischer, S. & Yamamoto, A. Two dimensional then layer chromatographic separation of polar lipids and determination of phospholipids by phosphorus analysis of spots. *Lipids* **5,** 494–496 (1970).
182. Alander, J. T. *et al.* A Review of Indocyanine Green Fluorescent Imaging in Surgery. *Int. J. Biomed. Imaging* **2012,** e940585 (2012).
183. Desmettre, T., Devoisselle, J. M. & Mordon, S. Fluorescence Properties and Metabolic Features of Indocyanine Green (ICG) as Related to Angiography. *Surv. Ophthalmol.* **45,** 15–27 (2000).
184. Beziere, N. *et al.* Dynamic imaging of PEGylated indocyanine green (ICG) liposomes within the tumor microenvironment using multi-spectral optoacoustic tomography (MSOT). *Biomaterials* **37,** 415–424 (2015).
185. Shemesh, C. S., Moshkelani, D. & Zhang, H. Thermosensitive Liposome Formulated Indocyanine Green for Near-Infrared Triggered Photodynamic Therapy: In Vivo Evaluation for Triple-Negative Breast Cancer. *Pharm. Res.* (2014). doi:10.1007/s11095-014-1560-7
186. Lozano, N., Al-Ahmady, Z. S., Beziere, N. S., Ntziachristos, V. & Kostarelos, K. Monoclonal antibody-targeted PEGylated liposome-ICG encapsulating doxorubicin as a potential theranostic agent. *Int. J. Pharm.* (2014). doi:10.1016/j.ijpharm.2014.10.045
187. Pansare, V. J., Hejazi, S., Faenza, W. J. & Prud'homme, R. K. Review of Long-Wavelength Optical and NIR Imaging Materials: Contrast Agents, Fluorophores, and Multifunctional Nano Carriers. *Chem. Mater.* **24,** 812–827 (2012).
188. Ruan, J. *et al.* DiR-labeled Embryonic Stem Cells for Targeted Imaging of *in vivo* Gastric Cancer Cells. *Theranostics* **2,** 618–628 (2012).
189. Kalchenko, V. *et al.* Use of lipophilic near-infrared dye in whole-body optical imaging of hematopoietic cell homing. *J. Biomed. Opt.* **11,** 050507 (2006).
190. Sipkins, D. A. *et al.* In vivo imaging of specialized bone marrow endothelial microdomains for tumour engraftment. *Nature* **435,** 969–973 (2005).
191. Hadjidemetriou, M. *et al.* In Vivo Biomolecule Corona around Blood-Circulating, Clinically-Used and Antibody-Targeted Lipid Bilayer Nanoscale Vesicles. *ACS Nano* (2015). doi:10.1021/acsnano.5b03300
192. Azar, F. S. & Intes, X. *Translational Multimodality Optical Imaging*. (2008).
193. Anastasio, M. A. & Riviere, P. L. *Emerging Imaging Technologies in Medicine*.

(2012).
194. Repenko, T. *et al.* Water-soluble dopamine-based polymers for photoacoustic imaging. *Chem. Commun.* **51,** 6084–6087 (2015).
195. Song, W. *et al.* Comprehensive studies of pharmacokinetics and biodistribution of indocyanine green and liposomal indocyanine green by multispectral optoacoustic tomography. *RSC Adv.* **5,** 3807–3813 (2014).
196. Leamon, C. P., Cooper, S. R. & Hardee, G. E. Folate-liposome-mediated antisense oligodeoxynucleotide targeting to cancer cells: evaluation in vitro and in vivo. *Bioconjug. Chem.* **14,** 738–747 (2003).
197. Kunjachan, S. *et al.* Noninvasive Optical Imaging of Nanomedicine Biodistribution. *ACS Nano* **7,** 252–262 (2013).
198. Fridman, R., Benton, G., Aranoutova, I., Kleinman, H. K. & Bonfil, R. D. Increased initiation and growth of tumor cell lines, cancer stem cells and biopsy material in mice using basement membrane matrix protein (Cultrex or Matrigel) co-injection. *Nat. Protoc.* **7,** 1138–1144 (2012).
199. Sawant, R. R. & Torchilin, V. P. Challenges in Development of Targeted Liposomal Therapeutics. *AAPS J.* **14,** 303–315 (2012).
200. Mouse models of prostate cancer. *Publ. Online 20 Sept. 1999 Doi101038sjonc1203037* **18,** (1999).
201. Arraud, N. *et al.* Extracellular vesicles from blood plasma: determination of their morphology, size, phenotype and concentration. *J. Thromb. Haemost.* **12,** 614–627 (2014).
202. Ertl, P., Rohde, B. & Selzer, P. Fast Calculation of Molecular Polar Surface Area as a Sum of Fragment-Based Contributions and Its Application to the Prediction of Drug Transport Properties. *J. Med. Chem.* **43,** 3714–3717 (2000).
203. Pronk, S. *et al.* GROMACS 4.5: a high-throughput and highly parallel open source molecular simulation toolkit. *Bioinformatics* **29,** 845–854 (2013).
204. van Gunsteren, W. *et al. Biomolecular Simulation: The {GROMOS96} manual and userguide*, ISBN 3 7281 2422 2, (1996).
205. Bangaru, M. L. Y. & Karande, A. A. Biochemical characterization of recombinant chicken Riboflavin carrier protein. *Mol. Cell. Biochem.* **308,** 1–7 (2008).

10 Table of figures, schemes and tables

10.1Figures

10.2 Schemes

10.3 Tables

11 Publications and scientific communications

Publications:

- **Beztsinna N**., Tsvetkova Y., Al Rawashdeh W., Frih B., Lammers T., Kiessling F., Bestel I. Amphiphile derivatives of riboflavin for tumour-targeted optoacoustic contrast agents. (*in preparation*)

- **Beztsinna N**., Tsvetkova Y., Bartneck M., Lammers T., Kiessling F., Bestel I. An amphiphilic building block for targeting nanomedicines *via* riboflavin transporter systems. (*submitted*)

- **Beztsinna N**., Solé M., Taib N., Bestel I. Bioengineered riboflavin in nanotechnology. *Biomaterials* - 2016*, 80***,** pp 121–133.

- Tsvetkova Y., **Beztsinna N**., Jayapaul J., Weiler M., Arns S., Shi Y., Lammers T., Kiessling F. Refinement of adsorptive coatings for fluorescent riboflavin-receptor-targeted iron oxide nanoparticles. *Contrast Media Mol Imaging* – 2015, Aug 11. doi: 10.1002/cmmi.1657.

- Aimé A., **Beztsinna N**., Patwa A., Pokholenko A., Bestel I., Barthélémy Ph. Quantum dot Lipid Oligonucleotide Bioconjugates: Towards a new anti-microRNA nanoplatform. *Bioconjugate Chemistry*– 2013, *24* (8), pp 1345–1355.

- Leus I.V., Skorik E.D., **Beztsinna N.V**., Shtemenko N.I. Influence of ligand structure on anticancer and antioxidant properties of Rhenium cluster compounds (ua). *Visnyk of Dnipropetrovsk University. Biology. Ecology*. – 2009, *17* (3), pp. 46–53.

Communications:

1. **ECIS 2015**, 6-11 September 2015, poster: RIBOFLAVIN BIO-INSPIRED AMPHIPHILES: FROM PHYSICOCHEMISTRY TO BIOMEDICAL APPLICATIONS, *Bordeaux*
2. **WMIC 2015**, 2-5 September 2015, **oral communication:** RIBOFLAVIN AMPHIPHILES FOR TUMOR-TARGETED NANOMEDECINES, *Honolulu*
3. **EMIM 2015**, 18-20 March 2015, **oral communication** SPECIFIC DELIVERY OF TARGETED NANOSYSTEMS VIA RIBOFLAVIN TRANSPORTERS TO CANCER CELLS, *Tuebingen*
4. **SFNano Annual Meeting**, 9-12 December 2014, **poster**: NEW AMPHIPHILE RIBOFLAVIN DERIVATIVES FOR BIOMEDICAL APPLICATIONS, *Nancy* ***(poster prize)***
5. **XXIII International Symposium on Medicinal Chemistry - EFMC-ISMC 2014** 7-11 September 2014 **poster**: NEW AMPHIPHILE RIBOFLAVIN DERIVATIVES FOR BIOMEDICAL APPLICATIONS, *Lisbon*
6. **RICT 2014 Interfacing Chemical Biology and Drug Discovery. 50th International Conference on Medicinal Chemistry** 2-4 July 2014 **poster:** IMPLEMENTATION OF A HUMAN SERUM ALBUMIN-BASED PLATFORM FOR microRNA DELIVERY, *Rouen*
7. **RICT 2014** 2-4 July 2014 **poster:** Riboflavin derivatives – based bioinks for bioprinting in the context of Keratokonus, *Rouen*

8. **Young Scientist Symposium in Therapeutic Chemistry** 24-25 March 2014 **poster** Riboflavin derivatives – based bioinks for bioprinting in the context of Keratokonus, *Montpellier (**poster prize***)

9. **RNA club** 24 September 2013 **oral communication**: Amphiphile oligonucleotides – agonists of TLR7, *Bordeaux*

10. **49th International Conference on Medicinal Chemistry RICT 2013** 3–5 July 2013 **poster**: AMPHIPHILE microRNA MIMIC-BASED PLATFORM FOR HEPATOCELLULAR CARCINOMA THERAPY, *Nice*

11. **SFR TecSan Symposium** 27 June 2013 **poster: VITA-BIOPRINT:** RIBOFLAVIN AMPHIPHILE DERIVATIVES FOR KERATOCONUS TREATMENT BY BIOPRINTING APPROACH, *Bordeaux **(poster prize)***

12. **French Annual meeting of Young Medicinal Chemists** 7–8 February 2013 **poste**r AMPHIPHILE microRNA MIMIC-BASED PLATFORM FOR HEPATOCELLULAR CARCINOMA THERAPY, *Paris **(poster prize)***

13. **Annual meeting of Pharmaceutical Society of Bordeaux** 31 January 2013 **oral communication**: Targeted auto-vectorised oligonucleotides for the spesific delivery of microRNAs in hepatocellular carcinoma, *Bordeaux*

14. **GTRV Symposium** 3-5 December 2012 **poster**: AMPHIPHILE microRNA MIMIC-BASED PLATFORM FOR HEPATOCELLULAR CARCINOMA THERAPY, *Paris*

Titre : Dérivés amphiphiles de la riboflavine pour le développement de nano-systèmes à ciblage tumoral

Résumé :

La riboflavine (RF) est une vitamine essentielle pour la croissance et le développement cellulaire. Elle possède des propriétés physico-chimiques intéressantes et est internalisée dans les cellules par des transporteurs spécifiques. Le premier objectif de ce projet était de synthétiser des dérivés amphiphiles de la RF (RFA) et d'étudier leurs capacités d'auto-assemblages. Le second objectif était d'insérer les RFA dans des liposomes et d'évaluer leur efficacité de ciblage tumoral *in vitro* et *in vivo*. La préparation des différents RFA repose sur l'ajout d'un lipide en différentes positions de la RF. L'un d'eux, de type phospholipide (RfdiC14) a été capable de former des objets tridimensionnels de taille µm constitués de lamelles multicouches dont l'architecture et la dynamique sont très différentes de celles des phospholipides classiques. L'insertion de RfdiC14 dans des liposomes est efficace et n'influence pas leurs propriétés physico-chimiques. Les liposomes fonctionnalisés ont montré une internalisation cellulaire spécifique dans les lignées A431, PC3 et HUVECs. Afin de tester l'efficacité du ciblage tumoral *in vivo*, un analogue de RfdiC14 portant un espaceur PEG a été préparé puis inséré dans des liposomes péguylés. Grâce à un marquage adéquat (ICG et DiR), leur accumulation tumorale a été suivie par imagerie photoacoustique dans un modèle A431 et leur biodistribution évaluée par imagerie µCT/FMT dans un modèle PC3. Les résultats montrent une légère amélioration de l'accumulation tumorale dans les xenogreffes A431 et une augmentation du ciblage vasculaire dans le modèle tumoral PC3. La biodistribution globale des liposomes marqués est comparable à celle des contrôles.

Mots clés :

Amphiphile, riboflavine, auto-assemblage, nanosystèmes, ciblage actif, cancer

---

Title: Riboflavin-based amphiphiles for tumour-targeted nanosystems

Abstract:

Riboflavin (RF) is an essential vitamin for cell growth and development. It possesses interesting physicochemical properties and is internalised by the cells through specific transporters. The first aim of this study was to prepare amphiphile derivatives of RF (RFA) and study their auto-assembly. The second aim was to insert RFA into established drug delivery systems and test their tumour-targeting potential *in vitro* and *in vivo*. RFA were prepared by the molecule functionalisation with lipid moieties in different positions. One of them, a phospholipid-like derivative (RfdiC14) was able to self-assembly in aqueous solutions into µm-sized 3D objects constituted from slightly curved multilayer lamellas. The bilayer architecture and dynamics were very different from ordinary phospholipids. In contrast, the insertion of small amount of RfdiC14 in a liposome did not influence membrane dynamics and physicochemical characteristics. RfdiC14-functionalised liposomes displayed high and specific uptake *in vitro* in A431, PC3 cells and HUVECs. The efficiency of RF targeting was also tested *in vivo.* For that purpose, liposome composition was optimised and a new RF amphiphile with a PEG spacer between RF and lipid was prepared. The tumour accumulation of the liposomes labelled with ICG was studied by photoacoustic imaging in A431 tumour model. The biodistribution of DiR labelled liposomes was accessed by combined µCT/FMT imaging in PC3 tumour model. The results show slight improvement of the tumour accumulation in A431 xenographts and the enhancement of vascular targeting in PC3 tumour model. The overall biodistribution of the RF-targeted liposomes was comparable to control.

Keywords:

Amphiphile, riboflavin, auto-assembly, nanosystems, active targeting, cancer

---

Institut de Chimie et de la Biologie des Membranes et Nano-objets

[C.B.M.N. (UMR 5248), CNRS-Université Bordeaux 1-IPB

Allée Geoffroy St Hilaire, Bat B14, 33600 Pessac, France**]**